



**FINAL REPORT**

1191 | 2019 – Frankfurt am Main

# AdBlue Deposits

## AdBlue Deposits

Grundlegende experimentelle und numerische Untersuchungen zur Ablagerungsbildung  
und -zersetzung aus AdBlue in SCR-Systemen

Fundamental experimental and numerical investigations on the deposit formation  
and decomposition from AdBlue in SCR-systems

© 2019 FVV – Frankfurt am Main

**Das Urheberrecht an diesem Bericht mit sämtlichen Beilagen verbleibt der FVV.  
Ohne schriftliche Genehmigung der FVV darf der Bericht weder kopiert noch vervielfältigt werden.**

All rights reserved. No part of this publication may be reproduced or transmitted, in any form or by any means, electronic, mechanical, photocopying, recording, without the written permission of the FVV.

**Die FVV übernimmt keine Gewähr für die Richtigkeit, Genauigkeit und  
Vollständigkeit der Angaben sowie die Beachtung privater Rechte Dritter.**

The FVV assumes no legal liability or responsibility for the correctness, accuracy and completeness of the information or for the observance of third-party rights.

# AdBlue Deposits

Project no. 1262

---

## Fundamental experimental and numerical investigation on the deposit formation and decomposition from AdBlue in SCR-systems

---

### Final report

#### Abstract:

Based on legislation for diesel engines a further minimization of emissions of nitrogen oxides ( $\text{NO}_x$ ) is essential. The selective catalytic reduction (SCR) is therefore an efficient and widely used method, often in combination with other emission control devices. In SCR systems, urea is injected into the tailpipe as an urea-water solution (UWS). Water evaporation and decomposition of the urea content yield to an ammonia production in front of the SCR catalyst. Due to highly transient conditions and a limited mixing length incomplete spray evaporation may lead to droplet impingement on the tailpipe, where wall film is formed on low load points. Accumulated liquid film can induce solid formation due to urea crystallization and by-product formation, which impedes the SCR efficiency.

This work deals with interaction of AdBlue sprays with hot tail pipes, resulting wall film formation and accumulation of deposits from liquid film. For investigations in application scale, a lab test bench at KIT and an engine test bench at TUW are installed, which enable experiments on film- and deposit formation under realistic conditions. Generated solid deposits are sampled for detailed analysis of topology and chemical composition by thermogravimetric analysis (TGA) and high performance liquid chromatography (HPLC).

Based on kinetic data from the experiments an existing kinetic model for urea decomposition was extended. Together with developed models for spray/wall interaction, heat transfer and an approach for substantial speed up of simulations, for the first time physical as well as chemical processes in the mixing section of SCR systems are depicted in 3D-CFD simulations. Furthermore a new kinetic model is introduced, that is mainly based on thermodynamic data and equilibrium processes and which allows a detailed prediction on urea decomposition and deposit formation with all upcoming experimental effects.

The objective of the research project was achieved.

---

Scope of report:	127 pages, 89 figures, 26 tables, 92 references
Duration:	01.01.2017 – 30.04.2019
Funding organisations:	BMW i / IGF no. 177 EN, BMVIT / FFG grant no. 855718, FVV Funds and CORNET
Coordinating association:	FVV (The Research Association for Combustion Engines eV)
Participating association:	FFOe (Fachverband der Fahrzeugindustrie Österreichs)
RTD performers:	Institut für Technische Chemie und Polymerchemie (ITCP), Karlsruhe Institute of Technology (KIT) Head: Prof. Olaf Deutschmann Prof. Jan-Dierck Grunwaldt

RTD performers: Institut für Fahrzeugantriebe und Automobiltechnik  
(IFA), Technische Universität Wien (TUW)  
Head: Prof. Bernhard Geringer

Research associates / authors: Marion Börnhorst (ITCP)  
Christian Kuntz (ITCP)

Uladzimir Budziankou (IFA)  
Prof. Thomas Lauer (IFA)

Project user committee chair: Johannes Scholz (IAV GmbH)

Scientific advisory committee chair: Dr.-Ing. Tobias Lösche-ter Horst (Volkswagen AG)

Related reports: R590

## Acknowledgement

This report is the scientific result of a research project undertaken by the FVV (The Research Association for Combustion Engines eV) and the FFOe (Fachverband der Fahrzeugindustrie Österreichs). It was performed by the Institute for Chemical Technology and Polymer Chemistry (ITCP) at Karlsruhe Institute of Technology (KIT) under the direction of Prof. Dr. Olaf Deutschmann and Prof. Dr. Jan-Dierck Grunwaldt and by the Institute of Powertrains and Automotive Technology (IFA) at TU Wien (TUW) under the Direction of Prof. Dr. Bernhard Geringer.

The FVV and the FFOe would like to thank the professors Deutschmann, Grunwaldt and Geringer and their scientific assistants – Marion Börnhorst (ITCP), Christian Kuntz (ITCP), Uladzimir Budziankou (IFA) and Prof. Dr. Thomas Lauer (IFA) – for the implementation of the project. Special thanks are due to the AiF (German Federation of Industrial Research Associations eV) and FFG (Austria Research Promotion Agency) for funding of the project within the framework of the collective research networking (CORNET) programme. The project was conducted by an expert group led by Johannes Scholz (IAV). We gratefully acknowledge the support received from the chairman and from all members of the project user committee.

The research was carried out in the framework of the industrial collective programme (IGF/CORNET no. 177 EN). It was supported by the Federal Ministry for Economic Affairs and Energy (BMWi) through the AiF (German Federation of Industrial Research Associations eV) based on a decision taken by the German Bundestag. The work of TU Wien was funded by the Federal Ministry of Transport, Innovation and Technology (BMVIT) through the Austria Research Promotion Agency (FFG, grant number 855718).

The presented computational results of TU Wien have been achieved using the Vienna Scientific Cluster (VSC).

Supported by:





## Table of contents

1	Executive summary .....	1
2	Introduction.....	3
2.1	Selective Catalytic Reduction .....	5
2.2	Challenges in Ammonia Preparation.....	6
3	State of the art.....	9
3.1	Solid Formation from Liquid Film .....	9
3.2	Urea Decomposition .....	9
3.3	Modeling Urea Decomposition in SCR Systems .....	13
4	Project Execution and Results .....	17
4.1	Experimental setups and procedure .....	17
4.1.1	Lab test bench at KIT.....	17
4.1.2	Engine test bench at TUW.....	20
4.1.3	Analytical methods.....	22
4.2	Experimental results .....	24
4.2.1	Deposit formation at steady-state conditions.....	24
4.2.2	Deposit formation at transient conditions .....	38
4.2.3	Thermogravimetric decomposition of urea and its by-products.....	45
4.3	Kinetic and CFD modeling .....	48
4.3.1	Numerical setups.....	48
4.3.2	Modeling physics .....	51
4.3.3	Injection source approach.....	58
4.3.4	Urea decomposition model .....	61
4.3.5	Integration of kinetic model to CFD.....	64
4.4	Simulation results .....	67
4.4.1	Simulation of Thermogravimetric Decomposition .....	67
4.4.2	Simulation of Lab test bench.....	71
4.4.3	Simulation of engine test bench.....	79
4.5	Revised Kinetic Model for Urea Decomposition .....	88
5	Summary & Outlook.....	91
6	Appendix.....	93
6.1	Bibliography.....	93
6.2	List of Abbreviations and symbols.....	98
6.3	List of figures .....	101
6.4	List of tables .....	105
6.5	Attachments.....	107



## 1 Executive summary

Selective Catalytic Reduction (SCR) is the most promising technical aftertreatment solution to decrease nitric oxide emissions of vehicles propelled with diesel engines. It is therefore a key technology to achieve a compliance with global future emission legislation, e.g. beyond EURO VI (EU) and TIER 2 BIN 2 (USA) for passenger cars. The reducing agent ammonia, which is added to the exhaust gas via the carrier fluid urea, reduces the nitric oxides to nitrogen and carbon dioxide in a SCR-catalyst.

In spite of its complexity, the technology is presently the state-of-the-art solution for heavy duty vehicles and the most common solution for diesel passenger cars. More stringent future emission legislation will force the off-road sector to introduce measures like SCR to decrease nitrogen oxide, too.

The research goal of this project, namely to avoid deposit formation from the carrier fluid urea in the exhaust system, is the most urgent problem of SCR-systems at the moment. Therefore, the whole industrial branch of diesel propelled vehicles reaching from passenger cars to container ships is affected by the issues that were addressed in the framework of this project.

Diesel engines are the prevailing power source in the transport sector and have a share of approx. 40 % for passenger cars in Europe. This project will therefore have a considerable impact on future engine development and is of high interest for SMEs that are concerned with the engine combustion process or the exhaust aftertreatment.

Design optimizations of SCR exhaust gas aftertreatment systems (EATS) to prevent or minimize deposit formation caused by injection of UWS (urea-water-solution, AdBlue) are currently mainly based on time consuming and cost-intensive experimental results. Currently available numerical approaches for this issue are not sufficient to significantly decrease these testing efforts. For a significant reduction of experimental costs and development time the process of deposit formation in SCR-EATS needs to be further investigated and fundamentally understood. Based on this, a numerical method needs to be developed and optimized in order to predict the formation of urea deposits without time and cost intensive testing.

This issue is going to become even more important in the future because NO<sub>x</sub>-emissions and thus the amount of needed AdBlue are going to increase due to the optimization of internal combustion engines in order to utilize all available potentials for CO<sub>2</sub> reduction.

The project target was therefore to fundamentally understand and model the deposition process of solids in the tailpipe section downstream of the AdBlue injection point. In detail, the dependence of deposit formation from the operating conditions, namely spray and exhaust properties, the injection position, the material properties of the walls as well as the temperature of the turbulent exhaust flow were experimentally investigated on a laboratory as well as an engine test bench.

A comprehensive modelling approach was established that reproduces all physical and chemical effects (turbulent flow, spray, liquid film, kinetics) on their specific time scales and with the necessary spatial resolution. This is beyond the present capabilities. The predicted quantity of the deposit formation and decomposition rate is an important information for a design optimization. The new approach was validated against the extensive experimental database from the two test beds.

The knowledge gained in this project and the modelling approach derived from this knowledge will help manufacturers of exhaust gas treatments to understand the process of deposit formation and therefore to optimize the process in terms of design and operating conditions in order to reach an improved performance. The provided experimental data and the investigated strategies will help to understand the process of deposit formation and the sensitivity on operating conditions, such as temperature, dosing strategy and exhaust conditions.

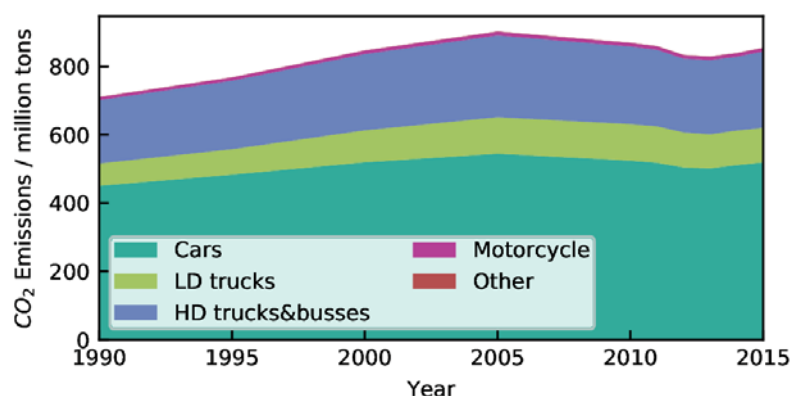
The developed numerical approach is capable to predict the location, the amount and the composition of liquid film and solid deposits. Although an approach for the strong reduction of computational time was provided, simulating real-scale systems at realistic time scales, e.g. for a

complete driving cycle, will remain a challenge. By the provided simulation approach, different conditions and strategies can be tested without conducting expensive experiments. The use of the developed numerical method is going to increase the competitiveness of the companies using this methodology and will eventually lead to the creation of new jobs in this field. This is especially true for those (SME) who are working in the field of EATS development and manufacturing and do currently not have the capability to gather the necessary test results by themselves. Furthermore, this method will also help to develop optimized urea preparation paths leading to weight optimized EATS and thus contributing to the reduction of overall CO<sub>2</sub> emissions.

## 2 Introduction

Exhaust gas after-treatment of diesel engines has remained a complex and challenging task during the past decades. Not only the continuously tightened emission regulations but also the need for advanced fuel efficiency have raised a strong demand for efficient exhaust gas after-treatment technologies.

Diesel fuel combustion is largely employed in both on-road vehicles as passenger cars and trucks as well as off-road mobile applications, e. g. ships, and stationary applications, e. g. for power generation. The development of modern combustion and particularly diesel engines, however, is in a conflict between actual benefits, environmental requirements as well as political and public discussions. The highest demands are placed on both the reduction of pollutant emissions and the fuel consumption, as carbon dioxide ( $\text{CO}_2$ ) emissions are a major cause of the climate change [1]. Additionally, limited access to fossil resources has to be considered raising the need for alternative, sustainable fuels. Emissions from on-road combustion engines contribute to the climate problem, if only to a limited extent. In the EU, 24 % of the greenhouse gas emissions were attributed to the transport sector in 2016 considering  $\text{CO}_2$  and  $\text{CO}_2$  equivalents of methane, nitrous oxides, sulphur hexafluoride, hydrofluorocarbons and perfluorocarbons [2]. Public perception of the emissions problem in traffic, however, is currently much larger. Especially as power unit in light and heavy duty diesel vehicles combustion engines experience wide public attention.



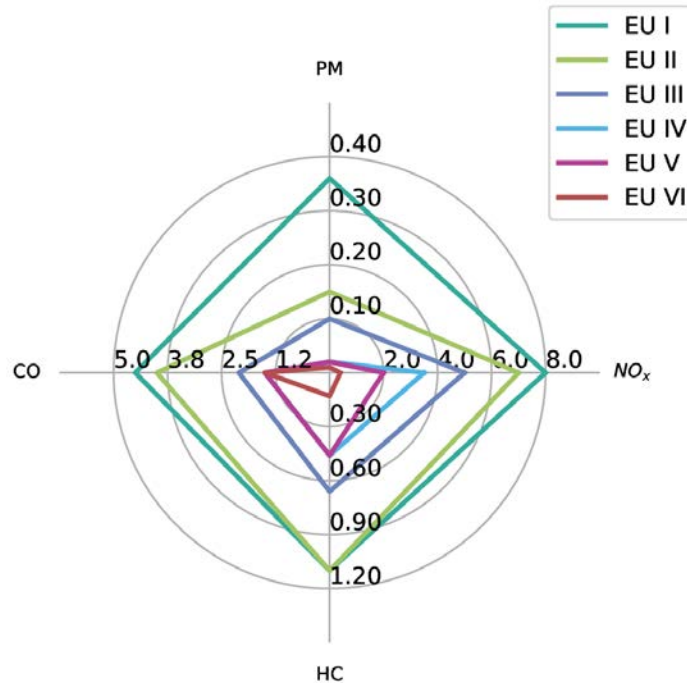
**Figure 2.1:  $\text{CO}_2$  emissions through transportation in the European Union [2].**

Figure 2.1 shows the continuous rise of emissions through transportation in the past. Emissions from light and heavy duty vehicles show an increasing trend. As the transport of goods largely relies on diesel powered trucks and ships, diesel engines will continue to play a role and to contribute to the overall emissions for the next decades [3]. In Germany, the traffic volume for road freight transport is estimated to grow by 17.6 % until 2030 [4]. For passenger cars, the combustion engine is expected to be gradually substituted by hybrid and electric power trains during the next decades. Furthermore, natural gas is treated as one of the most promising alternative fuels [5]. However, for operation of natural gas engines, a trade-off between efficiency and  $\text{NO}_x$  emissions has to be found [3]. Similar problems arise for hydrogen engines facing high  $\text{NO}_x$  emissions for efficient, lean combustion [6]. In contrast to light duty vehicles, until now there is no commercially feasible alternative for heavy duty vehicles [3,7]. In order to meet today's and future emission legislations for both light and heavy duty, efficient exhaust gas after-treatment is indispensable.

Besides water and carbon dioxide, both diesel and gasoline combustion inevitably leads to the production of other harmful emissions such as carbon monoxide (CO), hydrocarbons (HC), particulate matter (PM) and nitrogen oxides ( $\text{NO}_x$ ) as a result of incomplete combustion. For gasoline engines, three-way catalysts represent the most efficient technology to minimize CO, HC and  $\text{NO}_x$  emissions. In this system,  $\text{NO}_x$  are reduced by unburned CO and HC on noble metal catalysts. Here, the air/fuel ratio is decisive as an excess of oxygen results in an oxidation of

CO and HCs instead of  $\text{NO}_x$  reduction. Since diesel engines are operated under lean conditions (excess of oxygen), other methods have to be applied to efficiently reduce emissions.

Exhaust gas emission limits have been gradually tightened since 1992 with the introduction of the European Directive 91/441/EEC (EURO I). Figure 2.2 shows the increasingly stringent emission regulations exemplary for heavy-duty diesel vehicles.



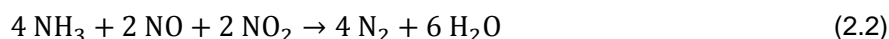
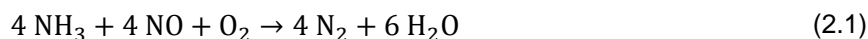
**Figure 2.2: European emission regulations for heavy-duty vehicles [2]. All units in g/kWh.**

EURO VI standard has been applied since 2014. Compared to EURO V the emission limits for trucks and busses for PM are decreased by about 67 %, the  $\text{NO}_x$  limit by 80 %. Furthermore, an emission limit for the number of particles was introduced together with EURO VI. A similar phased plan as for heavy-duty vehicles is defined for passenger cars (EURO 1-6). Successive EURO emission standards have led to a substantial reduction in emissions of exhaust gas PM and other pollutants such as CO and HC. However,  $\text{NO}_x$  emissions from road traffic have not been reduced as much as expected with the introduction of EURO standards since 1992. Exhaust emissions under real driving conditions are often higher than in laboratory tests. In order to mitigate the high emissions from passenger cars on the road, which in recent years have revealed a significant deviation from laboratory testing, the European Commission has developed the RDE Test Procedure applying from September 2017. This procedure reflects the actual emissions more accurately using on-board analytics to measure emission concentrations during a realistic on-road test. From September 2019, new passenger cars certified according to EURO 6d-TEMP or EURO 6d are tested using RDE procedure. Here, the nitrogen oxide emissions may exceed the lab test limit by a factor of 2.1. For passenger cars with diesel engine, the  $\text{NO}_x$  limit for test bench measurement is  $80 \text{ mg km}^{-1}$ , while the RDE limit is  $168 \text{ mg km}^{-1}$ . Further, the conditions of laboratory tests have been tightened by introduction of a more realistic test cycle, the WLTP.

The continuous decrease of emission limits and the high demands on the new test procedures require efficient exhaust gas after treatment of diesel engines in a wide operating range and for highly transient conditions. Depending on application, boundary conditions for the DeNO<sub>x</sub> after-treatment system are exhaust gas temperatures of up to  $650^\circ\text{C}$  and velocities from  $5$  to  $100 \text{ m s}^{-1}$  [8].

## 2.1 Selective Catalytic Reduction

SCR catalysts using ammonia as reductant have been commercialized for  $\text{NO}_x$  removal in the stationary sector for decades. Selective catalytic reduction of nitrogen oxide emissions describes the conversion of  $\text{NO}_x$  to nitrogen ( $\text{N}_2$ ) and water on a catalyst using ammonia as reducing agent. Commonly applied SCR catalysts are vanadia, Cu-zeolites and Fe-zeolites prepared on a monolithic support. Depending on the  $\text{NO}_2$ : $\text{NO}_x$  ratio and temperature different reactions occur on the catalyst. Equation (2.1) shows the *standard* SCR reaction. The fastest and preferred reaction is presented in Equation (2.2), the *fast* SCR reaction. This is commonly promoted by a DOC converting  $\text{NO}$  to  $\text{NO}_2$ . An excess of  $\text{NO}_2$  results in the *slow* SCR reaction, (2.3), which is undesirable since it may yield  $\text{N}_2\text{O}$  as by-product.



The catalyst performance is mainly dependent on the catalyst composition and aging condition. The  $\text{NO}_x$  conversion efficiency strongly depends on the gas temperature. The light-off region for commonly used SCR catalysts is 200-300°C.

Due to its toxic properties and resulting safety issues, ammonia is supplied by an aqueous urea solution. The majority of mobile SCR applications carry a 32.5 wt-% urea solution commercially named *AdBlue*<sup>®</sup> in Europe and Diesel Exhaust Fluid (DEF) in the USA. The urea concentration of 32.5 wt-% was chosen because it marks the eutectic mixture of urea and water resulting in the lowest possible melting/freezing point of -11°C. The precursor liquid is sprayed into the tailpipe in front of the SCR catalyst, as shown in Figure 2.3.

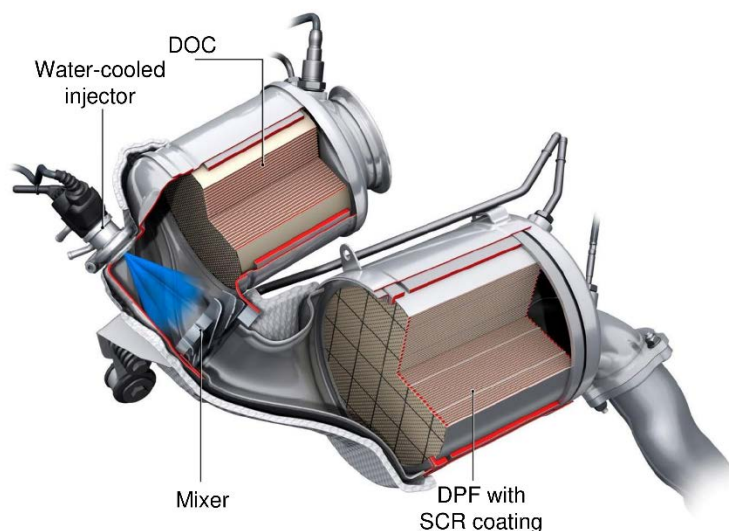


**Figure 2.3: Close-coupled exhaust gas after-treatment system with SCR coated DPF [9].**

In the mixing section the spray droplets evaporate and ammonia is generated by two-step decomposition of urea. Here, complete conversion of urea to ammonia and a homogeneous distribution of ammonia over the tailpipe cross-section in front of the SCR catalyst is necessary for efficient  $\text{NO}_x$  removal. In case of a non-homogeneous distribution or excess of ammonia due to highly transient operating conditions, it may exit the SCR catalyst referred to as ammonia slip. To support spray preparation, mixing devices are commonly placed between the injection position and SCR catalyst (Figure 2.3) maintaining multiple functions. By generation of turbulence, mixing devices promote uniform inlet conditions for the SCR catalyst and hence, increase ammonia uniformity and decrease ammonia slip as shown in Figure 2.4.

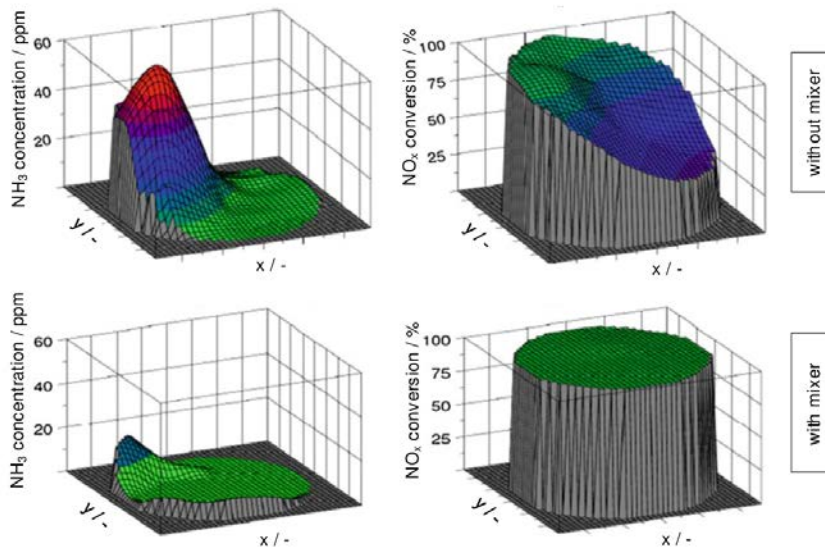


**Figure 2.4: Influence of an optimized mixing device on  $\text{NO}_x$  reduction efficiency and ammonia slip, adapted from [10].**

Mixing elements serve as impingement target for large droplets and further enable secondary atomization. Due to exposure to the hot exhaust gas flow, their temperature adapts to the gas temperature resulting in high heat transfer to the impinging liquid. Mixing devices result in smaller droplet sizes and increased droplet temperatures for the post-impingement spray enhancing total spray evaporation. However, spray preparation and urea decomposition is not trivial and has remained a challenging task which will be discussed in Section 2.2. [10]

Mobile SCR systems are an efficient tool for  $\text{NO}_x$  abatement and are commonly installed in heavy duty vehicles and large size passenger cars. However, the additional efforts for *AdBlue*<sup>®</sup> fill-up and carriage, spray injection and urea decomposition raise recurring discussions about potential alternatives. Great effort has been put in finding alternative sources for ammonia in order to decrease size and cost of the system and to enable SCR application at low ambient temperatures. Approaches for alternative ammonia precursors are given by ammonium formate [11], methanamide [12], solid ammonium carbamate [13,14] and metal ammine chloride salts [15] representing only few examples. All these approaches maintain advantages and disadvantages in terms of melting point, ammonia storage capacity and ammonia yield. However, until now their qualities have remained insufficient for a substitution of urea as commercial SCR reducing agent.

In order to remove excess ammonia an ammonia slip catalyst (ASC) can be installed downstream the SCR catalyst to oxidize ammonia to  $\text{N}_2$  and water. Besides oxidation of unreacted ammonia, undesired formation of nitrous oxide may occur if  $\text{NO}$  is still present in the exhaust gas as a follow of poor urea conversion and mixing or an insufficient urea dosing amount. [10]

## 2.2 Challenges in Ammonia Preparation

SCR system efficiency heavily relies on ammonia uniformity in front of the catalyst entrance. High requirements raised by increasingly stringent emission legislations and the ongoing development of fuel-efficient engines result in the challenge of sufficient spray preparation for  $\text{NO}_x$  reduction with, at the same time, increasing urea dosing rates and decreasing exhaust

temperatures. Figure 2.5 shows a schematic of related processes and influencing factors for ammonia preparation in the in the mixing section of SCR systems.

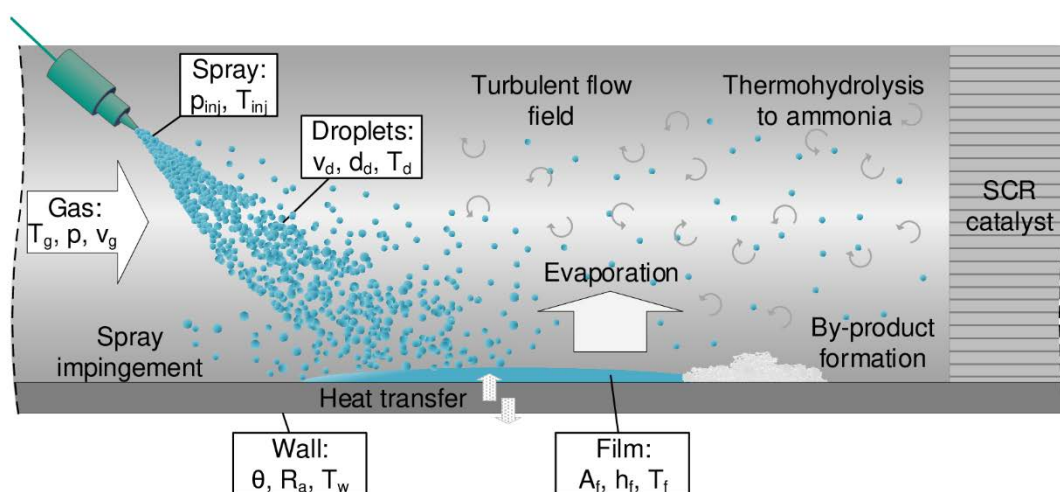


**Figure 2.5: Schematic of relevant physical and chemical processes in the mixing section of SCR systems.**

The formation of ammonia from UWS comprises, on the one hand, droplet evaporation through water evaporation and the thermal decomposition of the urea and, on the other hand, urea decomposition in the gas phase or on the catalyst surface. Due to the highly transient conditions in the tailpipe in terms of exhaust gas flow and temperature and the short distances between injector and SCR catalyst, complete spray evaporation over the wide range of operating conditions remains critical. The interaction of droplets with mixing elements, tailpipe walls and the catalyst structure is almost unavoidable considering the high dosing rates required today to achieve almost complete  $\text{NO}_x$  reduction. Near-engine positioning of injector, mixing elements and SCR catalyst as well as general spatial restrictions support these undesired phenomena. Furthermore, low exhaust temperatures resulting from increasingly fuel efficient engine operation impede sufficient spray preparation. Until now, UWS is commonly not injected below temperatures of  $180^\circ\text{C}$  in mobile applications in order to ensure efficient spray evaporation and urea conversion. Therefore, enhancing evaporation and diminishing spray/wall contact is a major objective, in order to decrease this injection threshold and reach sufficient conversion of  $\text{NO}_x$  over the total operating range.

Spray dispersion and deflection is mainly dependent on the complex interaction of system geometry and resulting flow field, injector mounting and its characteristics, such as injector type, spray angle, droplet size and velocity distribution. When spray impinges on a solid surface in the tailpipe, the exhaust conditions, such as flow velocity and temperature, and the impact conditions such as droplet inertia and wall temperature decide on the outcome of impingement. High thermal and kinetic energies dominating spray impingement lead to secondary atomization, which is beneficial in terms of ammonia generation. For low thermal and kinetic energies, spray impact may result in partial wetting of the surface. Consequently, the surface temperature is decreased by evaporative cooling enhancing further liquid deposition. By accumulation, liquid films are formed on the mixing elements and tailpipe walls [16–18]. Detachment of the liquid film on mixer blade edges can result in formation of large secondary droplets, which are at risk to hit the catalysts' front face before complete evaporation.

In dependence on temperature distribution and residence time, the urea content of the film can thermally decompose into ammonia and isocyanic acid. However, due to the high reactivity of the isocyanic acid, undesirable chemical reactions to solid by-products, such as biuret, triuret, cyanuric acid, ammelide and ammeline are possible [19–22]. Solid deposits formed from urea and its by-products modify the surface properties of mixer and tailpipe walls and hence, influence further spray/wall interaction. By decreasing ammonia production and affecting the flow field, ammonia uniformity is impaired. Increasing deposit growth results in a high backpressure and, in severe cases, in a total blockage of the tailpipe.



### 3 State of the art

As part of the project an extensive literature research about film formation in EATS and resulting solid deposit formation is done in work package (WP) 0. A summary is given below, which can serve as a good overview about different experimental and numerical works done in the past. Furthermore, newest findings served as basis of the work this project.

#### 3.1 Solid Formation from Liquid Film

Concerning deposit formation, the liquid film mass, area and temperature as well as its residence time is decisive for the amount and composition of solid deposits [23]. The evolution of solid by-products follows the reaction kinetics of thermal urea decomposition presented in Section 3.2. Few studies address the formation of harmful solid deposits due to urea injection at realistic operating conditions using engine test benches [24–28]. Deposits derived at different operating conditions are analyzed in terms of yield and composition. Analytical methods like thermogravimetric analysis (TGA), infrared (IR) spectroscopy, high performance liquid chromatography (HPLC) and x-ray diffraction (XRD) are applied to identify different urea by-products. However, a detailed investigation of deposition sources and correlations to the deposit composition is missing. More detailed investigations propose a classification of operating regimes regarding deposit formation based on experimental and numerical results [17]. For wall temperatures below 150°C, mainly crystalline urea is found in solid residues. At these temperatures, intense wall film formation bears the risk of liquid flowing into the SCR catalyst. Wall temperatures of 150 to 250°C represent critical conditions inducing large quantities of deposits. Here, even a blockage of the pipe can be observed by massive solid formation. Moreover, existing deposits are found to act as flow barrier leading to film accumulation near the deposits. Temperatures above 250°C are stated as not critical in terms of deposit formation. Generally, a strong relation between wall wetting and solids formation is observed. Concerning deposit composition, a dependence on the liquid film thickness is proposed. [17]

Smith et al. [26] focuses on wetting and deposit formation on mixer blades. By optical analysis, two types of deposit growth are observed: “damming growth” by liquid film reaching existing deposits before solidification and “peripheral growth” meaning solidification at the edge of existing deposits by capillary flow through the porous solid structure. Deposit formation is stated to be prevented at locations marked by continuous dilution of the liquid film by impinging solution or film transport. [26]

In this study, real scale experiments on film and deposit formation from urea injection under defined boundary conditions are presented in Section 4.2. Valuable information on film and deposit formation is gained and serves as database for both kinetic modeling of urea decomposition and CFD modeling of the overall mixing section as described in Sections 4.3 to 4.5.

#### 3.2 Urea Decomposition

Thermal decomposition of urea is a central process in SCR systems to provide the reducing agent ammonia. Urea melts at a temperature of 133°C and simultaneously starts to decompose in two steps. By thermolysis, urea reacts to isocyanic acid (HNCO) and ammonia (NH<sub>3</sub>) (Equation (3.1)). In a second step, isocyanic acid is hydrolyzed to ammonia and carbon dioxide (CO<sub>2</sub>) (Equation (3.2)).



Consequently, one urea molecule and one H<sub>2</sub>O molecule produce two ammonia molecules and one CO<sub>2</sub> molecule by thermal decomposition. Apart from thermolysis and hydrolysis reactions forming the reducing agent several side reactions may lead to formation of by-products of higher molecular weight, such as biuret, triuret, cyanuric acid, ammelide, ammeline or melamine [20]. By-product formation and their decomposition is mainly dependent on temperature.

Table 3.1 shows data on the melting and decomposition temperatures of urea and relevant by-products.

**Table 3.1: Physical properties of urea and relevant by-products**  
\* in water (20°C)  
\*\* decomposition prior to melting

Component	Molecular formula	Molar mass g mol <sup>-1</sup>	Melting point °C	Decomp. point °C	Solubility* g ℓ <sup>-1</sup>	Ref.
Urea	$CO(NH_2)_2$	60.06	132.7	132.7	1079	[29]
Biuret	$C_2H_5N_3O_2$	103.9	188-195	187	20	[30]
Triuret	$C_3H_6N_4O_3$	146.11	-	233	-	[29]
Cynuric acid	$C_3N_3(OH)_3$	129.08	**	250	2	[20,29,31]
Ammelide	$C_3H_4N_4O_2$	128.09	**	360	0	[20,32]
Ammeline	$C_3H_5N_5O$	127.11	**	360	trace	[20,32]
Melamine	$C_3H_6N_6$	126.12	**	300	3.2	[33]

The decomposition kinetics of urea and its by-products have been extensively studied by several groups [19–22,34–37]. Common experimental methods are TGA, differential scanning calorimetry (DSC), HPLC and FTIR.

A first detailed description of urea decomposition behavior was proposed by Schaber et al. [20] based on TGA, HPLC, FTIR and ammonium ion-selective electrode (ISE) measurements. Concluding from experimental results and literature data, 23 possible reactions including urea and its by-products biuret, cyanuric acid, ammelide, ammeline and melamine are presented. Furthermore, cyanate and cyanurate salts and cyanamide are proposed as possible intermediates of high temperature urea decomposition. Triuret production and decomposition is not accounted for in this study. The authors classify urea decomposition into four temperature regions. The first temperature regime from room temperature to 190 C comprises urea melting and vaporization starting at 133°C. With increasing temperature, urea decomposes to ammonia and isocyanic acid, the latter leading to biuret, cyanuric acid and ammelide formation. The second temperature region of 190 - 250°C is dedicated to biuret decomposition accompanied by several side reactions forming cyanuric acid and ammelide. At 225°C the melt is observed to be converted into a sticky, solid matrix, which is assumed to originate from ionic formations of different by-products without evidence. Besides small amounts of ammelide, ammeline and melamine, cyanuric acid is the main component observed at 250°C. The third temperature range from 250 to 360°C represents the sublimation and decomposition of cyanuric acid. Ammelide, ammeline and melamine are proposed to gradually decompose at temperatures above 360°C marking the fourth temperature region. The authors state elimination of ammelide at 600°C and ammeline at 700°C. High temperature residuals are not analyzed further. [20]

Eichelbaum et al. [19] proposes a reaction network for urea decomposition consisting of nine major reactions based on simultaneous TGA and differential thermal analysis (DTA) measurements coupled with gas chromatography (GC)/mass spectrometry (MS) gas analysis. Decomposition reactions of ammelide, ammeline and melamine are defined and total decomposition is observed for temperatures above 625°C. However, the proposed reaction scheme lacks in description of relevant parallel and equilibrium reactions of urea by-products. Acceleration of urea pyrolysis by different metal exchanged zeolites is demonstrated [19]. A more detailed reaction scheme was derived by the Kröcher group using flow reactor experiments and FTIR spectroscopy for gaseous and HPLC for solid reaction product analysis. The scheme covers

15 decomposition reactions [22]. Here, triuret production and decomposition is included and several reactions are proposed to be equilibrium reactions.

Figure 3.1 demonstrates a characteristic mass loss during thermal decomposition of urea measured by TGA. Clearly, urea decomposes in several stages as mentioned before. Results from TG measurements are commonly used to investigate the decomposition behavior of urea and its by-products. When analyzing urea derived deposits, the extent of respective mass loss stages indicates the samples composition. Moreover, TGA results deliver valuable data for kinetic reaction modeling.

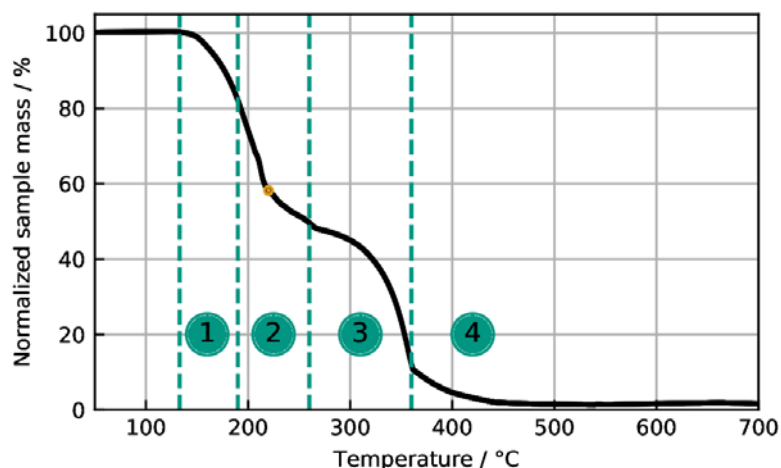


**Figure 3.1: Mass loss during thermal decomposition of urea measured by TGA with an initial sample mass of 60.3 mg and a heating rate of 2 K min<sup>-1</sup> (this work). Characteristic decomposition stages of urea are indicated as stated in literature [19,20]. 1: urea decomposition, 2: biuret decomposition, 3: cyanuric acid decomposition, 4: ammelide and ammeline decomposition. Solidification (matrix) as mentioned by Schaber et al. [20] is indicated by the orange dot.**

Based on the proposed reaction schemes, a first kinetic model for evaporation and decomposition of urea water solution was developed by Ebrahimian et al. [38]. The model describes urea decomposition to ammonia and isocyanic acid and the equilibrium reaction forming biuret. Reactions from biuret to cyanuric acid and from cyanuric acid to ammelide and isocyanic acid are included. Ammelide is assumed to decompose to gaseous by-products.

Gan et al. [39] deduce a semi-detailed kinetic model for urea decomposition based on the work of Schaber et al. [20] and Ebrahimian et al. [38]. The kinetic scheme contains 9 reactions and is applied together with a droplet evaporation model. The dependence of droplet diameter on evaporation time, relative gas velocity and gas temperature is presented. Temperature is identified as decisive factor for deposit yield. However, results deliver only a qualitative comparison of UWS droplet decomposition simulation with deposits derived at an SCR test rig. [39]

A kinetic model developed by Brack et al. [37] is based on the reaction network proposed by Bernhard et al. [22] and validated in detail against TGA and HPLC experimental data. The model includes formation and decomposition reactions of the most relevant by-products and reproduces the characteristic decomposition stages of urea adequately [37]. However, few important physical and chemical processes are not accounted for. A transformation of biuret to a solid *biuret matrix* species is stated for temperatures around 220°C based on visual observation of a solidification during heat-up. This phase transition is implemented to the model without further physical explanations. Ammelide decomposition is modeled as sublimation while further high molecular by-products are not included in the model. Figure 3.2 gives an overview on the reactions included in the model.

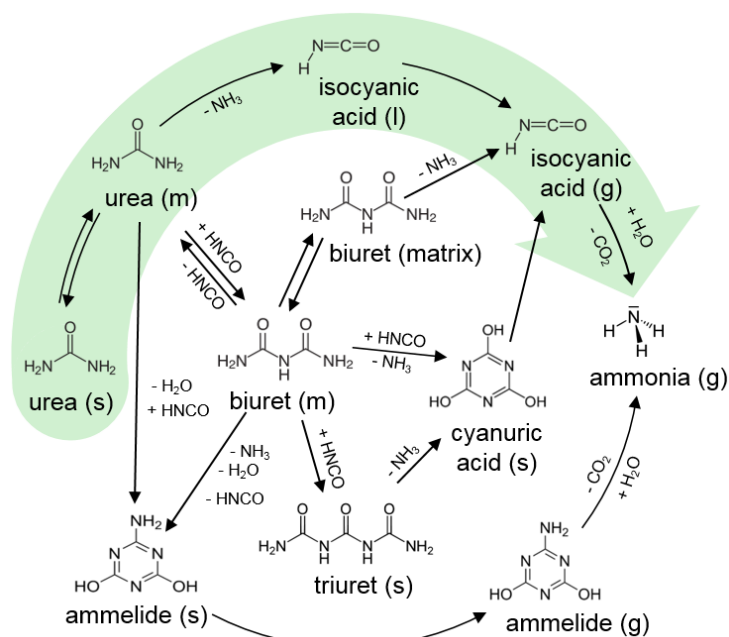
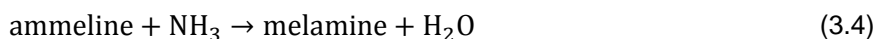
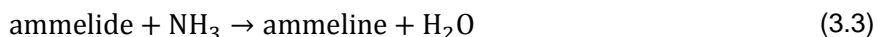


**Figure 3.2: Urea decomposition reactions included in kinetic model of Brack et al [37].**

In this work, the urea decomposition kinetics proposed by Brack et al. [37] are further developed. Details on the applied numerical and kinetic model are presented in Section 4.3.4.

In literature, various proposals for reaction pathways starting from ammelide at high temperatures are available [19,20,22,35]. Different authors propose amination reactions from ammelide to ammeline (3.3) and from ammeline to melamine (3.4) for temperatures above 250°C [19,20,22].



In thermal decomposition experiments, ammelide and ammeline are found in the sample mixture up to temperatures of 600°C and 700°C respectively [20]. Eichelbaum et al. [19] describe a polymerization of melamine to melem at 500°C and a subsequent decomposition of melem to  $(\text{CN})_2$  and HNCO for temperatures above 625°C. Other works mention melon as high temperature product of urea decomposition. So far, the final pyrolysis product has not been clearly identified in literature.

Thermogravimetric measurements have shown a strong influence of the experimental boundary conditions on urea decomposition kinetics. Besides the sample heating rate [20,34,35], decomposition behavior is highly sensitive to the geometric arrangement of the samples and respective crucibles [19,21,35]. Increased surface area of the sample is assumed to accelerate mass transport of gaseous products at the sample surface and their removal as it was shown by using TGA crucibles of different base areas [19]. This leads to an increase of urea conversion and reduction of by-product formation. The same effect was observed in investigations on the thermal decomposition of urea and its by-products using impregnated monoliths in addition to cup geometries in a flow reactor [21]. Further studies on decomposition of urea in impregnated monoliths state that the presence of water in the gas phase decreases by-product formation due to isocyanic acid hydrolysis [22]. Generally, an accelerated decomposition of urea is observed on surfaces catalyzing the hydrolysis of isocyanic acid if water is present to a sufficient amount [19,22,40–42]. Catalytic hydrolysis of isocyanic acid has been investigated experimentally by both kinetic measurements and diffuse reflectance infrared Fourier transform spectra (DRIFTS) studies [43–48] and by density functional theory (DFT) calculations [49,50]. Particular high activity for isocyanic acid hydrolysis was found for  $\text{ZrO}_2$  and  $\text{TiO}_2$  [43]. Regarding solid by-product formation from urea decomposition, positive effects of catalysts

dedicated to isocyanic acid hydrolysis have been observed [19,22,36,51]. Formed deposits reveal similar compositions as compared to measurements without catalysts but the catalyst increases the decomposition rate. However, an aging effect of the decomposed products on the catalyst surface was observed [36]. Furthermore, it was found that urea itself can contribute to a direct reduction of NO in the presence of a catalyst [36].

Obviously, isocyanic acid production and its consumption by hydrolysis drastically influence the formation of by-products. This study focuses on the processes in the mixing section of SCR systems and therefore on non-catalyzed urea decomposition. However, isocyanic acid reactions are particularly considered in experiments and simulations presented in this work. Experimental and numerical results on urea decomposition are discussed in Sections 4.2 to 4.5.

### 3.3 Modeling Urea Decomposition in SCR Systems

Numerical simulation of physical and chemical processes in the mixing section of SCR systems is a fundamental tool for system design and optimization. In particular, a correct prediction of ammonia generation and homogenization is important for dimensioning system geometry and catalyst. Furthermore, simulation of harmful deposit formation is desired in order to be considered in aftertreatment engineering. Computational fluid dynamics simulations are a powerful tool to study the complex physical interactions in the tailpipe. However, including chemical reactions in multiple phase simulations represents a challenge of high numerical effort. Especially the consideration of urea reactions in the liquid film in CFD simulations has remained as challenging task [17]. The objective of modeling the long-term development of solid deposits from urea injection gives rise to compromise solutions in the applied time steps. Figure 3.3 gives an overview on the different time step requirements of relevant physical and chemical phenomena.

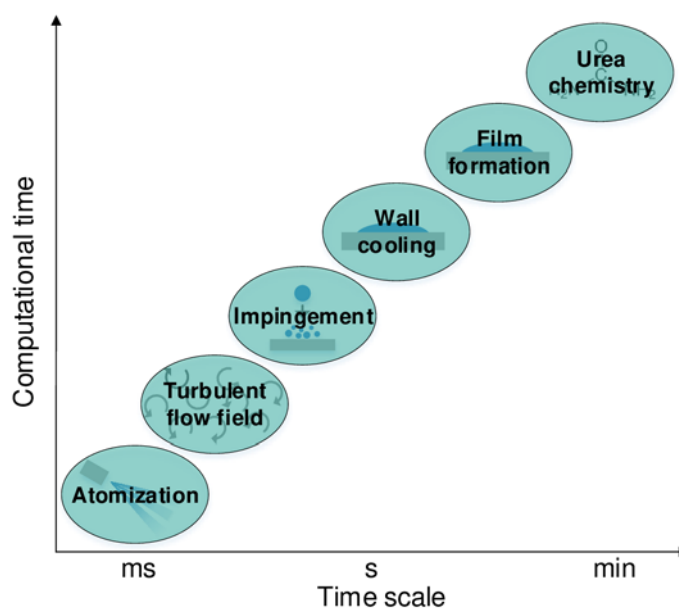


**Figure 3.3:** Time scales of relevant physical and chemical phenomena for comprehensive modeling of UWS decomposition and deposit formation.

Injection and flow of the dispersed spray takes place in milliseconds, whereas film formation and wall cooling occurs in timescales of minutes. Deposit formation from liquid films is bound to timescales from minutes to hours. A correct representation of the injection and spray propagation requires numerical time steps of less than milliseconds depending on injection and gas

velocities. Simulating film and deposit formation using this time step size would result in unreasonably high computational costs. A reliable and quantitative prediction of deposit formation requires a numerically effective approach to handle different timescale phenomena.

Existing models for simulation of SCR systems focus on primary spray atomization and propagation [52–54], effects of mixing elements concerning gas flow, droplet impingement and ammonia uniformity [26,55–57] and droplet evaporation [16,58–60]. Spray impingement and liquid film formation is another important aspect of numerical simulations [52,61,62].

Simulation studies considering urea thermal decomposition are mostly limited to ammonia forming reactions: urea thermolysis and isocyanic acid hydrolysis shown by Equations (3.1) and (3.2) [8,26,52,53,63–66].

In order to predict ammonia formation and mixing characteristics by CFD simulations, Kim et al. [63] apply a single kinetic rate model for urea decomposition from droplets. The kinetic rate is defined by an Arrhenius expression and adapted to experimental results for ammonia production. Spray behavior is modeled in a Lagrangian frame of reference by a discrete particle model included in the FLUENT software by Ansys [67]. Measured ammonia conversion efficiency agrees well to simulation results, while spacial distribution of ammonia is not compared. No further reactions are included in the model. [63]

An approach for comprehensive SCR simulation was proposed by Wurzenberger et al. [64]. 3D simulations are conducted in FIRE using Euler-Lagrange approach and discrete droplet model [68] for the dispersed phase. A 1D model for a honeycomb SCR catalyst is validated by literature data and the calculated rates are implemented to the CFD simulation as source terms. Standard, fast and slow SCR reactions are considered. Urea thermolysis is implemented as homogeneous gas phase reaction by a standard power law approach starting from gaseous urea. Isocyanic acid hydrolysis and other urea reactions are not accounted for. Results show satisfactory prediction of SCR reactions, while the urea decomposition model is not validated. [64]

First 3D simulations comprising multiphase interactions and two steps of urea decomposition were presented by Birkhold et al. [52]. In addition to turbulent flow and Lagrangian phase model including droplet evaporation, the model accounts for spray/wall interaction, wall heat transfer and two-component wall film formation. The Kuhnke model [69] and Wruck model [70] are applied for spray/wall interaction and impingement heat transfer respectively. A 2D finite volume model is used to model a wall film consisting of water and urea. Heat transfer from wall to fluid film is modeled by Nukiyama boiling [71]. Urea thermolysis and hydrolysis reactions are considered as homogeneous gas phase reactions using an interface of FIRE CFD software to the Chemkin chemistry solver. Simulations show good agreements to experimental data from Kim et al. [63] concerning ammonia conversion for different gas temperatures and velocities. Wall cooling is validated by experimental data from a spray impingement setup. Figure 3.4 shows simulation results for the liquid film thickness and urea content. The wall film is predicted for an injection of 0.83 g UWS at a gas temperature of 340°C. Simulated wall film thickness and concentrations are not approved. Wall film evaporation is considered, but no further reactions are included. However, this model enables the prediction of liquid deposition and indicates critical locations for solid formation. [52]

Other CFD studies mainly rely on the models developed by Birkhold regarding both multiphase physics and UWS droplet decomposition by thermolysis and hydrolysis [26,53,65,66]. Based on temperature and concentration data, deposition risk is derived from the simulations, indicating critical operating conditions and locations for solid by-product formation [26,66]. Smith et al. [26] developed a routine to evaluate the risk of deposit formation based on a choice of parameters describing wall film dynamics as well as temperature and concentration data of the liquid film. Figure 3.5 presents a visualization of the deposition risk on a mixer blade. However, secondary reactions leading to deposit formation from an existing liquid film are not included.

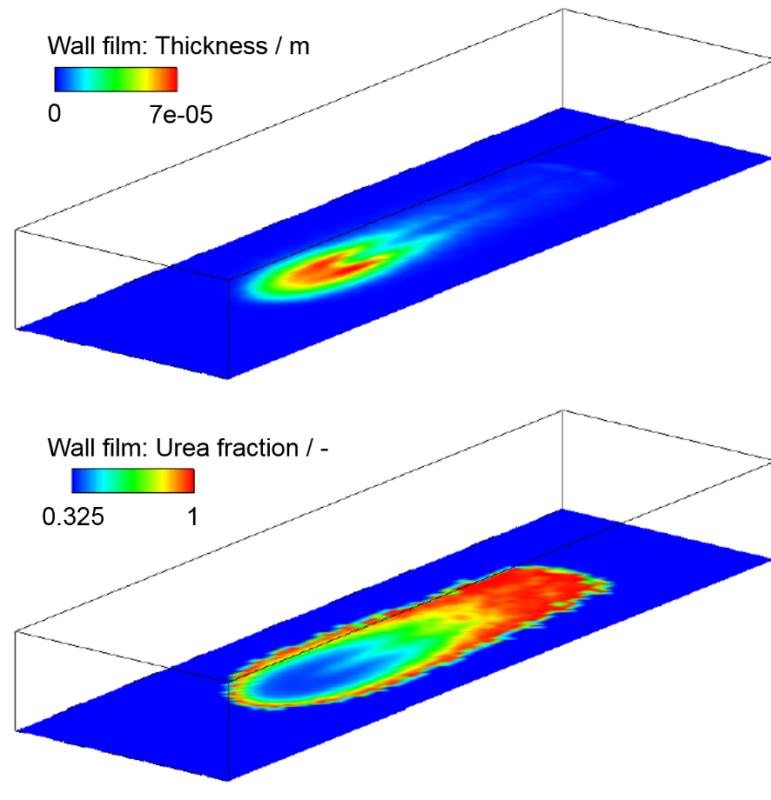


Figure 3.4: Simulation results for wall film thickness and urea concentration for an injection of 0.83 g UWS at a gas temperature of 340°C derived by a 3D simulation in FIRE [52].

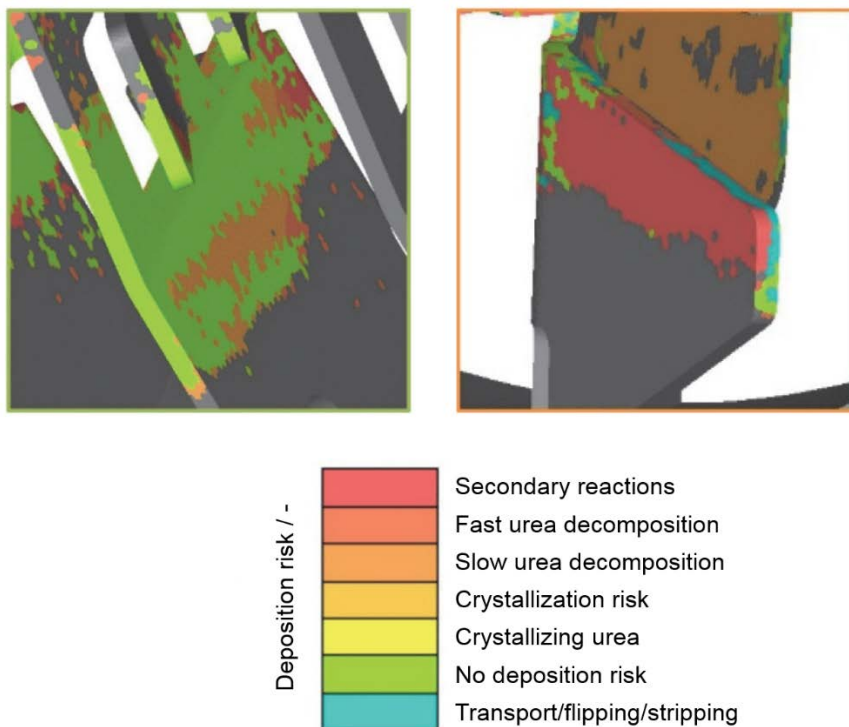


Figure 3.5: Deposition risk on the upstream area (left) and the rear blade side (right) calculated from liquid film simulation data such as velocity, temperature and concentrations. [26]

Habchi et al. [72] considered the competition of isocyanic acid hydrolysis and by-product formation by integration of a semi-detailed kinetic model for urea decomposition into a CFD simulation. The model comprises 12 reactions including the by-products biuret, cyanuric acid and ammeline. Despite a more detailed description of urea decomposition, the model lacks in physical property data of the different compounds as they are assumed to be equal to pure water. Further, no heat transfer model for liquid-solid contact is implemented resulting in wall temperatures equal to the gas temperature. From simulation results, two different temperature regimes are found for deposit formation. However, no model validation in terms of urea decomposition is presented. Furthermore, the simulation duration is limited to 1 s due to excessive computational costs. Computation time for one second of physical time amounts to one week using 256 cores. [72]

Existing models do not cover the multi-component nature of liquid films formed in SCR systems or the evolution of different solid by-products after evaporation. Moreover, high computational costs resulting from small time step requirements for the representation of the Lagrangian phase remain an obstacle which needs to be overcome in order to reliably predict deposit formation. In this work, a comprehensive modeling approach including all relevant physical and chemical processes leading to solid by-product formation is presented (Section 4.3).

## 4 Project Execution and Results

The following sections present the results of the different work packages of this project about experimental and numerical methods on deposit formation from urea injection. In Figure 4.1 the project schedule with all work packages and the 3 milestones is shown.

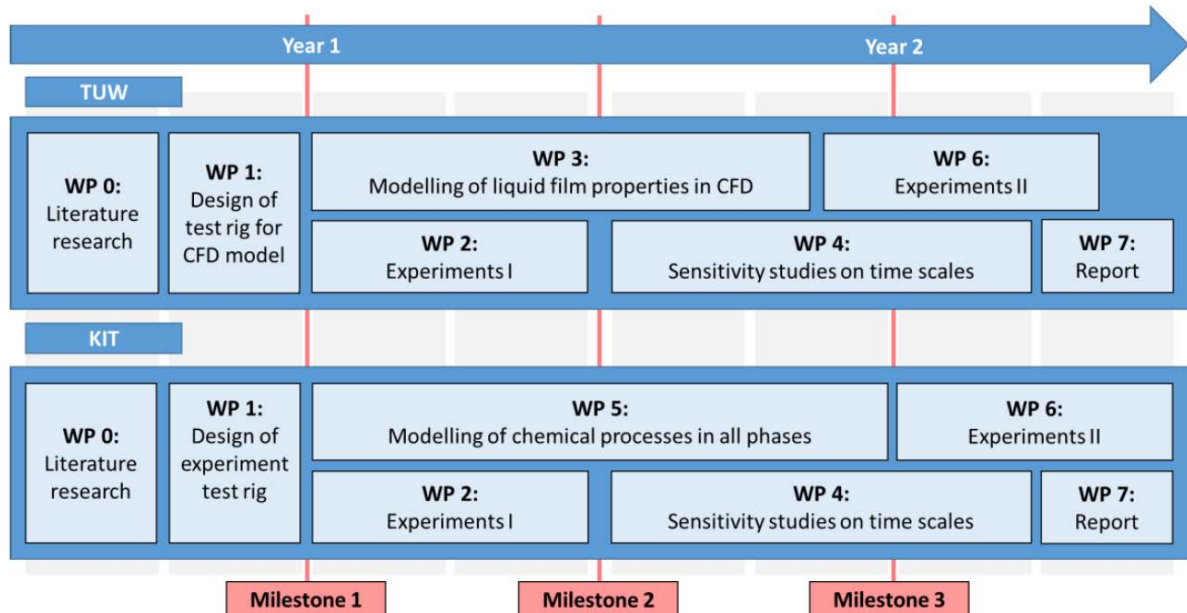


**Figure 4.1: Project schedule stating the different working packages and milestone.**

A literature research and an overview of previous works on AdBlue deposit formation as part of WP 0 is presented in Section 3. In WP 1 a lab test bench at KIT and an engine test bench at TUW with defined boundary conditions are designed and installed, which is the goal of milestone 1. The setups, analytical methods and experimental procedure are described in Section 4.1. First experiments with steady state conditions are conducted to investigate wall wetting, liquid pathways and deposit formation on both benches in WP 2. With analysis of the created deposits, milestone 2 is achieved. A first CFD model is created in WP 3 for modeling of injection, spray/wall interaction and impingement heat transfer at TUW. The CFD simulations are done with the CFD code StarCCM+ v13.06, which was agreed under all project members. The modeling of urea decomposition mechanism is carried out in a 0D multiphase tank reactor model in the DETCHEM software package, named DETCHEM<sup>MPTR</sup>. Furthermore an implementation into the CFD simulations is done as part of WP 5. By reaching milestone 3 the general capability to model deposit formation is demonstrated. The combined modeling approach is tested on the behavior and influence on the different time scales. In WP 6, the second experimental part is focused on transient conditions and possibilities to remove existing deposits. The report in WP 7 brings all parts together and documents a consistent work flow.

### 4.1 Experimental setups and procedure

Following, setups and methods at KIT and TUW for experimental investigations on deposit formation and their characterization are presented. With designing and installation of the two test benches WP 1 and milestone 1 are completed.

#### 4.1.1 Lab test bench at KIT

A hot gas lab test bench is set up to derive solid deposits from UWS injection under well-defined conditions over a wide range of operating parameters. A schematic illustration of the test rig is given in Figure 4.2.

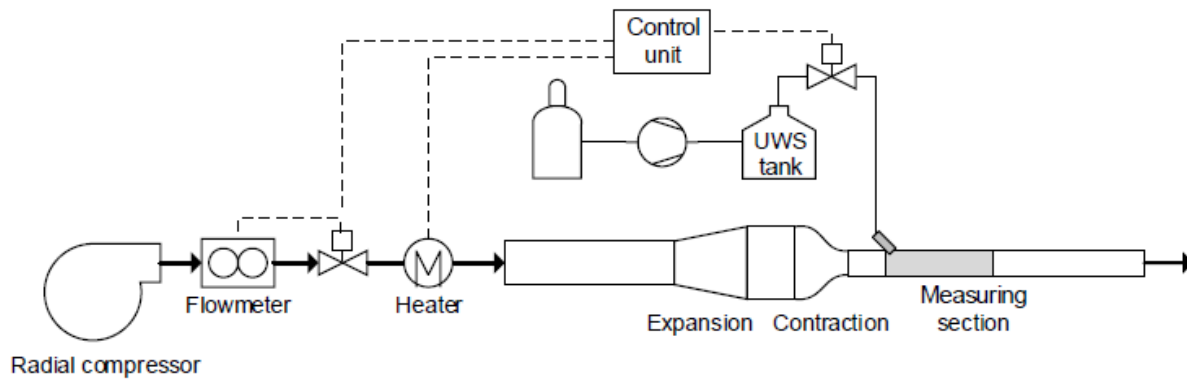
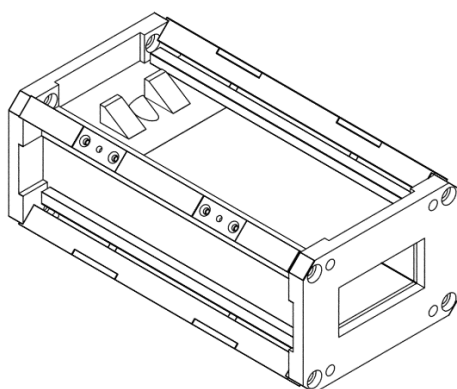
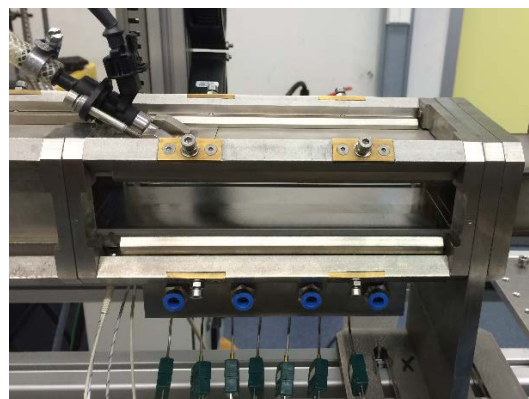


**Figure 4.2: Schematic of hot gas lab test bench setup for deposit generation.**

Furthermore, a photograph of the entire test rig and its housing is shown in Figure 6.1 in the Appendix. The flow arrangement is designed to provide defined inlet flow conditions. Gas is supplied by a radial compressor blowing ambient air into the system. The gas passes a flow meter (Bronkhorst In-Flow F-106BI) and an in-line electrical gas heater (Leister LE 5000 DF) before entering the inlet section of the flow arrangement with a diameter of 53 mm directing the gas flow through a cross section expansion followed by a smoothing section containing honeycomb structures to eliminate swirls. Downstream of the smoothing section the flow channel is contracted to a rectangular cross section of 60 mm x 30 mm representing the cross-sectional area of the measurement section. To reach a homogeneous velocity distribution in the measurement section, an optimized nozzle contour and a contraction ratio of  $K \geq 3$  is required [73]. Hence, the contraction ratio was chosen to  $K = 5$ . The nozzle contour was designed by a 5th order polynomial as described in [74]. Another honeycomb structure is arranged at the nozzle outlet in front of the measurement section. The measurement section has a length of 200 mm and provides optical access through borosilicate windows from three sides (side view and top view). While offering maximum visibility and flexible assembly, flow disturbance is avoided by the advantageous construction of the measurement box. The box is shown in Figure 4.3 and features an exchangeable bottom wall. One bottom wall is equipped with heating cartridges and coolant lines (Figure 4.3 (b)) for wall temperature control. These are arranged horizontally while eight thermocouples are included vertically with a distance of 1 mm to the surface for measurements of axial wall temperature profiles. Another bottom wall has a thickness of only 1 mm. This enables contact free temperature measurements of the bottom wall by infrared thermography. Here, wall temperature is not controlled directly but adapts to a steady state value  $T_{w,st}$  by convective heat transfer.



(a) Sketch of measurement box A



(b) Side view of box A

**Figure 4.3: (a) Engineering drawing and (b) photograph of measurement box A equipped with thermocouples, heating cartridges and coolant lines in the bottom wall.**

A commercial three-hole injector for UWS dosage is used. The injector is mounted together with a water cooling assembly for an injection angle of  $33^\circ$  to ensure adequate spray penetration and simultaneously allow for film and deposit build up. Flush installation of the injector tip into the top wall of the measurement chamber prevents flow disturbance. The three-hole injector features a droplet Sauter diameter of  $d_{32} = 168 \mu\text{m}$  and a static mass flow of  $3.1 \text{ kg h}^{-1}$ . The droplet size distribution measured without flow environment is given in Figure 6.2. UWS mass flow can be controlled by the injector valve duty cycle. The duty cycle  $DC$  defines the time ratio of the open and closed valve in one period  $T$  as displayed in Figure 4.4. The injection frequency  $f$  determines the length of one period.

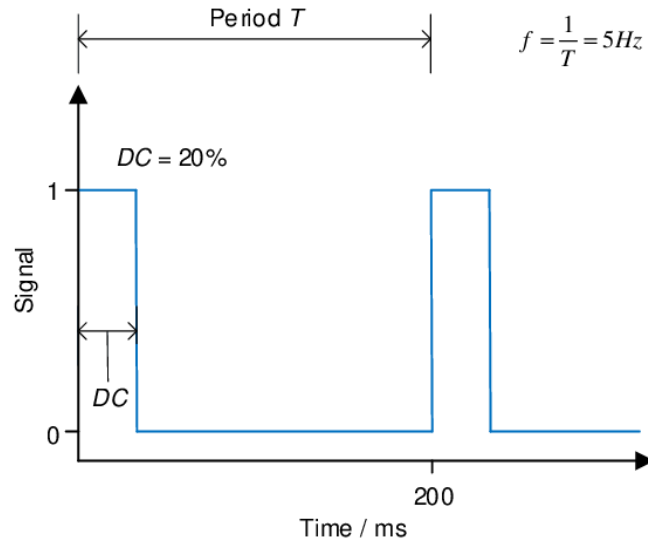


**Figure 4.4:** Valve signal for an exemplary period of 200 ms and a duty cycle of 20 % representing an valve opening time of 40 ms. Period length is determined from injection frequency (here: 5 Hz).

Calibration data for the injector mass flow is provided in Figure 6.3. The injector is connected to a commercial controller and a UWS supply tank operated at 5 bar.

An outlet section connected to the exhaust system follows the measurement section downstream. With a length of 1000 mm the outlet section eliminates disturbances formed in the exhaust system and prevents them from propagating upstream into the measurement section. All parts of the flow arrangement are made of stainless steel.

The setup provides a wide range of operating conditions for experiments, which are displayed in Table 4.1.

**Table 4.1: Operating range of test rig for investigations on deposit formation.**

Operating parameter	Symbol	Unit	min	max
Gas temperature	$T_g$	$^\circ\text{C}$	25	350
Gas flow	$\dot{V}_g$	$\text{L min}^{-1}$	0	3200
Gas velocity	$u_g$	$\text{m s}^{-1}$	0	30
Reynolds number	$Re$	-	0	75000
UWS mass flow	$\dot{m}_{UWS}$	$\text{kg h}^{-1}$	0	5.5

### 4.1.2 Engine test bench at TUW

The development of a modeling approach for deposit formation and decomposition requires a deeper understanding of physical and chemical processes occurring in the mixing section of exhaust systems. For this reason, a measuring section with optical access of heat resisting quartz glass was designed to study the most relevant processes under engine typical operating conditions. The CAD-model and the final set up at the test bed are shown in Figure 4.5.

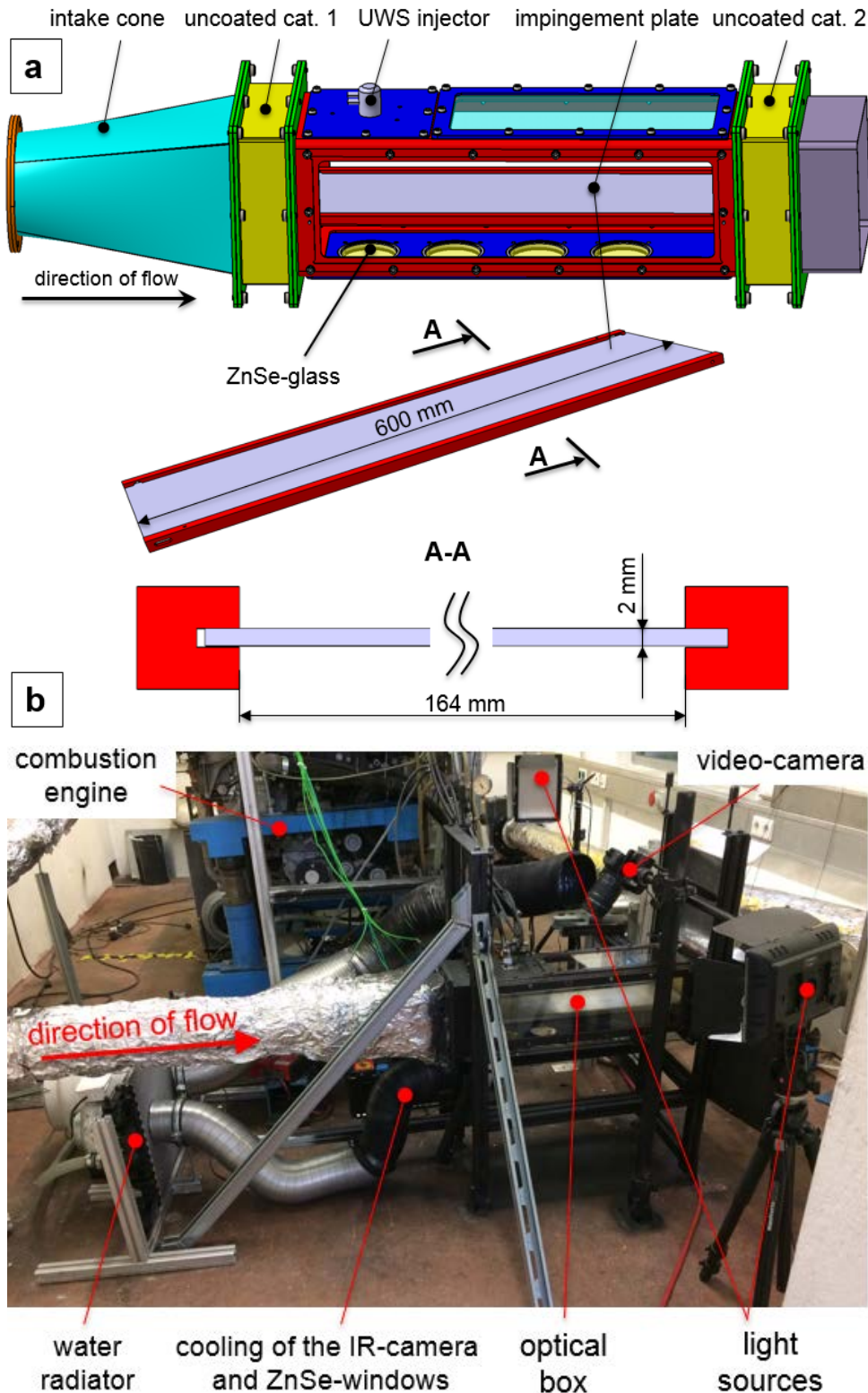


Figure 4.5: a - CAD-model of the measuring section with optical access, b – set up of the engine test bench for investigations of deposit formation and decomposition.

An inlet section with a cone angle of  $7^\circ$  followed by an uncoated substrate was implemented in order to generate a uniform, unidirectional flow with fine-scale, isotropic turbulence. Downstream of the measuring section a further uncoated substrate separated any liquid urea from the exhaust gas.

The measurement volume of the box was designed to enable optical access to the deposit formation process. The box had a 200 x 200 mm cross section and a length of 600 mm. The box length allows a wall film formation from injectors with different spray geometries as well as its unhindered propagation on the impingement plate. The large cross section of the box helped to avoid the contamination of the optical access by the spray and hence excluded the risk of glass destruction due to a thermal shock caused by direct contact with the liquid phase. The box body was made of stainless steel and was varnished with a thermal resistant black lacquer which enables temperature measurements of its surface with IR-thermography.

A horizontal impingement plate was placed at half height of the box. The dimensions of the plate were 599 mm x 173 mm x 2 mm. It was made of stainless steel X5CrNi18-10 which is widely used as construction material for exhaust pipes. The impingement plate was mounted with two U-section beams, shown in Figure 4.5a. This kind of mounting prevents the bending of the plate due to thermal gradients. The bottom side was varnished with black lacquer while the top side of the plate remained untreated. Additionally, a line pattern was carefully scratched in the lacquer for better spatial information. For calibration of the IR-camera two thermocouples were soldered on the bottom side of the plate within the observation area of the camera as shown in Figure 4.6.



**Figure 4.6: View on the bottom side of the impingement plate**

A two-stage turbocharged heavy duty diesel engine with 10.5 liter displacement was used as a source of exhaust gas. The engine is equipped with a DOC and DPF catalyst. Therefore, a clean exhaust gas with a desired mass flow up to 1200 kg/h and a gas temperature up to  $500^\circ\text{C}$  could be supplied to the measuring section. For temperature measurements at the box inlet, a thermocouple was placed in the center of the intake cone close to the surface of the first catalyst. The mass flow of the exhaust gas was measured with the mass flow meter of the type "Sensyflow FMT700-P".

For observation of the liquid film, formation and decomposition of the solid deposits, the box was equipped with three large borosilicate glass windows. The borosilicate glass has a high chemical resistance and temperature range up to  $500^\circ\text{C}$ , which makes it very well suited for measurements with hot exhaust gas. The video recording was carried out with a Canon EOS

650D. The maximal recording framerate was 24 Hz, the resolution 640x480 pixel. Air ventilation prevented the camera from overheating. Two LED lights were used to illuminate the impingement plate.

On the bottom side of the box two Zinc Selenide glasses were fixed. Zn-Se glass has a high transmissivity in the IR spectrum range and allows the measurement of the impingement plate's temperature distribution from below. The maximal operable temperature of Zn-Se glass is limited to 300 °C. The measurements were conducted with the IR-camera "thermoIMAGER TIM 640" which has a temperature range from -20 °C to 900 °C and enables a framerate of 32 Hz with a resolution of 640x480 pixel. Like the video camera, it was actively cooled.

The construction of the box's top side enabled the installation of different AdBlue injectors. The distance between the injector tip and the surface of the impingement plate was approximately 110 mm. AdBlue was supplied by a flexible and mobile supply and control unit that was already available at the IFA. 3 AdBlue injectors were chosen for the experimental investigations with the goal to cover a wide range of Weber-numbers ( $We$ ) and specific area loads of the sprays' footprint, which are known to have crucial impact on the spray impingement regimes and the wall cooling. The most important spray characteristics were verified at the IFA injector test bench. The comparison of producer-supplied data and data measured by IFA is summarized in Table 4.2.

**Table 4.2: Spray characteristics of the 3 investigated injectors**

Injectors	1	2	3
	original data/measured data		
Number of holes	3	3	1
Static mass flow, kg/h	3,1/3,18	7,27/7,32	5/5,02
Injection pressure(rel.), bar	5	5	9
Injection velocity, m/s	24/23	24/23	30/29
SMD, $\mu\text{m}$	100/84	155/178	30/38
Dv90, $\mu\text{m}$	285/230	-/380	85/110
We-number (calcul. with. SMD)	873/673	1353/1427	409/484
Spray angle, °	16/17	15/11	40/40
Angle beta, °	6/6	15/11	-
Injection frequency, Hz	1	1	1
Area Load, g/(mm <sup>2</sup> h)	47/48	109/99	5/4

#### 4.1.3 Analytical methods

Deposits sampled from the lab test bench at KIT and engine test bench at TUW are analyzed regarding chemical composition, decomposition behavior and surface structure. Furthermore, detailed thermal and kinetic analysis is performed by various methods to study the decomposition mechanism of urea and its by-products.

#### 3D Profile Measurements

The surface structure of selected, generated deposits is analyzed by 3D profile measurements. 2D surface profiles are detected using a laser profile sensor (Keyence LJ-V7200) with a resolution of 100  $\mu\text{m}$  in y-direction. By moving the sample along a magnetic guideway, surface

profiles are measured in a distance of 31  $\mu\text{m}$  in x-direction. Data assembly and post-processing, including a tilt correction, is executed in Matlab. The accuracy of height data in z-direction after post-processing is estimated to approximately 90  $\mu\text{m}$ .

### Thermogravimetric Analysis

A Netzsch STA 409 C instrument equipped with the thermal controller TASC 414/2 is used for thermogravimetric measurements. The following standard procedure is conducted for each deposit sample and for reference measurements. Representative samples are grinded and placed in a corundum crucible with an initial sample mass of 10-100 mg. The samples are heated from 40 to 700°C at a constant heating rate of 2 or 10 K  $\text{min}^{-1}$ . Furthermore, isothermal conditions can be applied for a defined time interval. Thermogravimetric analysis is performed in synthetic air (20.5 %  $\text{O}_2$  in  $\text{N}_2$ ) using a purge gas flow rate of 100  $\text{ml min}^{-1}$ . Different geometries of corundum crucibles are used to hold the samples during measurement: a cylinder-type crucible with an inner diameter of 6 mm and a height of 12 mm and a plate-type crucible of 15 mm inner diameter and a height of 5 mm. Crucible geometry, sample mass and heating rate are systematically varied for different samples in order to derive a large database for kinetic modeling. Pure urea (Merck,  $\geq 99.5\%$ ), biuret (Sigma Aldrich,  $\geq 98\%$ ), triuret (Sigma Aldrich,  $\geq 95\%$ ), cyanuric acid (Sigma Aldrich,  $\geq 98\%$ ), ammelide (Dr. Ehrenstorfer GmbH, 99%), ammeline (Sigma Aldrich, 97.9%), melamine (Fluka AG,  $\geq 99\%$ ) and a 32.5 wt.-% urea water solution are used for reference measurements. TGA determines the mass loss of a sample by evaporation and reactions under specified conditions and therefore gives information about the decomposition behavior. Experimental results from TGA measurements are normalized by the initial sample mass for comparison with simulation data and plotted over temperature (Equation (4.1)).

$$f(T) = \frac{m_{\text{sample}}(T)}{m_{\text{sample},0}} \times 100 \quad (4.1)$$

### High Performance Liquid Chromatography

HPLC analysis is used to quantify the chemical composition of derived deposits or samples taken from TGA. By this technique, a solution containing the sample is pumped through a column packed with adsorbent leading to a separation of the sample components by residence time. The samples are analyzed by a HPLC method developed in this work. A Hitachi VW12 HPLC instrument with L-2200 sampler is used for the measurements. A Waters IC-PAK Anion HC column represents the stationary phase. Downstream of the column, a L-2455 diode array detector is applied for signal analysis. The HPLC instrument is operated with a liquid flow of 0.5  $\text{ml min}^{-1}$  at 25°C. The applied method is specially developed for identification and quantification of urea and relevant by-products, including biuret, triuret, cyanuric acid, ammelide, ammeline and melamine and is based on previous literature studies [75,76]. Calibration is performed in advance by standard solutions. The mobile phase consists of a  $\text{Na}_2\text{HPO}_4$  buffer solution, which is adapted to  $\text{pH} = 10.4$  by adding NaOH. Filtration of the eluent is performed before usage in the HPLC. Respective samples are grinded and dissolved in the eluent. Depending on the sample properties, further dilution may be required to dissolve the sample or to meet respective calibration ranges. By this measurement technique, the composition of given samples is analyzed with an accuracy given in Table 4.3.

**Table 4.3: Measurement accuracy for quantitative determination of different components by HPLC analysis**

<i>Component</i>	<i>Accuracy / %</i>
<i>Urea</i>	<i>&lt; 5</i>
<i>Biuret</i>	<i>&lt; 10</i>
<i>Triuret</i>	<i>&lt; 30</i>
<i>Cyanuric acid</i>	<i>&lt; 10</i>
<i>Ammelide</i>	<i>&lt; 20</i>
<i>Ammeline</i>	<i>&lt; 10</i>
<i>Melamine</i>	<i>&lt; 20</i>

## 4.2 Experimental results

Following, the results of experiments at the test bench at KIT and TUW are presented. The experiments were divided in different work packages at steady state (WP 2) and transient (WP 6) operating points to investigate deposit formation in various conditions. Furthermore, deposits and their decomposition are studied by TGA, HPLC and NMR.

### 4.2.1 Deposit formation at steady-state conditions

#### Experiments at lab test bench at KIT

As part of WP 2, experiments are performed at the lab test bench at KIT to create deposits. The deposit formation is studied qualitatively and quantitatively at varying operating conditions. For a gradual increase of deposit mass, three injection cycles of 40 min with a UWS mass flow of  $1 \text{ g min}^{-1}$  and a 15 min break, for water evaporation and deposit formation, in between the cycles, are conducted. The long-time injection experiments are performed in 4 different operating points OP 0 to OP 3. Furthermore, three operating points OP 4a to OP 4c are conducted with short time injection of 10s and a UWS mass flow of  $4.8 \text{ g min}^{-1}$ , which serve as a basis for the simulations of the lab test bench and are further discussed in Section 4.4.2. The operating conditions are listed in Table 4.4.

**Table 4.4: Lab test bench operating conditions for multiple injection experiments at steady state.**

OP	$T_{\text{gas}} [\text{°C}]$	$T_{\text{w,st}} [\text{°C}]$	$u_{\text{gas}} [\text{m/s}]$	Re [-]
0	150	90	8.6	11832
1	190	130	9.4	10982
2	280	175	11.3	9454
3	320	190	12.1	8903
4a	183	167	10.3	12329
4b	217	197	10.9	11444
4c	253	227	11.5	10594

Under incident flow conditions, crystallization and deposit formation are generally observed to start at the downstream edge of the liquid film resulting in bow-shaped deposits. Nevertheless, no solid deposits are formed in the spray impact region, during the injection period. Due to urea crystallization starting at the edge of the liquid film, where the evaporation rate reaches a maximum, solidification is at first attributed to continuous liquid supply and high temperatures and second, capillary suction of liquid into the porous deposit structure is assumed to promote

deposit growth. 3D topological data is obtained by laser profiling for representative samples. The solid structures of deposits derived at different operating conditions differ significantly in their dimensions as can be seen from the topographical images in Figure 4.7 and the evaluated structural data listed in Table 4.5.

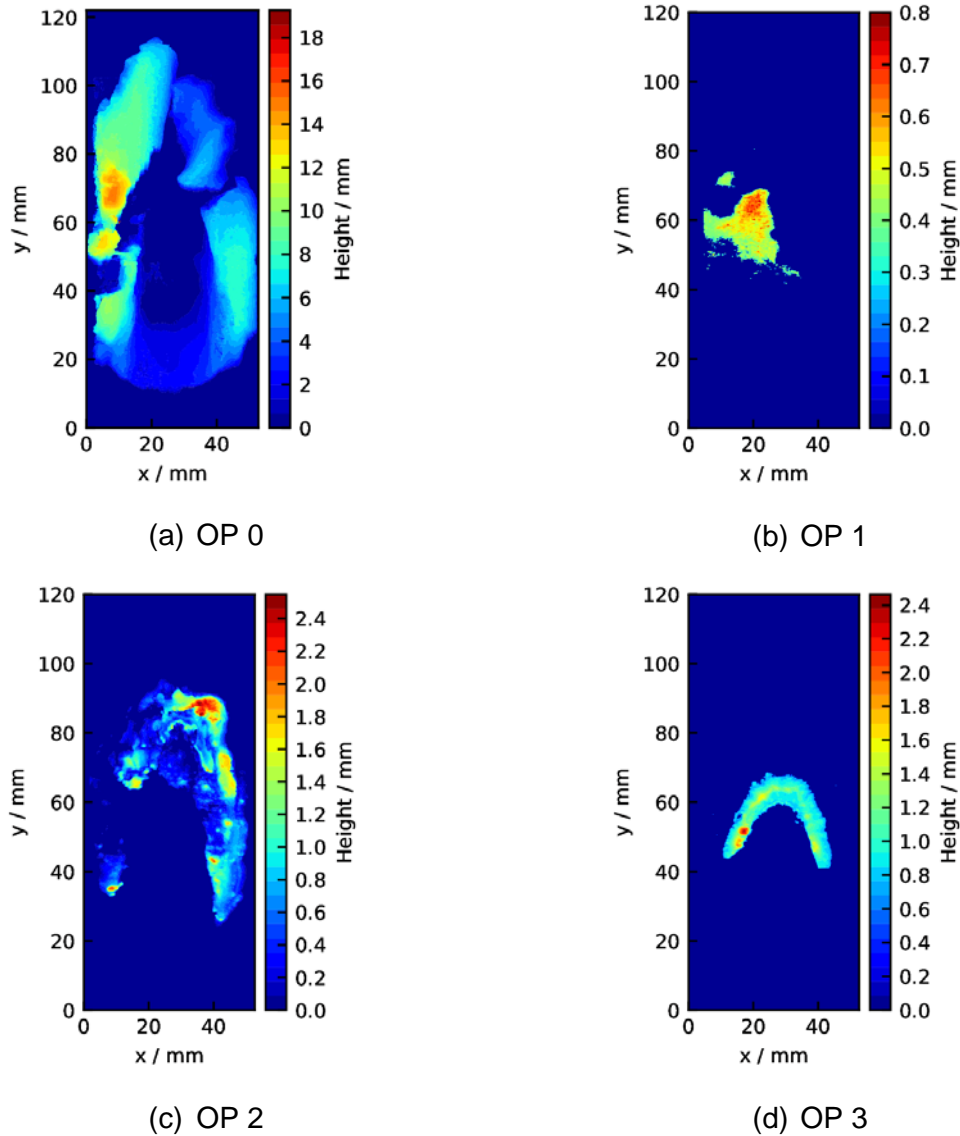


**Figure 4.7: Topographical image of deposits generated at OP 0 (a), OP 1 (b), OP 2 (c) and OP 3 (d). Positive y-direction represents the flow direction.**

**Table 4.5: Topographical data of derived deposits at different operating conditions.**

Deposit	Volume $cm^3$	Max. height $mm$	Mean height $mm$	Mass $g$
OP 0	16.87	19.25	5.24	13.13
OP 1	0.13	0.80	0.47	0.37
OP 2	0.83	2.55	0.57	1.47
OP 3	0.35	2.46	0.99	0.95

The largest volume and mass of deposit is generated at OP 0. As indicated in Table 4.5, deposit growth reaches its maximum at a height of 19.25 mm, which corresponds to more than 60 % of the flow channel height. About 17 % of the channel cross-section are occupied by

deposit on average. The large amount of solid results from relatively low gas and wall temperatures present at OP 0. Due to low temperatures, a composition of mainly urea crystals can be assumed. The deposit shows a crystalline and highly porous structure. As the gas temperature at OP 0 is only 150°C, it is not directly relevant to SCR application since UWS is commonly not injected below 180°C. However, this emphasizes the risk of severe deposit formation at low temperatures, yet present during start and shutdown of SCR systems. Conditions applied at OP 1 result in the smallest amount of solid residue. This is due to the temperature conditions inducing melting and slow decomposition. The resulting deposit reveals a smooth surface and appears like a solidified melt. Deposits from OP 2 are produced at the downstream edge of the liquid film formed during injection and are shown in Figure 4.8. Similar to OP 1, only a small amount of solids with a maximum height of 2.55 mm is left after multiple injection periods. The bow-shape is similar to the deposit derived at OP 3, but the deposit covered area is larger at OP 2. This can be explained by an increased film area formed at lower temperatures. For OP 2 and OP 3, sampled deposits feature a dense structure and partially a yellow-brownish coloring.



(a) OP 0



(b) OP 1



(c) OP 2



(d) OP 3

**Figure 4.8: Photographs of deposits generated at different operating points.**

Besides topological data, the deposit mass can be quantitatively investigated by comparison with the characteristic mass loss observed during UWS decomposition by TGA. The decomposition of urea and its by-products is discussed in the following Section 0. Figure 4.9 shows a decomposition curve of UWS measured by TGA, describing the mass loss of a UWS sample

over temperature. In addition to the TG measurement of UWS, the amount of collected deposits at different operating conditions is illustrated for different single and multiple injection experiments. For comparison with controlled UWS decomposition in the TG setup, the deposit mass is normalized by the overall injected mass. Results show that single injection experiments deliver a relative amount of deposits predicted by the UWS decomposition curve. In contrast, multiple injection experiments produce a highly decreased relative amount of solid deposits. The multiple injection procedure leads to a repeated contact of formed deposits with fresh solution. Due to the partial solubility of urea and its by-products in water, generated deposits may dissolve in the freshly injected UWS inducing further decomposition from the liquid phase.

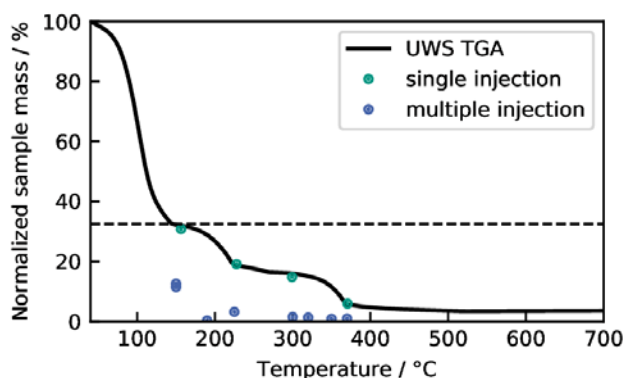


**Figure 4.9:** Thermogravimetric measurement of UWS decomposition compared to determined deposit mass from single and multiple injection experiments in relation to the totally injected amount of UWS. The dashed line indicates a relative sample mass of 32.5 % marking the beginning of urea decomposition in the TG experiment.

Deposits derived at different operating conditions are chemically analyzed to correlate composition with responsible operating conditions. Thermogravimetric analysis gives information on the decomposition behavior of deposit samples, from which one can deduce strategies for regeneration of urea derived deposits in SCR applications. Furthermore, characteristic decomposition stages reveal the deposit composition qualitatively. For quantitative analysis of chemical composition, additional HPLC measurements are conducted.

Figure 4.10 shows results of thermogravimetric analysis of deposits sampled from OP 0, 1 and 4c. Thermal decomposition data is compared to pure urea decomposition, enabling direct conclusions on the samples composition.

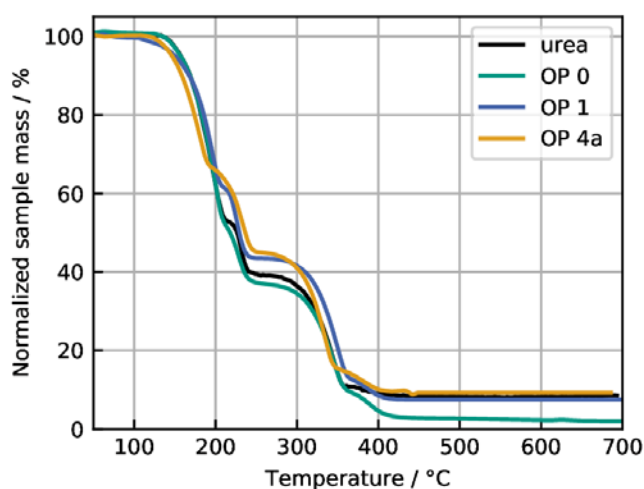


**Figure 4.10:** Thermogravimetric decomposition of deposit samples from OP 0, 1 and 4a compared to pure urea decomposition. Operating conditions are listed in Table 4.4.

Results show a similar decomposition behavior to pure urea, indicating urea as main component of the three deposits. For OP 0, HPLC analysis reveals a share of 96.6 % urea and very small amounts of biuret and triuret (Table 4.6). As wall temperatures lie below the urea decomposition temperature for OP 0, urea decomposition is not initiated resulting in solid deposits from nearly pure urea crystals. Deposits from OP 1 and 4a show similar decomposition behavior and HPLC results for composition. Wall temperatures close to 133°C cause melting of solid urea subsequent to film evaporation and crystallization. The residence time at the wall is highly increased for a molten film compared to a film from urea solution as for OP 0. The melt slowly decomposes in the hot gas flow leaving small amounts of solidified residues. In this temperature regime, urea decomposition is incomplete. Results from HPLC analysis show a similar deposit composition for OP 1 and 4a. Significant amounts of biuret, triuret and cyanuric acid are found in contrast to OP 0. This explains larger mass losses during TGA for the biuret and cyanuric acid stages compared to pure urea decomposition. Results indicate by-product formation at low temperatures, which is not predicted by the urea decomposition mechanism proposed by Brack et al. [37]. Detailed measurements on the urea decomposition kinetics are necessary to identify respective reactions.

A comparable amount of residual mass at  $T = 700^{\circ}\text{C}$  can be observed for OP 1 and 4a. This might be caused by biuret and triuret decomposition producing temperature-resistant by-products. 10.3 % of the biuret and 3.7 % of the triuret sample remain even at a temperature of  $600^{\circ}\text{C}$ , as discussed in Section 4.3.4. Significant amounts of residuals at high temperatures can be related to recovery values of the HPLC analysis of only 90.8 and 92.1 % respectively. The residual share cannot be assigned to the chemical compounds included in the HPLC method. Here, measurement errors of the HPLC discussed in Section 4.1.3 have to be accounted for. However, the presence of another, high temperature resistant substance is assumed which marks the residual mass observed in TGA measurements for high temperatures. This finding is crucial for further research concerning urea decomposition, since it hints at further reactions, which are not included in the available mechanisms.

The deposit derived at OP 4b is formed at temperatures around  $200^{\circ}\text{C}$ , indicating decomposition of urea and biuret. Figure 4.11 shows the result from thermogravimetric analysis compared to pure biuret decomposition.

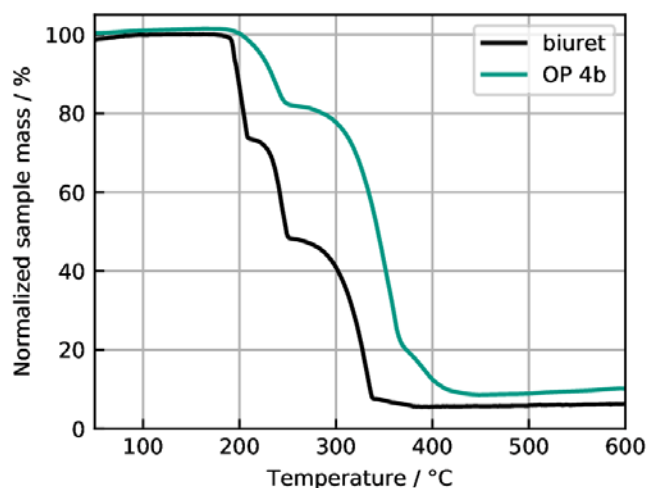


**Figure 4.11: Thermogravimetric decomposition of deposit samples from OP 4b compared to pure biuret decomposition. Operating conditions are listed in Table 4.4.**

As the first mass loss for the OP 4b deposit is found at approximately  $190^{\circ}\text{C}$ , urea is not present in the sample. This is underlined by HPLC analysis results (Table 4.6). Furthermore, large amounts of biuret and cyanuric acid and a considerable amount of ammeline is detected by HPLC, which fit the respective decomposition stages shown in Figure 4.11. At  $600^{\circ}\text{C}$ , 10 % of the deposit sample has remained compared to 6 % for biuret. The HPLC result shows the

lowest recovery value for OP 4b. Both indicates the presence of further components not included in the HPLC method.

Figure 4.12 shows the decomposition of three deposits derived at high temperatures compared to pure cyanuric acid decomposition.

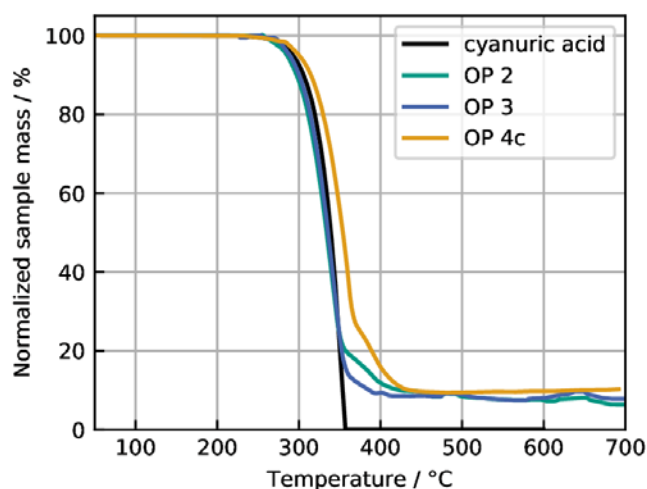


**Figure 4.12: Thermogravimetric decomposition of deposit samples from OP 2, 3 and 4c compared to pure cyanuric acid decomposition. Operating conditions are listed in Table 4.4.**

For all samples, a large mass loss is observed to start around 260°C, which is the decomposition temperature of cyanuric acid. Hence, cyanuric acid is found to be the main deposit component for OP 2, 3 and 4c. A second mass loss stage can be observed for  $T > 360^{\circ}\text{C}$  marking ammelide decomposition. These results are confirmed by HPLC analysis revealing a content of  $> 80\%$  of cyanuric acid and significant amounts of ammelide. Minor shares are detected for other components. The largest ammelide content is measured for OP 2, the smallest for OP 4c, which is in accordance with the size of respective mass loss stages presented in Figure 4.12. Compared to pure cyanuric acid, a residual mass of 7 to 10 % is observed for deposit samples from OP 2, 3 and 4c. This further indicates the presence of another compound not included in the HPLC method. The temperature resistant residues are assumed to originate from biuret and triuret reactions as indicated above. It is assumed, that ammelide present in the samples further contributes to the production of temperature resistant residues. Since the recovery of OP 2 is nearly 100 % and higher than for OP 3 and 4c, it is assumed that the detected urea content relies on measurement errors here. Urea decomposition is not observed by TG, since it would result in a visible mass loss around 133 C.

**Table 4.6: HPLC analysis results of derived deposits from lab test bench at steady conditions. All results are given in %.**

OP	0	1	2	3	4a	4b	4c
Urea	96.6	69.6	4.6	0.0	56.9	0.0	0.0
Biuret	0.4	16.6	trace	0.0	21.5	24.4	trace
Triuret	trace	trace	trace	0.0	5.4	0.0	0.0
Cyanuric acid	0.0	5.9	81.6	88.1	6.1	48.3	83.0
Ammelide	0.0	trace	12.2	7.1	0.8	13.6	14.3
Ammeline	0.0	0.0	1.4	trace	0	1.3	Trace
Melamine	0.0	0.0	0.0	0.0	0	0.0	0.0
Recovery	97.0	90.7	99.8	95.2	90.7	87.6	97.3

The influence of the gas phase composition on deposit formation was the focus on the second experimental work package (WP 6). For operating points 0 - 3, water was added additionally to the inlet stream in concentrations of 3 – 3.5 % and the same experiments with 3x40 min injection are conducted. As for the experiments without water, generated deposits during the injection brakes are mostly dissolved after the start of the next injection. After the last injection and the cool down of the setup, the generated deposits are analyzed. The generated deposits of OP 0, 1 and 2 are displayed in Figure 4.13. For OP 3 no deposits were formed after the experiments.

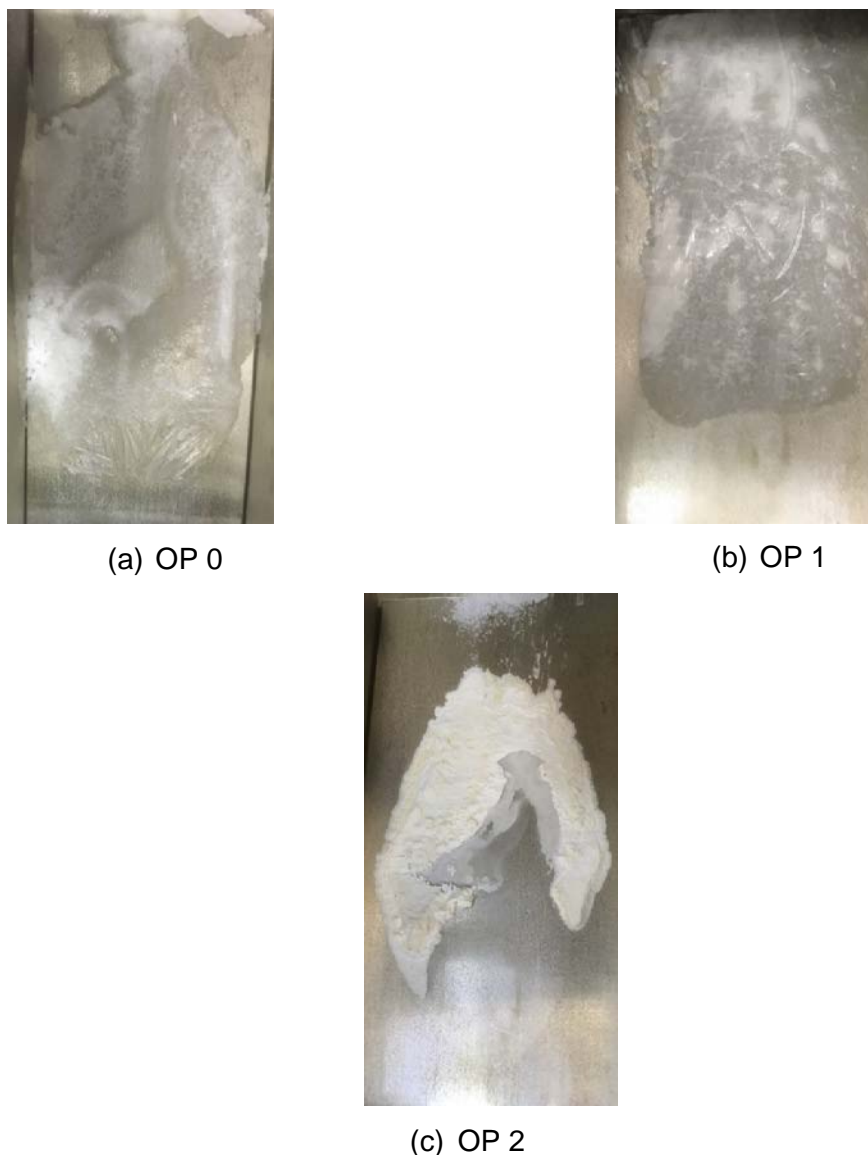


**Figure 4.13: Photographs of deposits generated at different operating points with additional water concentration of 3 – 3.5 %.**

The deposits display each a different visual pattern, but are similar to the experiments without water, assuming the same side product compositions. As it can be seen by a comparison of Table 4.6 and Table 4.7 the deposits of OP 0 with and without water have nearly the same composition of only solid urea. The composition of deposits generated with water at OP 1 slightly differ, especially for triuret and cyanuric acid, but the main component is still urea and the amount of biuret is more than 10 %. For OP 2 the deposits generated with and without water reveal a very similar composition. The deposits generated without water show a slightly increased cyanuric acid content. Since no deposits were formed for OP 3 with additional water in the inlet gas, a comparison is not available.

**Table 4.7: HPLC analysis results of derived deposits from lab test bench at steady conditions. All results are given in %.**

OP	0	1	2
Urea	97.8	78.5	4.5
Biuret	0.5	12.9	1.5
Triuret	trace	3.5	trace
Cyanuric acid	0.0	0.1	72.7
Ammelide	0.0	trace	12.0
Ammeline	0.0	0.0	1.3
Melamine	0.0	0.0	0.0
Recovery	98.3	95.0	92.0

Beside the composition of the deposits, also the total amount of generated deposits can be compared between experiments with and without additional water. Table 4.8 reveals a slight trend for a decrease of the totally deposited mass with addition of water in the exhaust gas. Especially for high temperatures, here for OP 3, additional water can help to form only very small amounts or even no deposits at all. This is explained by enhanced hydrolysis of isocyanic acid, which is a main reactant for deposits.

**Table 4.8: Deposit mass of experiments with and without additional water for OP 0 – 3.**

Deposit mass [g]	OP 0	OP 1	OP 2	OP 3
Experiments without water	13.13	0.27	1.47	0.95
Experiments with additional water	11.58	2.56	1.12	0

### Experiments at engine test bench at TUW

The steady-state operating conditions of the working package (WP) 2 were defined as shown in Table 4.9. The operating point (OP) 1 represents a part load point with low exhaust temperatures. An exhaust gas temperature above approx. 200 °C allows a relatively fast thermolysis of urea as well as a high conversion efficiency of NO<sub>x</sub> in a SCR catalyst. The conditions of OP3 are typical for a higher load point. Due to a higher concentration of NO<sub>x</sub> in the exhaust gas a high injection rate of UWS is assumed which increases the risk of deposit formation. However, the high temperature of solid walls may cause the reflection of liquid droplets on the hot surfaces due to Leidenfrost effect which hinders the formation of liquid film. OP 2 represents a medium load point of a diesel engine. Depending on the spray properties, such as area load and droplet Weber number, both Leidenfrost phenomena and liquid film formation can be expected at the exhaust gas temperature of 275 °C.

Due to different operating conditions, the mean flow velocity in the cross section of the optical box was changed from 10 m/s for OP1 up to 19 m/s for OP3. Consequently, a considerable deflection of the spray by the gas flow was observed.

**Table 4.9: Steady-state operating conditions of WP 2**

Operating conditions	Operating points		
	OP1	OP2	OP3
Exhaust gas mass flow, kg/h	800	1000	1200
Exhaust temperature, °C	200	275	350

The goal of WP 2 “Experiment I” was to visualize and quantify the different mechanisms of the liquid phase and the deposit formation for steady-state operating conditions. For this reason an appropriate AdBlue dosing was determined in order to observe solid deposits at all OPs. Therefore, a series of measurements with different injection rates was conducted. After each series the injection rate was increased until the first deposits were found. The maximum delay time for the start of deposit formation was set to 10 min. The measurement time of 20 min was defined as the maximum achievable simulation time with CFD. In the second step, measurements with substantially higher injection rates were carried out in order to accumulate a sufficient mass of solid deposit which could be analyzed with the TGA or HPLC method.

The first measurements at OP1 and OP2 have shown that the liquid film was accumulated at the area of the initial footprint and remained there until the end of the experiment. In order to provide a uniform liquid film motion at these operating conditions, the optical box was inclined by 18°. Table 4.10 gives an overview of the measurements matrix of the WP 2 “Experiment I”.

**Table 4.10: Measurements matrix of WP 2 “Experiment I”**

Operating Points		1	2	3
exhaust gas temperature, °C		200	275	350
exhaust gas mass flow, kg/h		800	1000	1200
inclination of the box, °		18		0
duration of a measurement, min		20		
injector 1, injection rate (mg/s)	first deposits	no deposits	44	106
	accumulation of deposits			132
injector 2, injection rate (mg/s)	first deposits		40	37
	accumulation of deposits			61
injector 3 injection rate (mg/s)	first deposits		132	418
	accumulation of deposits			

In the following, the characterization of the spray, the film and deposits with the different measurement techniques is briefly described.

### Spray deflection

The spray deflection by the exhaust gas flow has a strong impact on the position of spray impingement and the spray properties such as droplet Weber number. The correct numerical modelling of the spray deflection is a very important step in the simulation of deposit formation. Therefore, at the beginning of the WP 2, the spray deflection was documented for three chosen

injectors and three steady-state OPs. The observation of the spray deflection was conducted with the high speed camera "pco.dimax HD". The recording framerate was set to 3,000 Hz, the exposure time to 7  $\mu$ s. Two LED lights were used to expose the observation area. Figure 4.14 shows the test bench setup.

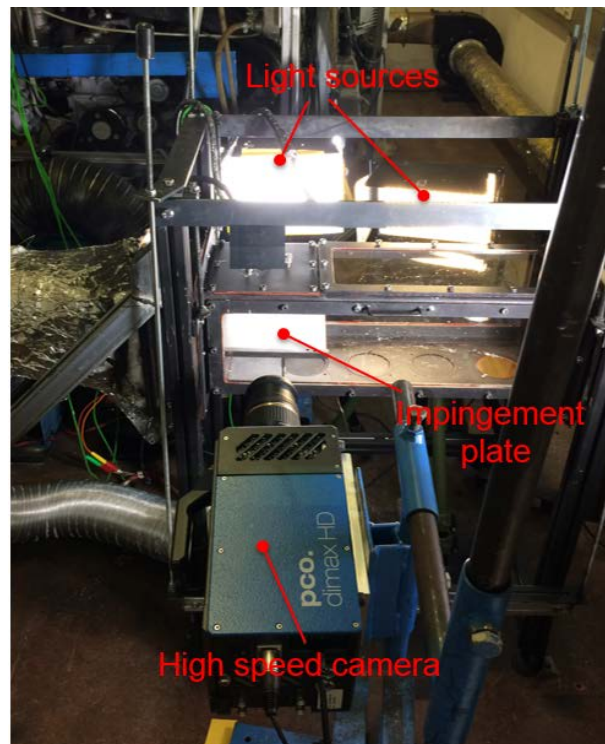


Figure 4.14: Test bench setup for spray observation with high-speed imaging

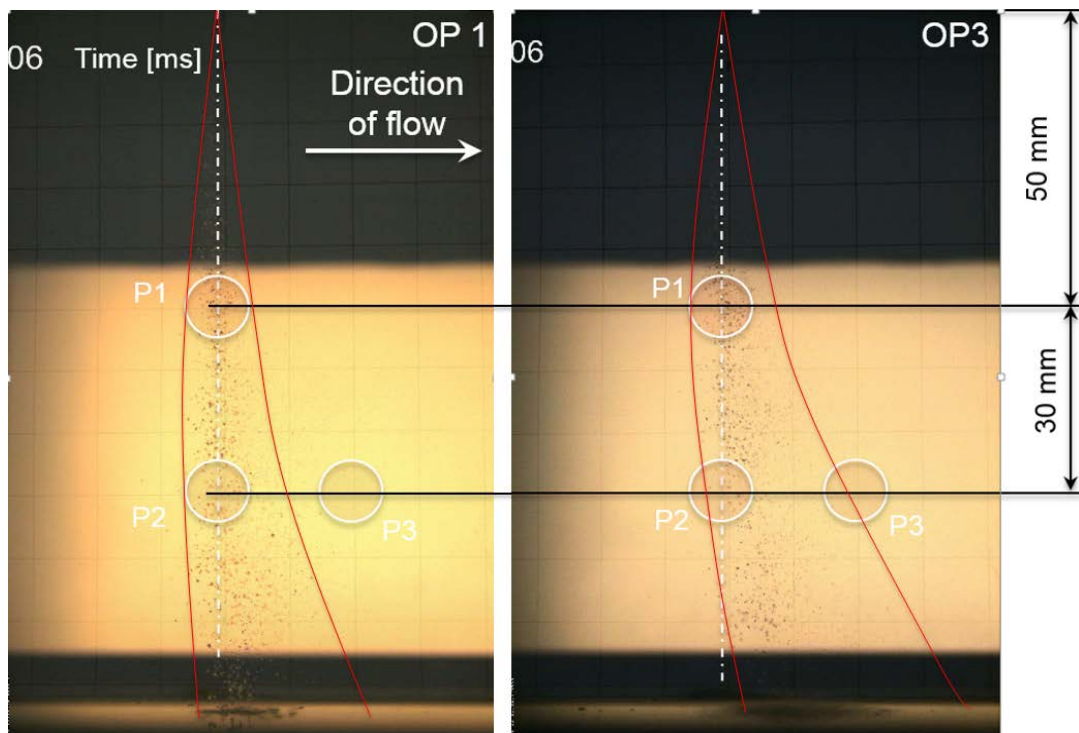


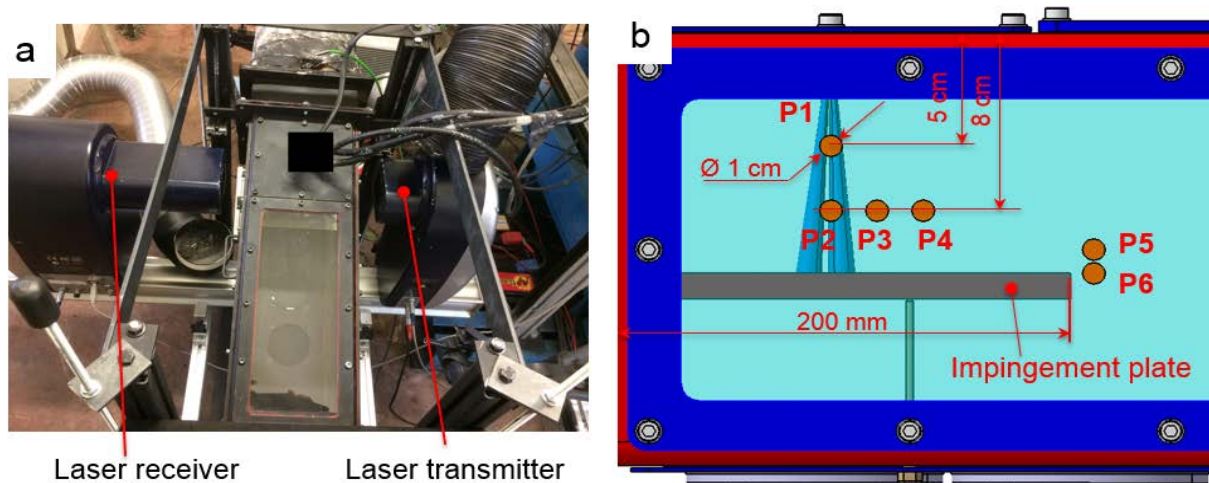
Figure 4.15: Visualization of spray deflection from the gas flow at 6 ms after SOI. Injector 2, OP1 (left) and OP3 (right)

Figure 4.15 illustrates an example of spray deflection by the gas flow for injector 2 and OPs 1 and 3. The red lines show the outer contours of the spray. Due to a higher gas flow velocity in the box, the spray deflection at OP 3 is more pronounced than at OP 1.

After 6 ms of injection the first droplets reached the surface of the impingement plate. Caused by a low temperature of the impingement plate at OP 1, droplets started to splash and form a liquid film on the surface. In contrast, the Leidenfrost effect at OP 3 leads to thermal breakup of the droplets and hinders liquid film formation. In contrast to OP 1, the impingement position at OP 3 was shifted by approx. 10 mm in the direction of flow.

In addition to the high speed imaging, measurements of droplet size distribution (DSD) were carried out at six defined positions as shown in Figure 4.16. They were conducted with a Spraytec laser diffraction system based on a helium-neon laser. A parallel laser beam with a diameter of 10 mm is expanded by the collimating optic which is located in a laser transmitter. The light from the laser is scattered when passing through the spray. The angle at which droplets diffract the light is inversely proportional to their size. The scattering pattern from the spray is captured by 45 individual detectors of the laser receiver. Each of them collects the light scattered by a particular range of angles. The intensity of light in each detector is analyzed to calculate the DSD in the measurement volume. The duration of each experiment was set to 10 s. During this time a series of 25,000 measurements was taken. At the end of an experiment an averaged DSD was calculated from the recorded series. The averaging is necessary in order to obtain a representative measurement result.

The location of the measurement positions (MP) P1-P4 was chosen to capture the DSD in a spray before its interaction with the impingement plate. The MP P5 and P6 were located at the end of the impingement plate slightly above its upper surface. They were used for measurements of the DSD after droplet impingement. With the measured data the droplet drag force model was validated.



**Figure 4.16: a - Test bench setup for measurements with laser diffraction, b - measurement positions**

Figure 4.17 shows exemplary a comparison of DSDs at the MP P1-P6 which were measured in a hot exhaust gas at two operating conditions. The green and red lines represent the cumulated mass distribution of droplets for OP1 and OP3, respectively. The spray was generated with injector 3 which has a wide opening cone of 40 ° and a fine spray with a measured Sauter mean diameter of 38  $\mu\text{m}$ . The black line in the diagrams illustrates the DSD in the spray measured under ambient conditions at a distance of 20 mm from the injector tip. It was used as a reference in order to evaluate the impact of the operating conditions on the DSD.

The comparison of the DSD at the MP P1 shows a shift of the droplet spectrum toward bigger droplet diameters. Small droplets were quickly deflected by the gas flow and therefore not detected in the measurement volume. As MP P1, the measurement volume of MP 2 crosses

the central axis of the spray cone. Its position is located 30 mm farther from the injector tip. Thus, the impact of the spray deflection from the flow is even more distinctive at this position. Only droplets with a size above 50  $\mu\text{m}$  can be observed there. Relative to the central axis of the spray cone, MP P3 and P4 were shifted 20 mm and 40 mm downstream. In contrast to MP 2, more small droplets were detected at these positions.

In comparison to the spray under ambient conditions a lot of small droplets were found at MP P5 and P6 at the mentioned operating conditions. At OP1 this was caused by the droplet splash which led to the formation of a high amount of secondary droplets, at OP3 by the thermal droplet breakup. It can be observed that the spray spectrum produced by the thermal breakup is slightly bigger than the spectrum produced by the droplet splash.

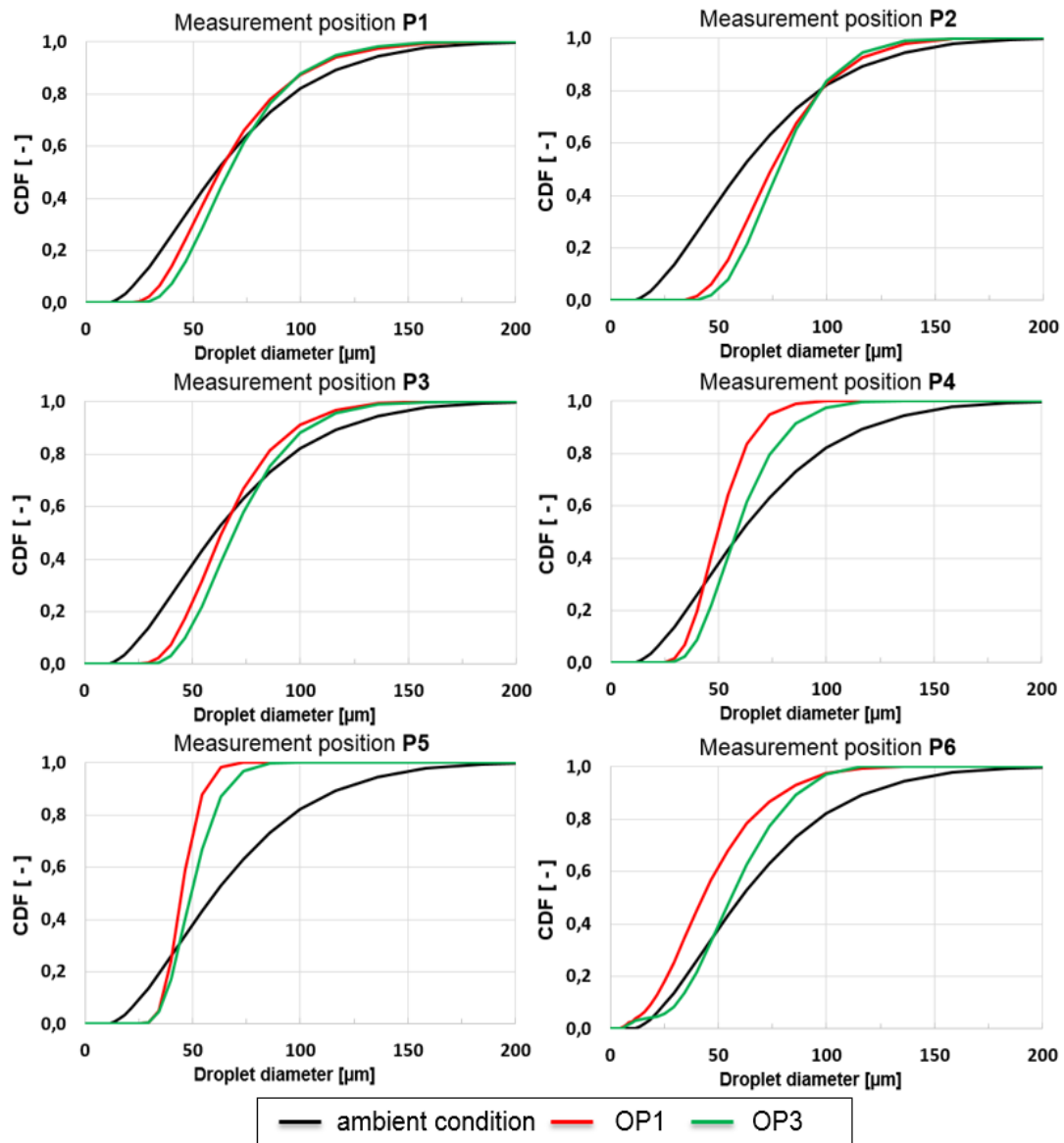
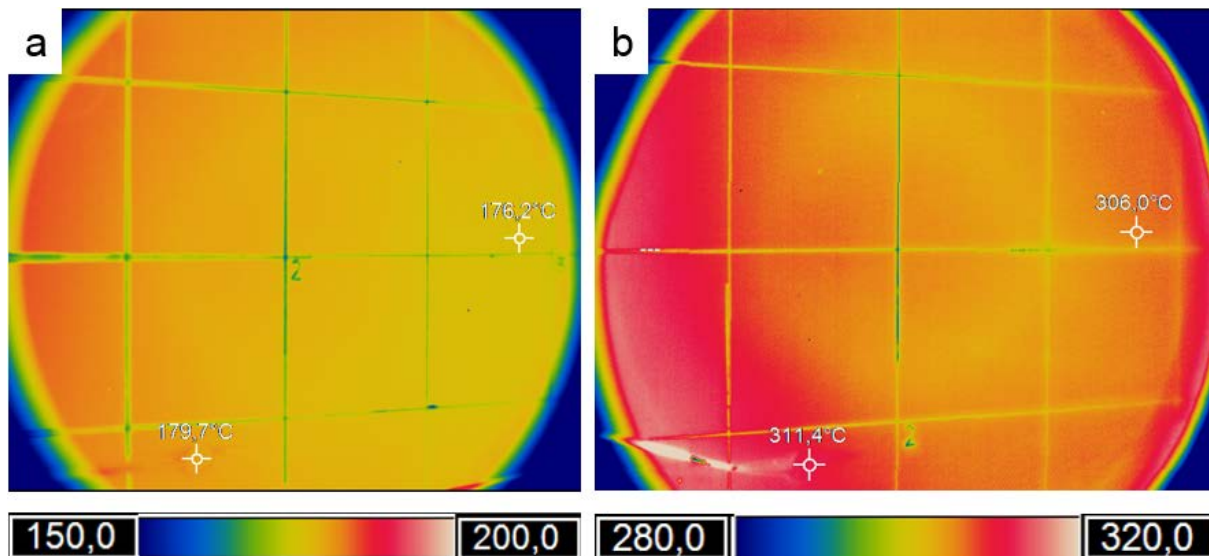


Figure 4.17: Droplet size distribution at measurement positions P1 - P6. Injector 3, OP1 and OP3

#### Surface temperatures and wall wetting

Figure 4.18 shows the plate temperature on its bottom side at the OP1 and OP3 which was reached after a warm-up phase without UWS injection. The measurements were carried out with the IR-camera from the first ZnSe-window. The measured area of the plate corresponds to the area of the initial footprint of the investigated sprays. Although the impingement plate

has contact with the hot exhaust gas on both sides, the plate temperature at OP1 is approx. 20 °C lower than the temperature of the exhaust gas. The temperature difference at OP3 is at least twice as high as at OP1. The obtained results can be explained by the Stefan-Boltzmann law, where the radiation power grows with the fourth power of the surface temperature.



**Figure 4.18: Temperatures of the impingement plate without UWS injection viewed from the first ZnSe-window. a –temperature measured at OP1, b – OP3**

For material temperatures above 250 °C the radiation has a considerable impact on the surface temperatures and cannot be neglected. Therefore, especially for OP 2 and OP 3 the modelling approach must take radiation into account. In order to obtain the necessary data for the CFD simulation, the radiation properties of the box surfaces were documented. The required data were determined by validation of the IR-camera against the measurement data obtained from a thermocouple. Table 4.11 illustrates the measured results.

**Table 4.11: Radiation properties of the surfaces in the optical box**

Surface	Emissivity	Reflectivity	Transmissivity	
Impingement plate	steel surface	0.1	0.9	0
	black varnished	0.96	0.04	0
Liquid film and solid deposits	0.85	0.15	0	
Catalyst	0.9	0.1	0	
ZnSe-windows	0.13	0.13	0.74	
Borosilikat windows	0.9	0.1	0	

Due to a low temperature of the impingement plate, no deposit formation was observed at OP1. Large droplets were formed at the area of the initial footprint. After reaching a certain size they slipped along the plate until entering the catalyst at the end of the box. In contrast to that, the plate temperature at OP2 was high enough to trigger deposit formation. Large droplets slid from the initial footprint half the distance to the second substrate and solid deposits were formed. The injection rate was sufficient to generate a considerable amount of deposits.

At high initial temperature of the impingement plate at OP3 caused Leidenfrost effect during the impingement of the droplets. As a result, the cooling efficiency of the spray was limited. Figure 4.19 illustrates the plate cooling with different sprays and different injection rates. At a

certain injection rate the surface temperature fell below a critical value which led to a liquid film formation and rapid plate cooling. The measurements revealed different values of the critical wall temperature for the three injectors which seems to be dependent on spray properties such as We-number and area load. Quissek et al. [77] reported a dependency of the critical wall temperature on the We-number measured with a droplet chain generator.

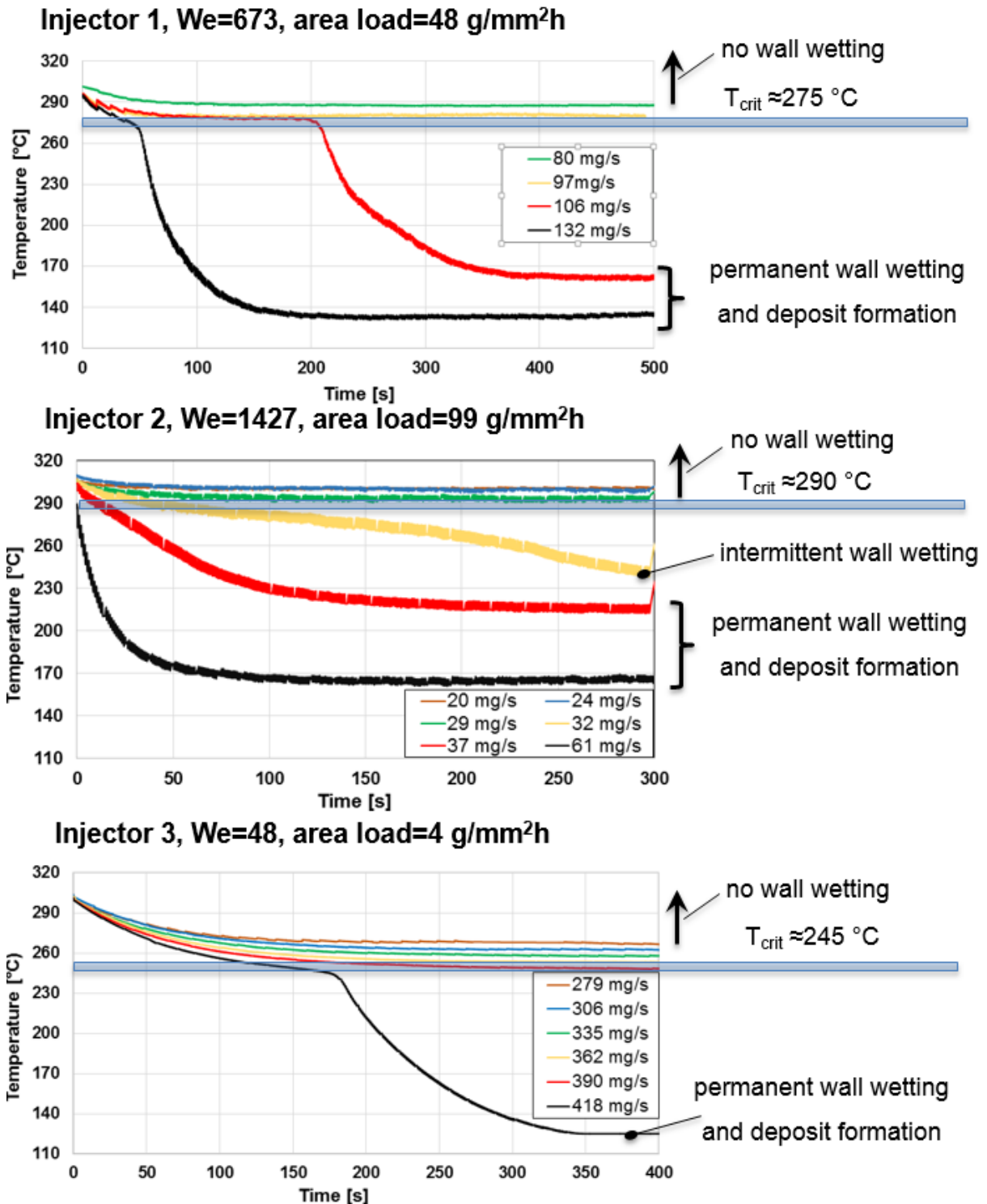
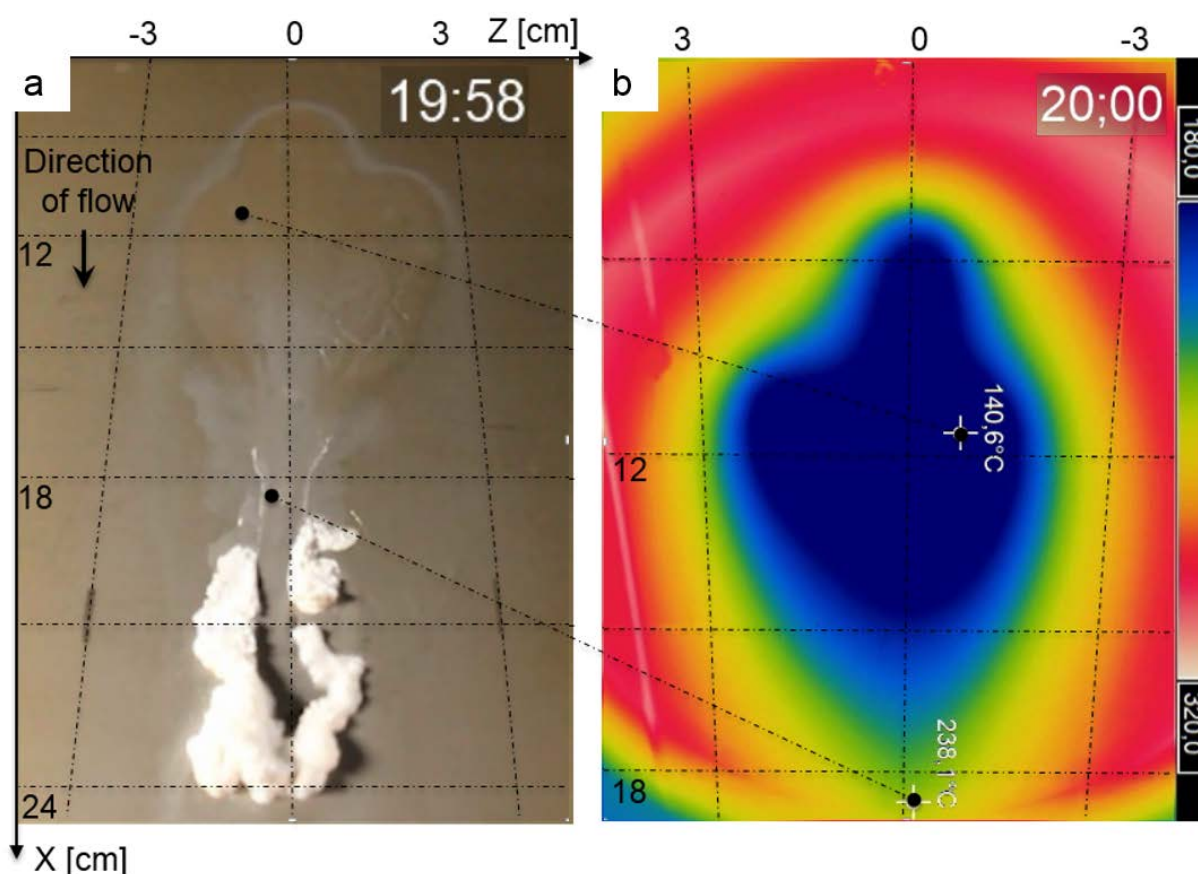


Figure 4.19: Impact of the spray characteristics and the injection rate on the wall cooling at OP3

Below the critical wall temperature both intermittent and permanent wall wetting were observed. However, only permanent wall wetting led to the formation of solid deposits.

Liquid film and deposit formation

Figure 4.20 shows exemplary solid deposits which were accumulated during the measurement time at OP3. The spray was produced by injector 1 with an injection rate of 132 mg/s. After approx. 55 seconds the critical wall temperature of 275 °C was reached in the footprint region and the first liquid film was created. Subsequently, the cooling efficiency rose rapidly and the temperature in the area of the initial footprint reached a constant value of approx. 140 °C. After 120 seconds of injection time the motion of the liquid film from the impingent area toward the second catalyst became visible. The first solid deposits were produced in the front of the film at a distance of approx. 100 mm from the initial footprint and thus blocked the further propagation of the film. The surface temperature at this area was approx. 240 °C. Film boiling and accumulation of solid deposits were observed.



**Figure 4.20: a - solid deposits after 20 min of injection, b - temperature of the impingement plate. OP3, injector 1, injection rate 132 mg/s.**

After each measurement solid deposits were removed from the impingement plate and saved in a hermetic container for further chemical analysis. The structure of the deposit was porous which can be explained by the intensive film boiling in the area of deposit formation. The TGA analyses of deposits were carried out at KIT and have revealed that the main component of all extracted deposits was cyanuric acid.

#### 4.2.2 Deposit formation at transient conditions

### Experiments at lab test bench at KIT

For further investigation of the previous results, experiments at transient conditions were conducted at the lab test bench at KIT, as part of WP 6. The experimental conditions, OP 5a to 5f, are listed in Table 4.12. The experiments are carried out with a time period of 2:1 of low and high temperature during injection. To generate a sufficient amount of deposits for subsequent analyses, the period was extended to 40/20 minutes with a 30-minute pause in between the injection, due to the heating ramp of the setup. The UWS mass flow is  $1 \text{ g min}^{-1}$  like in WP 2. Variable gas compositions are established by addition of water and NO. Furthermore, the effect of a ramp in temperature and gas flow on the resulting deposits is investigated.

**Table 4.12: Lab test bench operating conditions for multiple injection experiments at transient conditions.**

	OP 5a	OP 5b	OP 5c	OP 5d	OP 5e	OP 5f
$V_{\text{gas}}$ [L/min]	1152	1152	1152	1152	800	800
$u_{\text{gas}}$ [m/s]	10.7	10.7	10.7	10.7	7.4	7.4
$T_{\text{gas}}$ [°C]	200	200	200	200	200	200
H <sub>2</sub> O [%]	-	3.75	3.75	3.75	3.6	3.6
NO [ppm]	-	-	1000	-	-	-
Changes	-	-	-	T → 260	-	V → 1200

Deposits generated at 200°C for OP 5a – 5f are comparable to the deposits from OP 1, 4a and 4b, since similar gas temperatures are used. In fact, the composition of deposits from OP 5a, see Table 4.13, is well predicted by a mixture of the deposits from OP 1 and OP 4b. It consists of nearly even amounts of urea (26.7 %), biuret (29.8 %) and cyanuric acid (28.2 %) and some small amounts of triuret and ammelide, revealing that this operating temperature performs fast urea decomposition and biuret and cyanuric acid formation. It can be assumed, that urea injected in the first half of the experiment is totally converted into deposits, while urea injected at the end of the experiment is not fully decomposed until the cool down of the setup, resulting in the high urea content. During TG experiments, urea is usually already fully decomposed at temperatures around 190°C. With an additional water content of 3.75 % at OP 5b in comparison to OP 5a only slight changes in the deposit composition can be seen. As already determined in Section 4.2.1, experiments with additional water produce less deposits, due to enhanced hydrolysis of isocyanic acid. Furthermore the addition of 1000 ppm NO in OP 5c seem to have no significant influence on the deposit formation, since deposit composition and total deposit mass of OP 5b and 5c are more or less the same (see Table 4.13). Literature considers a temperature of 350 °C and higher having an influence to the process involving NO [78,79], which is not reached in these experiments. Therefore, NO is excluded off the gas feed for further experiments. Figure 4.21 shows photographs of the deposits from OP 5a, 5b and 5c, revealing only small deviations in deposit shape and appearance.

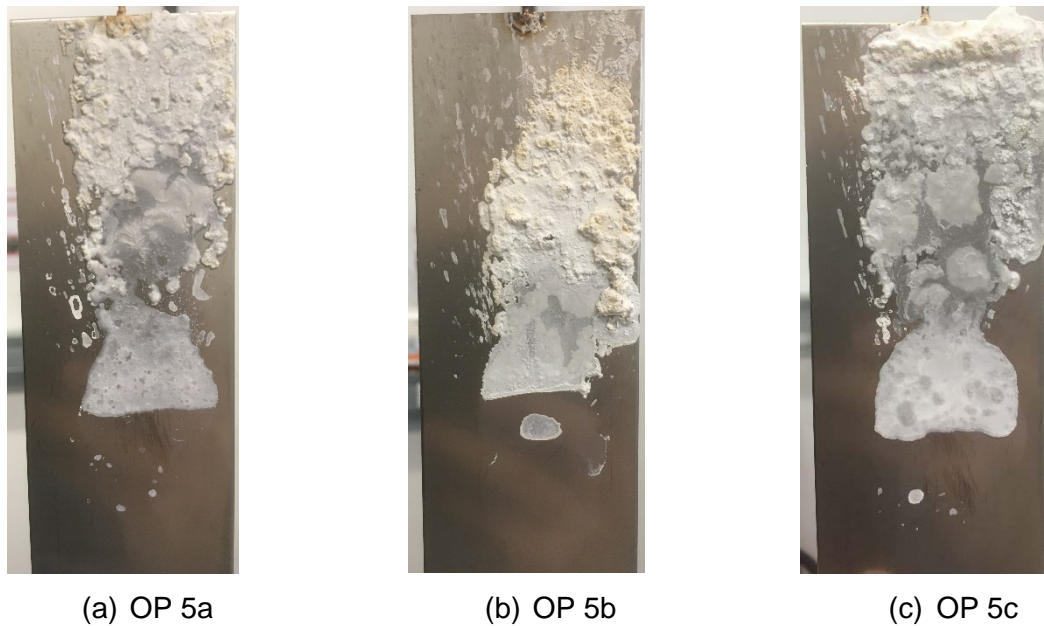


Figure 4.21: Photographs of deposits generated at operating points 5a – 5c.

Table 4.13: Total deposit mass and HPLC analysis results of derived deposits from lab test bench at transient conditions. Composition results are given in %.

OP	5a	5b	5c	5d	5e	5f
Total deposit mass [g]	1.39	0.93	1.03	0.63	0.42	0.62
Urea	26.7	16.5	12.7	7.1	18.2	3.9
Biuret	29.8	30.4	30.8	2.5	37.7	33.5
Triuret	5.8	6.6	6.1	Trace	31.2	5.1
Cyanuric acid	28.2	37.0	38.2	75.4	12.9	42.6
Ammelide	3.1	4.8	5.0	12.4	1.0	5.5
Ammeline	0.0	0.0	0.0	0.0	0.0	0.0
Melamine	0.0	0.0	0.0	0.0	0.0	0.0
Recovery	93.8	95.6	93.1	98.8	100.9	90.9

In operating point 5d, the dynamic and transient behavior of the system is tested. After the first injection period of 40 min, the temperature is increased from 200°C to 260°C during the 30 min injection pause. At 260°C, UWS is injected for another 20 min before the system is turned off and cooled down. The increased temperature of 260 °C is indicated as starting point for sublimation of cyanuric acid in several thermogravimetric experiments (see Section 0). Urea and biuret are expected to be mainly decomposed and derived products should dominate. HPLC analysis shows that the main component is indeed cyanuric acid, with small amounts of ammelide and undecomposed urea. The increased temperature furthermore leads to an increased overall decomposition, resulting in about 50% less deposits compared to experiments at steady 200°C, which is also visible in the photograph in Figure 4.22

The influence of volume flow and therefore gas velocity was the focus of experiments in OP 5e and 5f. For these operating points the volume flow was decreased by 30%. Due to less film transport by shear stress the film is flowing slower downstream. More film remains in the impingement area. Due to droplet impact on the wetted wall or film, splashing droplets and film spreading result in less deposits in the impingement area, but a lot of deposits in the channel

behind the measuring cell, see Figure 6.4 in the appendix. Only deposits from the wall of the measuring cell were analysed, resulting in a smaller total deposit mass as expected. Unusual is the high amount of triuret (31.2%) in the analyzed deposits. It is expected that the triuret reaction is heavily influenced by the HNCO concentration in the gas phase. A decreased flow rate leads to a longer residence time of HNCO in the boundary layer above the film, resulting in a promoted triuret formation. Due to the increased triuret formation, the amount of cyanuric acid is decreased, compared to OP 5b, see Table 4.13. If the flow rate is increased again, the wall film can move further down the pipe and less splashing occurs. In OP 5f the flow rate is held at 800 L/min for the first injection period, before it is increased to 1200 L/min during the injection pause. This increase in flow rate enhances the film transport downstream again, resulting in less splashing for the second injection period and therefore less deposits in the channel behind the measuring box. Furthermore, it affects the triuret formation, which is expected to occur in large parts during the injection break, due to lower HNCO concentrations in the boundary layer over the film like for OP 5a – 5c. The deposit composition of OP 5f is comparable to deposits generated in OP 5b and 5c, but with a decreased amount of urea. Photographs of the deposits from OP 5d – 5f can be seen in Figure 4.22 showing less deposits than OP 5a – 5c in Figure 4.21.

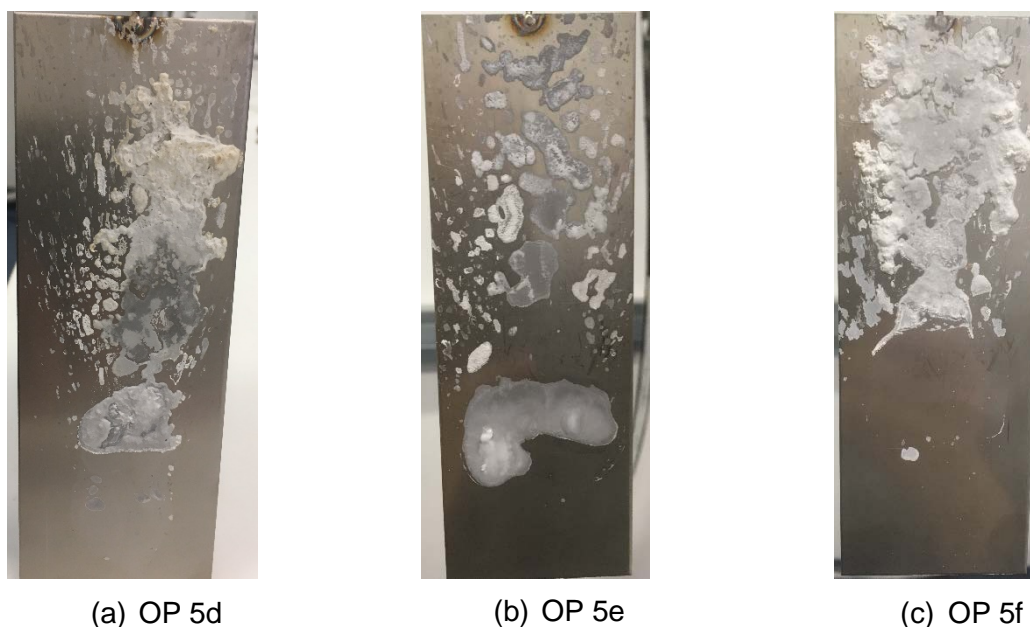


**Figure 4.22: Photographs of deposits generated at operating points 5d – 5f.**

The experiments of WP 6 at KIT lab test bench reveal the complex dynamics of UWS decomposition and deposit formation in the exhaust pipe. Amount and composition of the deposit is depending on the boundary conditions. Additional water in the gas feed enhances isocyanic acid hydrolysis, but also accelerates the side reactions. The resulting deposits might not be decomposable in the usual temperature range. Nevertheless, the total amount of deposits can be decreased by addition of water and dynamic heat adjustments. No influence of NO on the deposition amount and composition is detected under the applied conditions. Decreased gas flow rates lead to slower film transport and therefore enhanced splashing of impinging droplets on the film.

### Experiments at engine test bench at TUW

The focus of WP 6 “Experiment II” was the research on the decomposition of deposits if the operating conditions, such as gas temperature, exhaust mass flow rate or the amount of injected UWS, are changing. For the separation of different effects the measurements were divided into two parts as shown in Figure 4.23:

- Part “a” – change of the exhaust gas temperature while maintaining a constant mass flow rate of 1,000 kg/h. The deposits were generated during the first minutes of an experiment (4-7 min) under constant operating conditions. Then the exhaust gas temperature was increased steadily within 5-7 min to a higher value where the decomposition of the generated deposits was expected.
- Part “b” - change of the gas mass flow rate while maintaining a constant gas temperature. The solid deposits were accumulated during the first minutes of an experiment (5-7 min) under constant operating conditions and 600 kg/h exhaust gas mass flow. Then the gas mass flow rate was increased steadily within 12 seconds to 1,000 kg/h.

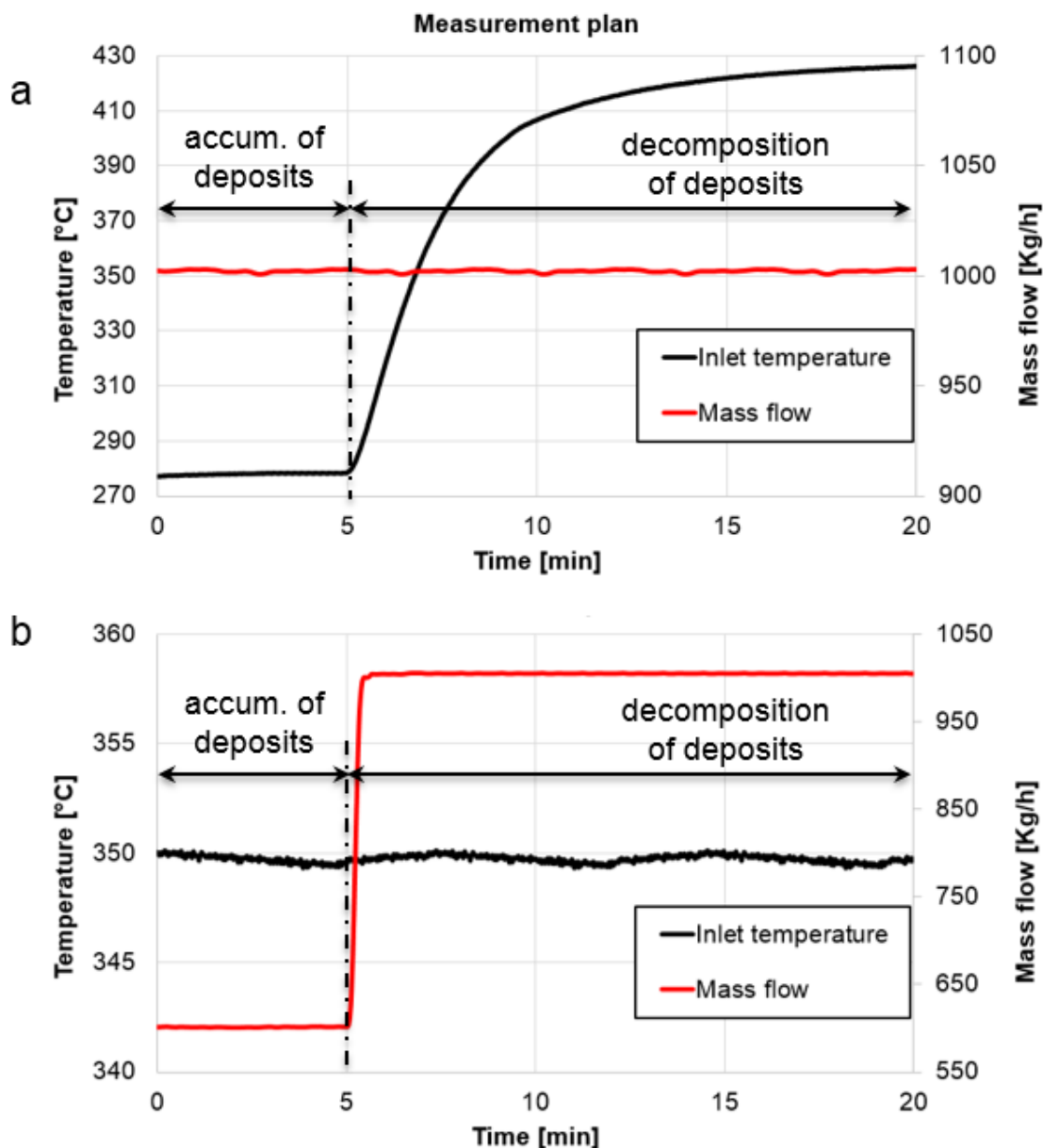


Figure 4.23: Transient operating conditions of WP 6. a - change of the gas temperature, b - change of the gas mass flow.

Table 4.14 shows the measurement matrix of WP 6. The green highlighted rows represent the measurements of part “a”, the blue rows part “b”. Most experiments (17) were carried out with injector 1. Four additional experiments with injector 3 were conducted to prove the validity of the measurement results with different spray properties. The values which were changed during a measurement are printed in bold. Similar to “Experiment I” the duration of every experiment was limited to 20 minutes. The formation and decomposition of solid deposits were observed with video and IR-technique. In experiments with exhaust gas temperatures above 350 °C the IR-thermography was not applied due to the durability of the ZnSe-glass.

**Table 4.14: Measurement matrix of WP6 “Experiment II”**

injector	measur. №	accumulation of deposits				time ramp	decomposition of deposits				total duration		
		$\Delta t_1$	$\dot{m}_{Ex.gas}$	$T_{Ex.gas}$	$\dot{m}_{UWS}$	$\Delta t_2$	$\Delta t_3$	$\dot{m}_{Ex.gas}$	$T_{Ex.gas}$	$\dot{m}_{UWS}$	$\Sigma\Delta t$		
		min	kg/h	°C	mg/s	min	min	kg/h	°C	mg/s	min		
1	1	4	1000	200	19	0	16	1000	200	0	20		
	2					5	11		275				
	3					7	9		350				
	4					9	7		425				
	5	5		1000	275	35	0		15	275		0	
	6						5		10	350		35	
	7											48	
	8											0	
	9						7		8	425		35	
	10	48											
	11	0											
	12	7		350	97	5	8		425	0			
	13					97							
	14	5		600	350	57	0		15	1000		350	0
	15											57	
	16											0	
	17											141	
3	18	5	1000	275	69	5	10	350	0				
	19	7		350	390		8	425					
	20	7	600	350	139	0	13	1000	350	139			
	21			425	404				425	0			

Due to the low initial plate temperatures of the measurements 1-4 no deposits were generated in the first part of the experiment. However, they were created from the liquid film during the following four minutes after increasing the exhaust gas temperature. On the contrary, the measurements with initial temperatures from 275 °C showed a fast deposit formation during the first minutes of the experiments.

The experimental observations revealed two main impact factors on the durability of solid deposits on the plate:

- Rise in exhaust gas temperature  
A fast deposit decomposition was observed if the temperature of the solid deposit was increased by at least 150 °C in comparison to its formation temperature.
- Removal of deposit due to its direct contact with spray  
If the UWS injection was not stopped after the first part of the experiment the spray deflection by the flow was increased due to the rise of the flow velocity in the box. Thus the position of the initial footprint and the solid deposits overlapped to some degree. A fast mechanical removal of the deposits by spray droplets was observed in the affected areas.

Figure 4.24 illustrates the results of experiment № 9. The first solid deposits became visible after 120 seconds of UWS injection. They were created close to the initial footprint in a region with a surface temperature of approx. 215 °C. At the end of the accumulation phase the exhaust gas temperature was increased within 7 min to 425 °C as shown in Figure 4.23a. Nevertheless, the maximum temperature at the deposition area only rose to 370 °C. However, this rise in temperature was high enough for fast decomposition of the accumulated deposits. At the end of the decomposition phase nearly all deposits were removed as shown in Figure 4.24b.

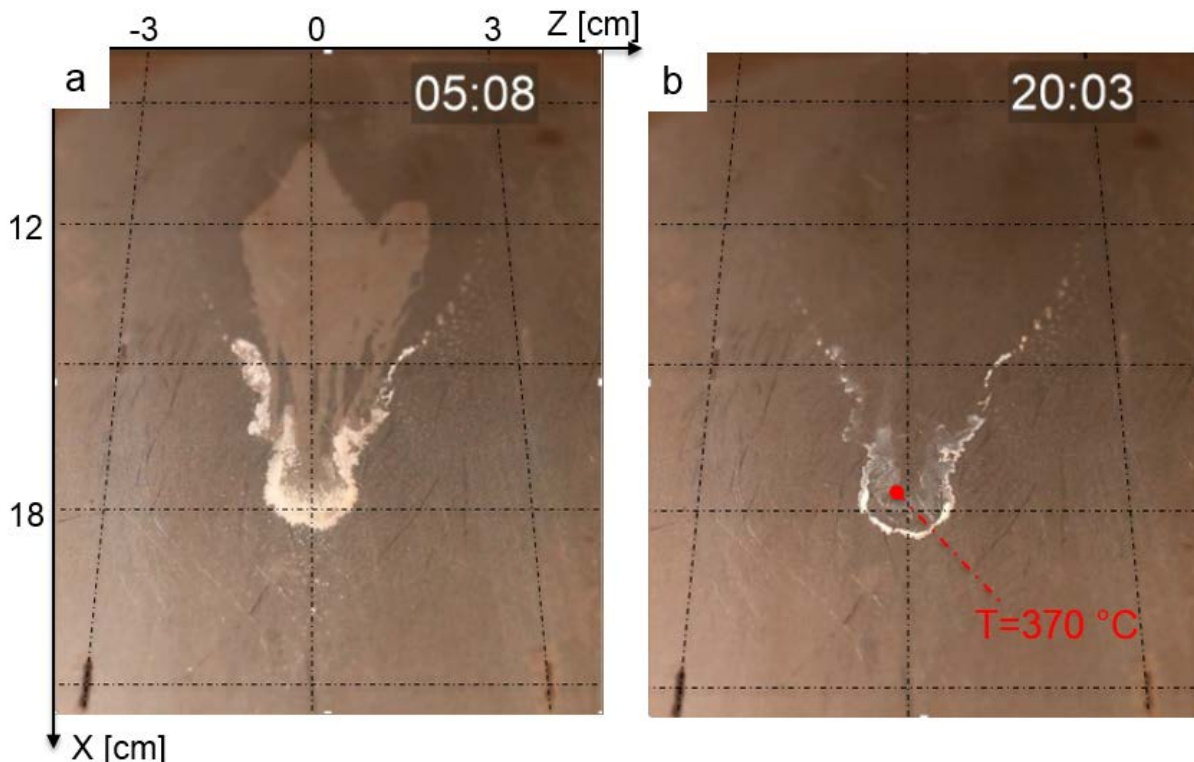


**Figure 4.24: Results of measurement № 9. a - solid deposits at the end of the accumulation phase, b - solid deposits at the end of the decomposition phase**

Figure 4.25 illustrates exemplarily the results of experiment № 21. AdBlue was injected with injector 3. The produced spray had a low area load and a small droplet spectrum with low We-numbers. Due to the high initial plate temperature of approx. 360 °C a high injection rate was necessary to cool the plate below the critical wall temperature. The first liquid film was found after 120 seconds of injection, first deposits after 190 seconds. The accumulation phase was

extended to 7 minutes in order to generate a sufficient amount of deposits. Figure 4.25a shows the video observation of the film and deposits after 7 min. In the left picture, the footprint of the spray and the liquid film can be observed. Shear stress from the exhaust flow pushes the film downstream to plate regions with higher temperatures. There, deposits are created wherever the film stagnates. Subsequently the UWS injection was stopped and the exhaust mass flow rate was rapidly increased to 1000 kg/h as shown in Figure 4.25b. The plate temperature in the deposition area rose by approx. 140 °C due to a higher heat transfer from the exhaust gas and the lack of water evaporation from AdBlue. Consequently a fast deposit decomposition was observed. Nevertheless a noticeable amount of deposit was found at the end of the experiment. The HPLC analysis, which was carried out at KIT, showed that the remaining deposits consisted of 64 % ammeliid and 30 % ammelin. The residual was an unknown substance.

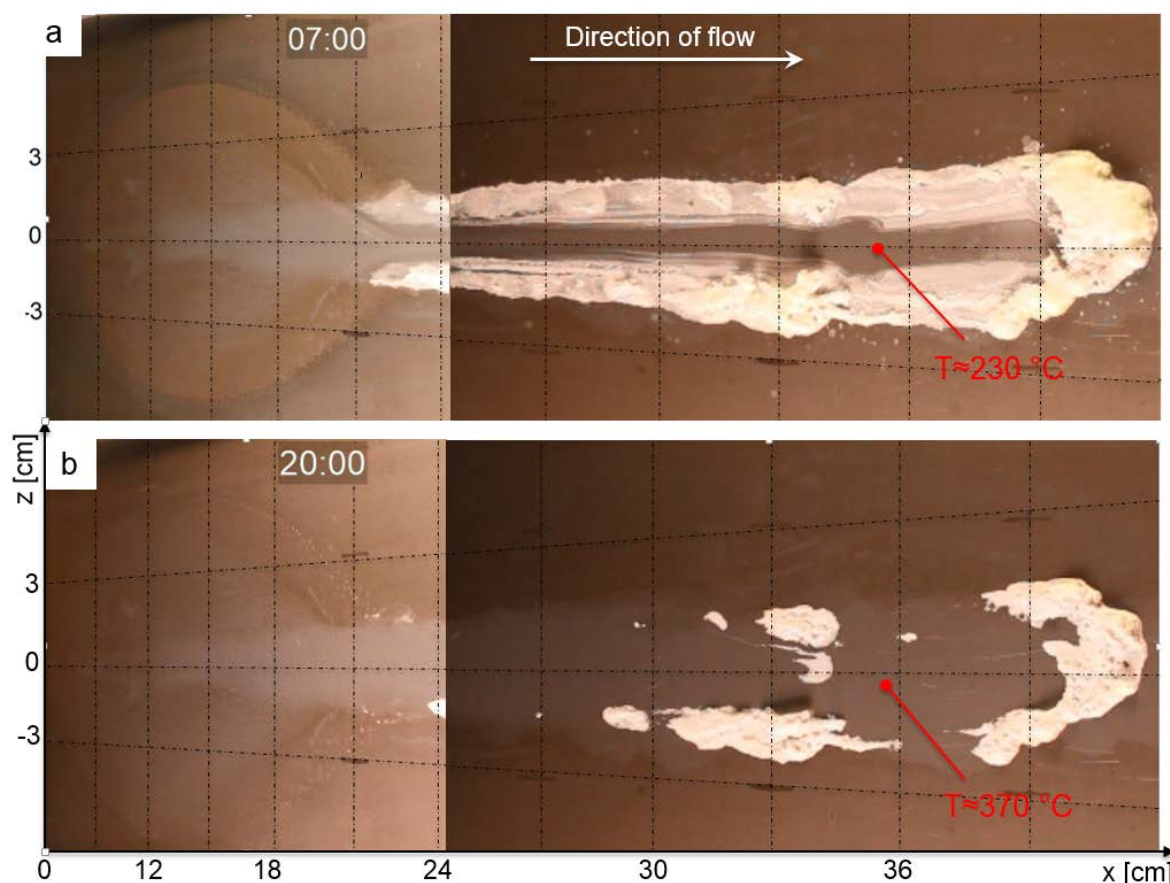


**Figure 4.25: Results of measurement № 21. a - solid deposits at the end of the accumulation phase, b - solid deposits at the end of the decomposition phase.**

### 4.2.3 Thermogravimetric decomposition of urea and its by-products

Thermogravimetric analysis is used to study the decomposition behavior of urea and its by-products in detail. It delivers data on decomposition temperatures and characteristic stages and can further be used for qualitative conclusions on the sample composition when analyzing urea deposits.

Figure 4.26 shows TGA results for urea and all relevant by-products included in this study. Here, a heating rate of 2 K min<sup>-1</sup> is applied for an initial sample mass of 5 mg.

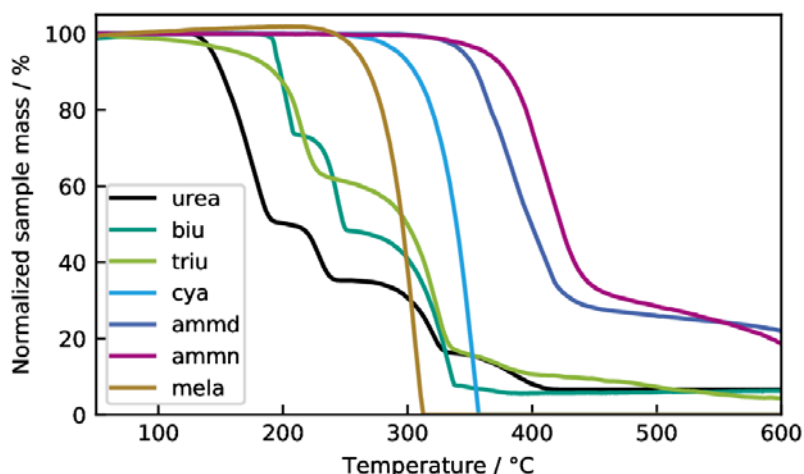


**Figure 4.26: Thermogravimetric decomposition of urea and its by-products. Experiments are performed with an initial sample mass of 5 – 6 mg in the cylinder-type crucible using a heating rate of 2 K min<sup>-1</sup>.**

Urea decomposition starts at 133°C and is followed by biuret and triuret decomposition producing cyanuric acid and ammelide. Decomposition of cyanuric acid and ammelide is initiated at 250°C and 360°C, respectively. Ammelide is assumed to react to ammeline, which starts decomposing subsequently. Ammeline is proposed to react to melamine by Bernhard et al [22]. In other works, melamine is only found to be present in small amounts at 250°C. Experiments shown in Figure 4.26 reveal the start of melamine decomposition at 250°C. Since it is fully decomposed at temperatures above 300°C, melamine, which is formed during ammeline decomposition, is assumed to decompose instantaneously.

Detailed decomposition schemes and kinetic models have been proposed by several authors [19,20,37]. In order to generate a sufficient database for kinetic modeling, various analyses of urea and by-product decomposition are performed at different experimental boundary conditions. A variation of experimental boundary conditions is observed to affect the decomposition kinetics as shown in Figure 4.27, which is in accordance to previous findings [19,22,35].

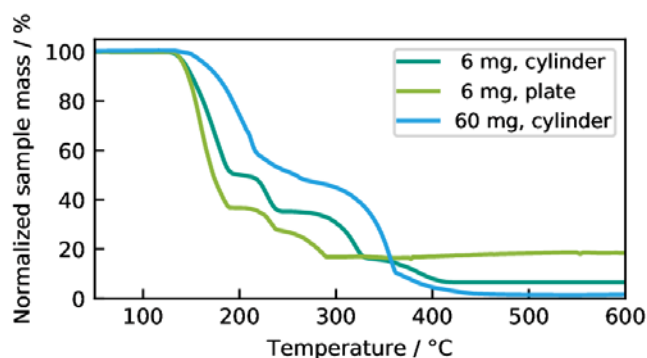


**Figure 4.27: Effect of experimental boundary conditions on urea thermal decomposition. Experiments are performed using different initial sample masses and cylinder types, but an identical heating rate of 2 K min<sup>-1</sup>.**

Figure 4.27 shows decomposition of pure urea samples of varying initial sample mass and crucible geometries. The main difference in crucible geometry is the diameter, as the plate crucible features a 2.5 times larger diameter. While maintaining identical initial sample mass, the use of the plate crucible reveals faster decomposition kinetics compared to the cylinder crucible. Furthermore, a higher residual mass is obtained for the plate geometry. By varying the initial sample mass using the cylinder crucible, faster decomposition is observed for the small initial mass. This clearly reveals the importance of the surface-to-volume ratio of the sample. Here, isocyanic acid release at the sample surface plays a major role since it is in-

volved in most of the reactions forming by-products. Results show that a high surface-to-volume ratio promotes urea decomposition, which is due to interface reactions occurring at the sample surface. An increase of interfacial area accelerates mass transport of gaseous products. Previously proposed kinetic models are not able to predict the effect of a varying surface-to-volume ratio on urea decomposition [23].

The mentioned compounds bear the risk to be produced in the mixing section of SCR systems from liquid UWS deposition and solidification. However, according to respective decomposition temperatures, solid deposits in SCR systems can partially be regenerated by high exhaust gas temperatures. As Figure 4.26 shows, the decomposed samples produce residues which are temperature resistant up to 700°C. The nature of these final decomposition products has not been investigated in literature. Figure 4.28 shows the mean residual mass determined from multiple TGA measurements of urea and its by-products at 600°C.

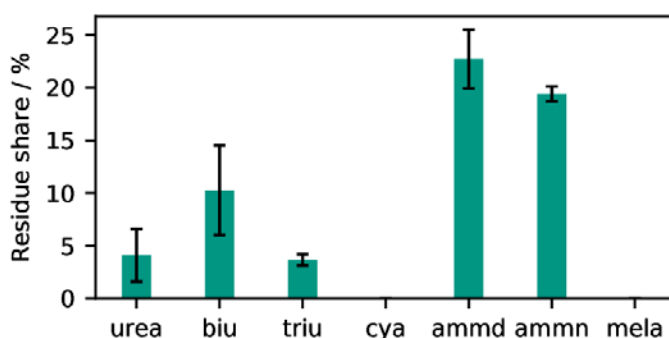


**Figure 4.28: Mean residual mass from thermogravimetric decomposition of urea and its by-products.**

Amelide and ammeline (ammn) leave the highest relative amount of temperature resistant residues of about 20 %. Urea, biuret and triuret further result in small shares of residues, whereas cyanuric acid and melamine (mela) are observed to fully decompose. Since urea, biuret and triuret decomposition leads to amelide production, these residues are assumed to originate from amelide as well. Respective amelide decomposition stages can be seen in Figure 4.26.

Generated residues are collected for triuret, amelide and ammeline and analyzed by nuclear magnetic resonance (NMR).  $^1\text{H}$ - and  $^{13}\text{C}$ -NMR analyses are performed at the Institute of Organic Chemistry at Karlsruhe Institute of Technology. Results show identical peak distributions for the three samples and are depicted in Figure 4.29 for amelide.

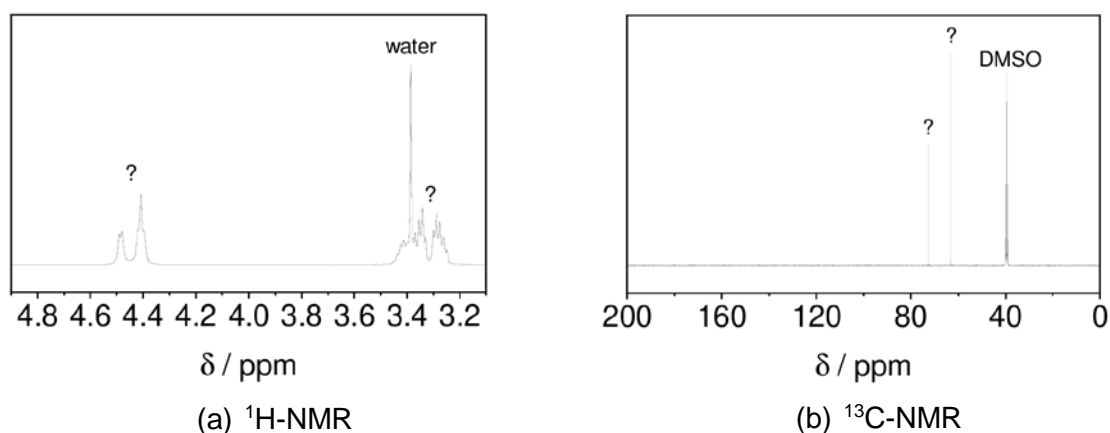


**Figure 4.29: NMR analysis results of amelide residue at 600°C.**

Comparable results achieved for residues from triuret and ammeline TGA are shown in Figure 6.5 and Figure 6.6 in the appendix. The illustrated peaks reveal that the sample does not contain aromatic compounds, which would result in peaks  $> 100$  ppm for the  $^{13}\text{C}$ -NMR spectrum. Besides the solvent peaks, the results do not clearly reveal the structure of the present compound. From these data, the resulting compound from ammelide, ammeline and triuret decomposition up to  $600^\circ\text{C}$  is assumed to form an amine or alcohol. Further investigations, e. g. by mass spectrometry or elementary analysis, should help to clarify the structure of the resulting compounds.

### 4.3 Kinetic and CFD modeling

In the following, setups for CFD simulation and the applied physics are described. 0D simulations of the urea decomposition kinetics are performed using a kinetic model adapted from Brack et al. [37]. Furthermore, and the decomposition kinetics are integrated into the 3D CFD simulations.

#### 4.3.1 Numerical setups

Following the numerical setups for 3D simulations of urea decomposition in flow setups with and without injection are presented.

##### Thermogravimetric Analysis

For simulation of thermogravimetric decomposition, a geometry is generated representing the TGA setup as shown in Figure 4.30.

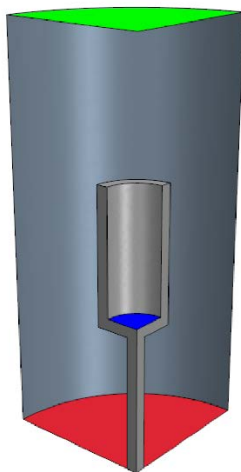


**Figure 4.30: Geometrical setup for numerical simulation of thermogravimetric decomposition of various samples.**

The geometry consists of a cylinder containing the holder and the sample crucible exposed to incident flow. To reduce computational costs, the height of the cylinder representing the fluid domain is reduced to 36 mm, which is three times the height of the cylindrical crucible. In the experimental setup, the crucible is placed in the center of a cylindrical oven with a height of 164.5 mm. The inner diameter of the crucible is 6 mm and the diameter of the fluid domain is 26.5 mm which is identical to the experimental setup. For the simulations, only one quarter of the cylindrical domain is used. A mesh of 30,000 cells with a base size of 0.8 mm is generated by automatic meshing functions. In order to enable heat-up of the crucible according to experimental data, heat conduction is strongly increased for the crucible. Further, the crucible surface temperature at the inlet is defined as boundary conditions to meet the inlet gas temperature. The inlet gas temperature and flow boundary conditions are adapted to experimental conditions. The liquid film is initiated with a composition corresponding to the experiments and with a constant thickness in the shell region.

Time steps of 5 to 20 ms are chosen with 10 inner iterations to achieve convergence. Since some experiments only show a mass loss for a certain temperature range, simulations are performed in respective ranges in order to save computational costs. The liquid film mass is tracked over temperature in order to compare the results to experimental data and DETCHEM<sup>MPTR</sup> simulations.

### Lab test bench at KIT

For application of the overall model to the realistic boundary conditions inside the hot gas test rig, the setup of the experimental measurement section is transferred to a simulation domain. The geometry represents the rectangular channel of the flow setup described in Section 4.1.1. Physical properties of the solid walls are taken from [80]. Since the focus of this work is the integration of a chemical kinetic model to the CFD simulation, the flow duct in front of the measurement section is not included in the model in order to save computational costs. Since a monolith is arranged at the entrance of the measurement section, a homogeneous velocity distribution is assumed as gas inlet boundary condition. A mesh consisting of 1.25 Mio. fluid, 300,000 solid and 30000 shell cells of 1 mm base size is generated by automatic meshing functions. The CFD geometry of the lab test bench at KIT can be seen in Figure 4.31. In addition to presented configurations, a Lagrangian phase is defined, which is initiated by three injector nozzles and represents a 32.5 wt.-% urea water solution. Interaction of spray and wall is defined as multiphase interaction, where the Bai-Gosman model is applied. Model parameters are adapted from Smith [81]. Using two-way coupling the interaction between particles and flow field is modeled in both directions. As for simulation of the thermogravimetric setup, the reaction model of the liquid film calls user coded functions for calculation of production rates.

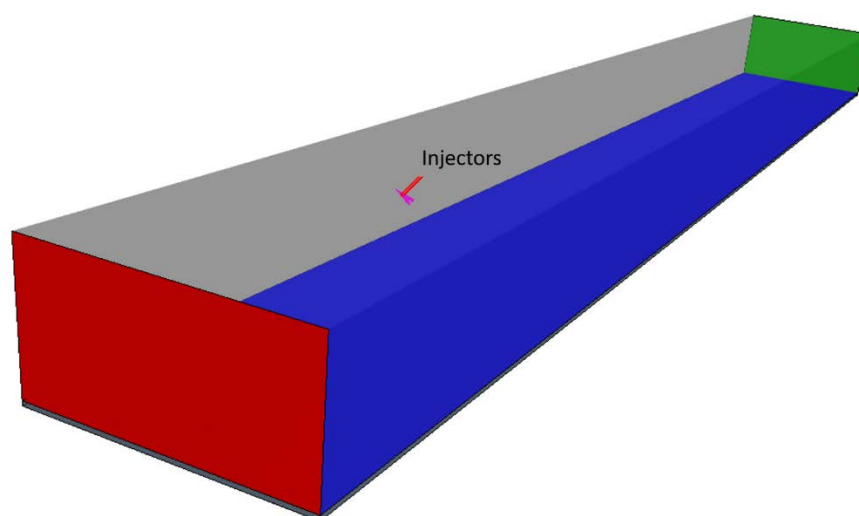


**Figure 4.31: Illustration of CFD Geometry of the lab test bench at KIT.**

The simulation boundary conditions are adapted to respective experimental conditions in terms of gas temperature and flow, dosing strategy and wall temperature. Before simulating the injection process, steady-state simulations are run to calculate stationary flow field and temperatures, which are then used as boundary conditions for transient simulations including injection. Applied time steps are adapted to the required model complexity in order to reach sufficient accuracy while maintaining feasible computational costs.

Before the actual simulation, one injection cycle of 0.2 s is simulated with spray injection and a fixed time step of 0.2 ms and 3 inner iterations. This way, all impinging droplets on the wall can be recorded and used as sources in the later simulation through the injection source approach (see Section 4.3.2).

Due to the use of sources instead of spray simulation a higher time step can be used in the actual simulation. In the first 0.02 s, during injection time, a time step of 2 ms is used to split

the injection sources in at least 10 parts. Afterwards, a time step of 10 ms is used during an injection break. When injection is complete the time step is finally increased to 20 ms.

Per time step 7 inner iteration are used to reach convergence. Here, an injection duration of 10 s with a duty cycle of 10 % and resulting film formation, evaporation and decomposition are simulated for a physical time of 2 minute to test the chemical model implementation.

**Engine test bench**

The numerical modeling of deposit formation and decomposition was carried out with the CFD code StarCCM+ v13.06, which was decided by the working group participants. However, the developed methodology can also be implemented in other commercial CFD codes. The CAD model of the optical box, as shown in Figure 4.5a, was imported in the code and a volume mesh was generated. In order to reduce simulation effort, only the regions shown in Figure 4.32 were used for further numerical investigations. The inlet conditions of the box were taken from the flow simulation of the whole test bench geometry which is shown in Figure 4.5.

The box geometry was divided into several regions which are marked with different colors. Due to different physical properties, these regions were assigned to different physics continua. For the modeling of the liquid film, a shell region was created on the top side of the impingement plate. In order to represent the uncoated catalyst downstream the box, a volume mesh was extruded from the outlet of the fluid region.

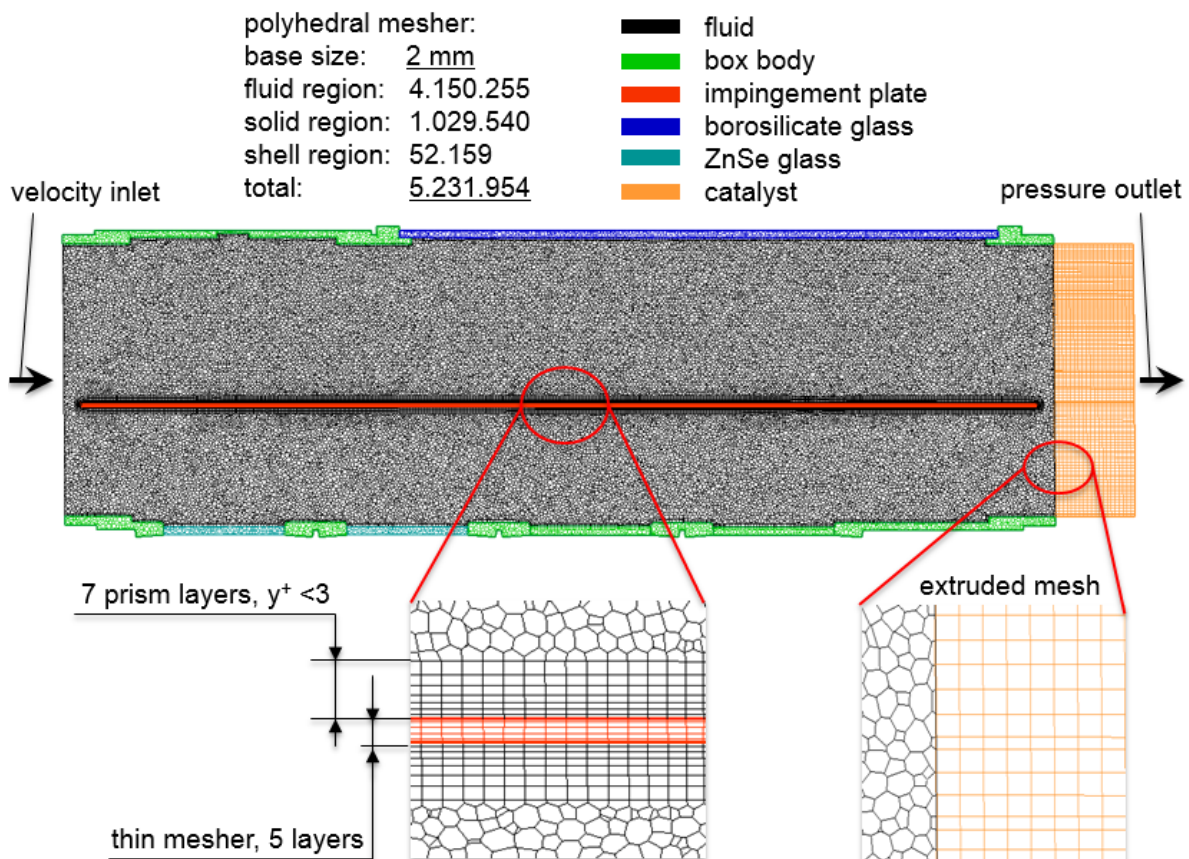


**Figure 4.32: Numerical mesh of the measuring section**

A grid dependency analysis was carried out to optimize the simulation effort and accuracy in the following numerical investigations. Three mesh structures with a base size of 3, 2 and 1.5 mm were built to find an appropriate numerical mesh. For this purpose the parameters velocity field inside the optical box, turbulent kinetic energy in the area close to the impinge-

ment plate, temperature of the plate and surface heat transfer were compared. The investigation has shown that the numerical mesh with a base size of 2 mm provided reasonable modeling results with an acceptable computational effort. Investigations on the wall treatment of the impingement plate were conducted due to its importance for the heat and mass transfer between the gas flow and liquid film or solid wall respectively. The plate temperature at steady-state conditions, as shown in Table 4.9, was modeled with low and high  $y^+$  wall treatment approaches. The comparison between the simulated and measured plate temperature revealed the need for a resolution of the boundary layer with at least 7 prism layers and the use of the low  $y^+$  approach. The thickness of the first prism layer near the solid wall is approx. 400  $\mu\text{m}$ , which allowed the modeling of a liquid film with a thickness up to this value. Due to a large volume of the box and a base size of 2 mm the total cell number reached 5,231,954.

#### 4.3.2 Modeling physics

The physics modeled in StarCCM+ comprises an Euler-Lagrange approach for the gas flow and UWS injection, spray/wall interaction, liquid film formation and evaporation. Applied physical models were mainly based on the work by Fischer [80] and the SCR best practices guide by the software producer [81]. Figure 4.33 gives a rough overview of the most important models and their hierarchy in the modeling of the deposit formation and decomposition. It is obvious that the modeling of deposit formation must start with accurate boundary conditions, i.e. turbulent flow, temperature and heat transfer. The hierarchical structure clarifies that complex deposit modelling includes all upstream models like Schiller-Naumann drag force model or Bai-Onera droplet impingement model. Only after their validation, the modeling of deposit formation with the complex chemistry solver including the DETCHEM<sup>MPTR</sup> routine can be conducted.

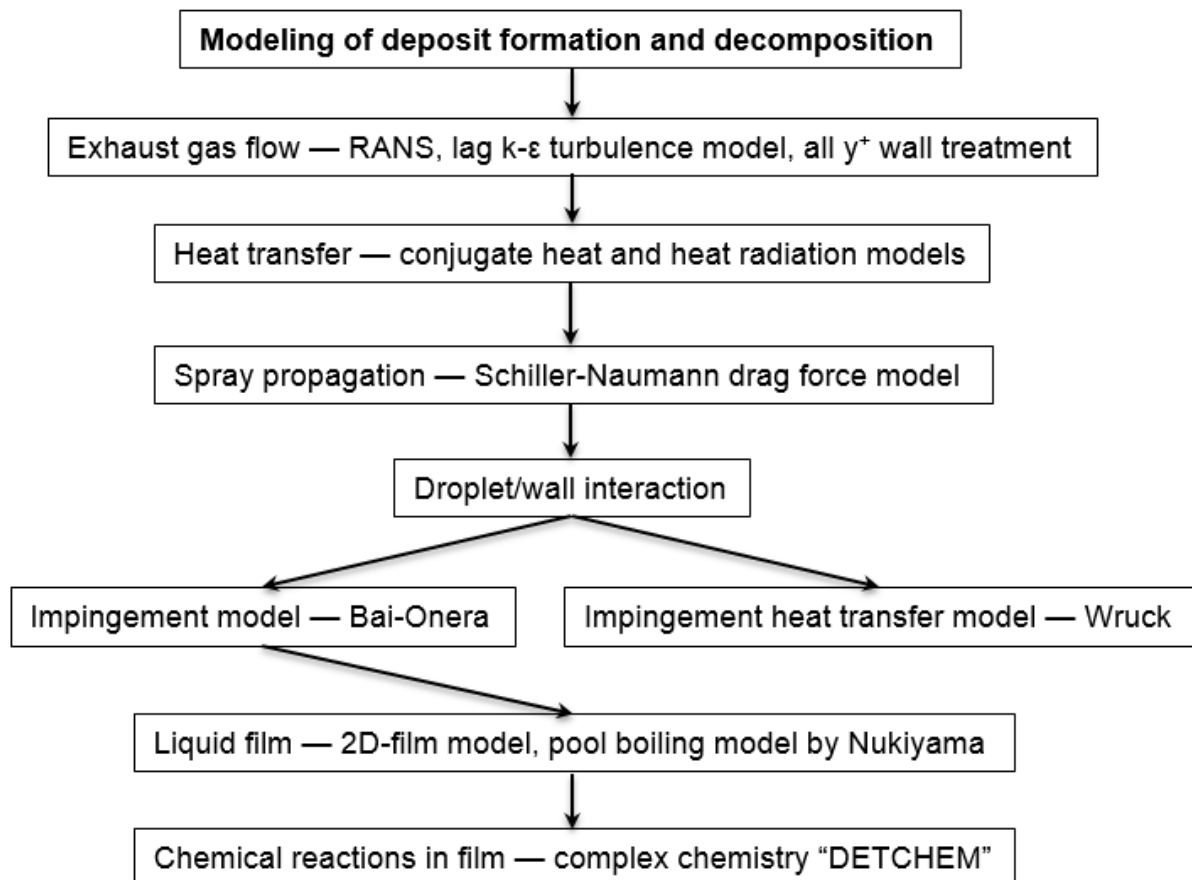


Figure 4.33: Workflow of submodels to simulate deposit formation and decomposition

For the modeling of the gas flow, a RANS (Reynolds-averaged Navier-Stokes) approach was used with a Lag Elliptic Blending  $k$ - $\varepsilon$  realizable turbulence model. Compared to the measurement data, this model combined with the low  $y^+$  wall treatment provided the best simulation results of the plate temperature prior to injection. The obtained results will be presented in section 4.4. The number of species in the gas phase was substantially increased compared to Fischer's work due to evaporation of new species from the film and Lagrangian phase. The new species of the mentioned phases and their link between each other will be discussed in Section 4.3.4 and Section 4.3.5.

Due to the fact that the outer walls of the optical box were not thermally insulated, convection and heat radiation were modeled on the corresponding boundaries in the CFD model. The convective heat transfer coefficient was estimated to  $15 \text{ W/m}^2\text{K}$ , the ambient temperature to  $30 \text{ }^\circ\text{C}$ . For the modeling of the heat radiation, both inside the box and on its outer wall, the Gray Thermal Radiation (GTR) model was applied. Furthermore the absorption of the radiation by the exhaust gas was not considered. Therefore, in addition to the GTR model, the Surface-to-Surface (S2S) radiation model was used to analyze the radiation heat transfer between the surfaces inside the box. The radiation properties were set as shown in Table 4.11.

Prior to simulating the injection process, steady-state simulations were run to calculate stationary flow field and temperatures, which were then used as initial conditions for transient simulations with UWS injection. The UWS spray was initialized with characteristic injector data shown in Table 4.2.

#### Droplet trajectories

The validation of the spray deflection by the flow against the measured data showed an over-estimation of the drag coefficients of the droplets within a size range of  $25\text{-}300 \text{ }\mu\text{m}$ . Therefore the previously used Schiller-Naumann correlation [82] for the drag coefficient was modified with the Cunningham correction factor [83] in order to reduce the drag force for small droplets. The modified Schiller-Naumann correlation is given by equation (4.2):

$$C_d = \begin{cases} \frac{24}{Re_d \cdot C_p} (1 + 0.15 \cdot Re_d^{0.68}) & Re_d < 10^3 \\ 0.44 & Re_d \geq 10^3 \end{cases} \quad (4.2)$$

with  $Re_d$  as droplet Reynolds number and  $C_p$  as the Cunningham correction factor

$$C_p = 1 + 90 \cdot Kn_p \cdot \left( 1 - 2 \frac{-0.015}{Kn_p} \right) \quad (4.3)$$

and  $Kn_p$  as Knudsen number, given by

$$Kn_p = \frac{k_b \cdot T_g}{\sqrt{2} \cdot \pi \cdot d_g^2 \cdot p_g \cdot D_d} \quad (4.4)$$

where  $k_b = -1.38 \cdot e^{-23} \text{ m}^2 \cdot \text{kg} \cdot \text{s}^{-2} \text{K}^{-1}$  - Boltzmann constant,

$d_b = 2.8\text{e-}10 \text{ m}$  - mean molecule diameter in gas phase,

$T_g$  - gas temperature,

$p_g$  - absolute gas pressure,

$D_d$  - particle diameter.

In comparison to the original Cunningham correction factor  $C_p$ , the coefficients in equation (4.3) were adapted to find the best agreement between the simulated and measured results.

Figure 4.34 shows the comparison between the original and modified Schiller-Naumann correlation. The three different colors illustrate the droplet spectra of the investigated injectors. While the droplet spectrum of injector 2 is hardly affected by changes of the drag coefficient model, the drag coefficient of the small droplets of injectors 1 and 3 were reduced by 20 - 30 %.

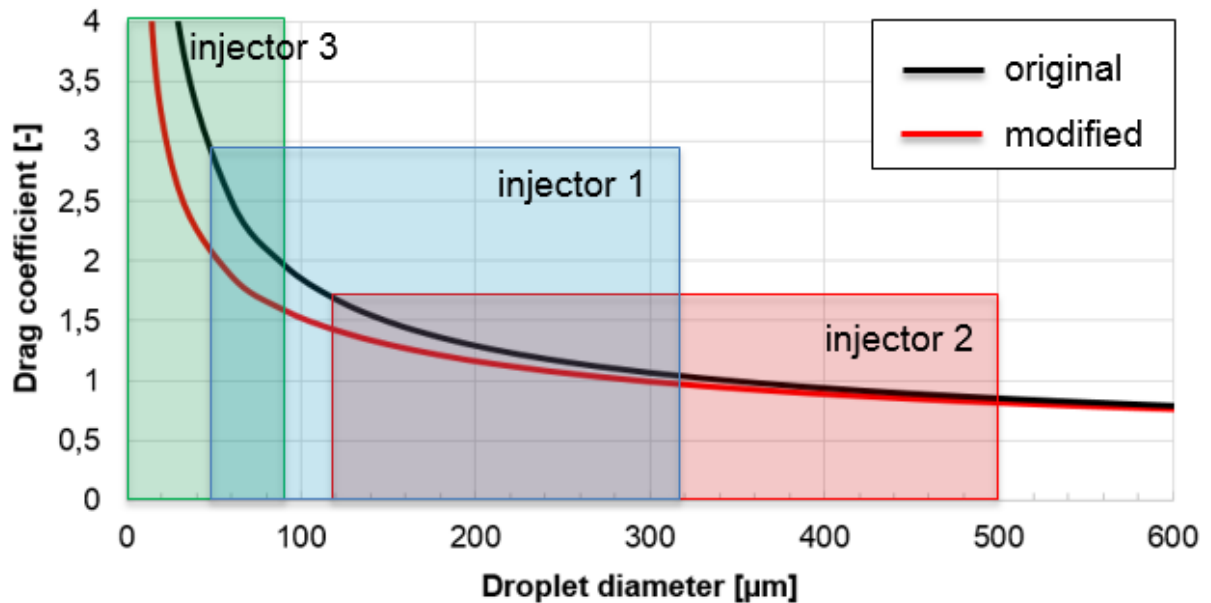
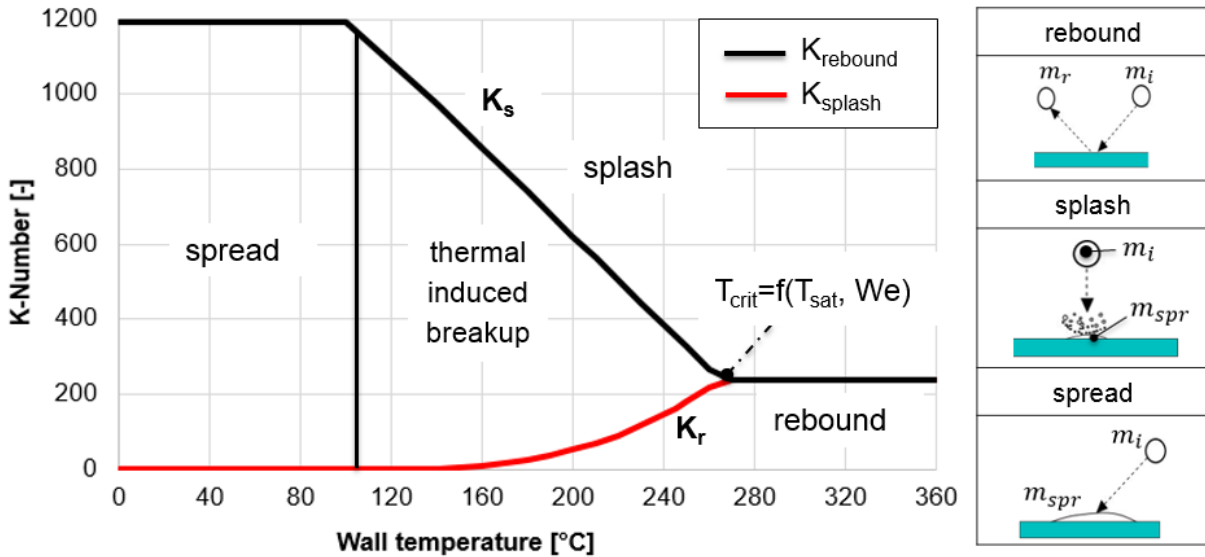


Figure 4.34: Droplet drag coefficients modeled with original and modified Schiller-Naumann correlation for the relative slip velocity between the phases at 20 m/s.

#### Droplet impingement

For the modeling of wall impingement the three impingement diagrams proposed by Satoh, Bai-Gosman and Bai-Onera are available in StarCCM+. In contrast to the other models, the Bai-Onera model offers a higher flexibility in the determination of the impingement regimes. Therefore, this model was chosen for further numerical investigations. The validation of the Bai-Onera model against the measurement results revealed the necessity of its adaption and the introduction of a new impingement regime. Figure 4.35 illustrates the modified Bai-Onera diagram. In comparison to the original model implemented in StarCCM+ [84], the value of the critical wall temperature  $T_{crit}$  in the modified model depends on both saturation temperature of the droplet  $T_{sat}$  and the normal Weber number  $We_n$ . Further, similar to the work of Quissek et al. [77], the regime “thermal induced breakup (TBU)” was introduced.



**Figure 4.35: Modified Bai-Onera wall impingement model**

The definition of the critical wall temperature is given in equation (4.5).

$$T_{crit} = \min(T_{sat} + 0.02 \cdot We_n + 152 \text{ °C}; 290 \text{ °C}) \quad (4.5)$$

The transition between splashing and spreading is defined with the blending function  $K_s$ :

$$K_s = \begin{cases} K_0 & T^* \leq 0 \\ K_0 + T^*(K_1 - K_0) & 0 < T^* < 1 \\ K_1 & T^* \geq 1 \end{cases} \quad (4.6)$$

with

$$K_0 = A \cdot La^{-0.18} \cdot Oh^{-0.4} \quad (4.7)$$

and

$$T^* = \frac{T_w - T_{sat}}{T_{crit} - T_{sat}} \quad (4.8)$$

where  $A = 1000$ ,  $K_1 = 240$ ,  $La$  - Laplace number,  $Oh$  - Ohnesorge number and  $T_w$  - wall temperature.

The transition between spreading and rebound is defined by the function  $K_r$ :

$$K_r = \begin{cases} 0 & T^* \leq 0 \\ K_1 \cdot (T^*)^\gamma & 0 < T^* < 1 \\ K_1 & T^* \geq 1 \end{cases} \quad (4.9)$$

where  $\gamma = 5$ .

As mentioned above the regime “thermal induced breakup” was introduced for:

$$\begin{cases} 0 < T^* < 1, \\ K_r < K < K_s \end{cases} \quad (4.10)$$

with

$$K = We_n \cdot Oh^{-0.4} \quad (4.11)$$

Figure 4.36 shows the thermal induced breakup on a hot surface according to [77]. The droplet impinges at the wall and forms a wall film that immediately becomes superheated. Formation

and bursting of bubbles creates a large amount of small secondary droplets ejected from the film in all directions, regardless of the impact angle of the primary droplet.

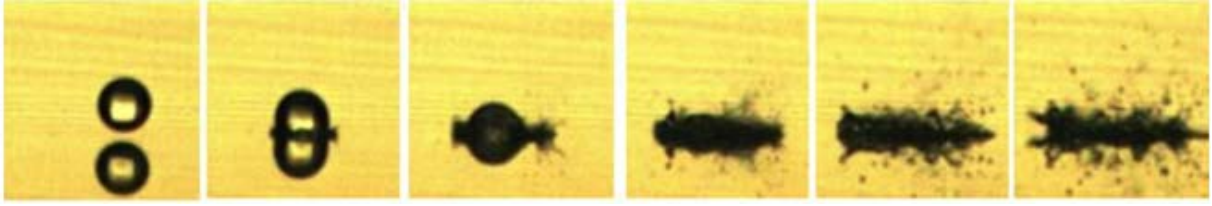


**Figure 4.36: Impingement regime of thermal induced breakup [77]**

The model parameters that have an impact on the mass remaining on the surface after droplet splash  $m_{splash}$  and TBU  $m_{TBU}$  were validated against measurement data. The adapted correlations are given in equations (4.12) and (4.13):

$$m_{splash} = \begin{cases} (1 - r_s) \cdot m_0 & T^* \leq 0 \\ (1 - r_s) \cdot m_0 \cdot (1 - (T^*)^n) & 0 < T^* < 1 \\ 0 & T^* \geq 1 \end{cases} \quad (4.12)$$

where  $m_0$  – incident droplet mass,  $r_s = 0.575$  – statistical mean value of the splash ratio,  $n=6$ ,

$$m_{TBU} = \begin{cases} m_0 & T^* \leq 0 \\ m_0 \cdot (1 - (T^*)^m) & 0 < T^* < 1 \\ 0 & T^* \geq 1 \end{cases} \quad (4.13)$$

where  $m = 3$ .

Figure 4.37 illustrates the impact of the wall temperature on mass fraction of a droplet that spreads on the wall. In order to demonstrate the behavior of droplets in different impingement regimes two droplets with appropriate diameters and K-numbers were considered exemplarily that impinge in the splash and thermal induced breakup regime. The droplet with the high K-number (read line) splashes under all conditions and only a minor mass fraction of liquid remains at the wall. If the wall temperatures approaches the critical temperature the mass fraction is steadily decreasing until no liquid mass spreads on the surface at the critical temperature of 267 °C. The droplet with the lower K-number is located in the spread regime for low temperatures, i.e. it completely forms liquid film after impingement. As soon as the threshold to the thermal induced breakup regime (TBU) is reached the deposited liquid mass decreases and reaches zero as soon as the critical temperature of 256 °C is reached. The difference of 11 °C between the two critical temperatures underlines the dependency of this parameter from the We-number.

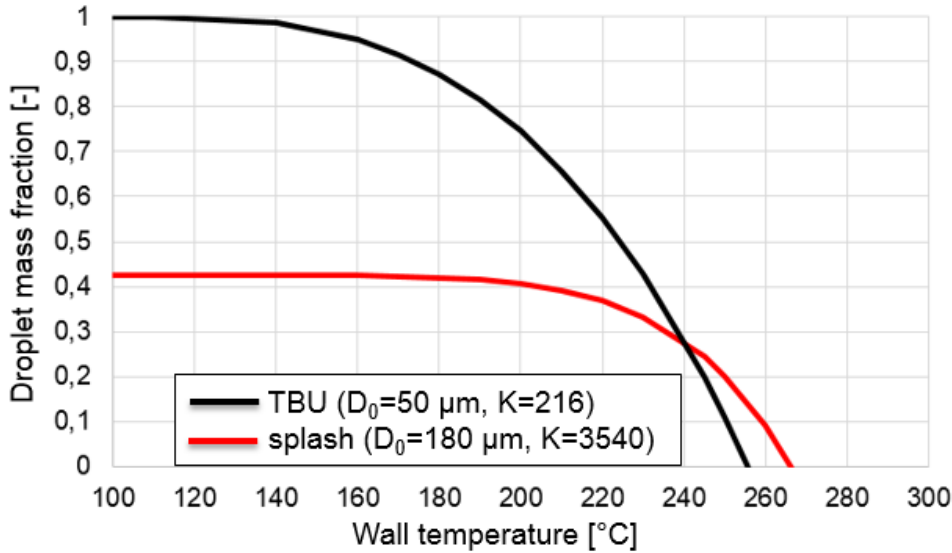


**Figure 4.37: The mass fraction of droplets that spread on the surface in splash (red line) and TBU regime (black line)**

#### Heat transfer during impingement

As mentioned above, no wall wetting occurs above the critical wall temperature due to an insulating vapor cushion between droplet and surface. Nevertheless, the heat transfer between droplet and wall must be taken into account in order to include the important transition from non-wall wetting to wall wetting regimes. The heat  $Q_{imp}$  can be described with equation (4.14) by Wruck [70]:

$$Q_{imp} = A_{cont} \cdot h_{wd} \cdot (T_w - T_d) \cdot c = A_{cont} \cdot \frac{2 \cdot \sqrt{t_{cont}} \cdot b_w \cdot b_d}{\sqrt{\pi} \cdot (b_w + b_d)} \cdot (T_w - T_d) \cdot c \quad (4.14)$$

where  $h_{wd}$  is the impingement heat transfer coefficient,  $b_w$  and  $b_d$  the heat penetration coefficients evaluated with the materials of the wall and the droplet,  $T_w$  and  $T_d$  the temperatures of wall and droplet and  $c$  the particle count in a parcel.

As long as a droplet has only an elastic deformation during the impingement with a hot wall, the effective contact area  $A_{cont}$  can be calculated with the correlation from Akao et al. [85]. If a droplet splashes on a surface,  $A_{cont}$  is limited to a certain value and does not increase further with rising  $We_n$ -number [70]. The  $We_n$ -number at which the transition between elastic deformation and droplet breakup takes place, was found based on the impingement diagram proposed by Quissek et al. [77]. The correlation for  $A_{cont}$  on the basis of the measurement data presented in chapter 4.2:

$$A_{cont} = \begin{cases} \frac{\pi}{4} \cdot (0.52 \cdot D_0 \cdot We_n^{0.38})^2 & We_n < 50 \\ \frac{\pi}{4} \cdot (2.5 \cdot D_0)^2 & We_n \geq 50 \end{cases} \quad (4.15)$$

where  $D_0$  is the incident droplet diameter.

The contact time  $t_{cont}$  between droplet and wall is given by equation (4.16):

$$t_{cont} = \begin{cases} \frac{\pi}{4} \cdot \sqrt{\frac{\rho_d \cdot D_0^3}{\sigma_d}} & We_n < 50 \\ \sqrt{\frac{\pi}{2}} \cdot \left(\frac{\rho_d \cdot D_0^5}{\sigma_d \cdot u_n^2}\right)^{0.25} & We_n \geq 50 \end{cases} \quad (4.16)$$

where  $\rho_d$  and  $\sigma_d$  are droplet density and droplet surface tension, respectively, and  $u_n$  the normal component of the droplet velocity relative to the wall.

In order to model partial droplet evaporation above the critical wall temperature, a simplified approach proposed by Smith [79] was chosen in the present work. Instead of a manipulation of the impingement heat transfer model available in StarCCM+, single droplets were completely evaporated after their impingement on a hot surface. In contrast to the work by Smith, the evaporation probability  $pe$  was calculated for each droplet depending on the impingement heat (4.17).

$$pe = \frac{Q_{imp}}{m_d \cdot \Delta h_d} [-] \quad (4.17)$$

where  $\Delta h_d$  is the evaporation enthalpy and  $m_d$  the droplet mass.

Figure 4.38 illustrates the evaporation probability of the two different droplets that were introduced in Figure 4.37. It is obvious that the evaporation efficiency of the small and slow droplet (black line) is considerably higher than that of the large and fast droplet (red line).

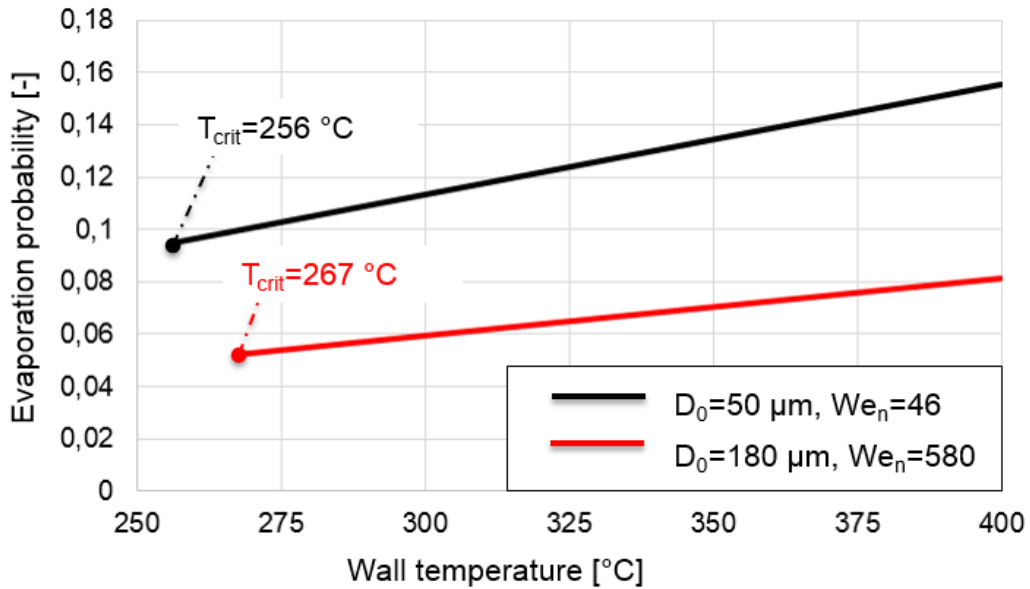


Figure 4.38: Evaporation probability of droplets of different size on a hot surface,  $T_w > T_{crit}$

The StarCCM+ fluid film model was used to simulate thin liquid films on solid surfaces. The liquid film was modeled as a shell region at the interface between gas and solid phase and represents one cell layer. Consequently, the liquid film is a two-dimensional area on the solid wall. Due to the modeling of the deposit formation in the liquid film, the film model was extended with new components. Their properties will be described in Section 4.3.5.

The liquid film may interact with its environment. Available models for gravity-driven fluxes, shear force, film stripping, film evaporation and boiling were used. The setting of the boiling and evaporation model were applied as proposed by Fischer [80].

### 4.3.3 Injection source approach

The numerical prediction of deposit formation and decomposition requires modeling of physical and chemical processes with different time ranges:

- wall cooling, film formation, growth and decomposing of deposits - time range of minutes
- chemical reactions - time range of milliseconds
- spray propagation and droplet impingement - time range of microseconds

With regard to the simulation wall time, the modeling of the spray propagation and the droplet impingement is most critical. The presence of the Lagrangian phase in the simulation domain limits the reasonable simulation time step to the range of approx. 0.1-0.7 ms and increases the modeling effort proportionally to the injection time. Moreover, these processes are periodic and thus should be modeled many times until the simulation of the deposit formation or decomposition is completed.

In order to overcome the issues described above and thus accomplish the modelling of deposit formation and decomposition with typical time ranges, an injection source approach was developed. In this approach the numerical parcels that represent the spray are substituted by source terms of mass, momentum and energy that are directly applied to the film and gas phase. The source terms for both phases were calculated simultaneously during a single injection event. These preparatory simulations were carried out for numerous wall temperatures and the resulting source terms were stored for the use in the following transient long time simulation. One setup can be used as long as the operating conditions remain constant, i.e. as long as the spray deflection and the impingement positions of droplets are not changing. When simulating transient operating conditions the source terms must be updated continuously with the specific combination of spray and exhaust mass flow.

With this approach, it was possible to increase the simulation time step to a range of 5-10 ms. Furthermore, the computing time of a simulation time step was reduced by approx. 25 %. Even with detailed chemistry a simulation time of 45 s/day was achieved when using one computer core per 30.000 cells. That is well beyond typical capabilities.

### Calculation of the source terms of the gas phase

The calculation was carried out in the following steps:

1. The simulation model is set up as mentioned above and a steady-state simulation without the spray injection is conducted to calculate stationary flow- and temperature fields. The calculated data is saved in the simulation file as initial condition for the following transient simulations including injections.
2. The simulation is restarted with an implicit unsteady solver using the pre-calculated initial conditions. The UWS spray is initialized with characteristic injector data shown in Table 4.2. The injection time is set to 20 ms. The parcel stream  $\dot{p}$  was chosen according to equation (4.18):

$$\dot{p} = \frac{\Delta t \cdot 200}{2e^{-4} s} \cdot \left[ \frac{\text{parcels}}{\text{time step}} \right] \quad (4.18)$$

where  $\Delta t$  is the simulation time step.

In general, the whole number of injected parcels should provide a good statistical representation of the spray droplets in the fluid domain.

The simulation of one injection cycle (1 s) is conducted. During the simulation time following values are cumulated in each fluid cell:

- a. Normalized mass of water and urea evaporated from droplets

$$\bar{m}_{gi} = \frac{Y_i \cdot \Delta t}{t_{inj} \cdot V_c}, \left[ \frac{g}{s \cdot m^3} \right] \quad (4.19)$$

where  $Y_i$  is the evaporation rate of species  $i$ ,  $t_{inj}$  the injection time and  $V_c$  the volume of a fluid cell.

- b. Normalized evaporation heat

$$\bar{Q}_g = \frac{Q_{ev} \cdot \Delta t}{t_{inj}}, [W] \quad (4.20)$$

where  $Q_{ev}$  is the heat flux that is used for droplet evaporation in the given cell .

- c. Normalized momentum

$$\bar{p}_g = \frac{F_d \cdot \Delta t}{t_{inj} \cdot V_{c,i}}, \left[ \frac{N}{m^3} \right] \quad (4.21)$$

where  $F_d$  is the drag force from the droplet to the gas phase.

The values of  $Y_i$ ,  $Q_{ev}$ ,  $F_d$  are typically accessible in commercial CFD codes.

The values  $\bar{m}_{gi}$ ,  $\bar{Q}_g$ ,  $\bar{p}_g$  are cumulated for each volume cell with sum-monitors applied in CCM+ and saved in the simulation file via a volume data mapper. The obtained data  $\sum \bar{m}_{gi}$ ,  $\sum \bar{Q}_g$ ,  $\sum \bar{p}_g$  are source terms for mass, energy and momentum, respectively. These source terms represent the spray impact on the gas phase. The terms are normalized to the injection time and therefore can be applied to each desired injection time in further simulations. The equation (4.22) gives an example for the application of the energy source:

$$Energy\ source = \begin{cases} \sum \bar{Q}_g & t_{cycle} \leq t_{inj} \\ 0 & t_{cycle} > t_{inj} \end{cases} \quad (4.22)$$

where  $t_{cycle}$  is the cycle time.

Other source terms are applied in a similar way. The temperature of species, which are introduced in the gas phase by the mass source, was estimated to be 100 °C.

### Calculation of the source terms of the fluid film phase

As mentioned above, the calculation of source terms to the film phase was conducted simultaneously with those to the gas phase. During the transient simulation of one injection cycle, properties of the impinged droplets were analyzed and the following values were determined:

- a. Mass of an impinged droplet which remains at the impingement position if  $T_w < T_{crit}$  (hereafter called as "stick mass").

As shown in Figure 4.35 and Figure 4.37, the stick mass depends on the droplet K-number and the surface temperature. As long as the operating conditions are not changing, the impact of the gas flow on a droplet is not changing as well. Therefore, for steady-state operating conditions, the stick mass depends only on the surface temperature. In order to obtain a mass source which is valid for different surface temperatures, stick mass should be calculated for different temperatures in advance, e. g.: 280, 260, 240, 220, 200 and 160 °C. These values cover the temperature range with the highest changing gradients of the stick mass. Below  $T_w = 160$  °C the temperature impact on the impingement process can be considered as negligible. The stick mass for different surface temperatures  $T_i$  is determined with equation (4.23):

$$m_{stick,Ti} = \begin{cases} m_{splash} & K > K_{s,Ti} \text{ and } T_i^* < 1 \\ m_{TBU} & K_{r,Ti} < K \leq K_{s,Ti} \text{ and } 0 < T_i^* < 1 \\ m_{spread} & K \leq K_{s,Ti} \text{ and } T_i^* \leq 0 \\ 0 & K \leq K_{r,Ti} \text{ and } T_i^* < 1 \end{cases} \quad (4.23)$$

Due to the fact that the impact droplets consist of water and urea,  $m_{stick,Ti}$  should be determined separately for both species:

$$m_{stick,Ti}^i = m_{stick,Ti} \cdot w_i \quad (4.24)$$

where  $w_i$  is the mass fraction of the species "i" in a droplet.

The obtained values are normalized to the injection time and the surface size of a cell  $A_{c,i}$  at the impingement position.

$$\bar{m}_{stick,Ti}^i = \frac{m_{stick,Ti}^i}{t_{inj} \cdot A_{c,i}} \left[ \frac{g}{s \cdot m^2} \right] \quad (4.25)$$

- b. Impingement heat  $Q_{imp}$  transferred from a hot surface to a droplet if  $T_w \geq T_{crit}$ .

For steady-state operating condition the value of  $Q_{imp}$  depends only on the surface temperature. Similar to the stick mass, the impingement heat is calculated for different surface temperatures in advance, e. g.: 450, 300, 280, 260 and 240 °C. The impingement heat for different surface temperatures is calculated with equation (4.26):

$$Q_{imp,Ti} = A_{cont} \cdot h_{wd} \cdot (T_{w,i} - T_d) \cdot c \quad (4.26)$$

where c is the particle count in a parcel. The obtained values are normalized to the used injection time:

$$\bar{Q}_{imp,Ti} = \frac{Q_{imp,Ti}}{t_{inj}}, [W] \quad (4.27)$$

- c. Normalized momentum from a droplet to the film :

$$\bar{p}_f = \frac{F_d \cdot \Delta t}{t_{inj} \cdot A_{c,i}}, \left[ \frac{N}{m^3} \right] \quad (4.28)$$

where  $F_d$  is the force from a droplet to the film. It is usually accessible in commercial CFD codes.

- d. Product of the droplet mass and temperature  $m_{di} \cdot T_{di}$

This product is necessary for the further calculation of the mass averaged temperature of the source species.

The values  $\bar{m}_{stick,Ti}^i$ ,  $\bar{Q}_{imp,Ti}$ ,  $\bar{p}_f$  and  $m_{di} \cdot T_{di}$  were mapped to the film region for each time step and cumulated for each surface cell with sum-monitors within CCM+. The data was saved in the simulation file via a volume data mapper. The cumulated value  $\Sigma \bar{p}_f$  was the source term of momentum which was applied to the film region during injection time.

In order to obtain mass and heat sources which are valid for the current surface temperature, a linear interpolation between corresponding values of  $\Sigma \bar{m}_{stick,Ti}^i$  or  $\Sigma \bar{Q}_{imp,Ti}$  was carried out. Figure 4.39 illustrates exemplarily the mass and heat source for a surface cell. A strong impact of the surface temperature on both sources can be observed. With a rising surface temperature the mass source term drops continuously until its minimum at 280 °C is reached. In contrast to that, the Leidenfrost effect appears at the temperature of 260 °C and thus, the

impingement heat source starts to rise. The overlapping of the mass and heat sources in the temperature range of 260-280 °C is caused by the impingement of droplets with different normal We-numbers.

In order to obtain the correct mass averaged temperature of the species produced by the mass sources, the cumulated product of  $m_{di} \cdot T_{di}$  must be divided by the cumulated impinged mass:

$$T_{species} = \frac{\sum(m_{di} \cdot T_{di})}{\sum m_{di}}, [^{\circ}\text{C}] \quad (4.29)$$

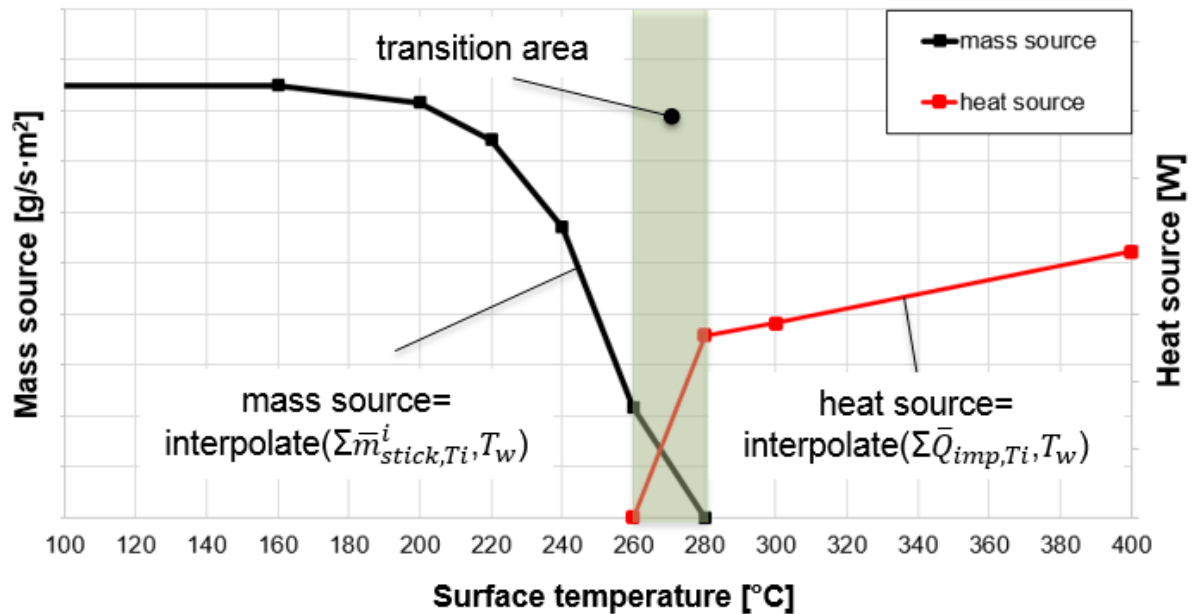


Figure 4.39: Temperature impact on the mass and heat source for a given surface cell

#### 4.3.4 Urea decomposition model

For simulation of urea decomposition an adapted kinetic model proposed by Brack et al. [37] is used. For time-dependent simulations of the chemical kinetics the numerical simulation software DETCHEM™ is applied [88].

##### Numerical Model

The MPTR (Multiple Phase Tank Reactor) code of the DETCHEM™ software package [88] is used, which represents a 0D batch-type reactor model containing a gaseous phase and multiple condensed phases. A sketch of the DETCHEM<sup>MPTR</sup> model can be seen in Figure 4.40.

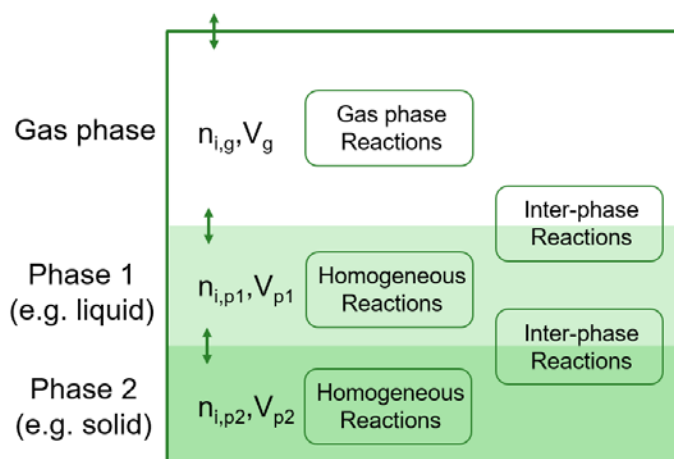


Figure 4.40: Sketch of the DETCHEM<sup>MPTR</sup> model.

The reactor model consists of a set of species  $S_i$ , which are grouped into sets of phases  $P_j$ . Each species belongs to exactly one phase, i. e. a phase transition of a chemical substance is handled by two different species. Each species is associated with thermodynamic data in form of the NASA polynomials [89]. The molar heat capacity  $c_{p,i}$ , molar enthalpy  $H_{m,i}$  and molar entropy  $S_{m,i}$  are computed as function of temperature based on 7 coefficients  $a_{1,i} \dots a_{7,i}$  for each species.

$$\frac{c_{p,i}}{R} = a_{1,i} + a_{2,i}T + a_{3,i}T^2 + a_{4,i}T^3 + a_{5,i}T^4 \quad (4.30)$$

$$\frac{H_{m,i}}{R} = a_{1,i}T + \frac{a_{2,i}}{2}T^2 + \frac{a_{3,i}}{3}T^3 + \frac{a_{4,i}}{4}T^4 + \frac{a_{5,i}}{5}T^5 + a_{6,i} \quad (4.31)$$

$$\frac{S_{m,i}}{R} = a_{1,i} \ln T + a_{2,i}T + \frac{a_{3,i}}{2}T^2 + \frac{a_{4,i}}{3}T^3 + \frac{a_{5,i}}{4}T^4 + a_{7,i} \quad (4.32)$$

The molar volume of a species is either defined by ideal gas-law for gaseous species  $V_{m,i} = RT/p$  or assuming a constant density for condensed species  $V_{m,i} = \rho_i/M_i$ . The phases are separated. Each phase occupies a volume

$$V_j = \sum_{S_i \in P_j} V_{m,i} \cdot n_i \quad (4.33)$$

The concentrations are expressed locally with respect to the corresponding phase, i. e.  $c_i = n_i/V_j$ . The reaction rates are mostly given in terms of Arrhenius expressions. Reaction  $R_k$  can be assigned a molar rate

$$r_k = A_k T^{\beta_k} \exp\left(-\frac{E_{a,k}}{RT}\right) \prod_{S_i \in R_k} c_i^{\tilde{\nu}_{ik}} \quad (4.34)$$

Homogeneous reactions are reactions with reactants from the same phase. However, the products of homogeneous reactions may be released to a different phase. Let  $\dot{n}_{ik}$  be the rate of production of species  $S_i$  by reaction  $R_k$ . Thus,

$$\dot{n}_{ik} = V_j \nu_{ik} r_k \quad \text{reactants} \subset P_j \quad (4.35)$$

Heterogeneous reactions are assumed to occur at the interface of two phases. The reactants can come from both phases, but can also come from only one of them. Here, the contact area between the phases shall be the cross-sectional area  $A$  of the crucible, i. e. the phases are considered to be stacked on top of each other in the cylindrical reactor. For an Arrhenius type of reaction, the production rate is likewise

$$\dot{n}_{ik} = A \nu_{ik} r_k \quad (4.36)$$

All phases are considered to be ideal mixtures. Thus, the chemical activity  $a_i$  of a species is  $p_i/p^\ominus$  for the gas-phase and the molar fraction for all other phases. The activities can also be expressed in terms of concentrations as  $a_i = c_i/c_i^\ominus$  with a reference concentration  $c_i^\ominus = p^\ominus/RT$  for gas-phase species and  $c_i^\ominus = \rho_i/M_i$  for condensed species.  $\ominus$  indicates standard conditions of 298.15 K and 101325 Pa. Then the rate of a reverse reaction can be linked to the equilibrium constant

$$K_{p,k} = \exp\left(-\frac{\Delta_{R_k} G^\ominus}{RT}\right) \quad (4.37)$$

$$K_{c,k} = K_{p,k} \cdot \prod_{S_i \in R_k} c_i^{\ominus \nu_{ik}} \quad (4.38)$$

$$r_k^{\text{reverse}} = \frac{r_k}{K_{c,k}} \quad (4.39)$$

A special case of a heterogeneous process is the phase transition between liquid and gas. For condensation, it is assumed that molecules hitting the phase boundary stick with an accumulation factor  $\alpha_c$ . Thus, kinetic gas theory yields

$$r_k^{condensation} = \alpha_c \sqrt{\frac{RT}{2\pi M_i}} c_i^g . \quad (4.40)$$

Applying the definition of the reverse rate (Equation (4.39)) results in the Herz-Knudsen equation for evaporation [90]

$$r_k^{evaporation} = \alpha_c \sqrt{\frac{RT}{2\pi M_i}} \frac{c_i^l}{h} \quad (4.41)$$

with the Henry constant

$$h = \frac{\rho_i^l}{p_i^{vap}} \frac{RT}{M_i} . \quad (4.42)$$

The batch-type reactor model consists of conservation equations for species and enthalpy:

$$\frac{dn_i}{dt} = \sum_{R_k} \dot{n}_{ik} \quad (4.43)$$

$$\frac{dH}{dt} = Ak_W(T^{extern} - T) \quad (4.44)$$

where temperature and total enthalpy are linked by

$$H = \sum_{S_i} n_i \cdot H_i(T) . \quad (4.45)$$

$k_W$  is a heat transfer coefficient. Since TGA experiments are driven by an external temperature profile, the value of the heat transfer coefficients is not very sensitive. It has to be finite, otherwise the solution would jump in case of phase transitions. For the simulation here a value of  $k_W = 200 \text{ Wm}^{-2}\text{K}^{-1}$  has been chosen. The system of differential-algebraic equations is solved by the solver LIMEX [91].

### Kinetic Model

The kinetic model proposed by Brack et al. [37] is adapted to experimental data on urea and by-product decomposition in terms of the Arrhenius parameters. Moreover, relevant phase transitions are implemented based on fundamental thermochemistry laws and substance-specific thermodynamic data. For details on the implemented thermodynamics the reader is referred to Tischer et al [92]. Phase transitions are defined as equilibrium reactions. The model considers urea, biuret, triuret, cyanuric acid and ammelide. Resulting kinetic parameters are given in Table 4.15.

**Table 4.15: Kinetic model for urea decomposition adapted and enhanced from Brack et al. [37].**

Reaction	$A_k$	$\beta_k$	$E_{A,k} / \text{kJ mol}^{-1}$
$\text{cya(s)} \rightarrow 3 \text{HNCO(l)}$	$1.000 \cdot 10^{12}$	0	150.42
$\text{biu(l)} \rightarrow \text{urea(l)} + \text{HNCO(l)}$	$1.107 \cdot 10^{20}$	0	208.23
$\text{urea(l)} + \text{HNCO(l)} \rightarrow \text{biu(l)}$	$6.517 \cdot 10^7$	0	93.45
$\text{urea(l)} \rightarrow \text{NH}_3(\text{g}) + \text{HNCO(l)}$	$9.500 \cdot 10^9$	0	95.50
$2 \text{biu(l)} \rightarrow \text{ammd(s)} + \text{HNCO(l)} + \text{H}_2\text{O(g)} + \text{NH}_3(\text{g})$	$2.337 \cdot 10^{20}$	0	250.76

## 4 Project Execution and Results

$\text{biu(l)} + \text{HNCO(l)} \rightarrow \text{cya(s)} + \text{NH}_3(\text{g})$	$3.397 \cdot 10^{11}$	0	143.68
$\text{biu(l)} + \text{HNCO(l)} \rightarrow \text{triu(s)}$	$9.091 \cdot 10^{10}$	0	150.97
$\text{triu(s)} \rightarrow \text{cya(s)} + \text{NH}_3(\text{g})$	$1.238 \cdot 10^{18}$	0	194.94
$\text{urea(l)} + 2 \text{HNCO(l)} \rightarrow \text{ammd(s)} + \text{H}_2\text{O(g)}$	$1.274 \cdot 10^8$	0	110.40
$\text{biu(l)} \rightarrow \text{biu(m)}$	$7.193 \cdot 10^{15}$	0	171.50
$\text{biu(m)} \rightarrow \text{biu(l)}$	$3.162 \cdot 10^9$	0	192.00
$\text{biu(m)} \rightarrow 2 \text{HNCO(g)} + \text{NH}_3(\text{g})$	$2.626 \cdot 10^{25}$	0	271.38
$\text{HNCO(aq)} + \text{H}_2\text{O(g)} \rightarrow \text{CO}_2(\text{g}) + \text{NH}_3(\text{g})$	$4.703 \cdot 10^2$	0	87.01
<b>Phase transitions</b>			
$\text{H}_2\text{O(g)} \rightleftharpoons \text{H}_2\text{O(l)}$	0.86	0.5	0
$\text{NH}_3(\text{g}) \rightleftharpoons \text{NH}_3(\text{l})$	0.88	0.5	0
$\text{NH}_3(\text{g}) \rightleftharpoons \text{NH}_3(\text{aq})$	0.88	0.5	0
$\text{NH}_3(\text{aq}) \rightleftharpoons \text{NH}_3(\text{l})$	0.88	0.5	0
$\text{urea(l)} \rightleftharpoons \text{urea(s)}$	0.47	0.5	0
$\text{urea(aq)} \rightleftharpoons \text{urea(s)}$	0.47	0.5	0
$\text{urea(aq)} \rightleftharpoons \text{urea(l)}$	0.47	0.5	0
$\text{HNCO(g)} \rightleftharpoons \text{HNCO(l)}$	0.55	0.5	0
$\text{HNCO(g)} \rightleftharpoons \text{HNCO(aq)}$	0.55	0.5	0
$\text{HNCO(aq)} \rightleftharpoons \text{HNCO(l)}$	0.55	0.5	0
$\text{ammd(s)} \rightarrow \text{ammd(g)}$	$1.000 \cdot 10^{11}$	0	245.67

### 4.3.5 Integration of kinetic model to CFD

In order to use the developed reaction mechanism of urea decomposition presented in Table 4.15 in the CFD simulation, it is necessary to implement the thermophysical properties of all relevant species. Further, kinetic data of urea decomposition and the MPTR algorithm has to be integrated to the CFD code. As an example, in the following the implementation is explained for StarCCM+, but the general method and integration can be applied in any other CFD software. For more information see the respective documentation or contact the software producer.

Thermophysical property data of all species involved in the urea decomposition mechanism are summarized in an attached species database, which can be loaded into StarCCM+. If available, property data is taken from the DETCHEM database and from literature, otherwise appropriate assumptions are made. For all species present in the gas and liquid phase, NASA polynomial data was transferred from the DETCHEM database to StarCCM+. Vapor pressure data is based on [92]. Since vapor pressure data have to be assigned for all species defined in the liquid phase due to StarCCM+ requests, pseudo vapor pressures of  $< 0.01$  Pa are introduced for  $273.15 \text{ K} < T < 923.15 \text{ K}$  for the pseudo-liquid species, which are solid under standard conditions. These pseudo-liquid species are introduced, due to the lack of implementation of solid species into the fluid film model in StarCCM+. For  $923.15 \text{ K} < T < 973.15 \text{ K}$ , an increase to 2 bar is defined until reaching constant state at 973.15 K. The viscosity of all liquid and dissolved species is approximated by standard data for water. Pseudo-liquid species

are given a viscosity of 0.1 Pa s in order to increase viscosity by by-product formation and reproduce confined film transport by solid formation. Gas phase species can be dissolved in the liquid phase. If no detailed data is available, their properties are approximated by property data for aqueous CO<sub>2</sub>. Due to the evaporation model, each vaporable species in the liquid phase has to be assigned a dedicated gas phase species. Table 4.16 shows the component mapping of all liquid species to their corresponding gas phase species in StarCCM+ Multiphase Interaction model. If no thermophysical data is available for a corresponding gas phase species, it is approximated by water vapor data. Species properties and respective polynomial data are summarized in

Table 6.3 to

Table 6.7 in the Appendix. Polynomial data for the heat capacity and thermal conductivity are given in Table 6.1 and Table 6.2 in the Appendix.

**Table 4.16: Component mapping of liquid species to their corresponding gas phase species in StarCCM+ Multiphase Interaction Model.**

Liquid species	Gas phase species
H2O(l)	H2O
Urea(aq)	Urea(aq)_g
Urea(l)	Urea(g)
NH3(aq)	NH3(aq)_g
NH3(l)	NH3(g)
HNCO(aq)	HNCO(aq)_g
HNCO(l)	HNCO(g)
CO2(aq)	Air

For integration of urea decomposition reactions a user code is developed, which contains the numerical and kinetic algorithm applied in the DETCHEM<sup>MPTR</sup> code. User codes enable the development of user defined functions that can be called by the different submodels in StarCCM+. The user code is written in C. Following, the structure of the user code is presented.

Initially, type definitions for variables and functions, user accessible data and mathematical functions are loaded. A user function is generated, which delivers the  $\omega$  array as output in units of mol kg<sup>-1</sup> s<sup>-1</sup>. The resulting array contains production data of all species and is formulated as the rate of change of the specific mole fraction  $z_i$ , which is given by

$$z_i = \frac{Y_i}{M_i} \quad (4.46)$$

in units of mol kg<sup>-1</sup>. The user function contains the MPTR algorithm for calculation of the species production and consumption rate. The mixture densities and the molar concentration of

all species in the liquid film is calculated based on the specific mole fraction, which is transferred from the CFD code. Since the MPTR algorithm relies on definitions of several phases, species concentrations for each phase are determined after calculating the total amount of each species and the volume of each phase.

The user code is compiled to a user library by the following shell command in Linux. For compilation, the user code file \*.c and the supplemental files uclib.h and UserAccessibleData.h need to be in the same directory. The user library \*.so can then be loaded to the CFD simulation. For more information and a compilation manual for Windows, see [86].

```
gcc -DDOUBLE_PRECISION -fPIC -shared *.c -o *.so
```

The user function can be called from the chemistry sub-model for calculation of the species production rates. Respective production rates (in  $\text{mol m}^{-3} \text{s}^{-1}$ ) are calculated in the CFD code from the  $\omega$  values by summation and division by the phase mass. Figure 4.41 illustrates the interface between the physical models in StarCCM+ and the user code containing the chemical kinetics.

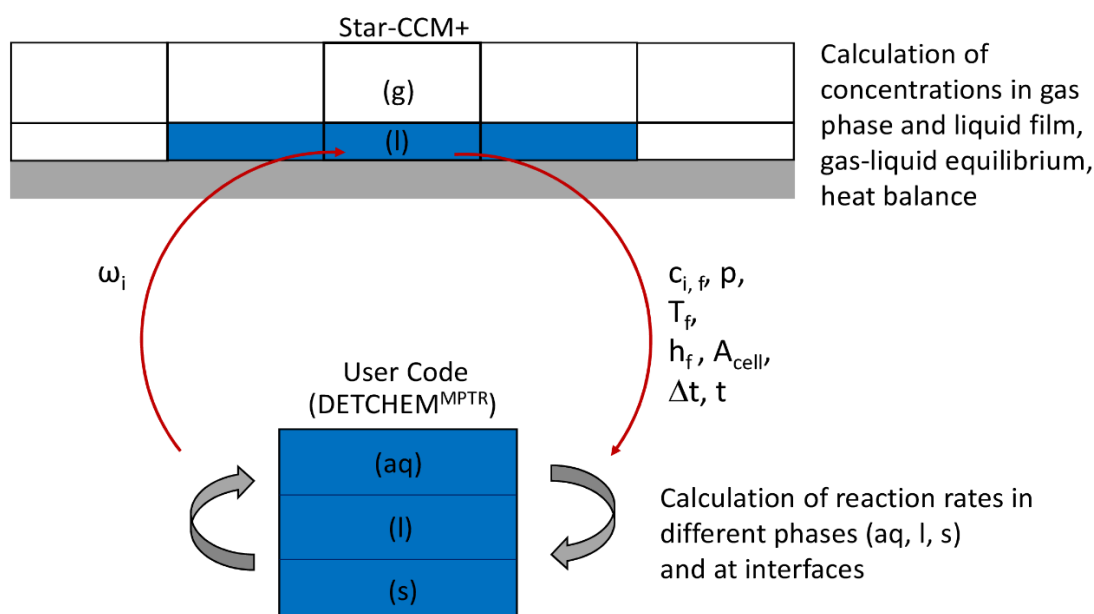


**Figure 4.41: Interface between StarCCM+ and DETCHEM based user code. Physical models in StarCCM+ solve for the concentrations in gas and liquid phase, the gas-liquid equilibrium and the heat balance. Species concentration, pressure, temperature, film thickness, cell area, time step and time data are transferred to the user code for each cell in the liquid film. Based on the MPTR algorithm, reaction rates are calculated by the user code and transferred to the chemistry model in StarCCM+.**

By the established interface, concentration, pressure, temperature, film thickness, cell area and time step data are transferred to the user code for each liquid film cell in each time step. The transfer of film thickness and cell area are possible since StarCCM+ v13.06, therefore older versions of the CFD software are not capable for using this user code. Based on these data and the implemented MPTR algorithm, reaction rates are calculated by the user code, which are delivered to the chemistry model in StarCCM+. Species concentrations in the liquid film are updated. Gas-liquid equilibria and all other physical processes are then calculated by physical models in StarCCM+.

Together with the report a Demo-CFD-File, the files for the User Code and a documentation for setting up all discussed models are handed in.

#### 4.4 Simulation results

In the following the results of the simulation of selected experiments of TGA and both test benches from Section 4.2 are presented. The applied models and the integration of urea decomposition kinetics are validated for various conditions.

##### 4.4.1 Simulation of Thermogravimetric Decomposition

Thermogravimetric decomposition of different samples in the cylinder crucible is simulated with a heating rate of  $10 \text{ K min}^{-1}$  in order to reduce total simulation time. Results are compared to experiments of identical boundary conditions in terms of sample mass loss over temperature. Furthermore, 0-D simulations are performed in DETCHEM<sup>MPTR</sup> to evaluate the implementation of the kinetic model. Figure 4.42 shows the stationary flow field and the temperature distribution during a simulation.

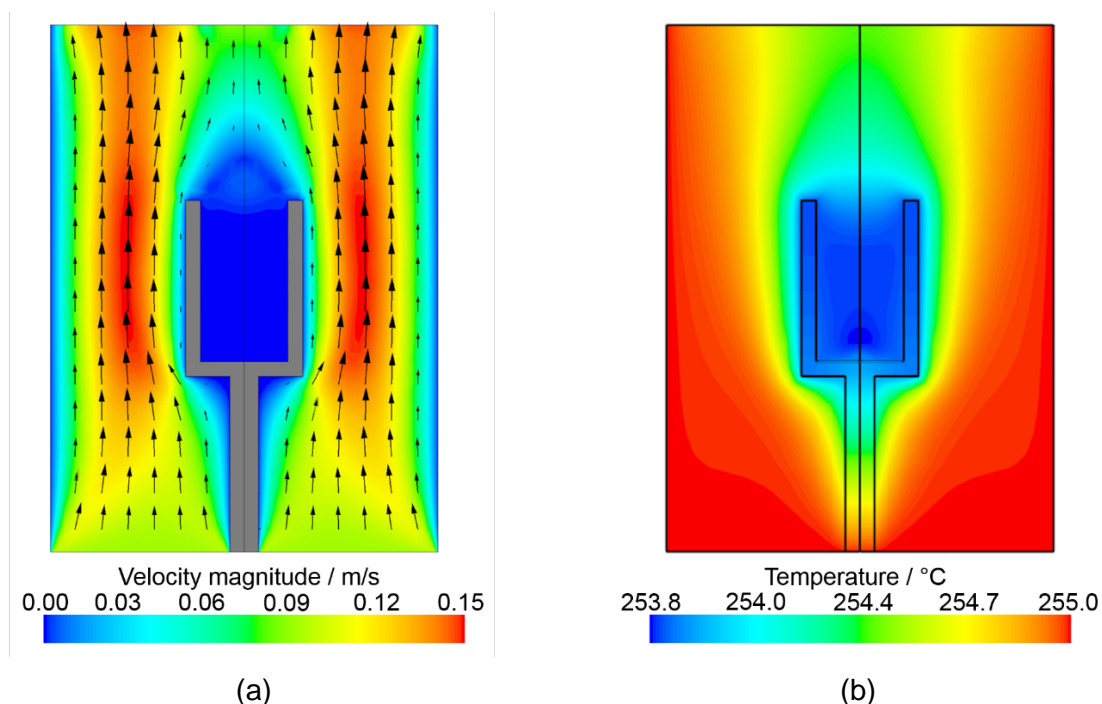
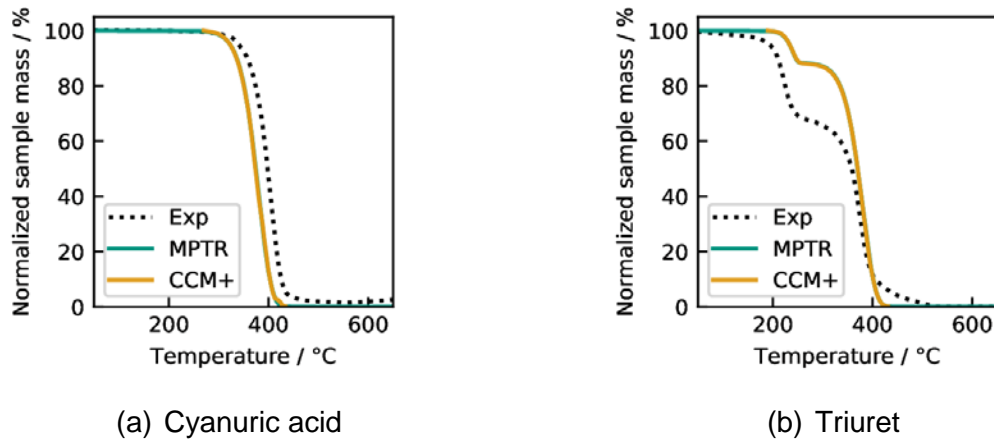


**Figure 4.42: Calculated stationary flow field and temperature distribution in TGA setup.**

The presented flow field shows very low velocities with a maximum of only  $0.15 \text{ m s}^{-1}$ . Consequently, mass transport of gaseous species evolving from the sample is mainly driven by diffusion, while convective flow is a minor contributor to mass transport out of the crucible. This strongly affects evaporation and equilibrium reactions at the sample surface, as the gas layer above the sample is assumed to be saturated. In order to correctly predict mass transport by diffusion, experiments and simulations are performed with pure water and respective model coefficients are adapted to experimental data. The temperature distribution shown in Figure 4.42 (b) reveals the boundary conditions at the inlet and at the outer walls. The lowest temperatures are observed in and above the liquid film as a result of evaporative cooling. However, a maximum temperature difference of only 1 K is found.

Next, the mass loss during decomposition of various samples is compared for simulations in StarCCM+, DETCHEM<sup>MPTR</sup> and experimental data. If not stated differently, an initial sample mass of 10 mg is used in the experiments and simulations. Generally, the sample mass is derived by addition of all liquid and solid components in the simulations.

Figure 4.43 shows the characteristic decomposition of cyanuric acid and triuret in a TGA experiment and corresponding simulations in both DETCHEM<sup>MPTR</sup> and StarCCM+.



(a) Cyanuric acid

(b) Triuret

**Figure 4.43: Thermogravimetric decomposition of cyanuric acid and triuret using a heating rate of 10 K min<sup>-1</sup>. Comparison of experimental data with results from 0D simulation in DETCHEM<sup>MPTR</sup> and 3D simulation in StarCCM+.**

Cyanuric acid decomposes in one step and is modeled by one reaction forming liquid isocyanic acid, which evaporates instantaneously due to a high vapor pressure. The kinetic model predicts the decomposition process well. Simulation in StarCCM+ produces identical results compared to the DETCHEM<sup>MPTR</sup> simulation. This agreement indicates a correct implementation of the kinetic scheme of cyanuric acid decomposition in the CFD model. From simulations in StarCCM+, molar concentrations of isocyanic acid can be predicted in the liquid film during decomposition, as shown in Figure 4.44.

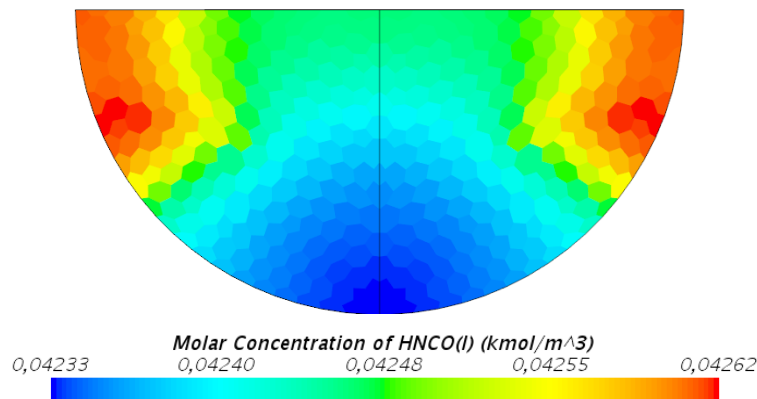


**Figure 4.44: Simulation result for molar concentration of isocyanic acid in the liquid film during cyanuric acid decomposition in StarCCM+.**

A homogeneous concentration distribution of isocyanic acid can be observed. This is due to a homogeneous temperature distribution in the liquid film and the overlying gas layer. Further, the applied clustering method results in identical isocyanic acid production rates in liquid film cells of similar temperature and chemical composition. Since temperature and chemical composition are nearly homogeneous throughout the shell region covering 185 cells in total, it is grouped to up to five clusters. Consequently, the user code algorithms is applied only up to five times per time step.

Decomposition of triuret comprises two steps. The first decomposition step is modeled by a reaction to cyanuric acid and ammonia, the second step represents the decomposition of cyanuric acid. Both simulations predict the experimental data well and deliver identical results. The first decomposition stage is slightly underpredicted and the third stage is not reproduced by the simulations. Small deviations to experimental data originate from deficits of the kinetic model, which is in further need of improvement as discussed above. However, results show a correct reproduction of the decomposition kinetics by the CFD simulation.

Figure 4.45 depicts results from TGA of biuret and urea samples and corresponding simulations.

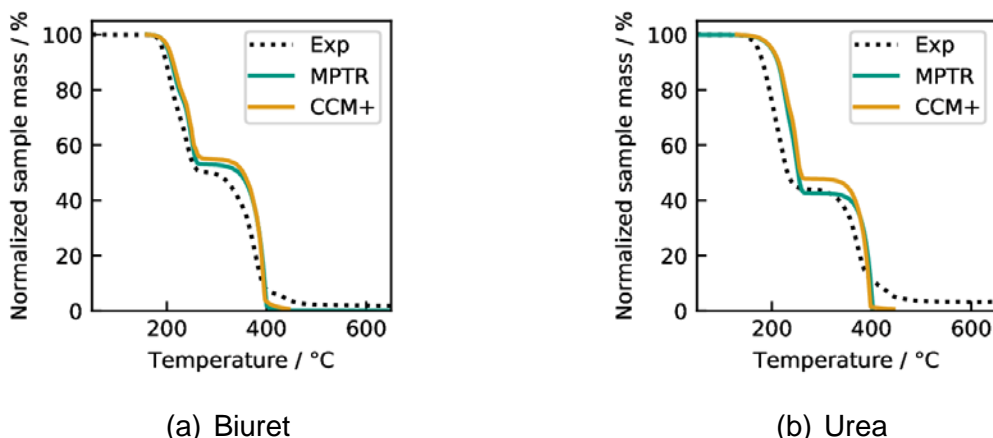


**Figure 4.45: Thermogravimetric decomposition of biuret and urea using a heating rate of  $10 \text{ K min}^{-1}$ . Comparison of experimental data with results from 0D simulation in DETCHEM<sup>MPTR</sup> and 3D simulation in StarCCM+.**

Biuret decomposes in three decomposition steps. The first stage is described by reactions forming urea, ammelide and the biuret matrix species, which is then decomposed together with urea forming also cyanuric acid. The second and third stage represent cyanuric acid and ammelide decomposition respectively. The simulation of the decomposition kinetics in DETCHEM<sup>MPTR</sup> predicts the experimental data well. In contrast to simulations for cyanuric acid and triuret, slight deviations between results from the DETCHEM<sup>MPTR</sup> and the CFD model are observed. These are attributed to inter-phase reactions playing a major role in biuret decomposition.

As the CFD model includes diffusion in the gas and liquid phase and furthermore is open to the surrounding flow, even if the velocity inside the crucible is negligible, the species transport is different from the closed 0D MPTR model. Moreover, this species transport affects the evaporation of species from the liquid film. For example, with more or less HNCO inside the film, due to different evaporation compared to the 0D model, the user code in the CFD simulation calculates different species production rates, resulting in a slightly different mass loss. For the decomposition of biuret this effect plays a major role, since a lot of decomposition reactions are depending on HNCO concentration inside the film.

Similar effects are observed for the comparison of experimental and simulation results for pure urea decomposition. In the first decomposition stage urea melts and decomposes from  $133^\circ\text{C}$  generating biuret and gaseous products. Biuret subsequently decomposes to cyanuric acid and ammelide, which then decompose representing the third and fourth decomposition stage. Again, the decomposition process is strongly affected by interface reactions and the accompanied release of gaseous products at the sample surface leading to slight deviations between the two simulations. Compared to experimental data, both simulations predict urea decomposition well. A slight shift to higher temperatures is observed for both simulations. Furthermore, the fourth decomposition stage is not predicted by the simulations. Adaption of kinetic parameters and a more detailed chemistry of ammelide decomposition are necessary to improve agreement.

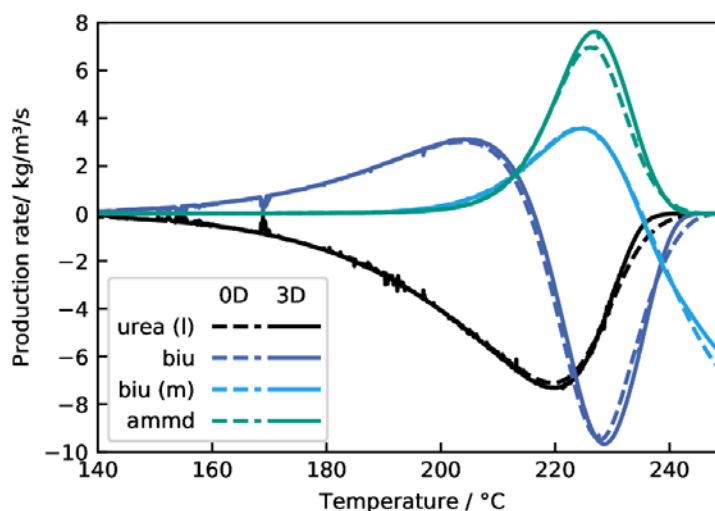


**Figure 4.46: Comparison of the production rates of selected species during urea decomposition calculated by the 0D batch reactor and the 3D CFD model.**

Figure 4.46 in the Appendix shows a comparison of the simulated production rates of selected species from DETCHEM<sup>MPTR</sup> and the CFD simulation. The diagram shows nearly identical production rates resulting from both models. When biuret decomposition is initiated for temperatures above 200°C, slight deviations are obtained, which are attributed to the limitations for implementation of interface reactions in the CFD code. However, results show that urea decomposition kinetics are excellently reproduced in the CFD simulation.

Since urea is supplied in an aqueous solution in SCR applications, further experiments and simulations are performed with an UWS sample. Figure 4.47 shows experimental and numerical results for the decomposition of UWS.

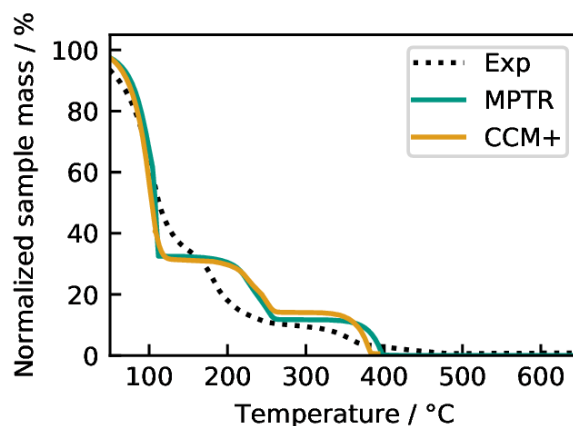


**Figure 4.47: Thermogravimetric decomposition of 27.5 mg urea water solution using a heating rate of 10 K min<sup>-1</sup>. Comparison of experimental data with results from 0D simulation in DETCHEM<sup>MPTR</sup> and 3D simulation in StarCCM+.**

In addition to urea decomposition reactions described above, a preceding mass loss stage is obtained from water evaporation. Experimental results show a gradually decreasing mass loss rate in the first stage, which is attributed to hygroscopic effects. Further, with advancing evaporation, solid urea crystals are formed and water can be bound in the porous structure. Since water is partially retained in the solid sample, the evaporation rate decreases. This results in the presence of water in the sample above the boiling point. Hygroscopic and crystallization effects are not part of the presented models. Therefore, both simulations do not completely agree with experimental results. This further leads to a slight shift of characteristic urea decomposition stages for both simulations. Results for the urea decomposition stages are comparable to pure urea decomposition presented above.

Presented results on the decomposition of urea and its by-products evaluate the implementation of the DETCHEM<sup>MPTR</sup> algorithm and the corresponding kinetic model into the CFD simulation in StarCCM+. The test case of thermogravimetric analysis shows a good agreement of simulation results with experimental data. Slight deviations to experimental results originate from the kinetic model and might be improved by further developing urea decomposition kinetics. Differences between DETCHEM<sup>MPTR</sup> and StarCCM+ simulations are observed for cases including interface reactions and evaporation. For the actual purpose of simulating deposit formation in flow setups and real applications, high gas flow rates above potential liquid films are expected to reduce this effect.

#### 4.4.2 Simulation of Lab test bench

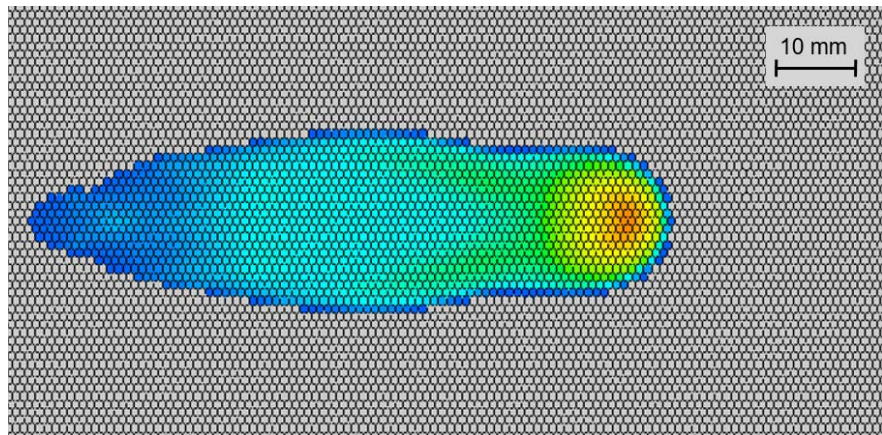
For application of the CFD model including chemical kinetics to realistic conditions, experiments at the lab test bench at KIT presented in Section 4.2.1 are simulated. In order to maintain feasible computational time, the simulated physical time is limited to 2 minutes, hence, short-term injections are simulated. Simulations comprise an injection of 10 s with a UWS mass flow of  $4.8 \text{ g min}^{-1}$  and the subsequent liquid film evaporation and reactions. Boundary conditions in terms of flow and temperature are adapted to experimental conditions in OP 4a, 4b and 4c (see Table 4.4). Since the focus of these simulation is the prediction of urea by-product formation, these operating conditions are chosen as they differ in temperature while maintaining similar gas velocities. Results presented in the following demonstrate the strong potential of the combined model to reliably predict deposit formation from urea injection.

The UWS spray is initiated from experimental data of the injection velocity and droplet size distribution. Due to comparable gas velocities, spray penetration inside the rectangular flow geometry is observed to be similar for the considered operation points. Slight differences are obtained due to increased droplet evaporation at higher temperatures. The first contact between droplets and wall is observed 2 ms after start of injection. Here, the impingement model decides on droplet/wall interaction based on the droplet We number and wall temperature. We numbers from 10 to 2500 are found. The impinging spray leads to formation of secondary droplets due to rebound or breakup effects. Compared to the primary spray, the droplet size distribution of secondary droplets is shifted to smaller droplet sizes. Since no measurements were performed on primary or secondary droplet size distributions in the flow channel, derived simulation spray data are not correlated with experimental results. Spray impingement further results in formation and growth of a liquid film, which is observed directly after spray impingement.

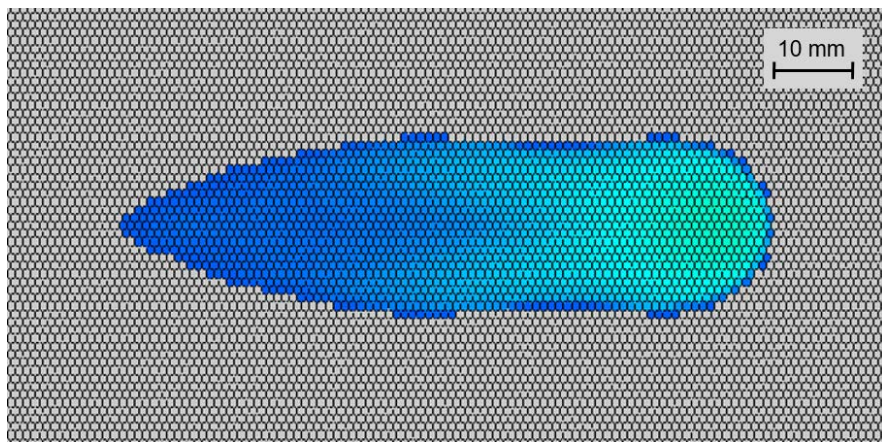
Due to the use of the Injection Source Approach (see Section 4.3.2), the spray simulation is done only for one injection event for each operating point. During this one injection, the spray evaporation and droplet/wall interaction is computed for various temperatures in advance, the values are cumulated and normalized over injection time and saved as sources in StarCCM+. These sources are used during the simulation to replace the time consuming, original spray modeling to achieve faster simulations.

The liquid film after 10 s of injection is positioned with a distance of approximately 55 mm to the injector nozzle for all three operating points in the experiments. In the simulation, this distance is underestimated by approximately 25 %. With increasing time, the deviation between experiment and simulation is reduced to 10 %. Since the adaption of drag model, heat transfer model and impingement model were developed throughout the project, not the final versions are used in this simulation, but these will further improve the agreement between experiments and simulation.

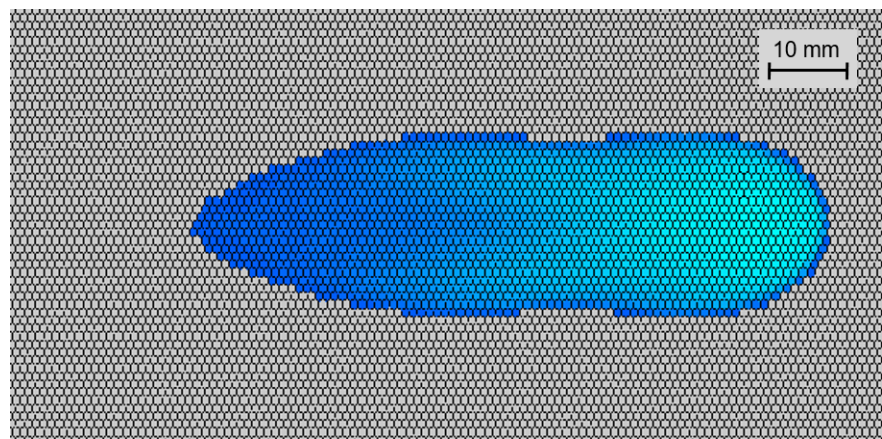
Simulation results on the extent of the liquid film are compared to experimental data. Figure 4.48 shows simulation data for the fluid film thickness derived at different time intervals after start of injection. Correlating photographs of the liquid film formation during the experiment are displayed in Figure 4.49. For comparison, both figures show identical image sections and scale.



(a) 10s



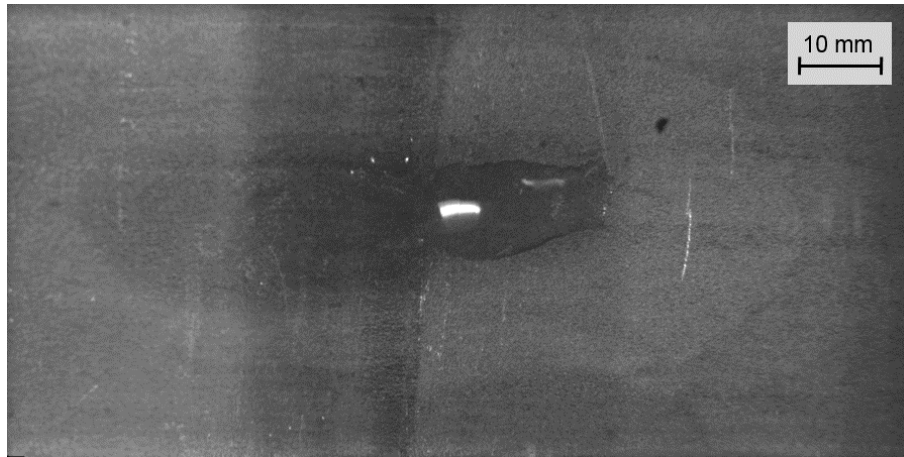
(b) 25s



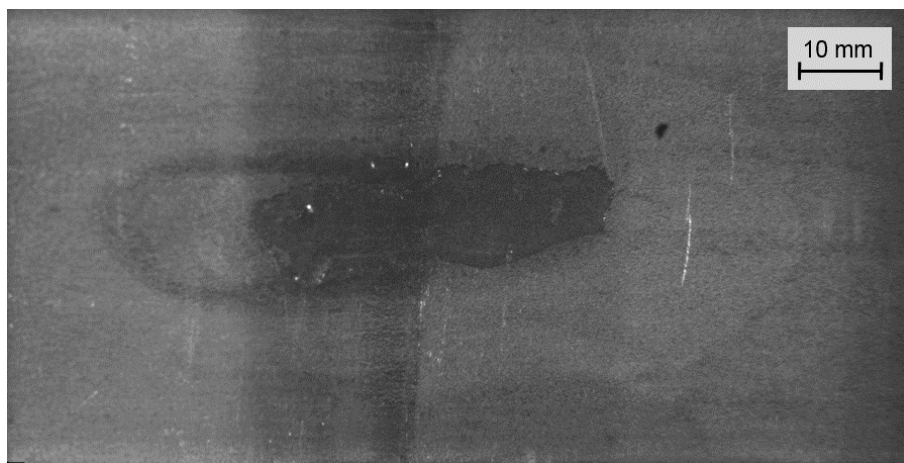
(c) 50s



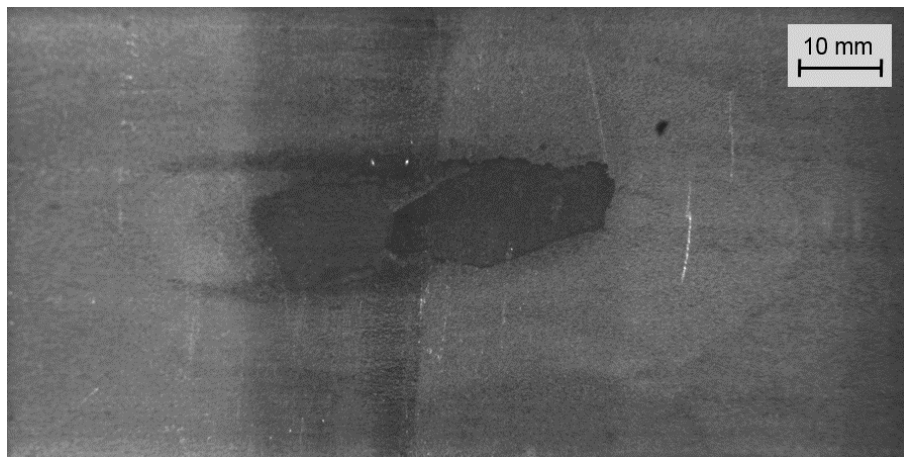
Figure 4.48: Simulated film thickness for OP 4a at different time intervals after start of injection.



(a) 10s



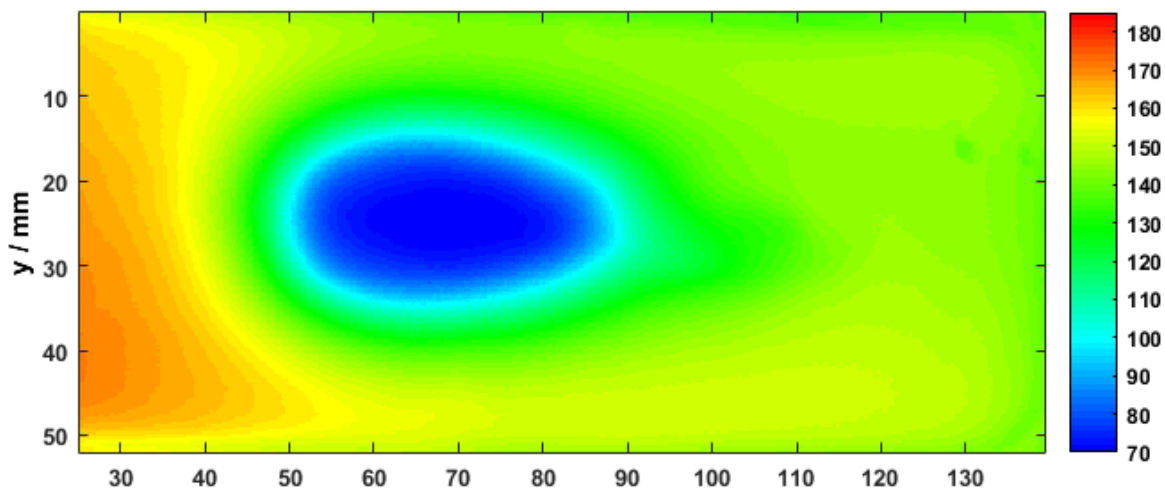
(b) 25s



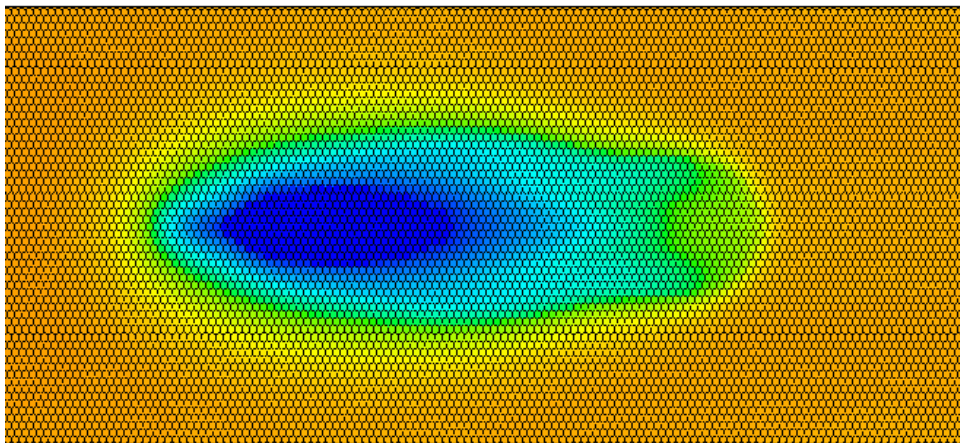
(c) 50s

**Figure 4.49: Liquid film formation for OP 4a at different time intervals after start of injection. The rectangular dark shadow is a result from the measurement setup. The three figures display the same image section and identical scaling compared to Figure 4.48.**

As already observed for the location of the liquid film with respect to the injection position, deviations in shape and transport dynamics of the liquid film are observed between experimental and numerical data. Note, that the wall film in the simulations contains both liquid and solid species. In the simulation, water is mostly evaporated and urea is almost completely crystallized after 25 s, due to temperatures below melting point.. Since solid urea is modeled as high viscosity liquid, solidification inhibits further film transport. Increasing wall temperatures after the end of injection induce melting and molten urea is transported further downstream as shown for  $t = 50$  s. In the experiment, complete solidification is observed at  $t = 50$  s. In contrary to the simulations, subsequent melting of urea does not induce further film transport downstream. Deviations between experimental and numerical results in location and shape of liquid film can be attributed to the different prediction of the wall temperature in the simulations, since the film flow is depending on species concentration and therefore the temperature. Figure 4.50 shows the experimental and simulated wall temperature distribution after 10 s at OP 4a.



(a) Experiment

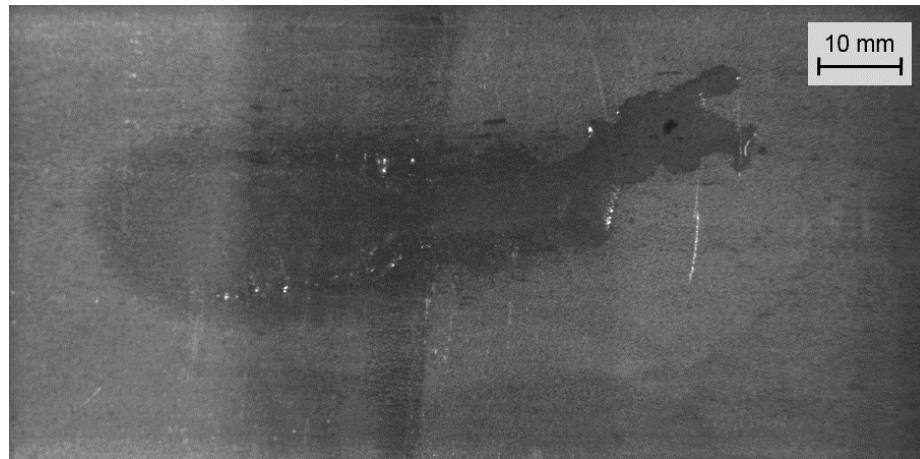


(b) Simulation

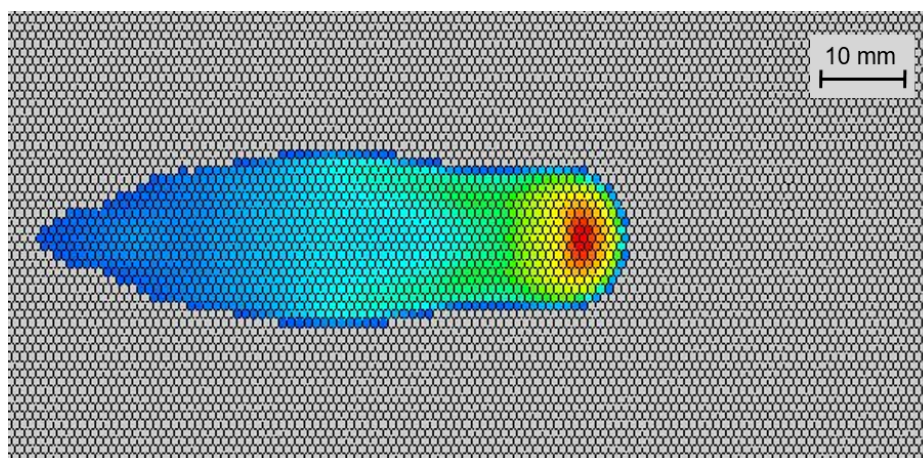
**Figure 4.50: Experimental and simulated wall temperature distribution in °C at the end of injection,  $t = 10$  s, at OP 4a.**

Strong evaporative cooling is observed for the film area in the experiments. In the simulations, a radial temperature gradient can be observed resulting in an increased mean temperature in the film area. This leads to increased evaporation, early urea precipitation and subsequent melting in the simulation compared to the experiments. Implementation of precise data on the viscosity of liquid urea, which is currently approximated by pure water viscosity, is assumed to result in a better agreement. Furthermore, film flow is not only dominated by viscosity, but can

be inhibited in the experiments due to solid formation. Solid urea or by-products can serve as a barrier for liquid flow. Since the solids are modeled as part of the liquid film, this effect cannot be reproduced by the simulations. For higher temperatures at OP 4b and 4c, a better prediction of the liquid film shape is observed as shown in Figure 4.51 and Figure 6.7.



(a) Experiment



(b) Simulation

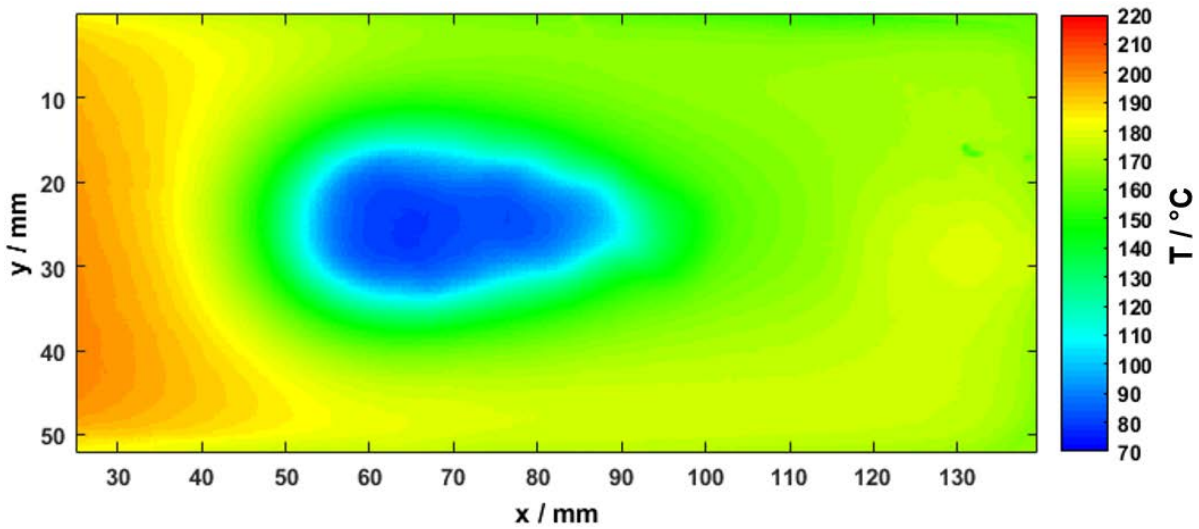


**Figure 4.51: Experimental and simulated film thickness for OP 4b at the end of injection,  $t = 10$  s.**

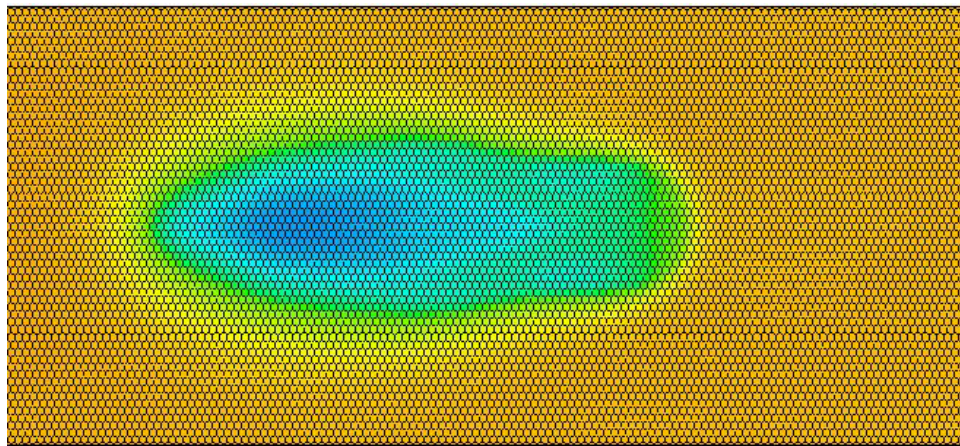
Due to higher temperatures at OP 4b and 4c water is evaporated faster and less solid urea is observed in the simulations before the end of impingement. This enables film flow and results in a better agreement with experimental results. Further, decreasing film thickness at the edge of the liquid film is well predicted by the simulations. However, slight deviations between experimental and numerical results remain regarding the liquid film shape, particularly the upstream part. In the simulations, the upstream film part adapts the shape of the initial spray footprint, which can exemplarily be observed in Figure 4.51 (b). This might be a result of underestimated drag of the injected spray from standard drag model. The presented model in Section 4.3.2 is expected to improve the simulations.

Heat transfer to impinging droplets and liquid film evaporation results in local cooling of the wall in the regions of liquid/wall contact. Hence, position and shape of the cooled area are

comparable to the liquid film. The wall temperature distribution at the end of injection at OP 4b is given in Figure 4.52.



(a) Experiment



(b) Simulation

**Figure 4.52: Experimental and simulated wall temperature distribution for OP 4b at the end of injection,  $t = 10$  s.**

The minimum wall temperature is reached at the end of injection. Generally, the temperature is slightly overpredicted in the simulations resulting in a minimum temperature differing by approximately 5 K. Furthermore, a stronger gradient in wall temperature is observed in the cooling region in the simulation. The improved impingement and heat transfer model is assumed to produce better numerical results.

As a result of the implemented kinetic model for urea decomposition, the evolution of by-products in the liquid film can be tracked temporally and locally. Since the simulated physical time comprises 2 min, the beginning of urea decomposition is monitored. Here, the shell region consists of 28,000 cells.

In the beginning of the simulations with injection of UWS the resulting film consists of mainly water and aqueous urea. Since water is evaporating, the aqueous urea starts to form liquid urea. With decreasing film and wall temperature, due to spray/wall heat transfer and evaporative cooling, the liquid urea starts to solidify. Figure 4.53 shows the spatial distribution of by-products formed from urea at OP 1 after 1 s.

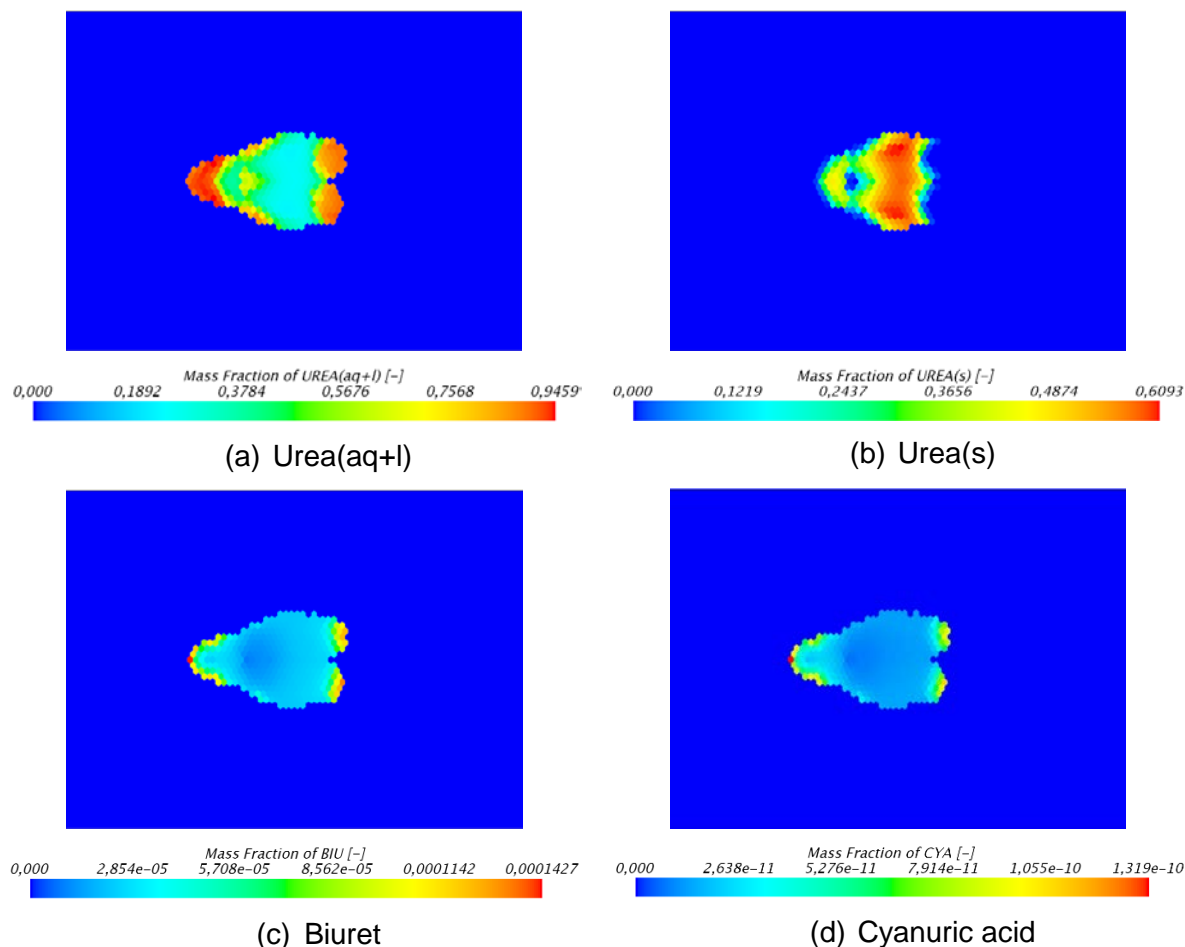


**Figure 4.53: By-product formation from liquid urea at OP 1 after  $t=1s$ .**

After 1 s urea has hardly decomposed resulting in a large amount of solid urea in the film. Molten urea is observed along the edge of the solid urea bulk and further downstream as it is transported by shear stresses due to its low viscosity and is formed due to higher temperatures. From the liquid urea melt, small amounts of solid by-products are formed by the reactions implemented through the user kinetic model. At temperatures of 185°C urea reacts to biuret, which in turn reacts to cyanuric acid. During the injection of 10 s more and more water and aqueous urea remain on the surface. Due to the decreased wall temperatures and evaporation of water the solubility limit of urea is reached and solid urea is formed out of the film. As already seen in Figure 4.53, liquid urea is formed mainly at the edge of the film. After the injection, water evaporates very fast and the film consists of mainly solid urea. With reaching 30 s of the experiment, the film is already heated above the melting point of urea again and the liquid film flows downstream the channel. In the liquid urea melt and due to increased temperatures, the by-product formation starts to form considerable amounts of biuret, cyanuric acid and ammelide which further limits the transport of the film, due to increased viscosity.

Figure 4.54 shows the fluid film thickness and mass fraction of liquid urea, biuret and ammelide at 4 minutes after start of injection at OP 4b. It can be seen, that urea has decomposed to considerable amounts of solid biuret and small amounts of ammelide. The composition of the film is nearly even, because after 4 minutes the cooling effect is negligible and the temperature of the wall and therefore also the film reached the steady state. Since the decomposition and deposit formation process is very slow, only the beginning is tracked. However, the model demonstrates the capability of predicting formation of individual by-products.

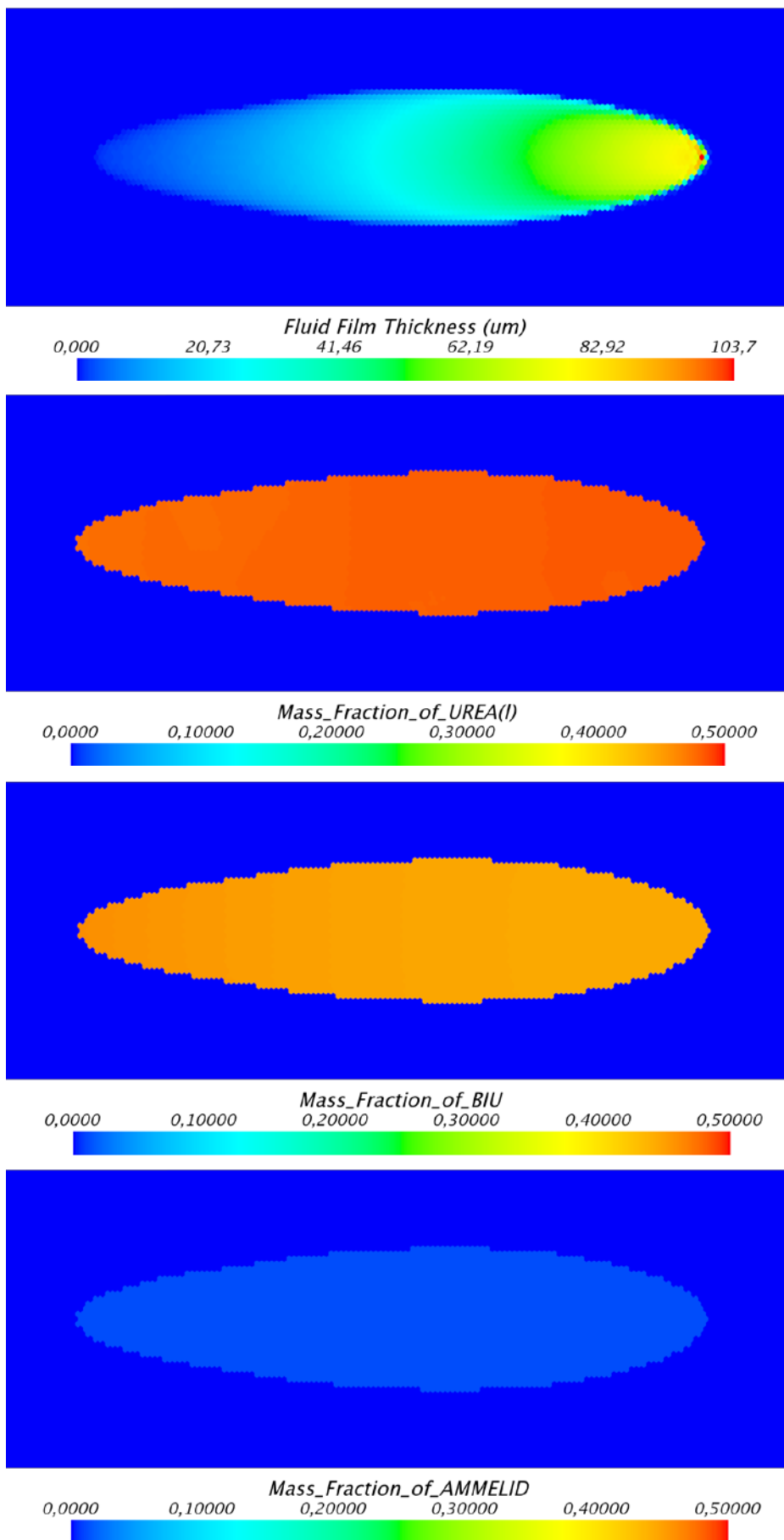


Figure 4.54: Liquid film thickness and by-product formation from liquid urea at OP 4b after t = 4 min.

Comparison of numerical with experimental data is only partially feasible, because experiments with short time injection of 10s produces too few deposits for a further analysis. Table 4.17 compares experimental data of deposit composition at OP 4b after a long-term injection of 3 x 40 min with simulation results derived in StarCCM+ at different (physical) time instants. The experimental analysis by HPLC reveals the ammeline content in addition to other by-products. Since ammeline is not considered in the applied kinetic model, the ammeline content remains zero for the simulation. Results show that the experimentally measured deposit composition cannot be reproduced by the simulation for a physical simulation time of 18 min. However, some conclusions can be drawn from the evolution of the deposit composition in the simulation over time.

**Table 4.17: Experimentally determined composition for deposits derived at OP 4b in comparison to simulation data resulting after different physical time instants and deposit mass divided by total injected mass.**

Component	Experiment		StarCCM+ 3D		
	%	3 x 40 min	4 min	8 min	18 min
Urea		0	57.47	5.9	0
Biuret		24	41.32	86.1	69.9
Triuret		0	0.004	0.05	0.4
Cyanuric acid		48.3	0.08	1.0	9.2
Ammelide		13.5	1.1	6.8	20.5
Ammeline		1.3	0	0	0
Recovery		87.6	100	100	100
Deposit Mass / Injected Mass		1.66	9.6	6.0	3.6

Table 4.17 demonstrates further decomposition of urea with time. After 18 min urea has completely decomposed and the resulting deposit mainly consists of biuret. Biuret further reacts to cyanuric acid and ammelide. As the temperatures at OP 4b are above the biuret decomposition point, biuret is expected to be gradually decomposed to ammelide and cyanuric acid with time. Consequently, the deposit composition in the simulation is assumed to approach the experimentally determined values.

In order to validate numerical results by experimental data on deposit composition, a significant reduction of computational costs is desirable to simulate more physical time. Increased experimental injection durations result in a sufficient amount of solid sample and enable detailed chemical analysis of the derived deposits. These results can be compared to long-term simulations.

With mentioned simulations, the general capability to model deposit formation within a suitable simulation environment is shown. The possibility to integrate urea decomposition as well as a approach to reduce simulation time are presented, whereby milestone 3 is reached.

#### 4.4.3 Simulation of engine test bench

Prior to modeling deposit formation and decomposition different submodels were validated against the measurement results received in WP 2. Comparison with the detailed test results showed that the models of droplet drag force, impingement and impingement heat transfer need modifications, see 4.3.2. In the following, selected simulation results with adapted and validated submodels will be presented.

As shown in Figure 4.33, the first step towards the simulation of deposit formation is the modeling of the exhaust gas flow and heat transfer inside the optical box. As mentioned in section

4.3.1, the gas flow was simulated with a RANS approach and a Lag Elliptic Blending  $k-\epsilon$  realizable turbulence model. The low- $y^+$  wall treatment approach was applied for the modeling of the boundary layers on both sides of the impingement plate. The GTR and S2S model were used for modeling of the radiation heat transfer between the inner walls of the box. The described combination of the applied models allowed to get correct initial temperature fields of the impingement plate for all simulated OPs. Figure 4.55 shows the comparison of the simulated and measured temperature field of the plate at the steady-state OP2 without UWS injection. An excellent agreement between both temperature fields can be observed. The maximal deviation of the simulated and measured results is below  $2\text{ }^\circ\text{C}$ .

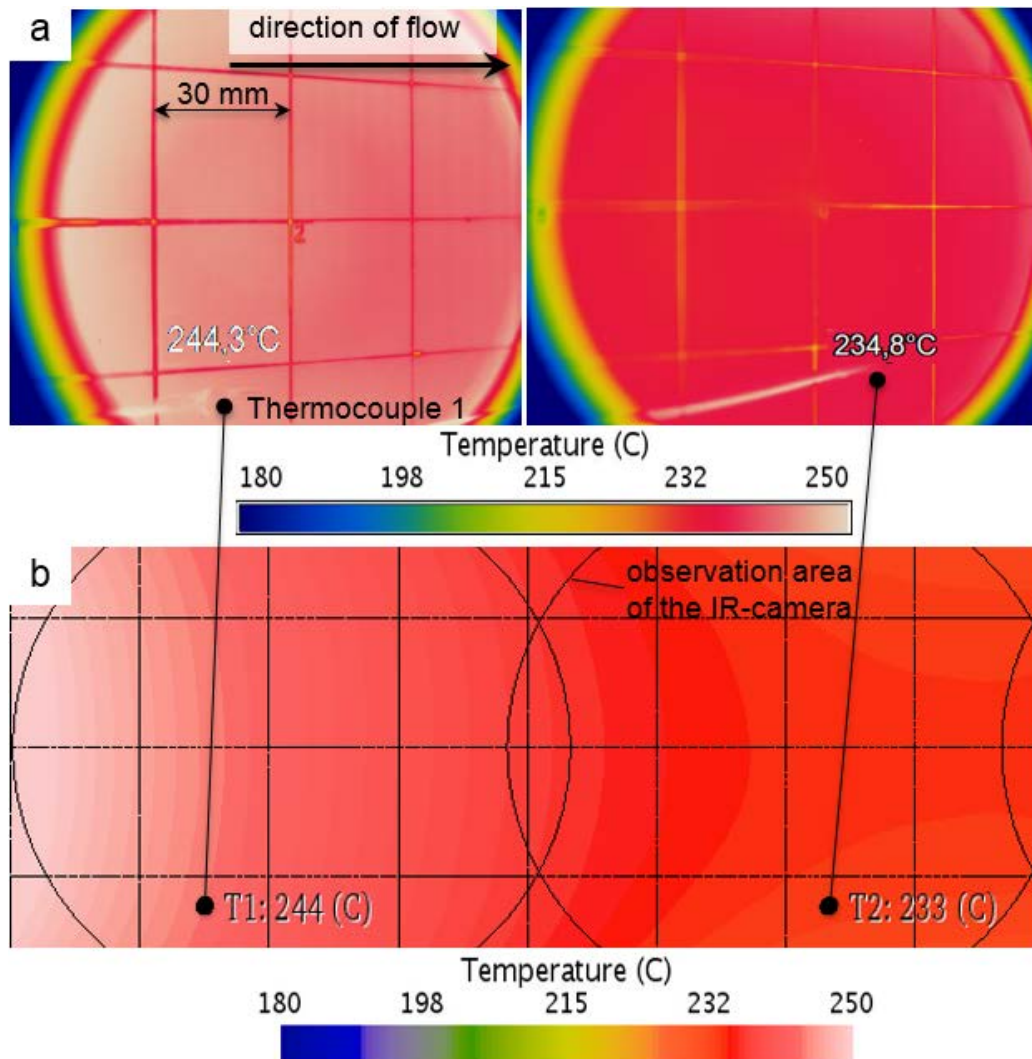


**Figure 4.55: Simulated (b) and measured (a) temperature fields of the impingement plate without UWS injection. OP 2, exhaust gas temperature –  $275\text{ }^\circ\text{C}$ , mass flow -  $1000\text{ kg/h}$**

After validation of the gas flow and heat transfer models, the simulations with UWS injection were carried out. The spray deflection by the hot gas flow was validated against the measurement data presented in section 4.2.1. For this purpose, the simulated droplet size distribution at measurement positions P1-P4 was compared with the measured data. Figure 4.56 shows exemplarily the comparison between simulated and measured results for injector 3 and OPs 1, 3. The red line illustrates the DSD in the spray measured for ambient conditions, the green line for operating conditions. The simulation results obtained with standard Schiller-Naumann correlation (black line) show a significant overestimation of the spray deflection. After modifying the drag force model as described in section 4.3.2, a good agreement with the measurement data was reached (blue line).

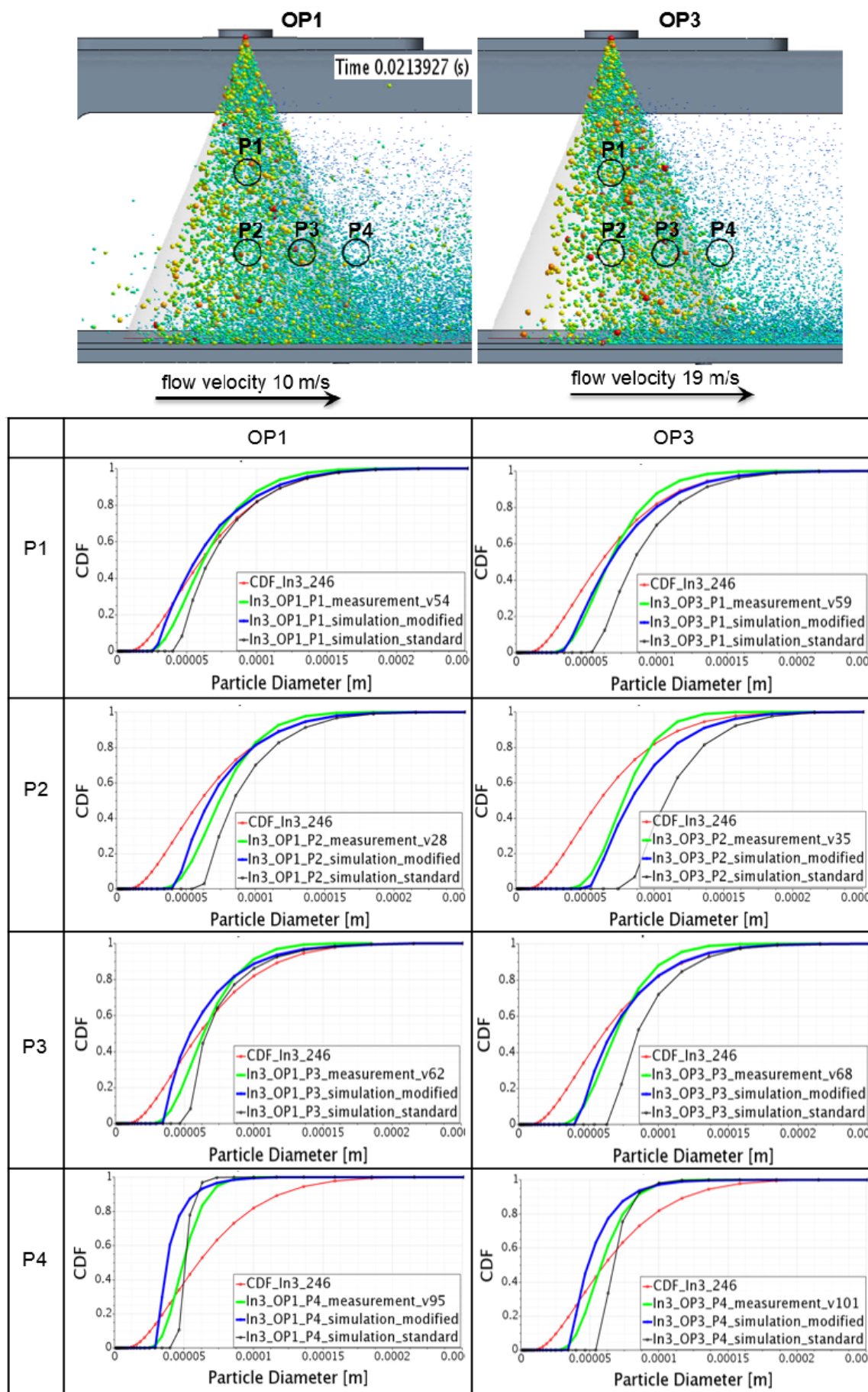
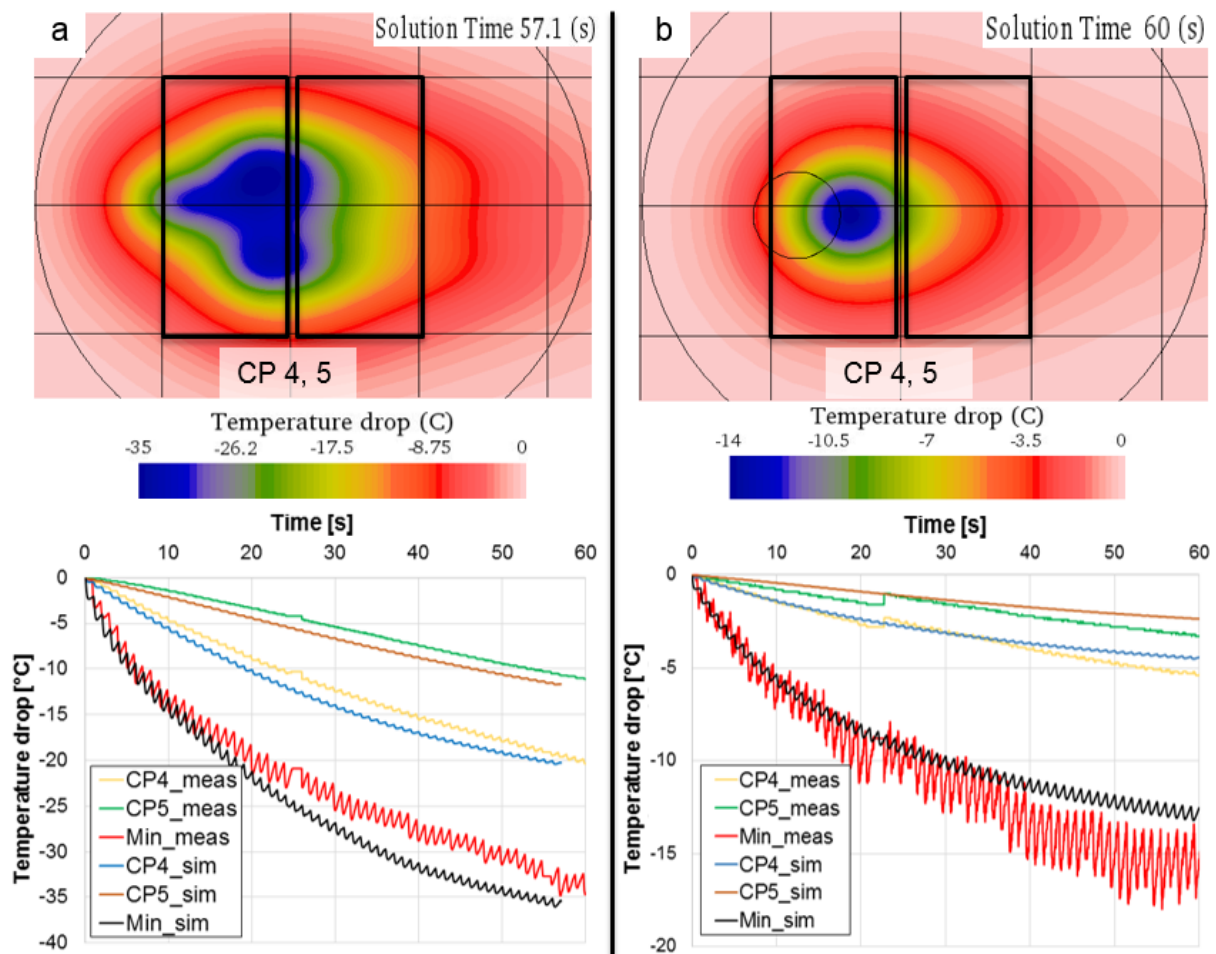


Figure 4.56: Simulated and measured droplet size distribution at the measurement positions P1-P4. OP 1 and 3, injector 3

In order to validate the droplet impingement and impingement heat transfer models, simulations with low injection rates were carried out in order to avoid the formation of a thick liquid film and solid deposits. The model validity was examined by comparing the simulated and measured temperature drop at the bottom side of the plate during the UWS injection. Under mentioned conditions, the temperature drop on the plate is direct proportional to the spray mass which remains on the plate after an injection, or to the impingement heat if the Leidenfrost effect is relevant. Figure 4.57 shows the comparison of the simulated and measured temperature drop at OP 2 and 3. The temperature drop was evaluated at the “constrained planes” (CP) 4, 5, which cover the impingement areas of both injectors 1 and 2. In addition, the minimal temperature drop was compared with the measured results. The simulation results obtained with the modified Bai-Onera impingement model (a) and the modified impingement heat transfer model by Wruck (b) showed a very good agreement with the measured data.



**Figure 4.57: Temperature drop at the bottom side of the impingement plate. a – OP 2, injector 1, injection rate 18 mg/s. b – OP 3, injector 2, injection rate 14 mg/s.**

For validation of both, the liquid film model and the integrated kinetics of urea decomposition, two steady-state simulations with injectors 1 and 2 at OP3, as well as one transient simulation No. 5 (see Table 4.14) were carried out. To speed up the simulation time, the injector source approach described in the section 4.3.3 was applied. The source terms for the liquid film and the gas phase were calculated during a single injection event and further applied for the modeling of the liquid- and deposit formation. Even with detailed chemistry simulation times of 45 s/day was achieved by using of one computer core per 30.000 cells. That is well beyond typical capabilities.

Figure 4.58 illustrates a mass and impingement heat source calculated with injector 1 at OP 3 (see Table 4.9) and applied to the shell region of the surface. Due to a high initial temperature of the impingement plate above Leidenfrost temperature, no liquid film deposition occurs at the beginning and only the heat source is applied to the film region where the UWS droplets impinge on the surface ( $< 0$  because the plate is cooled), see Figure 4.59 left. In the right picture the absence of any liquid deposition due to the high surface temperature is shown.

After 60 s the plate temperature falls below the critical wall temperature due to the permanent cooling from the AdBlue injection. Now, the mass sources of water and urea are activated and the cooling is calculated as heat conduction between the liquid film and surface, see Figure 4.58b right. Therefore, in Figure 4.58b left the heat sources are zero at the locations where liquid mass is applied. The film mass was increasing continuously until the film thickness reached the value of approx. 400  $\mu\text{m}$ , which is equal to the thickness of the first prism layer in the fluid region. The further simulation of the deposit formation was not possible due to occur of convergence problems. The liquid film model available in Star CCM+ allows the modeling of the thin films with the maximal film thickness below the thickness of the first prism layer in the adjacent fluid region.

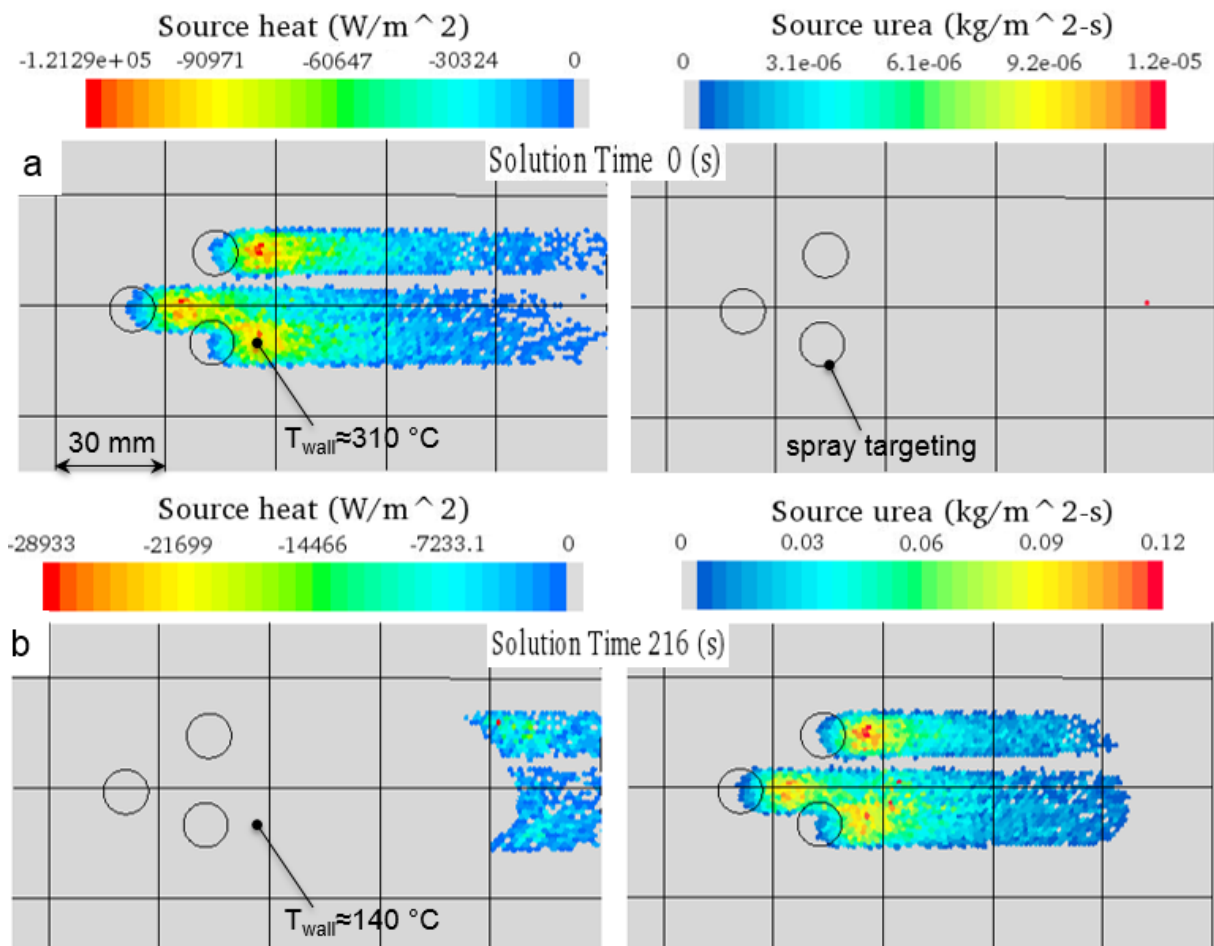


**Figure 4.58: Impingement heat and urea mass source at the beginning of the simulation (a) and after 216 second of the solution time (b). OP 3, injector 1, injection rate 132 mg/s**

Figure 4.59 shows the positions of the simulated and observed liquid film and solid deposits after 216 s experimental time. Generally, a reasonable agreement can be observed. In comparison to the measured data, the front of the modelled liquid film is approx. 30 mm closer to the initial foot print of the spray. This difference is mainly caused by the delay of 20 s between the occurrences of the first film in the simulation compared to the experiment. Nevertheless, the film velocity (approx. 1mm/s) is well predicted. Furthermore, most deposits are located close to the front of the liquid film, what correlates well with the experimental data. The film

temperature at this area is significantly higher than that at the position of the initial foot print. That accelerates the side reactions of the urea decomposition and leads to a faster formation of solid deposits.

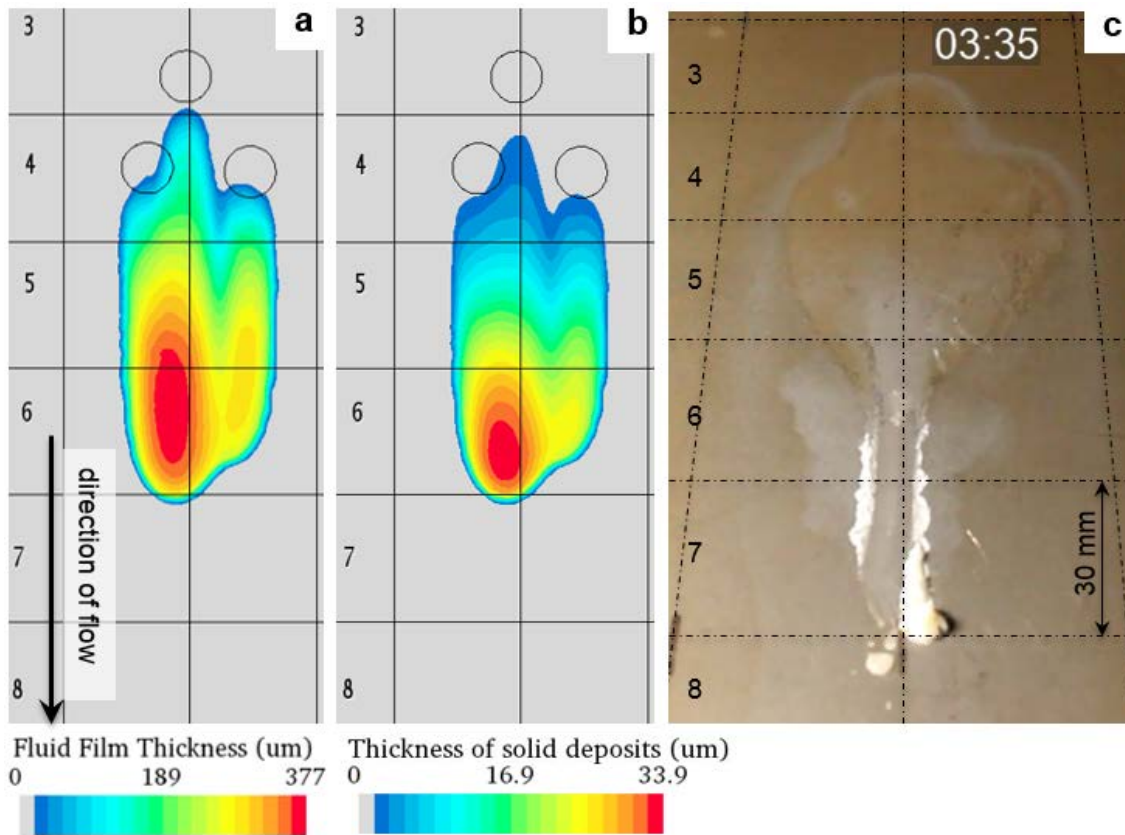


**Figure 4.59: Film and deposit formation on the impingement plate. a – simulated film thickness, b – simulated thickness of solid deposits, c – experimental result. OP3, injector 1, injection rate 132 mg/s**

Figure 4.60 illustrates the comparison of the simulated plate temperature drop with the IR-thermography measurement at the bottom side of the impingement plate. The simulated temperature drop in the area of the initial foot print is in good agreement with the measured data. The cooling area downstream of the initial foot print is slightly overestimated due to a wider front of the liquid film.

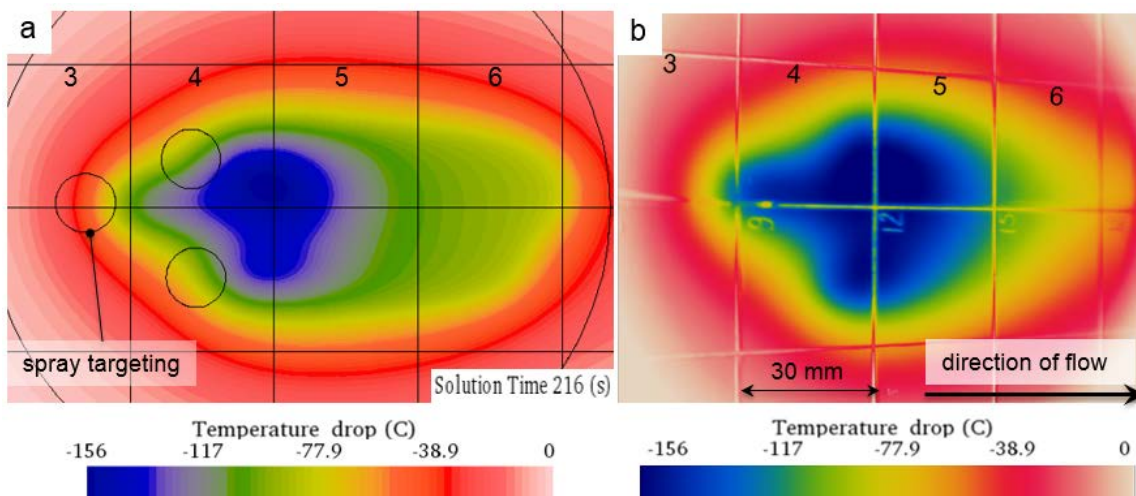


**Figure 4.60: Simulated and measured temperature drop at the bottom side of the impingement plate. OP3, injector 1, injection rate 132 mg/s**

The formation of the film components is plotted in Figure 4.61. The blue and red lines represent UWS and solid deposits, respectively. The following successive physical effects can be distinguished in the diagram: Leidenfrost effect, intermittent and permanent wall wetting. A fast deposit formation was observed after the liquid film left the area of the initial foot print (approx. 160 s). During the simulation time of 216 s, 52 mg of solid deposits were accumulated in the film. The main component of simulated deposits is biuret. In contrast to that, the real deposits consist mainly of cyanuric acid. These differences may refer to some inaccuracy of the kinetic model of urea decomposition as well as to fact that the simulation time was limited to 216 s.

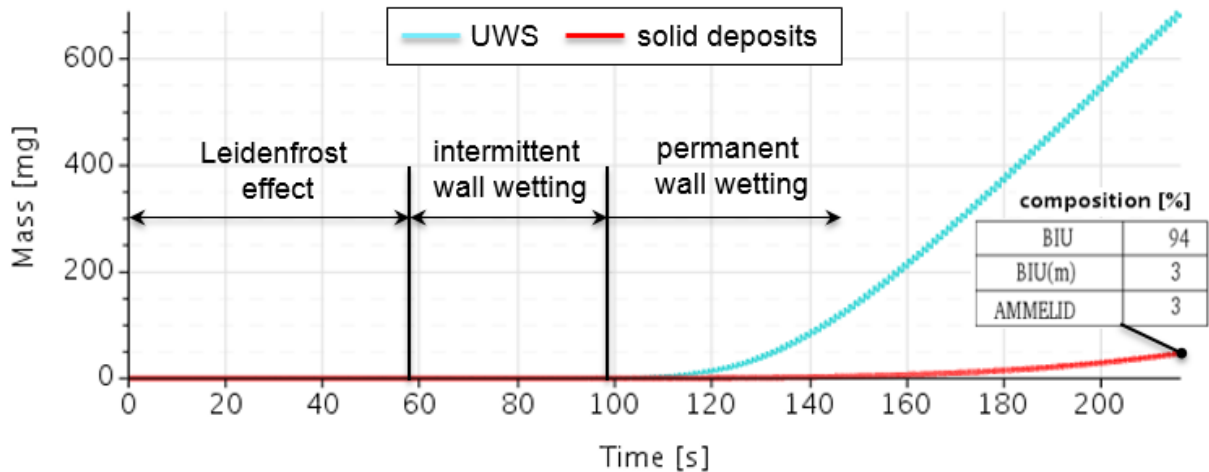


Figure 4.61: Simulated mass of UWS and solid deposits. OP3, injector 1, injection rate 132 mg/s

Figure 4.62 shows the simulated and observed solid deposit produced at OP3 with injector 2. Similar to the simulation mentioned above, the simulation time was limited to 180 s, when the film thickness exceeded the critical value. Nevertheless, the position of solid deposits at this time is well predicted. The solid deposits can be observed close to the initial foot print of the spray.

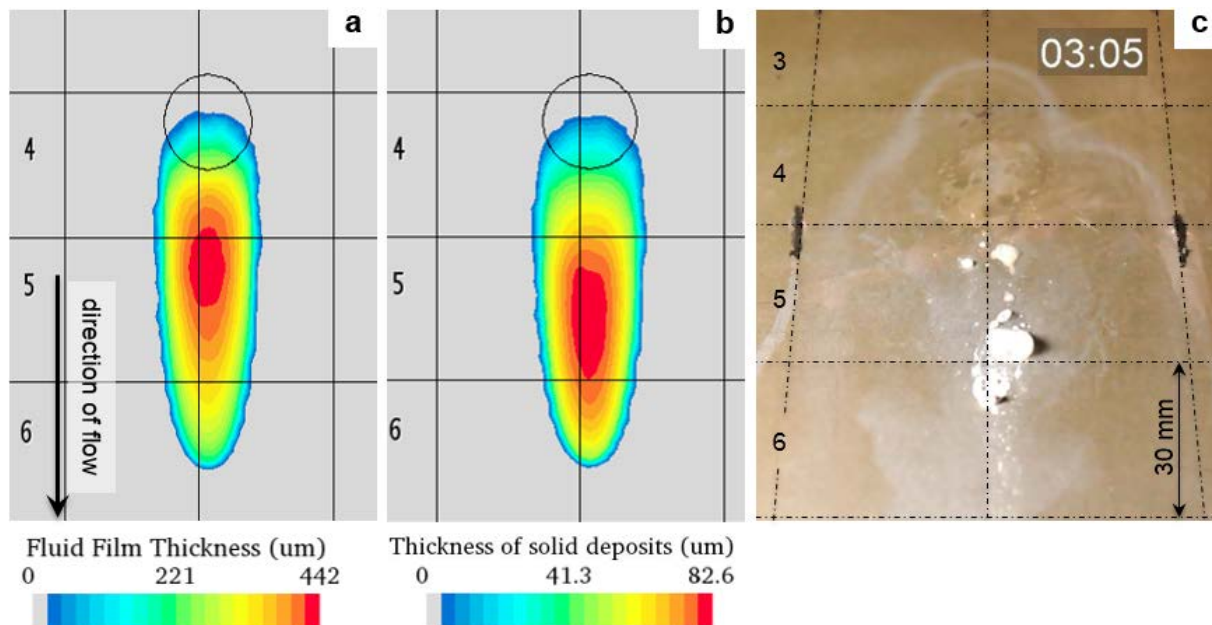
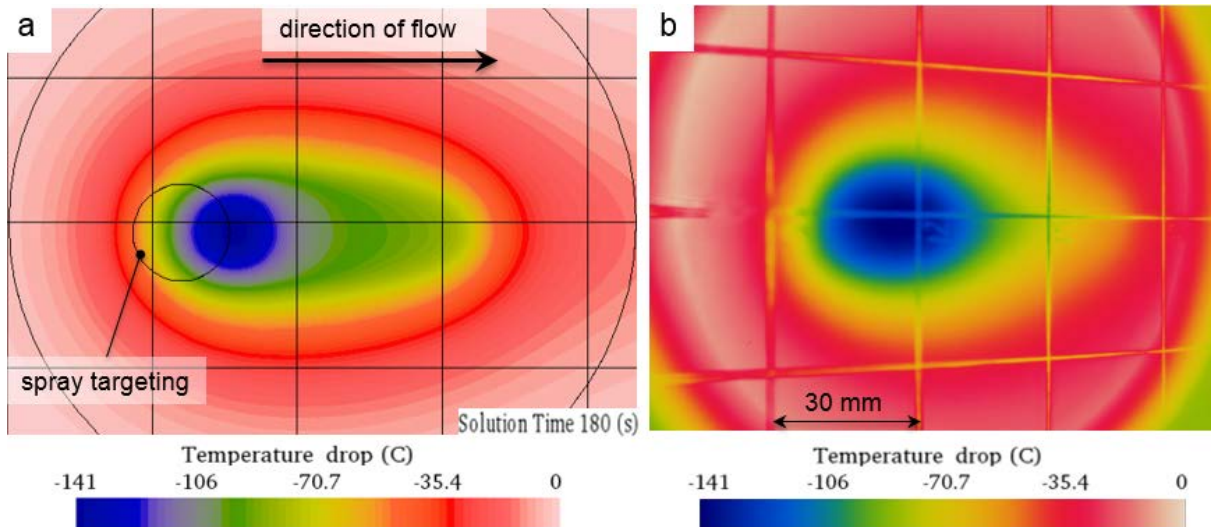


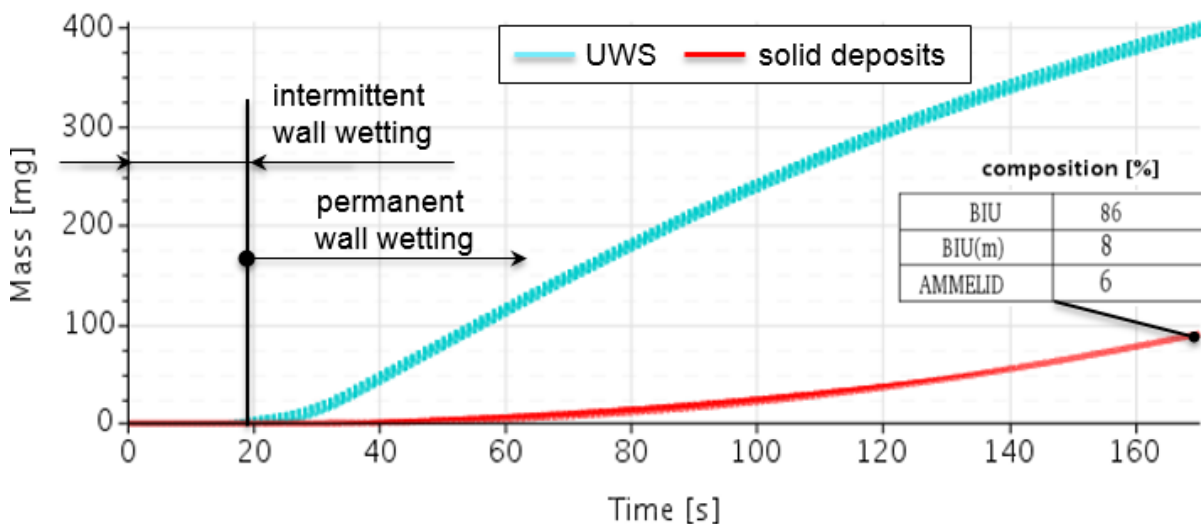
Figure 4.62: Film and deposit formation on the impingement plate. a – simulated film thickness, b – simulated thickness of solid deposits, c – experimental result. OP3, injector 2, injection rate 61 mg/s

Figure 4.63 allows the comparison of the simulated and measured temperature drop on the bottom side of the plate. Once again, a good agreement between the results can be observed. The position of the cooling area and the minimal temperature drop are well predicted.



**Figure 4.63: Simulated (a) and measured (b) temperature drop at the bottom side of the impingement plate. OP3, injector 2, injection rate 61 mg/s**

The formation of the film components is plotted in Figure 4.64. Due to high We-numbers of spray droplets and a high area load of the spray, the critical wall temperature was exceeded during the second injection cycle. The transition between the intermittent and permanent wall wetting occurred after 18 seconds. 90 mg of solid deposits were accumulated during the simulation time. The simulated deposits consist mainly of biuret (86 %), the real deposit of cyanuric acid.



**Figure 4.64: Simulated mass of UWS - and solid deposit. OP3, injector 2, injection rate 61 mg/s**

Figure 4.65 illustrates simulated and measured results of the transient experiment N<sup>o</sup>5 (see Table 4.14). The liquid film and the solid deposits were accumulated during the first part of the experiment, i.e. 300 s. The film propagation and the position of the solid deposits were well predicted. The width of the liquid film downstream the initial foot pint was overestimated. Further research work on critical fluid properties like the surface tension of liquid urea in dependency of the temperature may be therefore necessary. After 300 s the UWS injection was stopped. Hence, the film temperature started to rise and a fast film evaporation was observed. The further propagation of the film was inhibited due to a high viscosity of the solid deposits

dissolved in the film. Further research on liquid film properties depends on the film composition and film temperature is recommended.

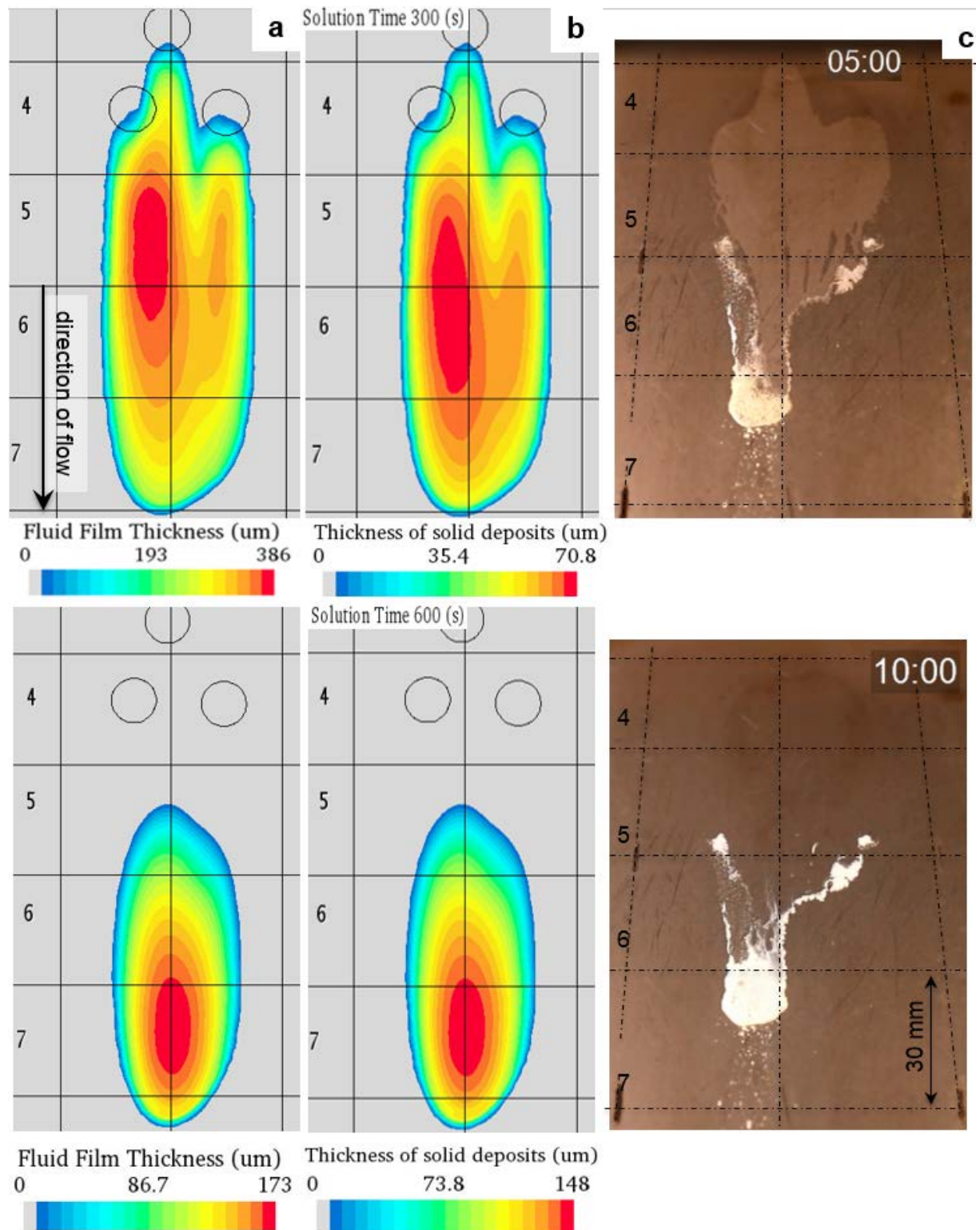


**Figure 4.65: Film and deposit formation on the impingement plate. a – simulated film thickness, b – simulated thickness of solid deposits, c – experimental result. Transient measurement N°5**

Figure 4.66 shows the comparison of the simulated and measured temperature drop at the end of the first part of the experiment. Once again, the temperature drop in the area of the

initial foot print is in a good agreement with the measured data. Due to a wider front of the film, the cooling area of the film downstream the initial foot print is overestimated.

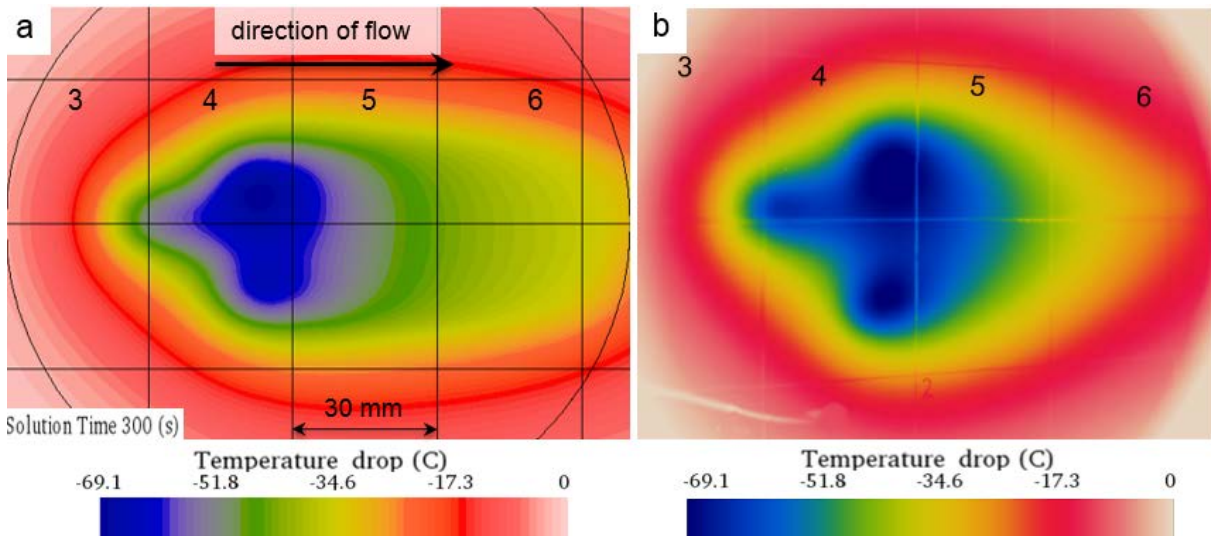


**Figure 4.66: Simulated (a) and measured (b) temperature drop at the bottom side of the impingement plate. Transient measurement N°5**

The formation and decomposition of the film components is plotted in Figure 4.67. Due to a low initial plate temperature, permanent wall wetting was observed. A fast deposit formation occurred after the liquid film left the area of the initial foot print (approx. 80 s.). The main component of simulated deposits at the end of the first part of the experiment was biuret (92 %). After 300 s the film temperature started to rise what caused the decomposition of biuret into ammellid (35 %), biuret matrix (24 %) and cyanuric acid (2 %). In contrast to that, the real deposits at the end of the experiment consisted mainly of the cyanuric acid.

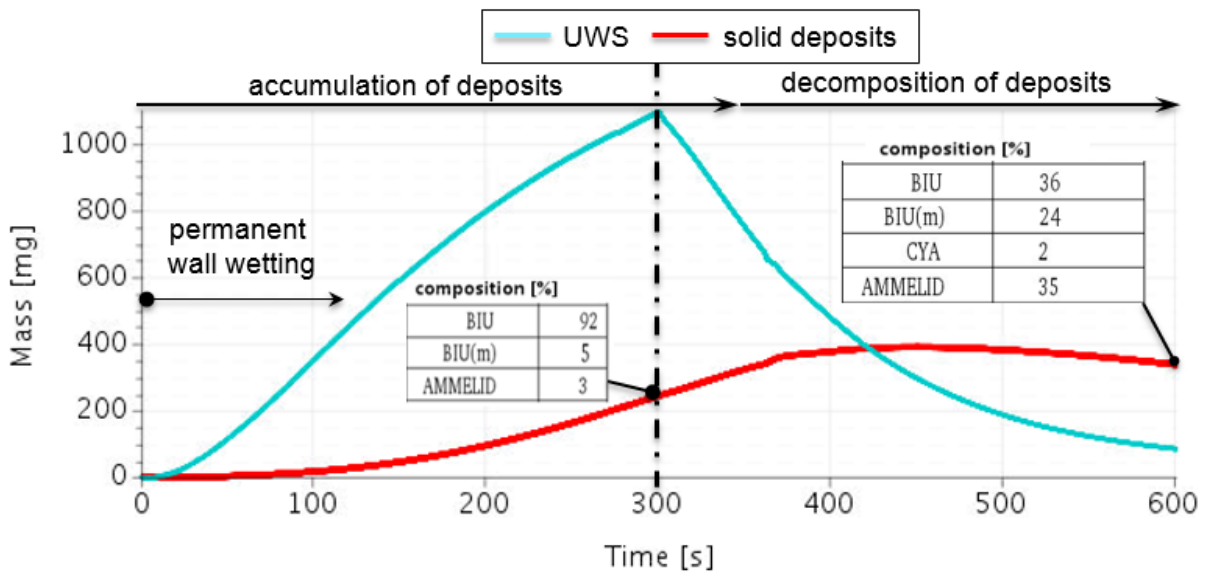


**Figure 4.67: Mass of UWS and solid deposits. Transient measurement N°5**

#### 4.5 Revised Kinetic Model for Urea Decomposition

Simulation results for 0D and 3D model presented in the Sections above have clearly shown some deficits of the existing kinetic model for urea decomposition. In particular, the solidification effect during heat-up of biuret is not sufficiently reproduced by the adapted model from Brack et al. [37], as it is modeled by an additional biuret matrix species. Furthermore, the decomposition process of triuret is only unsatisfactory modeled. Based on TGA and DSC data,

partly presented in this work, and further thermodynamic considerations, a revised kinetic scheme for urea decomposition is proposed by a collaborative investigation of S. Tischer, M. Börnhorst, J. Amsler, G. Schoch and O. Deutschmann [92]. The presented model is developed recently and was not available for simulations presented in Section 4.4.

The kinetic model proposed by Brack et al. [37] uses a matrix species to cover the effect of solidification around 220°C as discussed in Section 4.3.4. By thermodynamic calculations on the chemical potential, the phase transition temperature can be determined. As the chemical potential of solid urea equals the chemical potential of liquid urea at the melting point, a temperature of 133°C is calculated. For biuret, this calculation reveals a melting point of 233°C, which is not in accordance to common literature stating a melting point around 190 – 193°C [20,23]. Moreover, the phase diagram displayed in Figure 4.68, derived from thermodynamic data shows a eutectic mixture of urea and biuret.

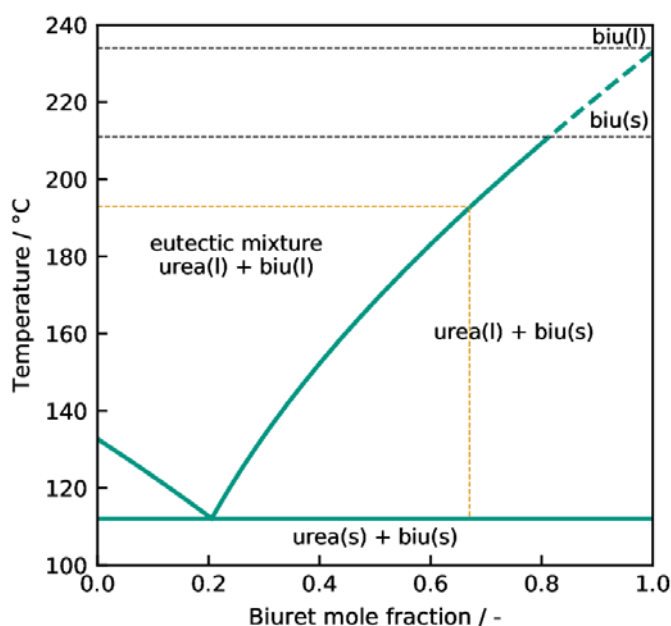


**Figure 4.68: Phase diagram of eutectic mixture of urea and biuret adapted from Tischer et al. [92]. The orange dotted lines indicate a composition of 67 % biuret and 33 % urea leading to melting of biuret.**

This explains the solidification effect observed around 220°C and further proves that current literature does not give the correct temperature value for biuret melting. The phase diagram reveals that biuret becomes liquid at 193°C in case of a mixture of 67 % biuret and 33 % urea. By decomposition of urea with increasing temperatures, the amount of urea is decreased and biuret becomes solid again. Based on these data, solidification of biuret is initiated for temperatures above 210°C before the actual melting point of biuret is reached at 233°C. [92]

A comprehensive overview on the simulation results of urea and by-product decomposition at different experimental conditions is given in Tischer et al. [92]. The DETCHEM<sup>MPTR</sup> numerical model presented in Section 4.3.4 is used for the simulations. Figure 4.69 shows a comparison of experimental and simulation results of urea decomposition.

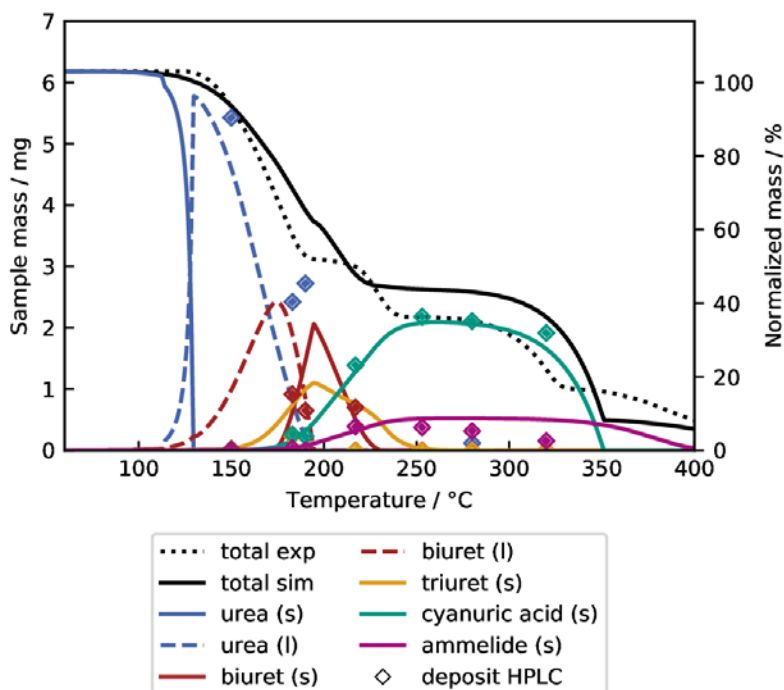


**Figure 4.69: Experimental and simulation results on urea decomposition. Simulation results for the overall sample mass and the evolution and consumption of relevant species is compared to urea TGA data and deposit compositions at different temperatures. Temperatures of corresponding deposit compositions are the gas temperatures of different experiments.**

Generally, a satisfactory agreement of the overall experimental and simulated mass loss during urea decomposition is achieved. The model reproduces four decomposition stages. The first stage comprises the liquid urea-biuret mixture, the second stage the biuret-triuret equilibrium. The third stage describes cyanuric acid sublimation while the fourth stage is attributed to ammelide decomposition. In contrast to the experiments, the urea-biuret and the biuret-triuret stage largely overlap in the simulations, which is attributed to the poor prediction of biuret and triuret decomposition due to a lack in thermodynamic data. Temperature intervals of the respective decomposition stages are slightly shifted in the simulation. In addition to the overall mass loss, simulation data on the production and consumption of relevant species is provided over temperature. In comparison to the simulation results on species formation and consumption, HPLC results of the deposit analysis presented in Section 4.2 is depicted in Figure 4.69. For comparison, HPLC data is scaled to the overall urea sample mass at different temperatures. In general, the model sufficiently reproduces the composition of the samples at different temperatures. Results demonstrate the capability of the revised model to predict the urea decomposition process not only in controlled TGA experiments, but also for deposit formation under realistic conditions.

## 5 Summary & Outlook

In the framework of this project, detailed experimental and numerical investigations on multi-phase, reacting flows in SCR systems were carried out. Consequences from urea water solution dosing into the hot exhaust, such as extensive spray/wall interaction with solid deposit formation were studied.

The goal of the project was the fundamental understanding of chemical and physical processes during UWS injection and deposit formation in SCR exhaust systems. Experiments were conducted on lab scale at KIT and on an engine scale at TUW in order to create a better understanding of spray/wall interaction, impingement heat transfer, the formation of wall film and solid deposits. Therefore, test benches were set up and advanced measuring techniques were applied in order to investigate the relevant physical and chemical processes.

Measurements at steady-state and transient operating conditions were carried out in order to provide a comprehensive experimental database that provides fundamental knowledge and allows the validation of numerical models. The whole process chain from spray formation, droplet impingement on a hot surface, film formation and wall cooling was investigated with high-speed and video imaging, laser diffraction and IR-thermography. The dimensions of the formed deposits were measured and both decomposition kinetics and chemical composition were analyzed in detail and discussed together with measured reference data of urea and its by-products. Experiments showed a decrease of the total mass of deposits sampled from the test rig for a multiple injection dosing strategy of up to 60 %. Due to the partial solubility of the formed by-products in UWS, solids were re-dissolved in the injected UWS leading to further decomposition.

Detailed chemical analyses of deposits derived at different operating conditions showed that the chemical composition of by-products formed from urea decomposition can be deduced from the decomposition stages of urea water solution identified by TG analysis and the decomposition mechanism of urea proposed by Brack et al. [37]. Hence, deposit composition is mainly dependent on temperature. Deposit composition was investigated by both TGA and HPLC. HPLC results were correlated to the respective decomposition stages detected by TGA. Deposits created at high temperatures were observed to require increased temperatures for decomposition. For deposits derived at temperatures below 200°C, urea represented the main component. With increasing temperature, the portion of urea was decreasing. Deposits derived in the temperature range of 200-250°C mainly consisted of biuret and cyanuric acid. Cyanuric acid and ammelide were the main components for deposits derived at higher temperatures. However, this study proposes the existence of further chemical compounds besides well-known by-products formed by urea reactions even at low temperatures. TGA experiments revealed portions of up to 10 % of these highly temperature resistant substances. Results showed that particularly biuret, triuret and ammelide decomposition produces large portions of residues stable up to 700°C. In contrast to existing literature stating high temperature operation as less critical with regard to deposit formation [17,24–26,66], these components were found to represent a high risk of deposit accumulation without a possible regeneration.

Based on kinetic data from thermogravimetric analysis and thermodynamic considerations, the urea decomposition model proposed by Brack et al. [37] was extended and kinetically adapted. The numerical model setup for simulating decomposition represented a 0D batch-type reactor including multiple condensed phases. By implementation of interface reactions, the effect of variable surface-to-volume ratios could be reproduced by the model. An increase of interfacial area was observed to positively affect urea decomposition in terms of solid by-product formation. Moreover, this model was implemented to a 3D CFD simulation by user coding. The CFD model included the turbulent two-phase flow, spray/wall interaction, film formation and evaporation. For the first time, relevant physical and chemical phenomena in the mixing section of SCR system were predicted by a comprehensive model. The implementation routine was tested by simulations of thermogravimetric decomposition of urea and various by-products. Results showed an excellent agreement of the predicted decomposition kinetics compared to the 0D model and experimental data.

Furthermore, the comprehensive modeling approach was applied to CFD simulations of turbulent exhaust flow on an engine test bed. Modifications and enhancements were developed for the droplet drag force model, the Bai-Onera impingement map and the Wruck heat transfer model based on the experimental database from the engine test bench. A good agreement was obtained between measurements and simulation with respect to spray impingement, film formation and material cooling due to heat conduction and water evaporation from the UWS. For the first time, local by-product formation from the liquid film could be investigated in the framework of a CFD simulation. The results were in a reasonable agreement with the chemical analysis of the deposits from the test bed. However, further improvements and validation will be necessary in the future.

Apart from the chemical and physical models, a numerical method based on the source term approach was implemented in order to substantially speed up the CFD simulations. With the source term methodology it was possible to pre-tabulate the sources of mass, momentum and energy for an injection event at given thermodynamic boundary conditions and substitute the spray simulation with these source terms in the transient simulations that covered time durations of several minutes. A considerable acceleration of the CFD simulation was reached that enabled the calculation of sufficiently long time intervals to take the chemistry of deposit formation into account. This project therefore provided a feasible numerical implementation method for chemical kinetics of urea decomposition and demonstrated the capabilities of the developed modeling approach. Apart from StarCCM+, which was used in this project, the workflow can be applied to other commercial CFD codes.

A revised kinetic model for urea decomposition was presented which showed an improved agreement between experiments and the numerical simulation of TGA. Future studies could include these kinetics to the CFD simulations of systems with UWS injection to achieve a better agreement with experimental data in terms of the decomposition kinetics.

Though the new simulation workflow provides a comprehensive approach to deposit modelling, it is limited by the boundary layer approach of the fluid film model and therefore restricted to small film and deposit heights. As a result it is not possible to simulate growing deposits that restrict the free flow area. Furthermore, solid deposits have to be modeled as pseudo-liquid species, because of a lack of possibility to include solid species into the fluid film model. Another restriction is the limited access to several values, such as gas phase concentrations, for the reactions in the fluid film. It is proposed to expand the fluid film model with suitable solutions for the mentioned problems to increase the possibilities, but also the accuracy of the presented workflow.

Future studies should investigate the influence of different surface properties, structures and roughness on the impingement process and deposit formation, which are observed to play a big role in real-life exhaust systems. In addition, the effect of catalytic coatings is of high interest. A fundamental study on the morphology of created deposits can help to understand the formation and decomposition process of deposits. If liquid film accumulates droplets may strip and re-impinge further downstream of the exhaust system resulting again in deposit formation. Investigations on the stripping process and the extension of the source term methodology to these scenarios should be addressed in the future.

Overall, the presented work in this project delivers a good basis for further investigations of the UWS injection and deposit formation to enhance the limits of SCR systems and ensure lower  $\text{NO}_x$  emission in the near future.

## 6 Appendix

### 6.1 Bibliography

- [1] Nationale Akademie der Wissenschaften Leopoldina, Saubere Luft. Stickstoffoxide und Feinstaub in der Atemluft: Grundlagen und Empfehlungen, 2019.
- [2] European Commission, EU transport in figures: Statistical pocketbook, Publications Office of the European Union, Luxembourg, 2018.
- [3] G.P. Merker, R. Teichmann, Grundlagen Verbrennungsmotoren, Springer Fachmedien Wiesbaden, Wiesbaden, 2018.
- [4] Bundesministerium für Verkehr und digitale Infrastruktur, Verkehr in Zahlen 2016/17: Daten und Fakten kompakt, 44th ed., DVV Media Group, Hamburg, 2016.
- [5] H.M. Cho, B.-Q. He, Spark ignition natural gas engines--A review, *Energy Conversion and Management* 48 (2007) 608–618.
- [6] C. White, R. Steeper, A. Lutz, The hydrogen-fueled internal combustion engine: A technical review, *International Journal of Hydrogen Energy* 31 (2006) 1292–1305.
- [7] O. Deutschmann, J.-D. Grunwaldt, Abgasnachbehandlung in mobilen Systemen: Stand der Technik, Herausforderungen und Perspektiven, *Chemie Ingenieur Technik* 85 (2013) 595–617.
- [8] F. Birkhold, U. Meingast, P. Wassermann, O. Deutschmann, Modeling and simulation of the injection of urea-water-solution for automotive SCR DeNOx-systems, *Applied Catalysis B: Environmental* 70 (2007) 119–127.
- [9] S. Knirsch, U. Weiß, A. Fröhlich, G. Pamio, J. Helbig, H. Ritter, The new generation of the Audi V6 TDI engine: 25 years of Technology - Dynamics - Innovation, 35th International Vienna Motor Symposium (2014).
- [10] I. Nova, E. Tronconi, Urea-SCR Technology for deNOx After Treatment of Diesel Exhausts, Springer New York, New York, USA, 2014.
- [11] A. Solla, M. Westerholm, C. Söderström, K. Tormonen, T. Härmä, T. Nissinen, J. Kukkonen, Effect of Ammonium Formate and Mixtures of Urea and Ammonium Formate on Low Temperature Activity of SCR Systems, SAE Technical Paper (2005).
- [12] O. Kröcher, M. Elsener, E. Jacob, New reducing agents for the low-NOx SCR technology, Proceedings of the 5th International Exhaust Gas and Particulate Emissions Forum, Ludwigsburg (2008).
- [13] B.R. Ramachandran, A.M. Halpern, E.D. Glendening, Kinetics and Mechanism of the Reversible Dissociation of Ammonium Carbamate: Involvement of Carbamic Acid, *The Journal of Physical Chemistry A* 102 (1998) 3934–3941.
- [14] J.G. Wilson, G. Hargrave, Analysis of a Novel Method for Low-Temperature Ammonia Production Using DEF for Mobile Selective Catalytic Reduction Systems, SAE Technical Paper (2018).
- [15] T.D. Elmøe, R.Z. Sørensen, U. Quaade, C.H. Christensen, J.K. Nørskov, T. Johannesen, A high-density ammonia storage/delivery system based on Mg(NH<sub>3</sub>)<sub>6</sub>Cl<sub>2</sub> for SCR - DeNOx in vehicles, *Chemical Engineering Science* 61 (2006) 2618–2625.
- [16] F. Birkhold, Selektive katalytische Reduktion von Stickoxiden in Kraftfahrzeugen: Untersuchung der Einspritzung von Harnstoffwasserlösung, PhD thesis, Karlsruhe, Germany.
- [17] W. Brack, B. Heine, F. Birkhold, M. Kruse, O. Deutschmann, Formation of Urea-Based Deposits in an Exhaust System: Numerical Predictions and Experimental Observations on a Hot Gas Test Bench, *Emission Control Science and Technology* 2 (2016) 115–123.

- [18] S. Grout, J.-B. Blaisot, K. Pajot, G. Osbat, Experimental investigation on the injection of an urea-water solution in hot air stream for the SCR application: Evaporation and spray/wall interaction, *Fuel* 106 (2013) 166–177.
- [19] M. Eichelbaum, R.J. Farrauto, M.J. Castaldi, The impact of urea on the performance of metal exchanged zeolites for the selective catalytic reduction of NO<sub>x</sub>: Part I. Pyrolysis and hydrolysis of urea over zeolite catalysts, *Applied Catalysis B: Environmental* 97 (2010) 90–97.
- [20] P.M. Schaber, J. Colson, S. Higgins, D. Thielen, B. Anspach, J. Brauer, Thermal decomposition (pyrolysis) of urea in an open reaction vessel, *Thermochimica Acta* 424 (2004) 131–142.
- [21] A. Lundström, B. Andersson, L. Olsson, Urea thermolysis studied under flow reactor conditions using DSC and FT-IR, *Chemical Engineering Journal* 150 (2009) 544–550.
- [22] A.M. Bernhard, D. Peitz, M. Elsener, A. Wokaun, O. Kröcher, Hydrolysis and thermolysis of urea and its decomposition byproducts biuret, cyanuric acid and melamine over anatase TiO<sub>2</sub>, *Applied Catalysis B: Environmental* 115-116 (2012) 129–137.
- [23] W. Brack, Untersuchung der Ablagerungsbildung durch Harnstofffolgeprodukte im Abgasstrang, PhD thesis, Karlsruhe, Germany.
- [24] V.O. Strots, S. Santhanam, B.J. Adelman, G.A. Griffin, E.M. Derybowski, Deposit Formation in Urea-SCR Systems, *SAE International Journal of Fuels and Lubricants* 2 (2009) 283–289.
- [25] S.Z. Bai, S.G. Lang, K.P. Yuan, Y. Liu, G.X. Li, Experimental Study of Urea Depositions in Urea-SCR System, *Advanced Materials Research* 937 (2014) 74–79.
- [26] H. Smith, T. Lauer, M. Mayer, S. Pierson, Optical and Numerical Investigations on the Mechanisms of Deposit Formation in SCR Systems, *SAE International Journal of Fuels and Lubricants* 7 (2014) 525–542.
- [27] C.L. Weeks, D.R. Ibeling, S. Han, L. Ludwig, P. Ayyappan, Analytical Investigation of Urea Deposits in SCR System, *SAE International Journal of Engines* 8 (2015).
- [28] S. Eakle, S. Kroll, A. Yau, J. Gomez, C. Henry, Investigation of Urea Derived Deposits Composition in SCR Systems and Their Potential Effect on Overall PM Emissions, *SAE Technical Paper* (2016).
- [29] S. Budavari, *The Merck Index Eleventh Edition*, Chemical & Engineering News 67 (1989).
- [30] Carl Roth GmbH + Co. KG, Sicherheitsdatenblatt gemäß Verordnung (EG) Nr. 1907/2006: Biuret, [www.carlroth.com](http://www.carlroth.com).
- [31] Merck KGaA, Sicherheitsdatenblatt gemäß Verordnung (EG) Nr. 1907/2006: Cyanursäure, <http://www.merckmillipore.com>.
- [32] B. Bann, S.A. Miller, Melamine And Derivatives Of Melamine, *Chemical Reviews* 58 (1958) 131–172.
- [33] Carl Roth GmbH + Co. KG, Sicherheitsdatenblatt gemäß Verordnung (EG) Nr. 1907/2006: Melamin, [www.carlroth.com](http://www.carlroth.com).
- [34] L. Stradella, M. Argentero, A study of the thermal decomposition of urea, of related compounds and thiourea using DSC and TG-EGA, *Thermochimica Acta* 219 (1993) 315–323.
- [35] A.G. Koryakin, V.A. Gal'perin, A.N. Sarbaev, A.I. Finkel'shtein, Thermography of urea and its pyrolysis products, *Zh. Org. Khim.* (Russian Journal of Organic Chemistry) (1971) 972–977.

- [36] H.L. Fang, H.F.M. DaCosta, Urea thermolysis and NO<sub>x</sub> reduction with and without SCR catalysts, *Applied Catalysis B: Environmental* 46 (2003) 17–34.
- [37] W. Brack, B. Heine, F. Birkhold, M. Kruse, G. Schoch, S. Tischer, O. Deutschmann, Kinetic modeling of urea decomposition based on systematic thermogravimetric analyses of urea and its most important by-products, *Chemical Engineering Science* 106 (2014) 1–8.
- [38] V. Ebrahimian, A. Nicolle, C. Habchi, Detailed modeling of the evaporation and thermal decomposition of urea-water solution in SCR systems, *AIChE Journal* 58 (2012) 1998–2009.
- [39] X. Gan, D. Yao, F. Wu, J. Dai, L. Wei, X. Li, Modeling and simulation of urea-water-solution droplet evaporation and thermolysis processes for SCR systems, *Chinese Journal of Chemical Engineering* 24 (2016) 1065–1073.
- [40] P. Hauck, A. Jentys, J.A. Lercher, On the quantitative aspects of hydrolysis of isocyanic acid on TiO<sub>2</sub>, *Catalysis Today* 127 (2007) 165–175.
- [41] P. Hauck, A. Jentys, J.A. Lercher, Surface chemistry and kinetics of the hydrolysis of isocyanic acid on anatase, *Applied Catalysis B: Environmental* 70 (2007) 91–99.
- [42] M. Eichelbaum, A.B. Siemer, R.J. Farrauto, M.J. Castaldi, The impact of urea on the performance of metal-exchanged zeolites for the selective catalytic reduction of NO<sub>x</sub>--Part II. Catalytic, FTIR, and NMR studies, *Applied Catalysis B: Environmental* 97 (2010) 98–107.
- [43] A.M. Bernhard, D. Peitz, M. Elsener, T. Schildhauer, O. Kröcher, Catalytic urea hydrolysis in the selective catalytic reduction of NO<sub>x</sub>: Catalyst screening and kinetics on anatase TiO<sub>2</sub> and ZrO<sub>2</sub>, *Catal. Sci. Technol.* 3 (2013) 942–951.
- [44] D. Peitz, A. Bernhard, M. Elsener, O. Kröcher, Laboratory test reactor for the investigation of liquid reducing agents in the selective catalytic reduction of NO<sub>x</sub>, *The Review of scientific instruments* 82 (2011) 84101.
- [45] O. Kröcher, M. Elsener, Materials for thermohydrolysis of urea in a fluidized bed, *Chemical Engineering Journal* 152 (2009) 167–176.
- [46] G. Piazzesi, M. Devadas, O. Kröcher, M. Elsener, A. Wokaun, Isocyanic acid hydrolysis over Fe-ZSM5 in urea-SCR, *Catalysis Communications* 7 (2006) 600–603.
- [47] G. Piazzesi, O. Kröcher, M. Elsener, A. Wokaun, Adsorption and hydrolysis of isocyanic acid on TiO<sub>2</sub>, *Applied Catalysis B: Environmental* 65 (2006) 55–61.
- [48] M. Kleemann, M. Elsener, M. Koebel, A. Wokaun, Hydrolysis of Isocyanic Acid on SCR Catalysts, *Industrial & Engineering Chemistry Research* 39 (2000) 4120–4126.
- [49] I. Czekaj, O. Kröcher, G. Piazzesi, DFT calculations, DRIFT spectroscopy and kinetic studies on the hydrolysis of isocyanic acid on the TiO<sub>2</sub>-anatase (101) surface, *Journal of Molecular Catalysis A: Chemical* 280 (2008) 68–80.
- [50] I. Czekaj, O. Kröcher, Decomposition of Urea in the SCR Process: Combination of DFT Calculations and Experimental Results on the Catalytic Hydrolysis of Isocyanic Acid on TiO<sub>2</sub> and Al<sub>2</sub>O<sub>3</sub>, *Topics in Catalysis* 52 (2009) 1740–1745.
- [51] A. Lundström, T. Snelling, P. Morsing, P. Gabrielsson, E. Senar, L. Olsson, Urea decomposition and HNCO hydrolysis studied over titanium dioxide, Fe-Beta and  $\gamma$ -Alumina, *Applied Catalysis B: Environmental* 106 (2011) 273–279.
- [52] F. Birkhold, U. Meingast, P. Wassermann, O. Deutschmann, Analysis of the Injection of Urea-Water-Solution for Automotive SCR DeNO<sub>x</sub>-Systems: Modeling of Two-Phase Flow and Spray/Wall-Interaction, *SAE Technical Paper* 2006-01-0643 (2006).

- [53] N.S. Nayak, The Evaporation and Spray Wall Interaction Behavior of Urea Water Solution (UWS) in Selective Catalytic Reduction (SCR) Systems of Modern Automobiles, SAE Technical Paper (2013).
- [54] A. Varna, A.C. Spiteri, Y.M. Wright, P. Dimopoulos Eggenschwiler, K. Boulouchos, Experimental and numerical assessment of impingement and mixing of urea-water sprays for nitric oxide reduction in diesel exhaust, *Applied Energy* 157 (2015) 824–837.
- [55] S. Fischer, R. Bitto, T. Lauer, C. Krenn, J. Tauer, G. Pessl, Impact of the Turbulence Model and Numerical Approach on the Prediction of the Ammonia Homogenization in an Automotive SCR System, *SAE International Journal of Engines* 5 (2012) 1443–1458.
- [56] U. Budziankou, T. Lauer, X. Yu, B.M. Schmidt, N. Cho, Modeling Approach for a Wiremesh Substrate in CFD Simulation, *SAE International Journal of Fuels and Lubricants* (2017).
- [57] J. Michelin, P. Nappez, F. Guilbaud, C. Hinterberger, E. Ottaviani, C. Gauthier, P. Maire, T. Couturier, Advanced Close Coupled SCR Compact Mixer Architecture, SAE Technical Paper (2015).
- [58] S. Kontin, A. Höfler, R. Koch, H.-J. Bauer, Heat and Mass Transfer accompanied by Crystallisation of single Particles containing Urea-water-solution, ILASS - Europe, 23rd Annual Conference on Liquid Atomization and Spray Systems (2010).
- [59] M. Stein, V. Bykov, U. Maas, The Effect of Evaporation Models on Urea Decomposition from Urea-Water-Solution Droplets in SCR Conditions, *Emission Control Science and Technology* 3 (2017) 263–274.
- [60] K. Nishad, A. Sadiki, J. Janicka, Numerical Investigation of AdBlue Droplet Evaporation and Thermal Decomposition in the Context of NOx-SCR Using a Multi-Component Evaporation Model, *Energies* 11 (2018) 222.
- [61] H. Smith, M. Zöchbauer, T. Lauer, Advanced Spray Impingement Modelling for an Improved Prediction Accuracy of the Ammonia Homogenisation in SCR Systems, *SAE International Journal of Fuels and Lubricants* (2015).
- [62] E. Abu-Ramadan, K. Saha, X. Li, Numerical Modeling of the Impingement Process of Urea-Water Solution Spray on the Heated Walls of SCR Systems, SAE Technical Paper (2012).
- [63] J.Y. Kim, S.H. Ryu, J.S. Ha, Numerical prediction on the characteristics of spray-induced mixing and thermal decomposition of urea solution in SCR systems, *Proceedings of ICEF04, 2004 Fall Technical Conference of the ASME Internal Combustion Engine Division* (2004).
- [64] J.C. Wurzenberger, R. Wanker, Multi-Scale SCR Modeling, 1D Kinetic Analysis and 3D System Simulation, SAE Technical Paper (2005).
- [65] A. Munnannur, Z.G. Liu, Development and Validation of a Predictive Model for DEF Injection and Urea Decomposition in Mobile SCR DeNOx Systems, SAE Technical Paper (2010).
- [66] S. Sadashiva Prabhu, N.S. Nayak, N. Kapilan, V. Hindasageri, An experimental and numerical study on effects of exhaust gas temperature and flow rate on deposit formation in Urea-Selective Catalytic Reduction (SCR) system of modern automobiles, *Applied Thermal Engineering* 111 (2017) 1211–1231.
- [67] ANSYS Inc., ANSYS Fluent CFD Software, 2019, [www.ansys.com](http://www.ansys.com).
- [68] J.K. Dukowicz, A particle-fluid numerical model for liquid sprays, *Journal of Computational Physics* 35 (1980) 229–253.
- [69] D. Kuhnke, Spray wall interaction modelling by dimensionless data analysis, PhD thesis, Aachen.

- [70] N. Wruck, Transientes Sieden von Tropfen beim Wandaufprall, PhD thesis, Aachen, Germany.
- [71] F.P. Incropera, D.P. DeWitt, T.L. Bergmann, A.S. Lavine, Fundamentals of heat and mass transfer, 7th ed., John Wiley & Sons, Hoboken, Netherlands, 2013.
- [72] C. Habchi, A. Nicolle, N. Gillet, Numerical Study of Deposits Formation in SCR Systems Using Urea-Water Solution Injection, *Journal of Materials Science and Nanotechnology* 6 (2018).
- [73] H. Oertel, Prandtl - Führer durch die Strömungslehre: Grundlagen und Phänomene, 13th ed., Springer Vieweg, Wiesbaden, 2012.
- [74] G.-G. Börger, Optimierung von Windkanaldüsen für den Ultraschallbereich, PhD thesis.
- [75] A.M. Bernhard, I. Czekaj, M. Elsener, A. Wokaun, O. Kröcher, Evaporation of urea at atmospheric pressure, *The journal of physical chemistry. A* 115 (2011) 2581–2589.
- [76] M. Koebel, M. Elsener, Determination of urea and its thermal decomposition products by high-performance liquid chromatography, *Journal of Chromatography A* 689 (1995) 164–169.
- [77] M. Quissek, T. Lauer, O. García-Afonso, S. Fowles, Identification of Film Breakup for a Liquid Urea-Water-Solution and Application to CFD, SAE Technical Paper (2019), doi:10.4271/2019-01-0983.
- [78] J.H. Baik, S.D. Yim, I.-S. Nam, Y.S. Mok, J.-H. Lee, B.K. Cho, S.H. Oh, Control of NO<sub>x</sub> Emissions from Diesel Engine by Selective Catalytic Reduction (SCR) with Urea, *Topics in Catalysis* 30/31 (2004) 37–41.
- [79] E. Seker, N. Yasyerli, E. Gulari, C. Lambert, R.H. Hammerle, NO<sub>x</sub> reduction by urea under lean conditions over single step sol-gel Pt/alumina catalyst, *Applied Catalysis B: Environmental* 37 (2002) 27–35.
- [80] Lucefin Group, Technical Card X5CrNi18-10: Nr. 14301 Austenitic stainless steel, [www.lucefin.com](http://www.lucefin.com), accessed 2 January 2019.
- [81] H. Smith, Modelling Deposit Formation in Automotive SCR Systems, PhD thesis, Vienna, Austria.
- [82] S. Fischer, Simulation of the urea-water-solutino preparation and ammonia homogenization with a validated CFD-model for the optimization of automotive SCR-systems, PhD thesis, Vienna, Austria.
- [83] Siemens, Siemens Product Lifecycle Management Software Inc., The Steve Portal: Selective Catalytic Reduction Best Practices by Steven Dowding, 2018, [www.thesteveportal.plm.automation.siemens.com](http://www.thesteveportal.plm.automation.siemens.com).
- [84] Schiller, L., and Naumann, Über die grundlegenden Berechnungen bei der Schwerkraftaufbereitung, *VDI Zeitschrift* (1933).
- [85] E. Cunningham, On the Velocity of Steady Fall of Spherical Particles through Fluid Medium, *Proceedings of the Royal Society A: Mathematical, Physical and Engineering Sciences* 83 (1910) 357–365.
- [86] Siemens, Siemens Product Lifecycle Management Software Inc., Simcenter STAR-CCM+ Documentation, Version 13.06 (2018).
- [87] J. Akao, K. Akaki, S. Mori, Moriyama A., Deformation behaviors of a liquid droplet impingement onto a hot metal surface, *Trans. ISIJ* (1980) 737–743.
- [88] O. Deutschmann, S. Tischer, S. Kleditzsch, V. Janardhanan, C. Correa, D. Chatterjee, N. Mladenov, H.D. Minh, H. Karadeniz, M. Hettel, V. Menon, A. Banerjee, DETCHEM Software package, 2018, [www.detchem.com](http://www.detchem.com).

- [89] A. Burcat, Burcat's Thermodynamic Data: Thermochemical species in polynomial form, [www.burcat.technion.ac.il](http://www.burcat.technion.ac.il).
- [90] T. Huthwelker, T. Peter, Analytical description of gas transport across an interface with coupled diffusion in two phases, *The Journal of Chemical Physics* 105 (1996) 1661–1667.
- [91] P. Deuffhard, E. Hairer, J. Zugck, One-step and extrapolation methods for differential-algebraic systems, *Numerische Mathematik* 51 (1987) 501–516.
- [92] S. Tischer, M. Börnhorst, J. Amsler, G. Schoch, O. Deutschmann, Thermodynamics and reaction mechanism of urea decomposition, *Physical Chemistry Chemical Physics* (2019).

## 6.2 List of Abbreviations and symbols

### Abbreviation

ASC *Ammonia Slip Catalyst*

DFT *Density functional theory*

DRIFTS *Diffuse reflectance infrared Fourier transform spectra*

DTA *Differential thermal analysis*

GC *Gas Chromatography*

HPLC *High Performance Liquid Chromatography*

IR *Infrared*

ISE *Ion selective electrode*

MPTR *Multiple phase tank reactor*

MS *Mass Spectrometry*

NMR *Nuclear magnetic resonance*

PM *Particulate matter*

RDE *Real Driving Emission*

TGA *Thermogravimetric Analysis*

UWS *Urea water solution*

WLTP *Worldwide harmonized Light-duty Test Procedure*

XRD *X-Ray Diffraction*

### Symbols

Symbols	Description
$\sum \bar{Q}_g$	heat source
$\sum \bar{m}_{gi}$	mass source

---

$\sum \bar{p}_g$	momentum source
$\dot{n}_{ik}$	Rate of production of species i from reaction k
$\tilde{\nu}_{ik}$	Concentration exponent
$\Delta_{R_k} G^\ominus$	Reaction free enthalpy
$\Delta h_d$	evaporation enthalpy
$h_{wd}$	impingement heat transfer coefficient
$A_{cont}$	effective contact area
$A_k$	Pre-exponential factor of reaction k
$C_p$	Cunningham correction factor
$D_d$	particle diameter
$E_{a,k}$	Activation energy of reaction k
$F_d$	force from droplet to the gas phase
$H_{m,i}$	Molar enthalpy of species i
$Kn_p$	Knudsen number
$K_{p,k}, K_{c,k}$	Equilibrium constants
$M_i$	Molar mass of species i
$Q_{ev}$	evaporation heat
$Q_{imp}$	impingement heat
$Re_d$	droplet Reynolds number
$S_{m,i}$	Molar entropy of species i
$T_{crit}$	critical wall temperature
$T_g$	gas temperature
$T_{sat}$	saturation temperature of droplet
$T_w$	wall temperature
$V_c$	volume of a fluid cell
$V_j$	Volume of phase j

---

$V_{m,i}$	Molar volume of species $i$
$We_n$	normal Weber number
$Y_i$	evaporation rate of a species $i$
$Y_i$	Mass fraction of species $i$
$b_d$	heat penetration coefficients of droplet
$b_w$	heat penetration coefficients of solid wall
$c_i$	Molar concentration of species $i$
$c_{p,i}$	molar heat capacity of species $i$
$d_b$	mean molecule diameter in gas phase
$k_b$	Boltzmann constant
$m_d$	droplet mass
$m_{splash}$	droplet splash mass
$n_i$	Molar mass of species $i$
$p_g$	absolute gas pressure
$r_k$	Molar reaction rate of reaction $k$
$t_{cont}$	contact time
$t_{inj}$	injection time
$u_n$	normal component of the droplet velocity relative to the wall
$z_i$	Specific mole fraction of species $i$
$\alpha_c$	Accumulation factor
$\beta_k$	Temperature exponent of reaction $k$
$\rho_d$	droplet density
$\sigma_d$	droplet surface tension
$\Delta t$	simulation time step
$h$	Henry constant
$H$	Total enthalpy

---

---

$La$	Laplace number
$Oh$	Ohnesorge number
$R$	Ideal gas constant $R = 8.31446 \text{ J mol}^{-1} \text{ K}^{-1}$
$c$	particle count in a parcel

---

### 6.3 List of figures

Figure 2.1: CO <sub>2</sub> emissions through transportation in the European Union [2].	3
Figure 2.2: European emission regulations for heavy-duty vehicles [2]. All units in g/kWh.	4
Figure 2.3: Close-coupled exhaust gas after-treatment system with SCR coated DPF [9].	5
Figure 2.4: Influence of an optimized mixing device on NO <sub>x</sub> reduction efficiency and ammonia slip, adapted from [10].	6
Figure 2.5: Schematic of relevant physical and chemical processes in the mixing section of SCR systems.	7
Figure 3.1: Mass loss during thermal decomposition of urea measured by TGA with an initial sample mass of 60.3 mg and a heating rate of 2 K min <sup>-1</sup> (this work). Characteristic decomposition stages of urea are indicated as stated in literature [19,20]. 1: urea decomposition, 2: biuret decomposition, 3: cyanuric acid decomposition, 4: ammelide and ammeline decomposition. Solidification (matrix) as mentioned by Schaber et al. [20] is indicated by the orange dot.	11
Figure 3.2: Urea decomposition reactions included in kinetic model of Brack et al [37].	12
Figure 3.3: Time scales of relevant physical and chemical phenomena for comprehensive modeling of UWS decomposition and deposit formation.	13
Figure 3.4: Simulation results for wall film thickness and urea concentration for an injection of 0.83 g UWS at a gas temperature of 340°C derived by a 3D simulation in FIRE [52].	15
Figure 3.5: Deposition risk on the upstream area (left) and the rear blade side (right) calculated from liquid film simulation data such as velocity, temperature and concentrations. [26]	15
Figure 4.1: Project schedule stating the different working packages and milestone.	17
Figure 4.2: Schematic of hot gas lab test bench setup for deposit generation.	18
Figure 4.3: (a) Engineering drawing and (b) photograph of measurement box A equipped with thermocouples, heating cartridges and coolant lines in the bottom wall.	18
Figure 4.4: Valve signal for an exemplary period of 200 ms and a duty cycle of 20 % representing an valve opening time of 40 ms. Period length is determined from injection frequency (here: 5 Hz).	19
Figure 4.5: a - CAD-model of the measuring section with optical access, b – set up of the engine test bench for investigations of deposit formation and decomposition.	20
Figure 4.6: View on the bottom side of the impingement plate	21
Figure 4.7: Topographical image of deposits generated at OP 0 (a), OP 1 (b), OP 2 (c) and OP 3 (d). Positive y-direction represents the flow direction.	25
Figure 4.8: Photographs of deposits generated at different operating points.	26

Figure 4.9: Thermogravimetric measurement of UWS decomposition compared to determined deposit mass from single and multiple injection experiments in relation to the totally injected amount of UWS. The dashed line indicates a relative sample mass of 32.5 % marking the beginning of urea decomposition in the TG experiment.....	27
Figure 4.10: Thermogravimetric decomposition of deposit samples from OP 0, 1 and 4a compared to pure urea decomposition. Operating conditions are listed in Table 4.4. ....	27
Figure 4.11: Thermogravimetric decomposition of deposit samples from OP 4b compared to pure biuret decomposition. Operating conditions are listed in Table 4.4.....	28
Figure 4.12: Thermogravimetric decomposition of deposit samples from OP 2, 3 and 4c compared to pure cyanuric acid decomposition. Operating conditions are listed in Table 4.4. ....	29
Figure 4.13: Photographs of deposits generated at different operating points with additional water concentration of 3 – 3.5 %.....	30
Figure 4.14: Test bench setup for spray observation with high-speed imaging.....	33
Figure 4.15: Visualization of spray deflection from the gas flow at 6 ms after SOI. Injector 2, OP1 (left) and OP3 (right) .....	33
Figure 4.16: a - Test bench setup for measurements with laser diffraction, b - measurement positions .....	34
Figure 4.17: Droplet size distribution at measurement positions P1 - P6. Injector 3, OP1 and OP3 .....	35
Figure 4.18: Temperatures of the impingement plate without UWS injection viewed from the first ZnSe-window. a –temperature measured at OP1, b – OP3 .....	36
Figure 4.19: Impact of the spray characteristics and the injection rate on the wall cooling at OP3 .....	37
Figure 4.20: a - solid deposits after 20 min of injection, b - temperature of the impingement plate. OP3, injector 1, injection rate 132 mg/s.....	38
Figure 4.21: Photographs of deposits generated at operating points 5a – 5c. ....	40
Figure 4.22: Photographs of deposits generated at operating points 5d – 5f.....	41
Figure 4.23: Transient operating conditions of WP 6. a - change of the gas temperature, b - change of the gas mass flow.....	42
Figure 4.24: Results of measurement № 9. a - solid deposits at the end of the accumulation phase, b - solid deposits at the end of the decomposition phase.....	44
Figure 4.25: Results of measurement № 21. a - solid deposits at the end of the accumulation phase, b - solid deposits at the end of the decomposition phase.....	45
Figure 4.26: Thermogravimetric decomposition of urea and its by-products. Experiments are performed with an initial sample mass of 5 – 6 mg in the cylinder-type crucible using a heating rate of 2 K min <sup>-1</sup> . ....	46
Figure 4.27: Effect of experimental boundary conditions on urea thermal decomposition. Experiments are performed using different initial sample masses and cylinder types, but an identical heating rate of 2 K min <sup>-1</sup> . ....	46
Figure 4.28: Mean residual mass from thermogravimetric decomposition of urea and its by-products.....	47
Figure 4.29: NMR analysis results of ammelide residue at 600°C.....	47
Figure 4.30: Geometrical setup for numerical simulation of thermogravimetric decomposition of various samples. ....	48
Figure 4.31: Illustration of CFD Geometry of the lab test bench at KIT.....	49

Figure 4.32: Numerical mesh of the measuring section.....	50
Figure 4.33: Workflow of submodels to simulate deposit formation and decomposition .....	51
Figure 4.34: Droplet drag coefficients modeled with original and modified Schiller-Naumann correlation for the relative slip velocity between the phases at 20 m/s. ....	53
Figure 4.35: Modified Bai-Onera wall impingement model .....	54
Figure 4.36: Impingement regime of thermal induced breakup [77].....	55
Figure 4.37: The mass fraction of droplets that spread on the surface in splash (red line) and TBU regime (black line) .....	56
Figure 4.38: Evaporation probability of droplets of different size on a hot surface, $T_w > T_{crit}$ ...	57
Figure 4.39: Temperature impact on the mass and heat source for a given surface cell .....	61
Figure 4.40: Sketch of the DETCHEM <sup>MPTR</sup> model.....	61
Figure 4.41: Interface between StarCCM+ and DETCHEM based user code. Physical models in StarCCM+ solve for the concentrations in gas and liquid phase, the gas-liquid equilibrium and the heat balance. Species concentration, pressure, temperature, film thickness, cell area, time step and time data are transferred to the user code for each cell in the liquid film. Based on the MPTR algorithm, reaction rates are calculated by the user code and transferred to the chemistry model in StarCCM+. ....	66
Figure 4.42: Calculated stationary flow field and temperature distribution in TGA setup. ....	67
Figure 4.43: Thermogravimetric decomposition of cyanuric acid and triuret using a heating rate of 10 K min <sup>-1</sup> . Comparison of experimental data with results from 0D simulation in DETCHEM <sup>MPTR</sup> and 3D simulation in StarCCM+. ....	68
Figure 4.44: Simulation result for molar concentration of isocyanic acid in the liquid film during cyanuric acid decomposition in StarCCM+. ....	68
Figure 4.45: Thermogravimetric decomposition of biuret and urea using a heating rate of 10 K min <sup>-1</sup> . Comparison of experimental data with results from 0D simulation in DETCHEM <sup>MPTR</sup> and 3D simulation in StarCCM+. ....	69
Figure 4.46: Comparison of the production rates of selected species during urea decomposition calculated by the 0D batch reactor and the 3D CFD model. ....	70
Figure 4.47: Thermogravimetric decomposition of 27.5 mg urea water solution using a heating rate of 10 K min <sup>-1</sup> . Comparison of experimental data with results from 0D simulation in DETCHEM <sup>MPTR</sup> and 3D simulation in StarCCM+. ....	70
Figure 4.48: Simulated film thickness for OP 4a at different time intervals after start of injection. ....	72
Figure 4.49: Liquid film formation for OP 4a at different time intervals after start of injection. The rectangular dark shadow is a result from the measurement setup. The three figures display the same image section and identical scaling compared to Figure 4.48. ....	73
Figure 4.50: Experimental and simulated wall temperature distribution in °C at the end of injection, t = 10 s, at OP 4a. ....	74
Figure 4.51: Experimental and simulated film thickness for OP 4b at the end of injection, t = 10 s. ....	75
Figure 4.52: Experimental and simulated wall temperature distribution for OP 4b at the end of injection, t = 10 s. ....	76
Figure 4.53: By-product formation from liquid urea at OP 1 after t=1s. ....	77
Figure 4.54: Liquid film thickness and by-product formation from liquid urea at OP 4b after t = 4 min. ....	78

Figure 4.55: Simulated (b) and measured (a) temperature fields of the impingement plate without UWS injection. OP 2, exhaust gas temperature – 275 °C, mass flow - 1000 kg/h ....	80
Figure 4.56: Simulated and measured droplet size distribution at the measurement positions P1-P4. OP 1 and 3, injector 3.....	81
Figure 4.57: Temperature drop at the bottom side of the impingement plate. a – OP 2, injector 1, injection rate 18 mg/s. b – OP 3, injector 2, injection rate 14 mg/s. ....	82
Figure 4.58: Impingement heat and urea mass source at the beginning of the simulation (a) and after 216 second of the solution time (b). OP 3, injector 1, injection rate 132 mg/s.....	83
Figure 4.59: Film and deposit formation on the impingement plate. a – simulated film thickness, b – simulated thickness of solid deposits, c – experimental result. OP3, injector 1, injection rate 132 mg/s.....	84
Figure 4.60: Simulated and measured temperature drop at the bottom side of the impingement plate. OP3, injector 1, injection rate 132 mg/s.....	84
Figure 4.61: Simulated mass of UWS and solid deposits. OP3, injector 1, injection rate 132 mg/s.....	85
Figure 4.62: Film and deposit formation on the impingement plate. a – simulated film thickness, b – simulated thickness of solid deposits, c – experimental result. OP3, injector 2, injection rate 61 mg/s.....	85
Figure 4.63: Simulated (a) and measured (b) temperature drop at the bottom side of the impingement plate. OP3, injector 2, injection rate 61 mg/s.....	86
Figure 4.64: Simulated mass of UWS - and solid deposit. OP3, injector 2, injection rate 61 mg/s .....	86
Figure 4.65: Film and deposit formation on the impingement plate. a – simulated film thickness, b – simulated thickness of solid deposits, c – experimental result. Transient measurement N <sup>o</sup> 5 .....	87
Figure 4.66: Simulated (a) and measured (b) temperature drop at the bottom side of the impingement plate. Transient measurement N <sup>o</sup> 5.....	88
Figure 4.67: Mass of UWS and solid deposits. Transient measurement N <sup>o</sup> 5.....	88
Figure 4.68: Phase diagram of eutectic mixture of urea and biuret adapted from Tischer et al. [92]. The orange dotted lines indicate a composition of 67 % biuret and 33 % urea leading to melting of biuret. ....	89
Figure 4.69: Experimental and simulation results on urea decomposition. Simulation results for the overall sample mass and the evolution and consumption of relevant species is compared to urea TGA data and deposit compositions at different temperatures. Temperatures of corresponding deposit compositions are the gas temperatures of different experiments. ....	90
Figure 6.1: Photograph of test rig setup showing the radial compressor, flowmeter and heater (left to right). Heated sections up- and downstream of the measurement section are installed inside a housing for safety reasons. ....	107
Figure 6.2: Droplet size distribution for the applied 3-hole injector measured without incident flow. ....	107
Figure 6.3: Calibration of UWS mass flow for the applied 3-hole injector. ....	107
Figure 6.4: Photograph of deposits generated at OP 5e at the tunnel behind the measuring cell. ....	108
Figure 6.5: NMR analysis results of triuret residue at 600°C. ....	108
Figure 6.6: NMR analysis results of ammeline residue at 600°C. ....	108

Figure 6.7: Experimental and simulated film thickness for OP 4c at the end of injection, $t = 10$ s. ....	117
Figure 6.8: Experimental and simulated wall temperature distribution for OP 4c at the end of injection, $t = 10$ s. ....	118
Figure 6.9: Simulation of the decomposition of derived deposits from OP 0 and 1 using the revised model. ....	119
Figure 6.10: Simulation of the decomposition of derived deposits from OP 2 and 3 using the revised model. ....	119

#### 6.4 List of tables

Table 3.1: Physical properties of urea and relevant by-products decomposition prior to melting	* in water (20°C)	**
	10	
Table 4.1: Operating range of test rig for investigations on deposit formation. ....	19	
Table 4.2: Spray characteristics of the 3 investigated injectors .....	22	
Table 4.3: Measurement accuracy for quantitative determination of different components by HPLC analysis .....	24	
Table 4.4: Lab test bench operating conditions for multiple injection experiments at steady state.....	24	
Table 4.5: Topographical data of derived deposits at different operating conditions.....	25	
Table 4.6: HPLC analysis results of derived deposits from lab test bench at steady conditions. All results are given in %.....	29	
Table 4.7: HPLC analysis results of derived deposits from lab test bench at steady conditions. All results are given in %.....	31	
Table 4.8: Deposit mass of experiments with and without additional water for OP 0 – 3. ....	31	
Table 4.9: Steady-state operating conditions of WP 2.....	32	
Table 4.10: Measurements matrix of WP 2 “Experiment I” .....	32	
Table 4.11: Radiation properties of the surfaces in the optical box.....	36	
Table 4.12: Lab test bench operating conditions for multiple injection experiments at transient conditions. ....	39	
Table 4.13: Total deposit mass and HPLC analysis results of derived deposits from lab test bench at transient conditions. Composition results are given in %.....	40	
Table 4.14: Measurement matrix of WP6 “Experiment II” .....	43	
Table 4.15: Kinetic model for urea decomposition adapted and enhanced from Brack et al. [37]. ....	63	
Table 4.16: Component mapping of liquid species to their corresponding gas phase species in StarCCM+ Multiphase Interaction Model.....	65	
Table 4.17: Experimentally determined composition for deposits derived at OP 4b in comparison to simulation data resulting after different physical time instants and deposit mass divided by total injected mass. ....	79	
Table 6.1: Polynomial data for the heat capacity of the solid wall used in the CFD simulation in StarCCM+ for KIT lab test bench. The solid wall consists of stainless steel. ....	109	

---

Table 6.2: Polynomial data for the thermal conductivity of the solid wall used in the CFD simulation in StarCCM+ for KIT lab test bench. The solid wall consists of stainless steel...	109
Table 6.3: Property data for all gas phase species for calculations in DETCHEM and StarCCM+. Due to requests of the evaporation model in StarCCM+, corresponding gas phase species have to be defined for all species present in the liquid phase. *calculation based on polynomial data given in Table 6.6 ** calculation based on NASA polynomial data given in .....	109
Table 6.4: Property data for all aqueous and liquid species for calculations in DETCHEM and StarCCM+. Solid species in DETCHEM are defined as pseudo-liquid species in StarCCM+. * calculation based on polynomial data given in Table 6.6 ** calculation based on NASA polynomial data given in Table 6.7.....	110
Table 6.5: Property data for all aqueous and liquid species for calculations in DETCHEM and StarCCM+. Solid species in DETCHEM are defined as pseudo-liquid species in StarCCM+. * calculation based on polynomial data given in Table 6.6 ** calculation based on NASA polynomial data given in Table 6.7.....	111
Table 6.6: Polynomial data for calculation of thermophysical properties in addition to Table 6.3 and Table 6.4.....	111
Table 6.7: NASA polynomial data for calculation of thermophysical properties in DETCHEM and in StarCCM+. The table includes all species in respective phases included in the kinetic model.....	114
Table 6.8: Reactions of ammeline decomposition implemented to the revised kinetic model [92].....	118

## 6.5 Attachments



Figure 6.1: Photograph of test rig setup showing the radial compressor, flowmeter and heater (left to right). Heated sections up- and downstream of the measurement section are installed inside a housing for safety reasons.

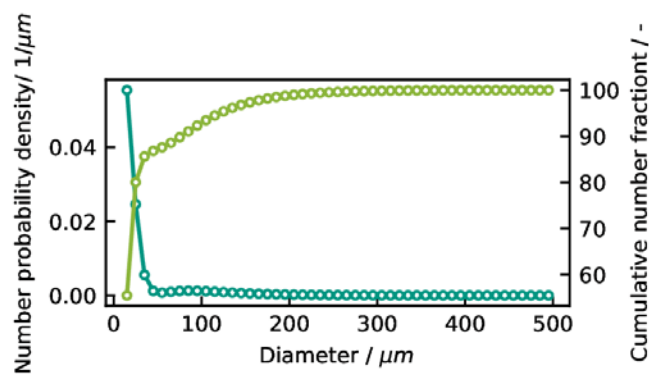
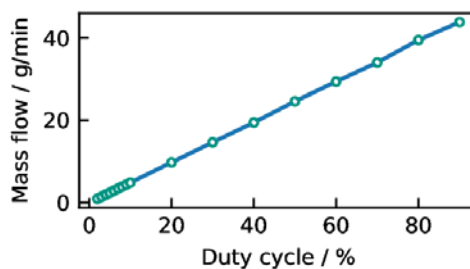


Figure 6.2: Droplet size distribution for the applied 3-hole injector measured without incident flow.



(a) 3-hole

Figure 6.3: Calibration of UWS mass flow for the applied 3-hole injector.

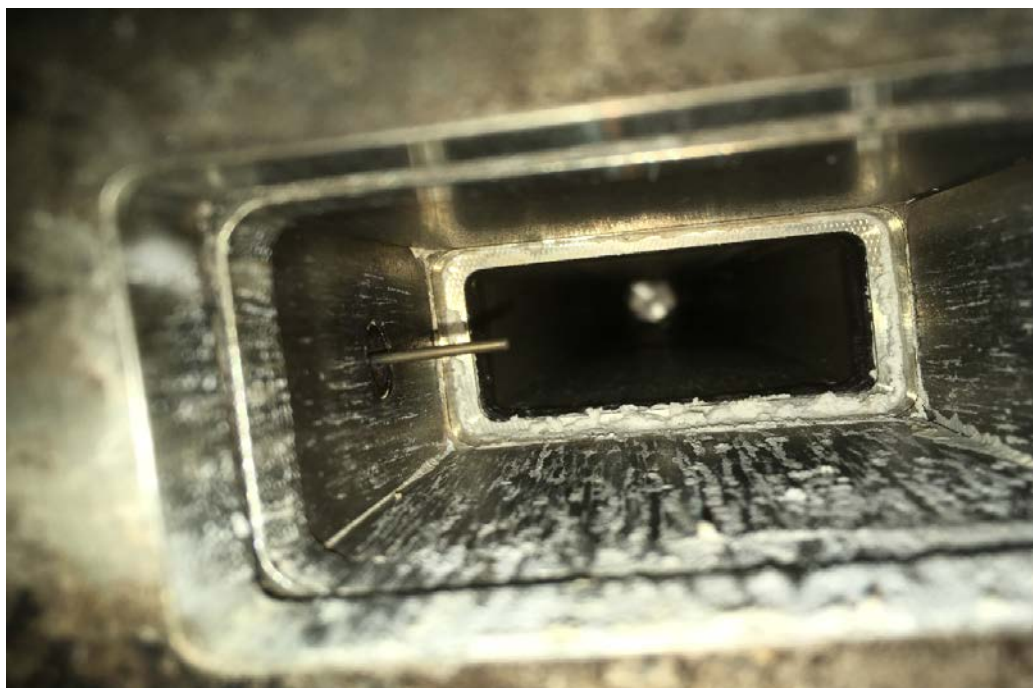


Figure 6.4: Photograph of deposits generated at OP 5e at the tunnel behind the measuring cell.

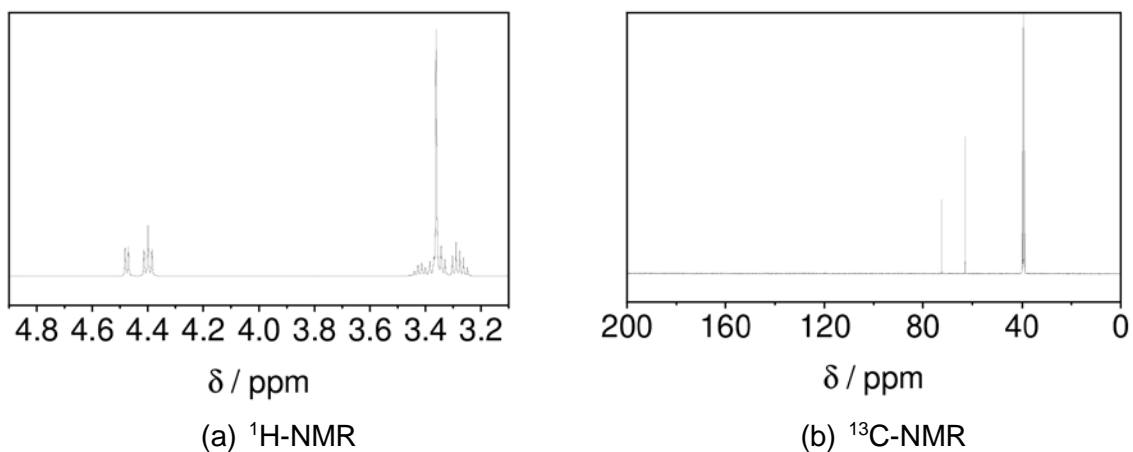


Figure 6.5: NMR analysis results of triuret residue at 600°C.

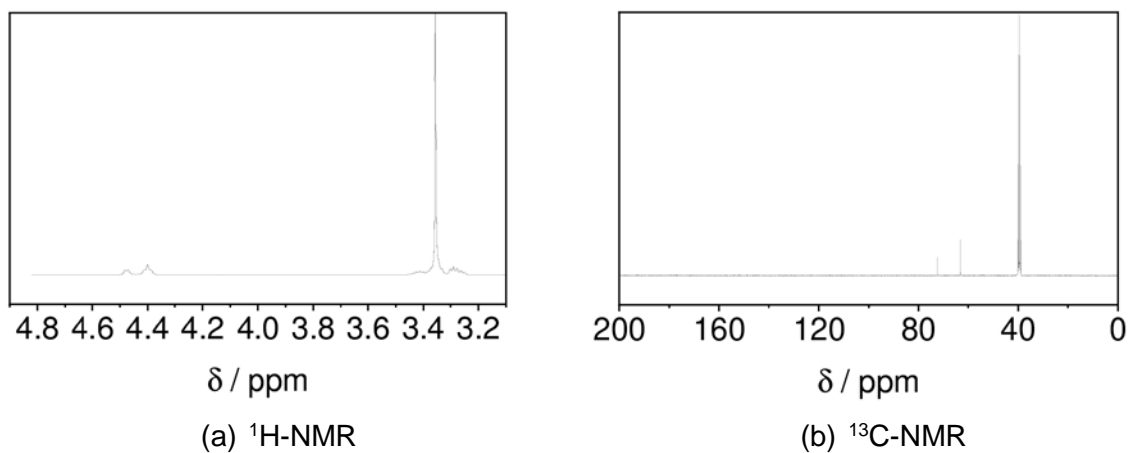


Figure 6.6: NMR analysis results of ammeline residue at 600°C.

**Table 6.1: Polynomial data for the heat capacity of the solid wall used in the CFD simulation in StarCCM+ for KIT lab test bench. The solid wall consists of stainless steel.**

Interval / K	Heat capacity / $\text{J kg}^{-1} \text{K}^{-1}$
273.15 – 473.15	$483.713889 + 0.055555 \cdot T$
473.15 – 673.15	$415.37 + 0.2 \cdot T$
673.15 – 873.15	$432.19875 + 0.175 \cdot T$
873.15 – 1073.15	$388.54125 + 0.225 \cdot T$

**Table 6.2: Polynomial data for the thermal conductivity of the solid wall used in the CFD simulation in StarCCM+ for KIT lab test bench. The solid wall consists of stainless steel.**

Interval / K	Thermal conductivity / $\text{W m}^{-1} \text{K}^{-1}$
273.15 – 373.15	$10.2363125 + 0.01625 \cdot T$
373.15 – 473.15	$11.8222 + 0.012 \cdot T$
473.15 – 573.15	$6.1444 + 0.024 \cdot T$
573.15 – 673.15	$10.7296 + 0.016 \cdot T$
673.15 – 1073.15	$15.44165 + 0.009 \cdot T$

**Thermophysical properties of relevant species for calculations in DETCHEM and StarCCM+**

Table 6.3 to 6.7 present thermophysical property data for all species involved in the simulations in both DETCHEM and StarCCM+. Species and respective properties are defined for each phase they might occur in. The DETCHEM<sup>MPTR</sup> model represents a batch reactor containing four phases: gas, liquid, aqueous and solid phase. Phase transitions are handled by two different species, e. g.  $\text{H}_2\text{O}(\text{l})$  and  $\text{H}_2\text{O}(\text{g})$  for the evaporation of water. The CFD model in StarCCM+ is limited to two phases: gas phase and liquid phase (spray and film). However, in the chemical calculations by the user code, which is applied for the liquid film cells, the liquid phase is divided to several phases defined in the DETCHEM<sup>MPTR</sup> model: liquid, aqueous and solid. Here, solid species are modeled as pseudo-liquids. In Table 6.3, property data for the gas phase species in DETCHEM and StarCCM+ is provided. Further properties required for simulations in StarCCM+ are taken from the internal species database of the software. Property data not available in literature or DETCHEM are approximated with water vapor data. For the simulation in StarCCM+ an enthalphy shift for gas and corresponding liquid species as described in the SCR Best Practice Guide [83] is done to have increased numerical stability. Therefore, all gas phase species have a Heat of Formation of 0 J/kg and the specific heat is calculated by polynomial data given in Table 6.6.

**Table 6.3: Property data for all gas phase species for calculations in DETCHEM and StarCCM+. Due to requests of the evaporation model in StarCCM+, corresponding gas phase species have to be defined for all species present in the liquid phase.**

\* calculation based on polynomial data given in Table 6.6

\*\* calculation based on NASA polynomial data given in Table 6.7

	Formular	Molecular weight	Density	Dynamic viscosity	Thermal conductivity	Heat capacity
Symbol		$M$	$\rho$	$\eta$	$\lambda$	$c_p$
Unit		g mol <sup>-1</sup>	kg m <sup>-3</sup>	Pa s	W m <sup>-1</sup> K <sup>-1</sup>	J kg <sup>-1</sup> K <sup>-1</sup>
Ammonia	NH <sub>3</sub>	17.03	0.7025	1.03E-05	0.0246	* / **
Carbon Dioxide	CO <sub>2</sub>	44.01	1.8082	1.49E-05	0.0170	* / **
Water	H <sub>2</sub> O	18.01	0.5953	*	*	* / **
Isocyanic acid	HNCO	43.03	0.5953	1.27E-05	0.0253	* / **
Air		28.97	1.1842	*	0.0260	* / **
Urea	CH <sub>4</sub> N <sub>2</sub> O	60.06	0.5953	1.27E-05	0.0253	* / **

Table 6.4 presents property data for all species in the liquid and aqueous phase. In addition, solid species data, which are defined as pseudo-liquid in StarCCM+, is given. If available, properties are calculated in dependence on temperature. Respective polynomial and NASA polynomial data is given in Table 6.6 and Table 6.7.

**Table 6.4: Property data for all aqueous and liquid species for calculations in DETCHEM and StarCCM+. Solid species in DETCHEM are defined as pseudo-liquid species in StarCCM+.**

\* calculation based on polynomial data given in Table 6.6

\*\* calculation based on NASA polynomial data given in Table 6.7.

	Formular	Phase	Molecular weight	Density	Dynamic viscosity	Thermal conductivity
Symbol			$M$	$\rho$	$\eta$	$\lambda$
Unit			g mol <sup>-1</sup>	kg m <sup>-3</sup>	Pa s	W m <sup>-1</sup> K <sup>-1</sup>
Urea	CH <sub>4</sub> N <sub>2</sub> O	l, aq	60.06	1320	*	*
Isocyanic acid	HNCO	l, aq	43.03	1140	1.49E-05	0.5000
Ammonia	NH <sub>3</sub>	l, aq	17.03	700	1.49E-05	0.5000
Carbon Dioxide	CO <sub>2</sub>	aq	44.01	2	1.49E-05	0.0170
Water	H <sub>2</sub> O	l	18.01	998	8.89E-04	0.6203
Urea	CH <sub>4</sub> N <sub>2</sub> O	l	60.06	1320	1.00E-01	*
Cyanuric acid	C <sub>3</sub> H <sub>3</sub> N <sub>3</sub> O <sub>3</sub>	s / pseudo l	129.09	2500	1.00E-01	0.5000
Biuret	C <sub>2</sub> H <sub>5</sub> N <sub>3</sub> O <sub>2</sub>	s / pseudo l	103.09	1470	1.00E-01	0.5000
Triuret	C <sub>3</sub> H <sub>6</sub> N <sub>4</sub> O <sub>3</sub>	s / pseudo l	146.12	1547	1.00E-01	0.5000
Ammeline	C <sub>3</sub> H <sub>5</sub> N <sub>5</sub> O	s / pseudo l	127.11	2220	1.00E-01	0.5000
Ammelide	C <sub>3</sub> H <sub>4</sub> N <sub>4</sub> O <sub>2</sub>	s / pseudo l	128.11	1573	1.00E-01	0.5000

**Table 6.5: Property data for all aqueous and liquid species for calculations in DETCHEM and StarCCM+. Solid species in DETCHEM are defined as pseudo-liquid species in StarCCM+.**

\* calculation based on polynomial data given in Table 6.6

\*\* calculation based on NASA polynomial data given in Table 6.7.

	Formular	Heat capacity	Critical Temperature	Saturation Pressure
Symbol		$c_p$	$T_{cr}$	$p_{sat}$
Unit		J kg <sup>-1</sup> K <sup>-1</sup>	K	Pa
Urea	CH <sub>4</sub> N <sub>2</sub> O	**	647.12	*
Isocyanic acid	HNCO	**	647.12	*
Ammonia	NH <sub>3</sub>	**	405.4	1.00E+06
Carbon Dioxide	CO <sub>2</sub>	**	304.21	6.43E+06
Water	H <sub>2</sub> O	**	647.12	*
Urea	CH <sub>4</sub> N <sub>2</sub> O	**	1073.15	*
Cyanuric acid	C <sub>3</sub> H <sub>3</sub> N <sub>3</sub> O <sub>3</sub>	**	1073.15	*
Biuret	C <sub>2</sub> H <sub>5</sub> N <sub>3</sub> O <sub>2</sub>	**	1073.15	*
Triuret	C <sub>3</sub> H <sub>6</sub> N <sub>4</sub> O <sub>3</sub>	**	773.15	*
Ammeline	C <sub>3</sub> H <sub>5</sub> N <sub>5</sub> O	**	1073.15	*
Ammelide	C <sub>3</sub> H <sub>4</sub> N <sub>4</sub> O <sub>2</sub>	**	1073.15	*

Table 6.6 lists polynomial data for calculation of species property data as indicated in Table 6.3, Table 6.4 and Table 6.5. Data is based on [92] or adapted as described in Section 4.3.4.

**Table 6.6: Polynomial data for calculation of thermophysical properties in addition to Table 6.3 and Table 6.4.**

Species	Property	T-Range / K	Polynomial
H <sub>2</sub> O (g)	$\eta$	273 - 1073	$2.37183 \times 10^{-6} + 9.58814 \times 10^{-9} \cdot T + 6.24661 \times 10^{-11} \cdot T^2 - 5.13493 \times 10^{-14} \cdot T^3 + 1.45102 \times 10^{-17} \cdot T^4$
	$\lambda$	273 - 1073	$6.90656 \times 10^{-3} + 1.12857 \times 10^{-5} \cdot T + 1.0834 \times 10^{-7} \cdot T^2 - 2.92043 \times 10^{-11} \cdot T^3$
	$c_p$	273 - 1073	$1937.7631 - 0.939844469 \cdot T + 0.00300928201 \cdot T^2 - 2.5327997 \times 10^{-6} \cdot T^3 + 8.17802463 \times 10^{-10} \cdot T^4$
Air	$\eta$		$-1.53230385 \times 10^{-7} + 7.94253829 \times 10^{-8} \cdot T - 6.97884315 \times 10^{-11} \cdot T^2 + 4.63380267 \times 10^{-14} \cdot T^3 - 1.25268703 \times 10^{-17} \cdot T^4$
	$c_p$	273 - 1073	$1019.94 - 0.0033436 \cdot T - 8.01623 \times 10^{-4} \cdot T^2 + 3.28637 \times 10^{-6} \cdot T^3 - 4.24779 \times 10^{-9} \cdot T^4 + 2.39922 \times 10^{-12} \cdot T^5 - 5.11598 \times 10^{-16} \cdot T^6$
HNCO (aq → g)	$c_p$	273 - 1073	$1047.47236 + 0.74928133 \cdot T - 2.61881 \times 10^{-4} \cdot T^2 + 4.17186 \times 10^{-8} \cdot T^3 - 2.48382 \times 10^{-12} \cdot T^4$

## 6 Appendix

HNCO (g)	$c_p$	273 - 1073	$432.837715 + 2.813341325 \cdot T - 0.00298245 \cdot T^2 + 1.65309 \times 10^{-6} \cdot T^3 - 3.4709 \times 10^{-10} \cdot T^4$
NH <sub>3</sub> (aq → g)	$c_p$	273 - 1073	$2608.997089 + 2.703930044 \cdot T + 0.010321184 \cdot T^2 - 9.90321 \times 10^{-6} \cdot T^3 + 3.36617 \times 10^{-9} \cdot T^4$
NH <sub>3</sub> (g)	$c_p$	273 - 1073	$2177.754886 - 2.776812966 \cdot T - 9.63818 \times 10^{-6} \cdot T^2 + 1.46869 \times 10^{-6} \cdot T^3 - 8.35801 \times 10^{-9} \cdot T^4$
Urea (aq → g)	$c_p$	273 - 573	$29026.8253 - 376.504722 \cdot T + 2.18420144 \cdot T^2 - 0.00673771954 \cdot T^3 - 1.16696573 \times 10^{-5} \cdot T^4 - 1.07307408 \times 10^{-8} \cdot T^5 + 4.0867648 \times 10^{-12} \cdot T^6$
		573 - 1073	$1356.868 + 2.25 \cdot T$
Urea (g)	$c_p$	273 - 1073	$-29.1692715 + 6.048893603 \cdot T - 0.006376417 \cdot T^2 + 3.27465 \times 10^{-6} \cdot T^3 - 6.11953 \times 10^{-10} \cdot T^4$
H <sub>2</sub> O (l)	$p_{sat}$	254 - 393	$-6.65755 \times 10^6 + 124987 \cdot T - 958.934 \cdot T^2 + 3.80451 \cdot T^3 - 0.00805133 \cdot T^4 + 8.19161 \times 10^{-6} \cdot T^5 - 2.66457 \times 10^{-9} \cdot T^6$
		393 - 5000	$202148 + 10 \cdot T$
Urea(l)	$\eta$	273 - 400	$2.44024 - 0.0327148 \cdot T + 0.000179418 \cdot T^2 - 4.98844 \times 10^{-7} \cdot T^3 + 6.9968 \times 10^{-10} \cdot T^4 - 3.94748 \times 10^{-13} \cdot T^5$
		400 - 800	$0.00477248$
	$\lambda$	273 - 633	$-1.34605 + 0.0144816 \cdot T - 3.87469 \times 10^{-5} \cdot T^2 + 4.85345 \times 10^{-8} \cdot T^3 - 2.61234 \times 10^{-11} \cdot T^4$
		633 - 800	$0.411306$
	$p_{sat}$	273 - 323	$0$
		323 - 363	$-1662.86 + 24.6745 \cdot T + 0.000179418 \cdot T^2 + 0.000434507 \cdot T^3 - 6.4457 \times 10^{-7} \cdot T^4 + 3.82449 \times 10^{-10} \cdot T^5$
		363 - 393	$-491184 + 6796.16 \cdot T - 37.6184 \cdot T^2 + 0.104128 \cdot T^3 - 0.000144134 \cdot T^4 + 7.98175 \times 10^{-8} \cdot T^5$
		393 - 433	$-8.81261 \times 10^7 + 1.08849 \times 10^6 \cdot T - 5378.35 \cdot T^2 + 13.2892 \cdot T^3 - 0.0164202 \cdot T^4 + 8.11673 \times 10^{-6} \cdot T^5$
		433 - 473	$24201.9 + 2.19083 \times 10^6 \cdot T - 19776.1 \cdot T^2 + 66.952 \cdot T^3 - 0.100759 \cdot T^4 + 5.68755 \times 10^{-5} \cdot T^5$
		473 - 487	$310000 + 3.02338 \times 10^7 \cdot T - 257239 \cdot T^2 + 821.075 \cdot T^3 - 1.1653 \cdot T^4 + 0.000620479 \cdot T^5$
		487 - 1073	$195122 + 10 \cdot T$
	$\lambda$	273 - 633	$-1.34605 + 0.0144816 \cdot T - 3.87469 \times 10^{-5} \cdot T^2$

Urea (s / pseudo-l)			$+ 4.85345 \times 10^{-8} \cdot T^3 - 2.61234 \times 10^{-11} \cdot T^4$
	$p_{sat}$	633 - 800	0.411306
		273 - 923	$0.001 + 1.28571 \times 10^{-5} \cdot T$
		923 - 973	$-3.6926 \times 10^6 + 4000 \cdot T$
		973 - 1073	200000
Isocyanic acid (l)	$p_{sat}$	223 - 973	$-14.4064 + 0.509877 \cdot T - 0.0649997 \cdot T^2 + 4.04446 \times 10^{-5} \cdot T^3 - 1.31466 \times 10^{-7} \cdot T^4 + 2.09294 \times 10^{-7} \cdot T^5 - 1.20866 \times 10^{-13} \cdot T^6$
Cyanuric acid, Biuret, Triuret, Ammeline, Ammelide (s / pseudo-l)	$p_{sat}$	273 - 923	$0.001 + 1.28571 \times 10^{-5} \cdot T$
		923 - 973	$-3.6926 \times 10^6 + 4000 \cdot T$
		973 - 1073	200000

In addition to property data presented above, NASA polynomial data given by the DETCHEM database is used for the simulations. Table 6.7 presents data for all species in all (possible) phases.

**Table 6.7: NASA polynomial data for calculation of thermophysical properties in DETCHEM and in StarCCM+. The table includes all species in respective phases included in the kinetic model.**

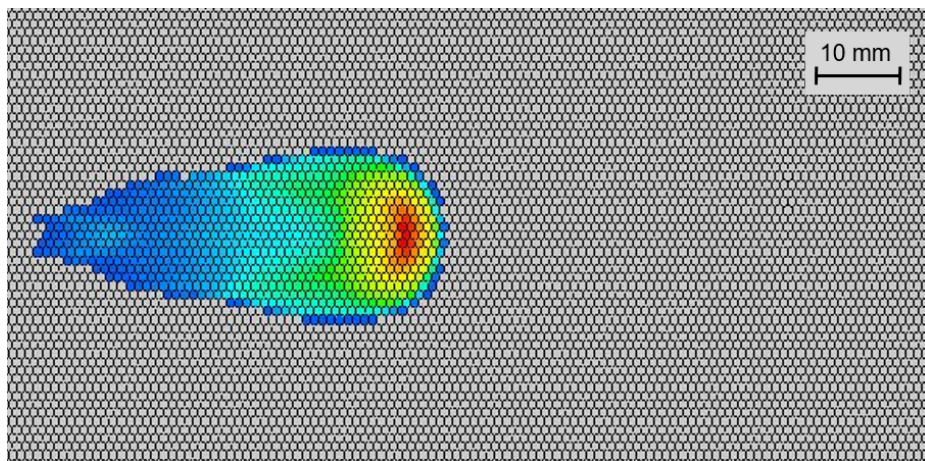
Species	T-Range / K	Coefficients						
		a <sub>1</sub>	a <sub>2</sub>	a <sub>3</sub>	a <sub>4</sub>	a <sub>5</sub>	a <sub>6</sub>	a <sub>7</sub>
NH <sub>3</sub> (g)	200 -1000	2.2043	0.0101	-1.47E-05	1.45E-08	-5.33E-12	-6525.4800	8.1273
	1000 - 5000	2.4619	0.0061	-2.00E-06	3.14E-10	-1.94E-14	-6493.2700	7.4721
CO <sub>2</sub> (g)	200 -1000	2.2757	0.0099	-1.04E-05	6.87E-09	-2.12E-12	-48373.2000	10.1886
	1000 - 5000	4.4536	0.0031	-1.28E-06	2.39E-10	-1.67E-14	-48967.0000	-0.9554
H <sub>2</sub> O (g)	200 – 1000	3.3869	0.0035	-6.35E-06	6.97E-09	-2.51E-12	-30208.1000	2.5902
	1000 - 5000	2.6722	0.0031	-8.73E-07	1.20E-10	-6.39E-15	-29899.2000	6.8628
HNCO (g)	200 – 1000	2.2401	0.0146	-1.54E-05	8.56E-09	-1.80E-12	-15459.0000	12.1662
	1000 - 5000	5.3005	0.0040	-1.41E-06	2.24E-10	-1.33E-14	-16199.5000	-3.1177
Urea (g)	200 – 1000	-0.2107	0.0437	-4.61E-05	2.37E-08	-4.42E-12	-7109.16901	26.0663
	1000 - 5000	10.3465	0.0090	-3.10E-06	4.90E-10	-2.89E-14	-9702.11531	-26.9745
Urea (l)	100 – 500	11.1862	0.0000	0.00E+00	0.00E+00	0.00E+00	-25645.821	-46.7960
	500 - 1000	11.1862	0.0000	0.00E+00	0.00E+00	0.00E+00	-25645.821	-46.7960
Urea (aq)	273 – 1000	5.2081	0.0088	-3.77E-06	6.09E-10	-3.26E-14	-24220.4558	-17.4688
	1000 - 5000	5.2081	0.0088	-3.77E-06	6.09E-10	-3.26E-14	-24220.4558	-17.4688
HNCO (l)	300 – 1000	11.7417	-0.0222	3.87E-05	-2.61E-08	6.24E-12	-20626.4000	-45.1280
	1000 – 5000	11.7417	-0.0222	3.87E-05	-2.61E-08	6.24E-12	-20626.4000	-45.1280
HNCO (aq)	273 – 500	5.4210	0.0039	-1.36E-06	2.16E-10	-1.29E-14	-20349.9000	-18.3046
	500 – 1000	5.4210	0.0039	-1.36E-06	2.16E-10	-1.29E-14	-20349.9000	-18.3046
NH <sub>3</sub> (l)	200 – 400	9.4797	-0.0218	3.81E-05	-2.48E-08	5.73E-12	-10392.8000	-37.4317
	400 - 1000	9.4797	-0.0218	3.81E-05	-2.48E-08	5.73E-12	-10392.8000	-37.4317

NH <sub>3</sub> (aq)	273 – 373	5.3441	0.0055	-1.97E-06	3.01E-10	-1.71E-14	-9551.8400	-17.8384
	373 - 1000	5.3441	0.0055	-1.97E-06	3.01E-10	-1.71E-14	-9551.8400	-17.8384
CO <sub>2</sub> (aq)	200 – 1000	2.2757	0.0099	-1.04E-05	6.87E-09	-2.12E-12	-48373.2000	10.1886
	1000 – 5000	4.4536	0.0031	-1.28E-06	2.39E-10	-1.67E-14	-48967.0000	-0.9554
H <sub>2</sub> O (l)	200 – 1000	12.7128	-0.0177	-2.26E-05	2.08E-07	-2.41E-10	-37483.2000	-59.1153
	1000 - 5000	-60.0837	0.0000	0.00E+00	0.00E+00	0.00E+00	22858.0000	424.0100
Urea (s/pseudo-l)	200 – 500	11.1862	0.0000	0.00E+00	0.00E+00	0.00E+00	-27392.2727	-51.0992
	500 – 1000	11.1862	0.0000	0.00E+00	0.00E+00	0.00E+00	-27392.2727	-51.0992
Cyanuric acid (s/pseudo-l)	273 – 1000	1.8930	0.0505	-2.41E-05	2.27E-13	-1.04E-16	-87211.4000	-7.6676
	1000 – 1000	1.8930	0.0505	-2.41E-05	2.27E-13	-1.04E-16	-87211.4000	-7.6676
Biuret (s/pseudo-l)	100 – 500	1.8930	0.0505	-2.41E-05	2.16E-12	-9.61E-16	-70439.7000	16.0478
	500 – 1000	1.8930	0.0505	-2.41E-05	2.16E-12	-9.61E-16	-70439.7000	16.0478
Triuret (s/pseudo-l)	100 – 500	1.8930	0.0505	-2.41E-05	2.16E-12	-9.61E-16	-70439.7000	16.0478
	500 – 1500	1.8930	0.0505	-2.41E-05	2.16E-12	-9.61E-16	-70439.7000	16.0478
Ammeline (s/pseudo-l)	273 – 500	0.1090	0.0729	-6.95E-05	3.79E-08	-8.96E-12	-38757.3000	-1.6283
	500 – 1500	0.1090	0.0729	-6.95E-05	3.79E-08	-8.96E-12	-38757.3000	-1.6283
Ammelide (s/pseudo-l)	273 – 500	0.1090	0.0729	-6.95E-05	3.79E-08	-8.96E-12	-38757.3000	-1.6283
	500 - 1500	0.1090	0.0729	-6.95E-05	3.79E-08	-8.96E-12	-38757.3000	-1.6283



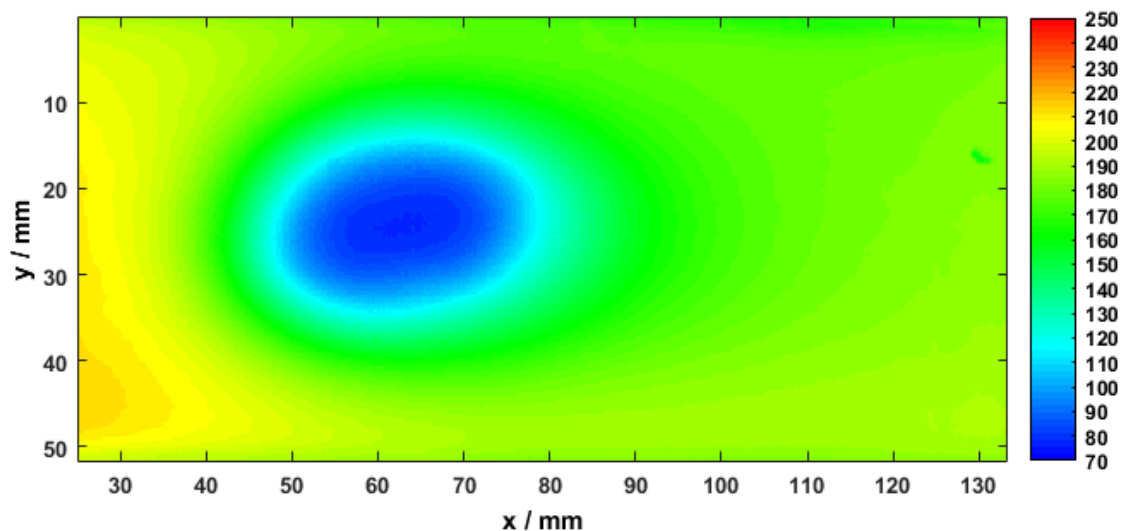


(a) Experiment

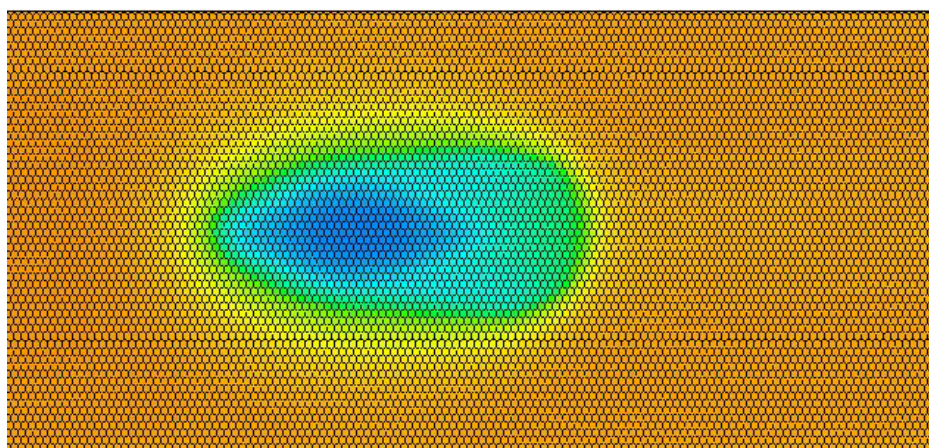


(b) Simulation

**Figure 6.7: Experimental and simulated film thickness for OP 4c at the end of injection,  $t = 10$  s.**



(a) Experiment



(b) Simulation

Figure 6.8: Experimental and simulated wall temperature distribution for OP 4c at the end of injection,  $t = 10$  s.

Table 6.8: Reactions of ammelide decomposition implemented to the revised kinetic model [92].

Reaction	$A_k$ (SI units)	$\beta_k$	$E_{A,k} / kJ mol^{-1}$
$3 \text{ ammd}(s) \rightarrow 2 \text{ ammn}(s) + \text{H}_2\text{NCN}(s) + \text{CO}_2(g)$	$1 \cdot 10^{10}$	0	165.67
$\text{ammn}(s) \rightarrow \text{HNCO}(g) + 2 \text{H}_2\text{NCN}(s)$	$5 \cdot 10^9$	0	165.67
$\text{ammn}(s) + 3 \text{H}_2\text{NCN}(s) \rightarrow \text{melem}(s) + \text{H}_2\text{O}(l) + \text{NH}_3$	$8 \cdot 10^{13}$	0	140.67
$\text{melem}(s) \rightarrow 6 \text{HCN}(g) + 2 \text{N}_2$	$6 \cdot 10^6$	0	165.67
$\text{H}_2\text{NCN}(s) \rightarrow \text{NH}(x) + \text{HCN}(g)$	$2 \cdot 10^5$	0	105.67
$3 \text{NH}(x) \rightarrow \text{NH}_3 + \text{N}_2$	$1 \cdot 10^5$	0	50.67

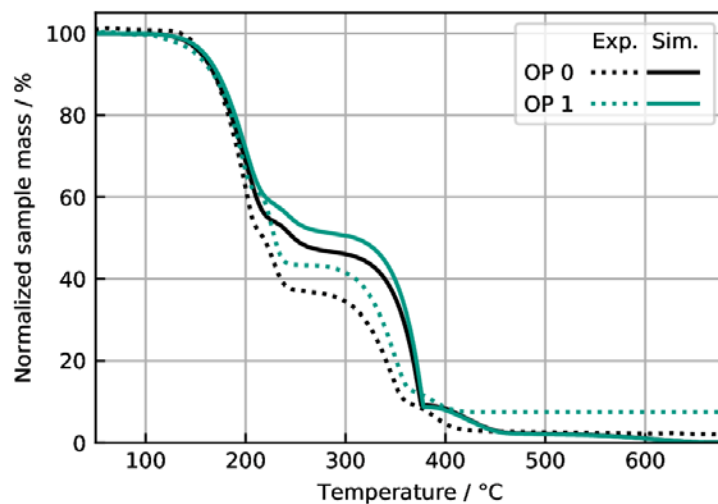


Figure 6.9: Simulation of the decomposition of derived deposits from OP 0 and 1 using the revised model.

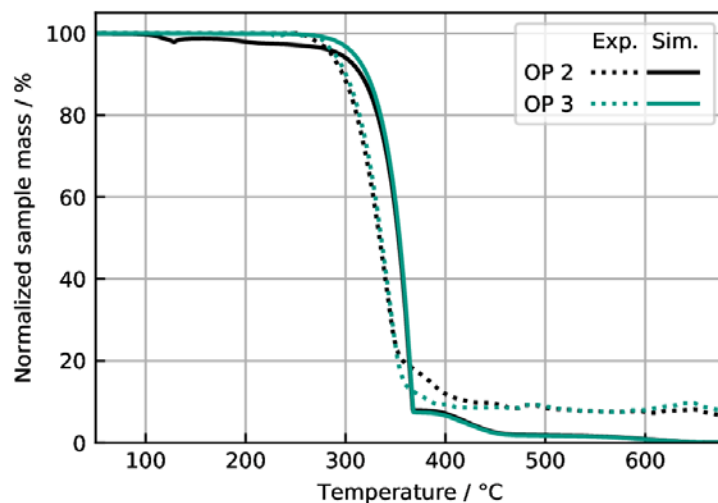


Figure 6.10: Simulation of the decomposition of derived deposits from OP 2 and 3 using the revised model.



**FÖRDERGEBER**  
FUNDING ORGANISATIONS

Bundesministerium für Wirtschaft und Energie  
Federal Ministry for Economic Affairs and Energy  
Arbeitsgemeinschaft industrieller Forschungsvereinigungen  
Federation of Industrial Research Associations

**KOOPERATIONEN**  
PARTNER ASSOCIATIONS

Forschungskuratorium Maschinenbau  
Mechanical Engineering Research Federation  
Verband Deutscher Maschinen- und Anlagenbau  
Mechanical Engineering Industry Association



**Forschungsvereinigung  
Verbrennungskraftmaschinen e.V.**  
Research Association  
for Combustion Engines

Lyoner Strasse 18  
60528 Frankfurt am Main, Germany

T +49 69 6603 1345

F +49 69 6603 2345

info@fvv-net.de

[www.fvv-net.de](http://www.fvv-net.de)